KNOWLEDGE GUIDED EMPIRICAL PREDICTION OF LANDSLIDE HAZARD

Saibal Ghosh

Examining committee

Prof.dr.ir. A. Stein	University of Twente
Prof.dr. F.D. van der Meer	University of Twente
Prof.dr. M. Jaboyedoff	UNIL, Switzerland
Dr. K. Ayyasami	GSITI, India
Dr. P. Reichenbach	CNR-IRPI, Italy

ITC dissertation number 190
ITC, P.O. Box 6, 7500 AA Enschede, The Netherlands

ISBN 978-90-6164-310-4
Cover designed by Benno Masselink / Job Duim
Printed by ITC Printing Department
Copyright © 2011 by Saibal Ghosh

UNIVERSITY OF TWENTE.

FACULTY OF GEO-INFORMATION SCIENCE AND EARTH OBSERVATION

KNOWLEDGE GUIDED EMPIRICAL PREDICTION OF LANDSLIDE HAZARD

DISSERTATION

to obtain
the degree of doctor at the University of Twente,
on the authority of the rector magnificus,
prof.dr. H. Brinksma,
on account of the decision of the graduation committee,
to be publicly defended
on Tuesday 5 July 2011 at 13:30 hrs

by

Saibal Ghosh

born on December 15, 1967

in Kolkata, India

This thesis is approved by
Prof. dr. Victor G. Jetten promotor
Dr. Cees J. Van Westen assistant promotor
Dr. Emmanuel John M. Carranza assistant promotor

Acknowledgements

My doctoral research would never have been completed had I not received the endless support from each of my revered teachers/supervisors, friends, colleagues and family members. I am indebted to my promotor, Prof. (Dr.) Victor G. Jetten and co-promotors Dr. Cees J. van Westen and Dr. Emmanuel John M. Carranza for considering me worthy of this research. I convey my special acknowledgements to Cees and John for supervising me at every step of my research and taking lot of pains in correcting and reviewing my scientific submissions. I consider myself extremely fortunate to get the opportunity to closely work with teachers like them and inculcated from them the principles like dedication to work, subtlety and criticality of scientific thinking, detailing of description and pruning of redundant issues etc. With their constant and able guidance, my sailing through this journey became smooth and enjoyable. I remain grateful to the Geological Survey of India for providing me this excellent opportunity of high-level research. I am immensely indebted to BGR, Hannover, Germany and CNR-IRPI, Perugia, Italy where I not only learned many modern techniques of landslide research but also got the opportunity to work with the eminent scientists like Dr. Andreas Günther (BGR), Dr. Fausto Guzzetti (CNR-IRPI), Dr. Paola Reichenbach (CNR-IRPI), and Dr. Mauro Cardinali (CNR-IRPI). I am grateful to all of them and Cees for the pains they took to visit my field area in Darjeeling Himalayas and for sharing their vast knowledge on the landsliding processes observed there. I am especially thankful to Dr. Mauro Cardinali (CNR-IRPI) for his unstinted support and guidance in my photo-interpretation work at GSI laboratory, Kolkata, India, which has been one of the founding pillars of my doctoral research. I also convey my sincere acknowledgements to Dr. Mauro Rossi (CNR-IRPI) for sharing his vast knowledge on computing about various geological applications. I would particularly like to acknowledge the intellectual and psychological supports I got from my two fellow research partners – Mr. Pankaj Jaiswal and Mr. Tapas Martha - at many of the critical junctures of my research. I must thank a number of ITC staff members: Dr. Paul van Dijk, Head (Research), Prof. Freek van der Meer, Chairman, ESA, Dr. Norman Kerle, Dr. Robert Hack, Gerard Reinink, Loes Colenbrander, Marion Pierik, Rébanna Spaan, Bettine Geerdink, Saskia Groenendijk, Aiko Mulder, Ard Kosters, Angel Sugiharto, Christie Agema, Ginie, Lakhsmi, Theresa van den Boogaard, Tineke Scholte, Benno Masselink, Job Duim and all others for their everlasting, and cordial assistance. I also thank to my Ph.D. colleagues in ESA department – Andre, Byron, Tolga, Sekhar, Enrique, Khamarrul, Xuanmei, Jahanzeb, Shaffique, Sumbal, Ajay, Prasun for their keen interest in science and sharing their own research experience with me. I cannot forget the association with my Indian brothers and sisters at ITC-Debanjan, Gourav, Paresh, Rishi, Iswar, Anandita, Maitreyi, Priyasmita,

Tanmoy, Divyani, Praveen, Sandip and all others with whom I shared many memorable moments there. I am indebted to Chinmoy Paul, Rabindra Nath Ghosh, D. N. Bhattacharya, T. B. Ghoshal, N. K. Sarkar, Shyamal Sinha, Nitish Das, Anshuman Acharya, M. Surendranath, Debasish Bhattacharya, Jaydip Mukherjee, Dipak Hazra, Tapan Paul, Abhinaba Roy, K. Ayyasami, Ashok Kumar, Samaresh Sanyal and Kanika Sanyal of GSI for their timely advice, suggestions, inspiration and help. I am also indebted to Dr. Sandip Som for sparing his valuable time for my DGPS survey. I owe special gratitude to Dr. Cees J. van Westen (my supervisor), Mr. N. Rajendran, Dr. L. P. Singh of GSI and Dr. Vinod Kumar (NRSC), without whose vision and active initiatives, this research project would never been envisaged and launched. I am grateful to my supervisor; Dr. Cees J. van Westen for translating the summary of my thesis in Dutch. I also thank the officials of the Sub-Divisional Office, the Municipality of Kurseong and the District Magistrate of Darjeeling for providing me the necessary logistics during fieldwork. But last and not the least, I dedicate my thesis to my wife (Rakhi) and son (Riju), without whose selfless sacrifice, I would never been able to see this day. I also convey my sincere gratitude to my mother-in-law (Khana Roy) and my younger brother (Saikat Ghosh), who took special care to look after my family whenever I was away from home.

Table of Contents

Acknowledgements ..... **i**
Table of Contents ..... **iii**

Chapter 1: Introduction **1**
1.1 Background 1
1.2 Landslide hazard and its prediction methods 2
1.2.1 Heuristic and data-driven methods of spatial prediction 3
1.2.2 Why are temporal and magnitude predictions difficult? 5
1.3 Research objectives 5
1.4 Research questions 6
1.5 Study area 7
1.5.1. Geology and structure 7
1.5.2 Topography and climate 9
1.6 Methodology and organisation of thesis 10

Chapter 2: Evaluating the existing method of landslide susceptibility mapping in India **13**
2.1 Introduction 13
2.2 BIS method of landslide susceptibility mapping 16
2.2.1 Rating and integration of factors 16
2.2.2 Validation of BIS landslide susceptibility maps 16
2.3 Empirical method of landslide susceptibility mapping 21
2.3.1. Comparison of WofE with LHEF ratings 21
2.3.2. WofE susceptibility maps and validation 24
2.4 Predictive capabilities of BIS and WofE methods 26
2.5 Conclusions and recommendations 27

Chapter 3: Generating event-based landslide inventory maps **29**
3.1. Introduction 29
3.2 Event based landslide inventory maps 31
3.2.1 Source data sets 31
3.2.2 Methods of landslide inventory mapping 32
3.3 Analysis of landslide inventories 33
3.4 Temporal probability estimation 38
3.4.1 DA modelling for rainfall - landslide event relationships 40
3.4.3 Calculation of exceedance probability 43
3.5 Magnitude probability estimation 44
3.5.1 Landslide magnitude-frequency analysis 44
3.5.2 Results and synthesis of magnitude-frequency analysis 44
3.6 Discussion 49

3.6.1 Incompleteness and data gaps in source data 49
3.6.2 Limitations in temporal probability estimation 50
3.6.3 Limitations in magnitude probability estimation 52
3.7 Conclusions 55

Chapter 4: Exploratory analysis of fault/ fracture and slope controls on rockslides 57
4.1 Introduction 57
4.2 Structures in Himalayan FTB and rock slope failures 58
4.3 Spatial patterns of rockslides 60
4.3.1 Fry analysis of point geo-objects 60
4.3.2 Application of Fry analysis for rockslide occurrences 62
4.3.4 Synthesis of Fry analysis on structural and topographic controls on rockslides 68
4.4 Spatial association of rockslides with fault/fractures and slope aspects 68
4.4.1 Distance distribution and proportion analysis 68
4.4.2 Spatial association of Sh_rs with faults/fractures and slope aspects 70
4.4.3 Synthesis of spatial association analyses 72
4.5 Spatial modelling of mutual fault/fracture and slope controls on rockslides 75
4.5.1 Conceptual framework 75
4.5.2 Evidential belief modelling 77
4.6 Discussion 87
4.7 Conclusions 90

Chapter 5: Rock slope instability analysis using structural orientations 93
5.1 Introduction 93
5.2 Input data 95
5.2.1 Field-based 3-D orientation data of rock discontinuities 95
5.2.2 Spatially distributed shear strength (Φ'_d) parameters 99
5.2.3 Digital topographic data 100
5.3 Spatial modelling of structural discontinuity orientations 101
5.3.1 DStM generation in Area A 101
5.3.2 DStM generation in Area B 103
5.4 Kinematical testing of rock slope instability 104
5.4.1 Identification of modes of rock slope failure 104
5.4.2 Rock slope instability in Area A 106
5.4.3 Rock slope instability in Area B 108
5.4.4 Evaluation of rock slope instability maps 109

5.5 Discussion 111
5.6 Conclusions 115

Chapter 6: Selecting and weighting of spatial factors of landslide susceptibility 117
6.1 Introduction 117
6.2 Data 119
6.3 Analytical methods 123
6.3.1 Spatial association analysis for categorical spatial factors 124
6.3.2 Spatial association analysis for continuous spatial factors 124
6.3.3 Weighting of predictors 126
6.4 Predictive models of landslide susceptibility 132
6.4.1 Weighted multi-class index overlay model using pre-selected predictors 132
6.4.2 Logistic regression model using all identified/mapped spatial factors 134
6.4.3 Model evaluation 135
6.5 Results 136
6.5.1 Spatial association analysis for categorical spatial factors 136
6.5.2 Spatial association analysis for continuous spatial factors 137
6.5.3 Weighting of spatial factors 139
6.5.4 Predictive modelling of susceptibility 141
6.6 Discussion 150
6.6.1 Modelling of predictor-target spatial associations 150
6.6.2 Pairwise modelling of predictor-target relationships 152
6.6.3 Integration of predictors and evaluation of susceptibility maps 153
6.7 Conclusions 154

Chapter 7: Integrating spatial, temporal and magnitude probability for medium-scale landslide hazard and risk estimation 157
7.1 Introduction 157
7.2 Source data sets and information 158
7.3 Landslide hazard and risk estimation methods 160
7.3.1 Prediction of landslide events and hazard scenarios 160
7.3.2 Landslide risk estimation 162
7.4 Results of hazard and risk estimation 166
7.4.1 Landslide hazard estimation 166
7.4.2 Landslide risk estimation 167
7.5 Discussion and conclusions 173

Chapter 8: Synthesis and conclusions 177
8.1 Introduction 177
8.2 Evaluating the existing method of landslide susceptibility mapping in India 178
8.3 Event-based landslide inventory mapping 178
8.4 Fault/fracture and slope controls on rocksliding 179
8.5 Rock slope stability analysis using structural orientations 180
8.6 Selecting and weighting spatial factors of landslide susceptibility .. 181
8.7 Developing quantitative methods for landslide hazard and risk analysis 182
8.8 Limitations and future scope of research 183

Summary 205
Samenvatting 209
Curriculum vitae 213
List of Publications 214
ITC Dissertation List 215

Chapter 1: Introduction

1.1 Background

Landslides are significant hazards that can be disastrous to human life and property. Recent global disaster assessment studies (Petley et al., 2005; Nadim and Kjekstad, 2009; OFDA/CRED, 2010) reveal that the countries with the highest risk to such disasters are mostly in the developing world such as Venezuela, Peru, Tadjikistan, Philippines, Colombia, India, China, Nepal etc., where the estimated landslide fatality rate exceeds one per 100 km^2 per year. According to the total landslide fatalities reported worldwide in the last decade, Kirschbaum et al. (2010) confirm that the developing countries account to about 80%, of which in India, nearly 8% of landslide fatalities are reported.

About 15% of India (~0.49 million km^2) including the mountain areas of the Himalayas, the Meghalaya plateau, the Western Ghats are landslide-prone (NDMA, 2009). During monsoon, those areas witness frequent landslide events triggered by rainfall. Those landslide-prone areas also belong to the maximum earthquake-prone areas in India (Zone-IV and V; BIS, 2002), where earthquakes of Modified Mercalli intensity VIII to IX can occur, and thus, are also prone to earthquake-triggered landslides. The risk to landslides in those areas is compounded by a high growth rate of population in the hilly towns of India (e.g., Darjeeling and Kurseong towns in the Eastern Himalayas witnessed population growths of 47% and 49% respectively, during 1991 - 2001, Census of India, 2001).

To mitigate the effects of such disasters, the Government of India has modified the disaster management policy by enacting the National Disaster Management Act in 2005. This act aims at adopting proactive and multidisciplinary approaches towards achieving disaster awareness and mitigation. The new policy emanates from the belief that investments in disaster-preparedness and mitigation are much more cost effective than expenditures on relief and rehabilitation (Guzzetti et al., 1999; NDMA, 2009). In this regard, predictive maps of landslide hazard, preferably at medium scales (1:25,000 to 1:50,000) are vital geo-information products that administrators/planners can use in formulating regional mitigation plans for landslide disasters. The aim of using medium-scale landslide hazard maps is to draft proper land-use zoning regulations in landslide-prone areas to alleviate, if not prevent potential loss of human life and damage to property.
In India, landslide hazard maps that are currently available are, at best, qualitative landslide susceptibility maps. That means, those maps are based

mainly on heuristic or knowledge-driven guidelines (e.g., BIS, 1998) for quickly assessing large areas where landslides can occur. Therefore, translating those maps into actual expected impacts of landslide events is difficult, if not impossible. To remedy this, it is important to develop a methodology for effective predictive mapping, at medium-scales, of landslide hazard. This methodology should consider the variability and complexities of the landslide-prone terrains, because diverse terrain conditions strongly control the landslide types and processes. Accordingly, the research described in this thesis has been taken up (2007-2010) in one of the geologically-complex and landslide-prone terrains in the Eastern Himalayas, India. This research was conducted under a joint research agreement between the Geological Survey of India (GSI; the nodal governmental agency engaged in landslide studies in India), the National Remote Sensing Centre (NRSC; Department of Space, Government of India) and the Faculty of Geo-Information Science and Earth Observation (ITC), University of Twente, The Netherlands.

1.2 Landslide hazard and its prediction methods

According to Varnes (1984) and UNESCO's IAEG Commission on landslides and other mass movements, "landslide hazard" is defined as the probability of occurrence of a damaging landslide phenomenon in a given area and in a given period of time. This definition incorporates concepts about geographical location and recurrence that answer where and when a damaging landslide phenomenon will occur. Guzzetti et al. (1999) modified that definition by incorporating the concept of magnitude of future event and, thus, redefined landslide hazard in a given area as a function of three parameters, namely, spatial, temporal and magnitude probabilities of landslide occurrence.

Estimating and mapping variations in likelihood of occurrence or susceptibility to landsliding is a fundamental step towards landslide hazard prediction. That step must be taken with care and prudence in view of their complex interactions with geo-environmental spatial factors (Guzzetti et al., 1999; van Westen et al., 2006). Mapping or spatial prediction of landslide susceptibility aims to identify where future landslides are likely to occur, based on the fundamental assumption that spatial factors that caused present and past landslides are likely to cause similar landslides in the future (Varnes, 1978; Carrara et al., 1995; Guzzetti et al., 1999). Thus, several knowledge-driven (heuristic) and data-driven methods of mapping landslide susceptibility make use of indirect or direct spatial relations between landsliding of a certain type and relevant spatial factors. For any quantitative landslide hazard estimation, in general data-driven methods of susceptibility mapping are preferred because the latter quantify the susceptibility criteria per mapping unit (e.g., a

pixel) and facilitate incorporation of results directly in the subsequent hazard assessment. Because the landslide susceptibility maps do not provide information about “when” (i.e., temporal probability) and “how big” (i.e., magnitude probability) future landslides will occur, according to the definition of “landslide hazard”, they have to be converted into landslide hazard maps (Cruden and Varnes, 1996; Fell et al., 2008). Thus, temporal and magnitude probabilities of landslide occurrence are further required to transform a landslide susceptibility map into a landslide hazard map.

An indication of the temporal probability of landslide occurrence can be determined empirically either through frequency analysis of past landslide events (Crovelli, 2000; Coe et al., 2004) or by establishing an empirical relation between intensities of triggering factors (e.g., rainfall) and frequencies of the corresponding past landslide events (Lumb, 1975; Caine, 1980; Brand et al., 1984; Crozier, 1999; van Westen et al., 2006) and thereby analysing the recurrence of such triggering rainfall events. An indication of the magnitude probability of future landslides can be obtained via magnitude-frequency analysis of past landslides using suitable probability or density distribution functions (Malamud et al., 2004). By integrating spatial, temporal and magnitude probabilities of landslide occurrence, a landslide hazard map can be prepared and can be used further to qualitatively or quantitatively estimate the landslide risks with respect to elements at risk in a given area.

1.2.1 Heuristic and data-driven methods of spatial prediction

Heuristic methods for spatial prediction of landslide occurrence can either be direct or indirect. A direct heuristic method, using a detailed geomorphological map, can result in a high accuracy of spatial prediction (e.g., Brabb, 1984), dependent on the experience of the expert applying the method, and the precision, dedication and time with which the study was carried out. In indirect heuristic methods, individual factors are assigned specified weight values or ratings that are solely based on subjective criteria (e.g., Hansen, 1984; Varnes, 1984). In one of such methods, that is prevalent in India (e.g., BIS, 1998), specified factor weights are considered regardless of existing landslide inventory maps and variations in terrain conditions. The use of standard weight values for the factor in different geomorphological/geological environments can lead to erroneous results and poor prediction, since attributes of factors and their respective causal relations with different types of landslides are spatially variable. The main limitations/problems of heuristic methods are related to the subjectivity involved in selecting, mapping, and weighting of the spatial factors for landslide susceptibility (van Westen et al., 2003). Although the same

subjectivity could be present in selecting and mapping of the factors for data-driven methods, but the relative importance of the factors is determined by more objective techniques. If heuristic methods are applied in areas where no landslide inventories are present, it is also difficult to validate the accuracy of the heuristic predictive maps. Although, one of the main advantages of heuristic methods is that they can allow site specific evaluations of the causal factors, and avoid the generalization that is often used in data-driven methods.

Since the late 1980s, the increasing popularity of geographic information system (GIS) has facilitated the application and development of various data-driven or empirical methods for landslide susceptibility mapping (Aleotti and Chowdhury, 1999), which are mostly statistical/mathematical and primarily based on observed data of landslides and relevant spatial factors. In GIS-based data-driven methods, spatial factors (or layers of evidence) are integrated with a landslide inventory map (target) using various mathematical/statistical integration techniques that can model relationships among layers of evidence with respect to targets (van Westen, 1993; Bonham-Carter, 1994; Chung et al., 1995). Landsliding is a complex physical phenomenon that is linked to the interplay of several spatial factors. Therefore, several authors (Neuland, 1976; Carrara, 1983; 1989; Baeza and Corominas, 2001; Ayalew and Yamagishi, 2005; Pradhan, 2010; Rossi et al., 2010a) promote application of data-driven/empirical methods based on multivariate statistics for predictive mapping of landslide susceptibility to reduce uncertainties and errors of prediction by being objective in analysis and by employing quantitative methods of validation.

Nevertheless, data-driven predictive methods (e.g., multivariate methods, artificial neural network (ANN)) can be undermined by shortcomings like a) the general assumption that landslides occur due to the same combination of factors throughout a study area, b) the ignorance of the fact that occurrence of certain landslide types is controlled by certain causal factors that should be analysed/investigated individually, c) the extent of control of some spatial factors can vary widely in areas with complex geological and structural settings (e.g., the Himalayas) and d) the lack of suitable expert opinion on different landslide types, processes and causal factors. Therefore, data-driven statistical/mathematical methods, even although efficient in predicting locations of landslides, can produce results that sometimes are not realistic or difficult to explain.

1.2.2 Why are temporal and magnitude predictions difficult?

Many researchers (Terlien, 1998; Guzzetti, 2000; van Westen et al., 2006) indicate that incorporation of temporal and magnitude probabilities with the information of spatial probabilities is by far one of the most difficult tasks in landslide hazard prediction because of the lack of sufficient data of past landslide events. Difficulties arise when data of past landslides are inadequate, source data are of different spatial and temporal resolutions, dates of landslide and rainfall do not match, rainfall records are discontinuous, rainfall stations are not available and landslide-triggering events do not exhibit systematic patterns, etc. (Chowdhury and Flentje, 2002; Gabet et al., 2004; van Westen et al., 2006). Some of the above difficulties pose serious limitations in generating landslide inventory maps by introducing inconsistent landslide densities and inaccurate estimates of size-frequency distributions that preclude correct determination of temporal and magnitude probabilities. In India, in particular, where this research was undertaken, neither formal research nor any institutional attempt has yet been established to systematically preserve the past landslide information, except for some isolated attempts in some smaller areas. Therefore, inadequacy and gaps in source data (e.g. temporal, spatial, scale), are common impediments to landslide hazard prediction in India. Thus, generating comprehensive landslide inventory maps and developing robust methods of using those maps for temporal and magnitude predictions of landslides in the Indian scenario are the challenging tasks that this research focuses on.

1.3 Research objectives

The susceptibility to (or, the spatial prediction of) landsliding of a certain type is a function of two types of spatial associations: (1) spatial associations of individual spatial factors with known landslides of a certain type; and (2) relative importance of individual spatial factors with respect to one another in relation to those known landslide occurrences. Methods of bivariate empirical analysis can model only the first type of spatial association but not the second type. In contrast, multivariate methods can model those two types of spatial associations simultaneously, but often include spatial factors that do not seem to have a direct relation with the landslide process (Baeza and Corominas, 2001; van Westen et al., 2008), and generally do not include the expert opinion. Thus, the main objective of this study is to develop suitable empirical methods for the analysis of spatial association at a medium-scale to (a) select the most appropriate spatial factors that realistically represent genetic associations with landsliding of a certain type and (b) determine the importance of every spatial factor with respect to other spatial factors in

relation to the landsliding type under study. These empirical techniques are meant to iteratively and instructively complement the understanding of complex landsliding processes for mountainous areas in the Himalayas.

The sub-objectives of this research are to:

1. Generate landslide inventory maps for different triggering events, based on the available information in the forms of landslide maps, images and archives. These maps should portray the landslide patterns and types of triggering events with a range of return periods, which can be used to analyse the temporal and magnitude probabilities;
2. Develop an exploratory analytical technique for understanding the mutual/exclusive spatial relation between regional structures (e.g., faults/fractures) and slope aspects with rockslides of a certain type.
3. Develop a specific method for analyzing different rock slope failure modes, by spatially incorporating the 3-D structural orientation data;
4. Analyze the spatial associations between landslide of specific types and a set of causal factors, using bivariate statistical methods for selecting and weighting the appropriate spatial factors and its combinations that are best in predicting the spatial pattern of these landslides;
5. Integrate the right and weighted spatial factors into landslide susceptibility maps for each type of landslides, using suitable statistical/mathematical integration methods.
6. Integrate the spatial, temporal and size probabilities of landslide events and convert the susceptibility maps into hazard maps;
7. Use the landslide hazard maps for subsequent risk analysis and estimate the probable losses due to future landslide events.

1.4 Research questions

Based on the various limitations and problems of landslide hazard prediction and the research objectives described in the preceding section, this research endeavoured to investigate the following main research questions.

a) What are the reasons for the poor prediction performance of the heuristic landslide susceptibility method (e.g., BIS, 1998) that is prevalent in India?
b) What are the limitations in generating landslide inventory maps for a region that has only limited landslide information? How do these limitations quantitatively affect the temporal and magnitude predictions?
c) Which types of spatial relationships exist between regional structural geological setting and slope instability, and how can this be included in a landslide susceptibility assessment in an active fold-thrust belt?

d) What are the main failure mechanisms that control rock slope instabilities? Can they be modeled spatially using rock discontinuity orientation data?
e) What spatial predictors and their inter-predictor weights are relevant in mapping of susceptibility to different types of landslides in a Himalayan environment?
f) What are the advantages and disadvantages of the different empirical predictive mapping methods for selecting and weighting of relevant spatial predictors?
g) Is it possible to convert medium-scale landslide susceptibility maps that are made using incomplete landslide inventories into useful landslide hazard maps?
h) Which methods of risk estimation are best suited in a region having limited information on historical landslides?
i) Is it possible to develop an improved method for medium-scale landslide susceptibility, hazard and risk assessment that can be applied by the Geological Survey of India or by other landslide scientists over diverse landslide-prone areas in India?

1.5 Study area

To pursue the objectives of this research, a landslide-prone terrain of about 90 km^2 in the surroundings of Kurseong town (Darjeeling district, West Bengal, India) was selected as a test area. It is situated within the structurally-complex fold-thrust-belt (FTB) in the Eastern Himalayas (Fig. 1.1), also locally known as the Darjeeling Himalayas.

1.5.1. Geology and structure

The study area represents the southern part of the Darjeeling klippe (Fig. 1.1b) which is part of a tectono-stratigraphic sequence of metamorphic rocks of the Himalayan FTB that borders the foreland molasse basin in the South (Figs. 1.1b-c). The southern boundary of this Himalayan metamorphic sequence is marked by a high-strain ductile shear zone, called the Main Central Thrust (MCT), coinciding with an inverted sequence of metamorphic rocks from kyanite grade to biotite-chlorite grade (Hubbard, 1996; Searle and Szulc, 2005) of the Central Crystalline Gneissic Complex (CCGC).

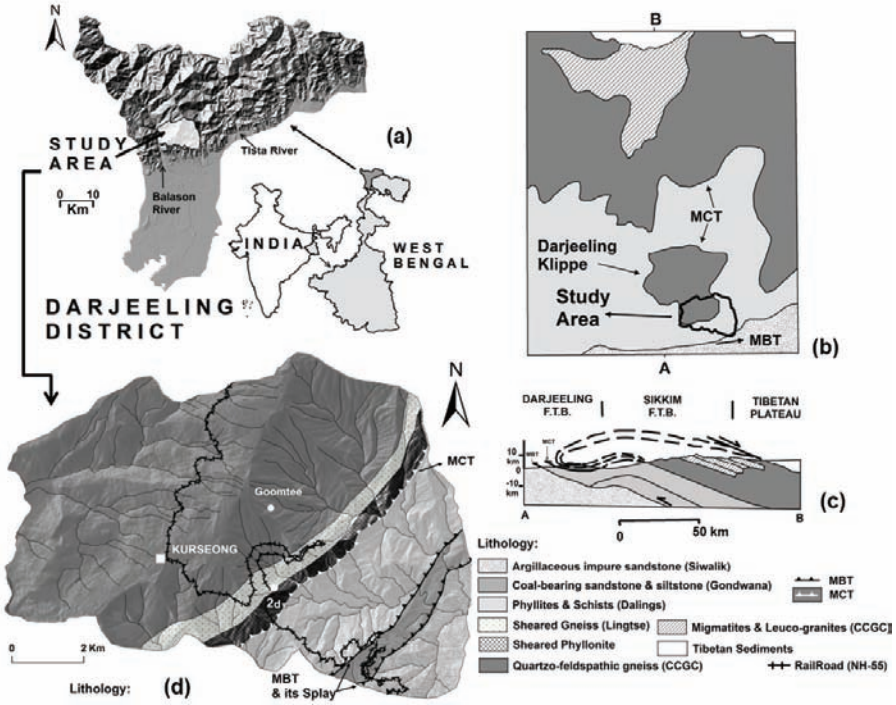

Fig. 1.1 Location map and geological maps of the study area. (a) geographic location; (b) schematic regional geological map (after Searle and Szulc, 2005); (c) schematic geological section of Darjeeling Himalaya (after Searle and Szulc, 2005); and (d) Medium-scale geological map of the study area.

The high grade metamorphic rocks of the CCGC are thrusted over the low grade meta-sedimentary rocks (schists/phyllites and quartzites) of the Daling Group along the MCT (Mallet, 1875; Sinha-Roy, 1982). Further to the South, the foreland molasse sediments (sandstone/shale) of the Siwalik Group are underlain by a thin intra-thrusted slice of minor coal-bearing clastic rocks (sandstone/siltstone) of the Gondwana Group. Towards the North, these Gondwana rocks are thrusted over by the Daling Group of meta-sediments along the southern-most front of Himalayan FTB known as the Main Boundary Thrust (MBT). The MCT and MBT represent the main regional structural discontinuities in the study area (Fig. 1.1). Along the basal part of MCT, a sheared phyllonite is exposed, and towards its immediate north, a thin intra-thrusted slice of coarse-grained sheared gneissic rocks (Lingtse Gneiss) is present as a prominent marker lithology adjacent to MCT in this part of Eastern Himalayan FTB (Fig. 1.1d). The CCGC, the Daling meta-sediments and other associated rocks in the FTB are overturned (towards north) and are highly foliated, with prominent foliations generally dipping towards north to northwest with moderate inclinations ranging from 30º to 50º. Due to intense

(ductile and brittle) deformation, the rocks in the FTB are folded, faulted and thrusted.

1.5.2 Topography and climate

In the study area, the topography is very rugged with elevations varying between 236 m and 2189 m (mean ≈ 1073 m, std. dev. ≈ 440 m; Fig. 1.2a) with a prominent centrally-located NE-SW ridge. The slope inclinations vary between 0° and 84° (mean ≈ 27°, std. dev. ≈ 12°; Fig. 1.2b). Slopes are gentle on the ridge tops but become steep toward stream banks. This is due to rapid under-cutting of streams in response to the active tectonic uplift of the Himalayas (Burbank et al., 1996; Binnie et al., 2007). In the area west of the major south-westerly-plunging ridge (Fig. 1.2c), most slopes have northerly aspects and mean to below mean inclinations. In the area east of the same ridge, most slopes have southerly aspects and mean to above mean inclinations (Fig. 1.2c). Active erosion of moderate to steep slopes results in continuous deposition of ample colluvial materials in depressions and flat areas below those slopes. Denudational geomorphic processes are common and are strongly influenced by streams flowing mostly southerly that are transverse to the main ENE trends of Himalayan thrusts (Fig. 1.1d). The climate is humid and the annual precipitation in the area varies between 2000 mm and 5000 mm (see chapter 3), with very high precipitation density during the monsoon from June to October (Soja and Starkel, 2007).

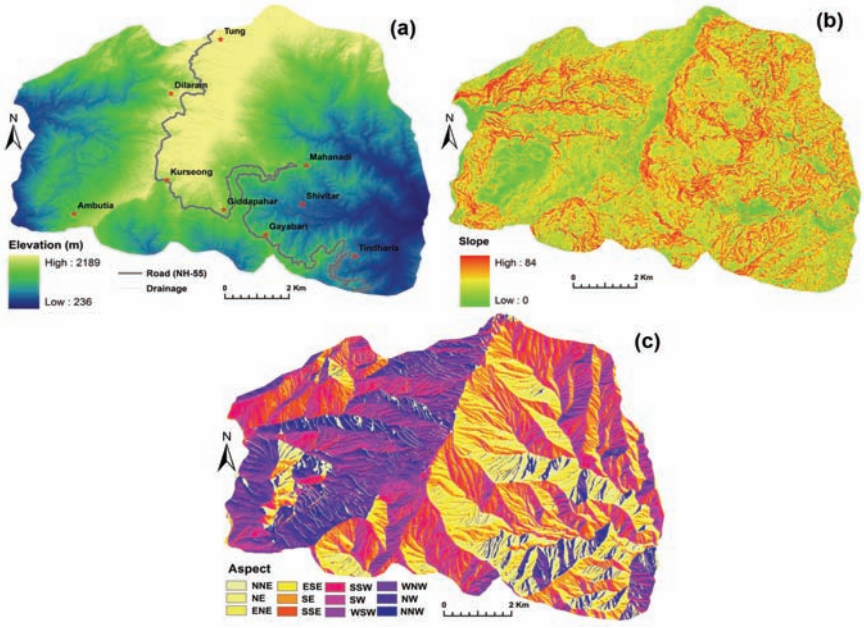

Fig. 1.2 Topography of the study area. (a) Elevation, (b) Slope inclination and (c) Slope aspects (classified into 12 classes based on 30o azimuth interval).

1.6 Methodology and organisation of thesis

The overall research methodology and organisation of this thesis can be explained through a schematic flow diagram (Fig. 1.3) that outlines the main steps followed in this research and highlights the links among the steps and chapters of this thesis. Apart from this introductory and concluding chapters (chapter 1 & 8), five chapters (chapters 2, 3, 4, 5 and 6) are published as research articles in ISI journals, and part of chapter 3 has also been published as full paper in an international conference proceeding. The chapter 7 is based on another research article that is currently under review in one of the ISI journals. To maintain continuity and coherence and to avoid unnecessary repetitions, the contents of the above publications are suitably adapted and incorporated as chapters of this thesis.

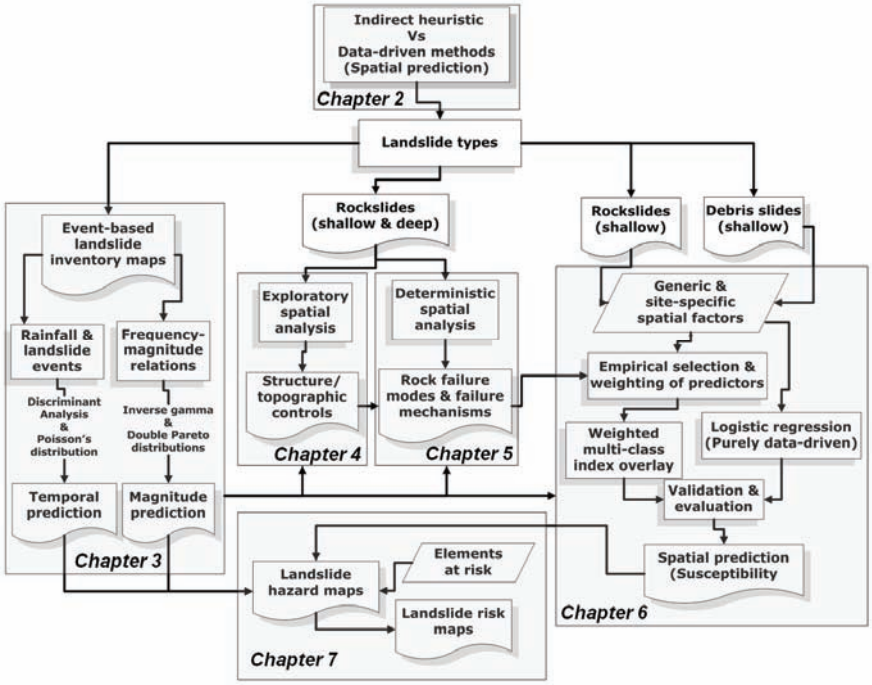

Fig. 1.3 Diagram showing organisation of thesis chapters and the major steps of analyses followed in the research.

Chapter-2 deals with evaluation and comparison of a standard Indian heuristic susceptibility method (e.g., BIS, 1998) and an empirical method (weights-of-evidence) of landslide susceptibility mapping. This study investigates the possible limitations of both methods of susceptibility mapping in order to develop flexible ratings/weights of factors based on local site conditions and their spatial relations with landslides. This study led to the understanding that developing knowledge on prevalent landslide types and processes and establishing empirically their spatial relations with different

site-specific spatial factors are essential for medium scale landslide susceptibility mapping. Chapter-2 is published in an ISI journal as "*A quantitative approach for improving the BIS (Indian) method of medium-scale landslide susceptibility*" (Ghosh et al., 2009a).

Chapter-3 deals with the generation of event-based landslide inventory maps using various data sources that are available in the study area covering a period of 40 years (1968-2007). Generation of inventory maps and their subsequent analyses led to a) understanding of the prevalent landslide types and processes in the study area, b) development of a conceptual model about its causal association with different geo-environmental factors, c) detailed insights into the spatio-temporal activity and evolution of different landslide types during the past 40 years, d) recognition of an empirical relationship between landslides and triggering rainfall events, and e) analysis of magnitude (size) and frequency of past landslides. The results of a) to c) are directly linked to the application of various empirical landslide susceptibility mapping methods that are described in the subsequent chapters (chapters 4, 5 and 6). The results of d) and e) led to the quantitative estimation of temporal and magnitude probabilities of landslides, which are discussed in chapter 3 and subsequently in chapter 7. Chapter-3 is based on two publications - i) "*Generation of event - based landslide inventory maps in a data - scarce environment: case study around Kurseong, Darjeeling district, West Bengal, India*" (Ghosh et al., 2009b) and ii) "*Generating event-based landslide maps in a data-scarce Himalayan environment for estimating temporal and magnitude probabilities*" (Ghosh et al., 2011a).

In an active FTB (e.g., the Himalayas), regional faults/fractures are surface manifestations of several, inherent brittle and ductile deformations in crustal rock masses which has plausible controls on landsliding. It is logical to think that structural controls on landsliding are not isotropic over a large area because types of structural features and distribution of stress generally vary widely with respect to prominent structural dislocation planes such as MCT/MBT (Fig. 1.1). Therefore, chapter-4 deals with various exploratory spatial analysis techniques to investigate controls of regional faults/fractures and slopes on both shallow and deep-seated rockslides in the study area. Chapter-4 is based on an ISI publication titled "*Spatial analysis of mutual fault/fracture and slope controls on rocksliding in Darjeeling Himalaya, India*" (Ghosh and Carranza, 2010).

The study described in chapter 4 reveals that various sub-types of rocksliding in the study area are controlled mutually by different sets of fault/fractures and similar sets of slope aspect. This supports that rock slope instability in

the study area is controlled by directional anisotropy of planar discontinuities in rock masses. Thus, chapter 5 focuses on spatial modelling of different rock failure modes (e.g., planar, wedge, topple, etc.) using spatially distributed rock discontinuity orientation data, topography and discontinuity shear strength parameters. The advantage of such method of spatial analysis is that, while modelling different rock failure modes, their contributing failure mechanisms are also simultaneously delineated as model results. Chapter-5 is based on an ISI publication on "*Rock slope instability assessment using spatially distributed structural orientation data in Darjeeling Himalaya (India)*" (Ghosh et al., 2010).

Chapter-6 deals with the application of the understanding and knowledge described in chapter-2 to chapter-5. By using various suitable empirical spatial association techniques, the most relevant spatial predictors of susceptibility to shallow landsliding (both rock and debris sliding) are selected. Using the results of the empirical spatial association analyses, the inter-predictor weights in relation to landslide types under study are determined using analytical hierarchy process (AHP) (Saaty, 1977; 1996). Then, the selected and weighted predictors are integrated via weighted multi-class index overlay to create landslide susceptibility maps. The results are compared and evaluated with a predictive mapping method of landslide susceptibility based on multivariate statistics (i.e., logistic regression). Chapter-6 is based on the ISI publication on "*Selecting and weighting of spatial predictors for empirical mapping of landslide susceptibility in Darjeeling Himalaya (India)*" (Ghosh et al., 2011b).

Chapter-7 deals with a) integration of information on spatial (chapter-6), temporal and magnitude predictions (chapter 3) of landslides to prepare different landslide hazard scenario maps and b) integrating the different landslide hazard scenario maps with the maps of elements at risk (e.g., buildings, roads and population) to model different consequences for estimating variations in losses and for generating medium-scale (1:25,000) landslide risk scenario maps. This is based on the ISI publication on "*Integrating spatial, temporal and magnitude probability for medium scale landslide hazard and risk analysis in Darjeeling Himalayas"* (Ghosh et al., Submitted in Landslides).

In the concluding chapter (chapter-8)**,** the conclusions pertaining to the each component of the entire research (chapters 2 to 7) for medium-scale (1:25,000 to 1:50,000) landslide hazard and risk analyses are summarised followed by recommendatory remarks on direction and scope for future research.

Chapter 2: Evaluating the existing method of landslide susceptibility mapping in India

In this chapter, the application of an indirect heuristic (knowledge-driven) method that is followed in India for medium-scale landslide susceptibility mapping (BIS, 1998) is evaluated, and compared with the application of an empirical/data-driven method of mapping landslide susceptibility. This chapter thus describes *"A quantitative approach for improving the BIS (Indian) method of medium-scale landslide susceptibility"* (Ghosh et al., 2009a) to demonstrate how the prediction performance of a knowledge-driven indirect method of mapping landslide susceptibility can be improved by using empirical relations between landslide occurrences and relevant spatial factors.

2.1 Introduction

In India, the Bureau of Indian Standards (BIS), the regulatory body that specifies scientific codes and practices, has formulated guidelines (BIS, 1998) for landslide susceptibility zonation at medium scales (1:50,000). The BIS guidelines recommend an indirect knowledge-driven (heuristic) approach to landslide susceptibility mapping according to the method originally proposed by Anbalagan (1992). Those guidelines provide specified weights or ranks to a set of pre-defined factors. Those weights or ranks are called Landslide Hazard Evaluation Factor (LHEF) ratings (Table 2.1). According to Anbalagan (1992), the LHEF rating scheme is based on subjective criteria specified by a group of experts engaged in landslide research. The LHEF ratings are applied irrespective of variations in terrain conditions and are determined without directly considering the existing landslide inventory maps.

Since the spatial extents of landslide factors and their respective causal association with different types of landslides and failure mechanisms are variable, the application of such specified LHEF ratings of factors can be inappropriate and can lead to poor landslide prediction rates when applied to many different areas. Moreover, the BIS method (Anbalagan, 1992; BIS, 1998) does not recommend any specific quantitative validation, but the predictive power of any model can only be compared and judged through an objective method of cross-validation. Therefore, in the present study, a more robust and internationally-accepted method of cross-validation is employed, through construction of success/prediction rate curves (Chung and Fabbri, 1999; Fabbri, 2003).

The objectives of this study were (a) to evaluate the performance of the existing BIS method with specified LHEF ratings and (b) to demonstrate that the performance of the BIS method can be improved by modifying the recommended LHEF ratings based on empirically-derived weights for factors in every study area and (c) to conceptually understand the importance of a-priori knowledge about landslide types to be examined and their relevant factors. This study involved comparing the results of the BIS method with the results of an adapted weights of evidence (WofE) modelling (Bonham-Carter, 1994) in two adjacent case study areas (Area 1 and Area 2 in Fig. 2.1) in Darjeeling district, West Bengal, India; situated just north and north-east of the main study area of this research (Fig. 2.1).

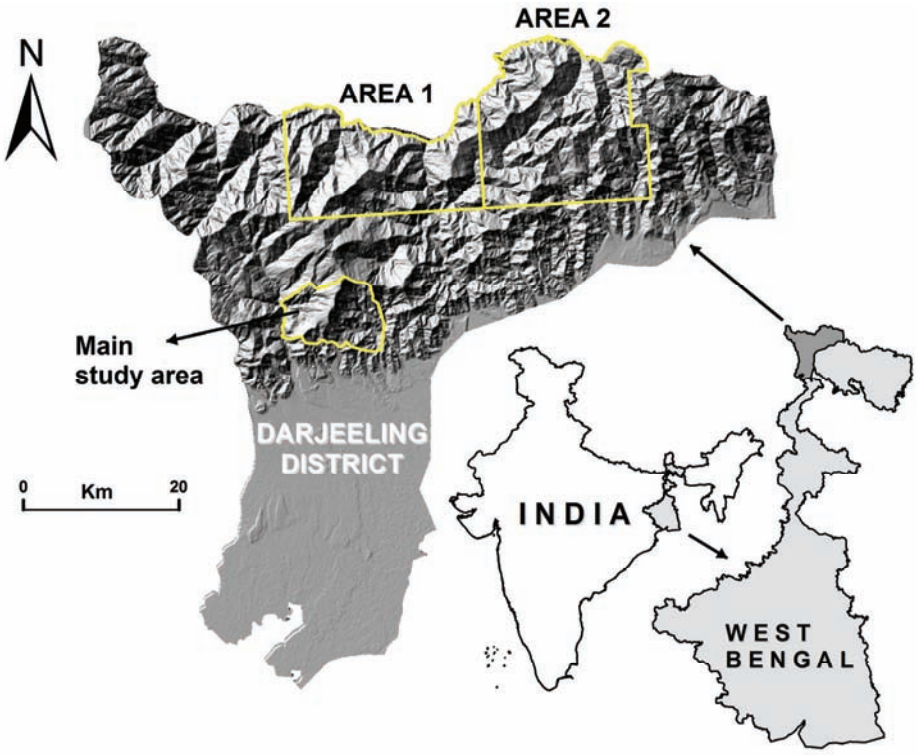

Fig. 2.1 Map showing locations of Area 1 and Area 2 with respect to the main study area of this research, where the subsequent studies discussed in this thesis (Chapter 3 to Chapter 7) were undertaken.

Table 2.1 LHEF ratings of different relevant factors of landslides (BIS, 1998; Anbalagan, 1992).

Geofactor	Description	Category		LHEF
Lithology	Rock type Type – 1** Highly weathered (4); moderately weathered (3); Slightly weathered (2) Type – 2 ** Highly weathered (4); Moderately weathered (3); Slightly weathered (2)	Type 1	Quartzite & Limestone	0.2
			Granite & Gabbro	0.3
			Gneiss	0.4
		Type 2	Sandstone & minor beds of claystone	1.0
			Poorly cemented sandstone with minor clay/shale	1.3
			Slate & phyllite	1.2
		Type 3	Schist	1.3
			Shale with interbedded clayey & non-clayey	1.8
			Highly weathered shale, phyllite & schist	2.0
	Soil type	Older well compacted alluvial fill material		0.8
		Clayey soil with naturally formed surface		1.0
		Sandy soil with naturally formed surface (alluvial)		1.4
		Debris comprising mostly rock pieces mixed with clayey/ sandy soil (colluvial) – older well compacted		1.2
		Debris comprising mostly rock pieces mixed with clayey/ sandy soil (colluvial) – younger loose material		2.0
Structure	Relationship of parallelism between the slope and vulnerable discontinuity	> 30°		0.20
		21° – 30°		0.25
		11° – 20°		0.30
		6° – 10°		0.40
		< 5°		0.50
	Relationship of dip of vulnerable discontinuity and inclination of slope	> 10°		0.3
		0° – 10°		0.5
		0°		0.7
		0° – (-10°)		0.8
		< -10°		1.0
	Dip of vulnerable discontinuity	< 15		0.20
		16° – 25°		0.25
		26° – 35°		0.30
		36° – 45°		0.40
		> 45°		0.50
	Depth of soil cover	< 5m.		0.65
		6 – 10m.		0.85
		11 – 15m.		1.30
		16 – 20m.		2.0
Slope	Escarpment / cliff	> 45°		2.0
	Steep slope	36° – 45°		1.7
	Moderately steep slope	26° – 35°		1.2
	Gentle slope	16° – 25°		0.8
	Very gentle slope	< = 15°		0.5
Relative relief	< 100m.			0.3
	101 – 300m.			0.6
	> 300m.			1.0
Landuse and land cover	Agricultural land / populated flat land			0.60
	Thickly vegetated forest area			0.80
	Moderately vegetated area			1.20
	Sparsely vegetated area with less ground cover			1.50
	Barren land			2.0
Hydro-geological conditions	Flowing			1.0
	Dripping			0.8
	Wet			0.5
	Damp			0.2
	Dry			0.0

2.2 BIS method of landslide susceptibility mapping

2.2.1 Rating and integration of factors

The BIS method suggests pre-defined LHEF ratings for different classes of six spatial factors of landsliding. These factors and their corresponding factor classes (Table 2.1) are specified and recommended for application to any landslide type and to any landslide-prone terrain in India for landslide susceptibility mapping at 1:50,000 scale. According to the BIS guidelines (BIS, 1998), integration of LHEF ratings of six factors is to be done in mapping units, preferably denoted by "slope facets". The six factors according to the BIS guidelines (1998) are lithology, structure, slope, relative relief, landuse and land cover and hydro-geological conditions (Table 2.1). To assign LHEF ratings per slope facet for each factor, a slope facet map is integrated with each of the factor maps in a GIS. Slope facets can be generated in a GIS by intersecting five slope classes (BIS, 1998; Table 2.1) and slope aspects classified at 30° azimuth intervals. In this study, slope inclinations and aspects were derived from the freely-available 1 arc second (90 m resolution) Shuttle Radar Topography Mission (SRTM) digital elevation model (DEM) data (Surendranath et al., 2008). The lithology and structure data were retrieved from the available 1:50,000 geological maps of the area, and, are supplemented later by additional field inputs during course of this research (Ghoshal et al., 2008; Surendranath et al., 2008). The landuse and land cover and hydro-geological data were spatially extracted from the visual interpretation of IRS 1D satellite imagery (LISS 3 FCC and Pan Images), later confirmed by limited field-checks. Although, at medium-scale, assessment of BIS-specified hydro-geological factors (Table 2.1) for a large area is difficult and riddled with high levels of subjectivity.

2.2.2 Validation of BIS landslide susceptibility maps

Following the BIS guidelines (BIS, 1998; Table 2.1; Section 2.2.1), thematic maps of six factors (lithology, slope, relative relief, geological structure, land use and land cover, and hydrogeology) were generated in a GIS in the two adjacent case study areas in Darjeeling Himalaya (Area 1 and Area 2). The two case study areas were considered because they have different spatial extents of landslide factors (Table 2.2). The LHEF ratings of six factors that are integrated in each slope facet are summed together to obtain the total estimated hazard (TEHD) per slope facet (Anbalagan, 1992; BIS, 1998). Finally, the resulting landslide susceptibility maps were classified into five classes according to the BIS-recommended ranges of TEHD values (Figs. 2.2a and 2.3a; Table 2.3).

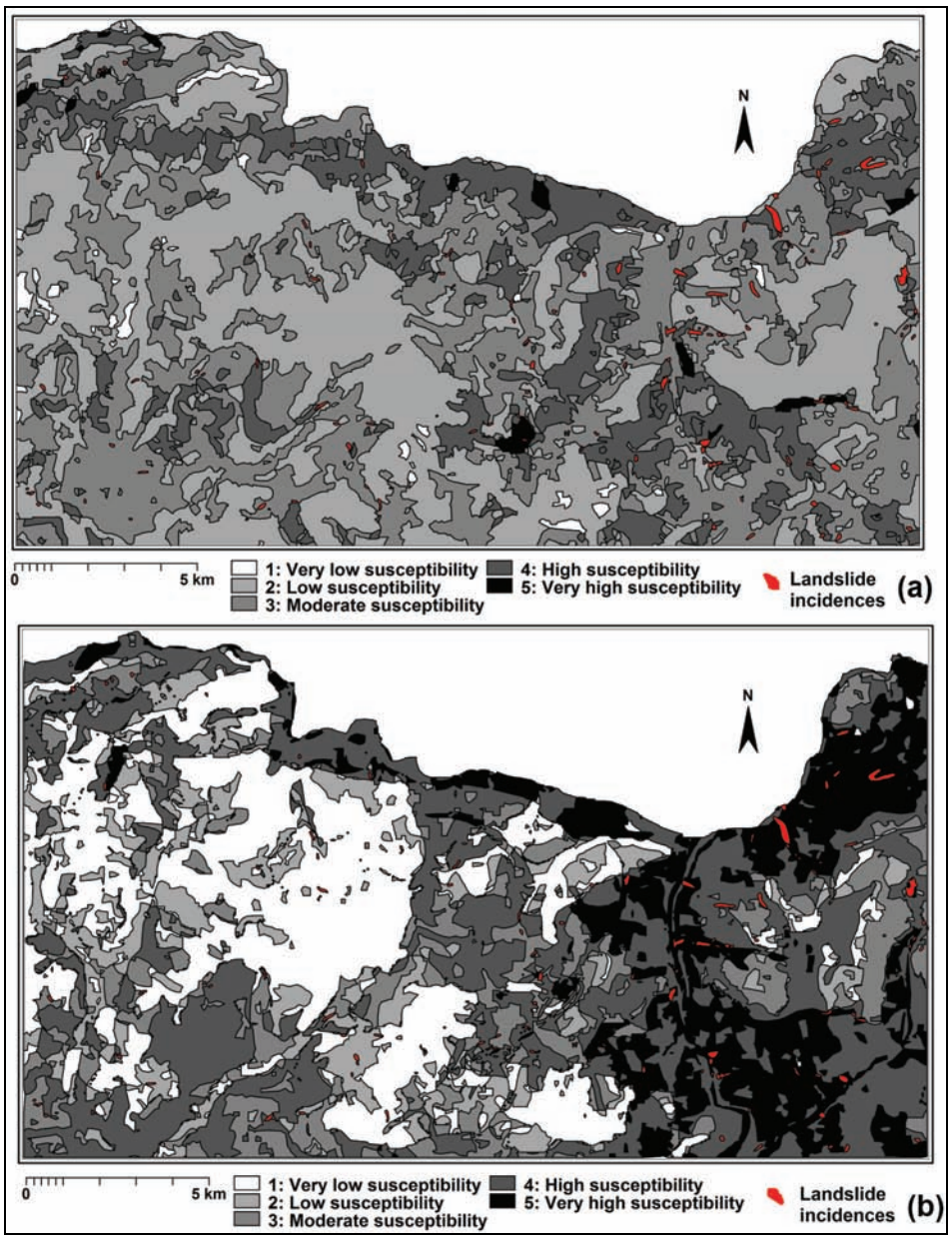

Fig. 2.2 Landslide susceptibility map of Area 1 according to (a) the BIS method and (b) the WofE method.

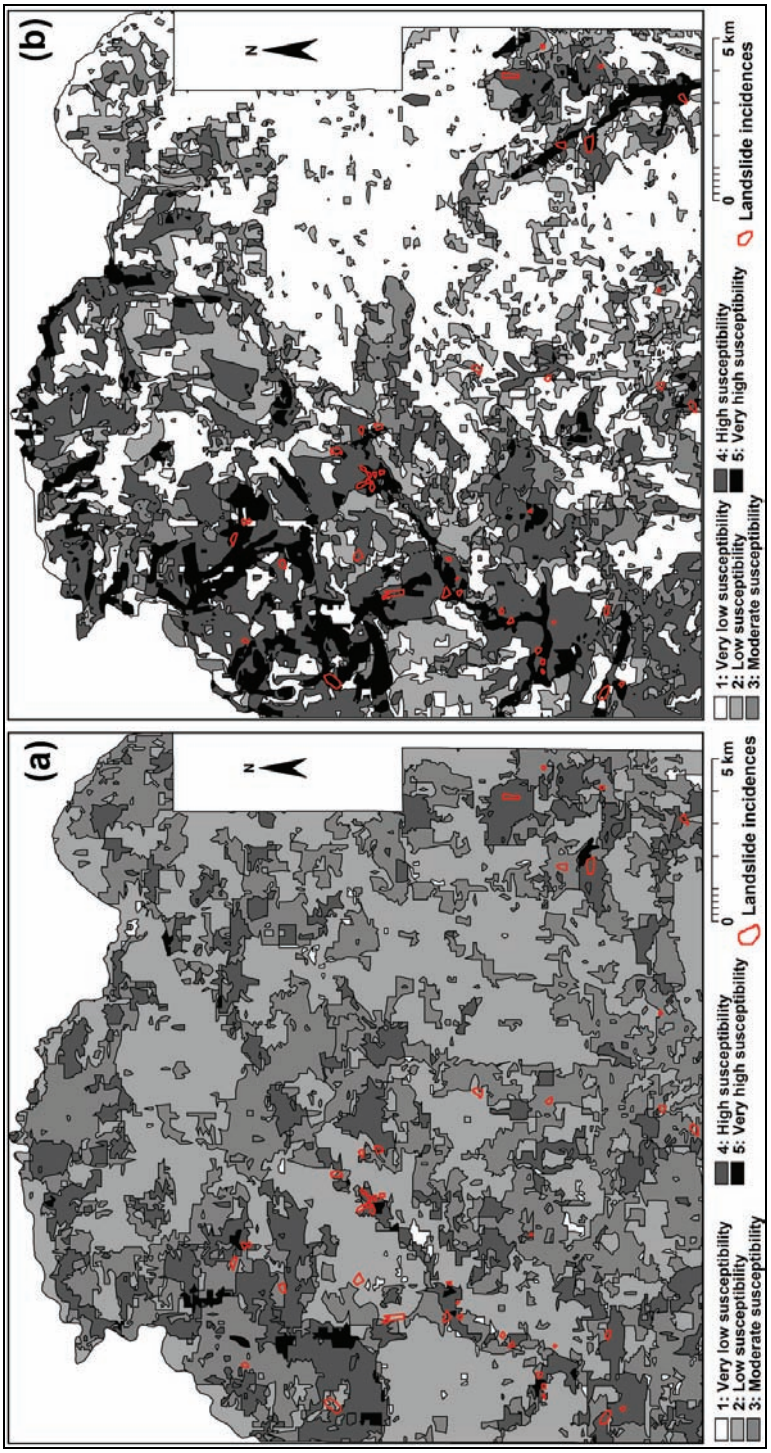

Fig. 2.3. Landslide susceptibility map of Area 2 according to (a) the BIS method and (b) the WofE method.

Table 2.2 Attributes of two case study areas (see Fig. 2.1).

Attributes	Area 1	Area 2
Map area	289 km^2	395 km^2
Number of landslide polygons	122	44
Landslide area	1.68 km^2	1.45 km^2
Landslide types	Predominantly rock slides, followed by few debris slides	Mixed types – near equal proportions of rock and debris slides; debris slide comparatively larger in dimension.
Causal mechanisms	Higher level of rock weathering, fragile lithology, predominance of moderate to steep slope, higher relief, higher anthropogenic activity etc.	Toe cutting by stream, fragile lithology, presence of sheared gneiss, predominance of thick loose and unconsolidated colluviums etc.
Morphometry	Predominant slopes are above 25° (50% of the area) and slopes steeper than 35° is 12% of the area.	Predominant slope is below 25° (64% of the area); slopes steeper than 35° is only 8% of the area.
Geology	Near equal area% of gneisses (33%) and fractured/sheared schists/phyllites (27%)	Predominance of competent gneissic rocks (33%) over fragile schists/phyllites (17%) and sheared gneiss (1%)
Landuse	Higher proportion of tea garden and agricultural areas (64%); forest (both thick and moderate) areas are comparatively lesser (27%).	Comparatively lower proportion of flat agricultural land (47%); forest areas (both thick and moderate) are proportionately higher (40%).

Table 2.3 Landslide susceptibility classes according to TEHD values (BIS, 1998).

TEHD Values	Landslide susceptible zone (LHZ)	
	Class	Category
< 3.5	1	Very Low Susceptibility
3.5 – 5.0	2	Low Susceptibility
5.0 – 6.0	3	Moderate Susceptibility
6.0 – 7.5	4	High Susceptibility
> 7.5	5	Very High Susceptibility

For validation of the BIS method, the resulting landslide susceptibility maps were combined with the landslide inventory maps of both the areas. The landslide inventory maps were prepared after collecting available past landslide information from reports/archives, old maps, remote sensing data, topographical sheets, and field inputs, although; the same was incomplete since the source data have long temporal as well as wide spatial gaps. For overall validation of the BIS landslide susceptibility maps, prediction rate curves (Fig. 2.4) were prepared by plotting the cumulative proportion of all known landslide areas (along y-axis) versus the cumulative proportion of the case study area, ordered from high to low TEHD values (Chung and Fabbri, 1999). If the prediction rate curve is steep then the corresponding landslide susceptibility map has a strong ability to predict areas that are most susceptible to landsliding. In Area 1, 30% of the map with highest TEHD values predicts 43% of the landslides (Fig. 2.4). In Area 2, 30% of the map with highest TEHD values contains 52% of the landslides (Fig. 2.4). Table 2.4 indicates the landslide density and the percentage of total landslides in different BIS susceptibility classes for the two areas. Although landslide density increases with increasing landslide susceptibility like the “landslide

abundance" values (Ghoshal et al., 2008), the differences in landslide densities between the landslide susceptibility classes in the two case study areas are generally small (Table 2.4). In addition, there are more landslides in the "low" and "moderate" classes (78% in Area 1 and 58% in Area 2) than in the "high" to "very high" classes in both case study areas (Table 2.4). This indicates that the recommended classification according to the specified ranges of TEHD values of the BIS-method (Table 2.3) tends to be ineffective to delineate or predict zones with actually high to very high landslide susceptibility. Therefore, the results corroborate further that the specified nature of LHEF ratings/weights of factors for diverse terrain conditions and the specified ranges of TEHD values for classification of susceptibility zones in the BIS guidelines can be ineffective.

Table 2.4 Area, density, and percentage of landslides in landslide susceptibility classes mapped in the two case study areas according to the BIS method.

Study area	Landslide susceptibility		Cross-validation		
	Class	Area covered (km^2)	Area (km^2) of known landslides	Landslide density	% total landslide area
Area 1	Very low	4	0.00	0.00	0
	Low	119	0.27	0.23	16
	Moderate	113	1.04	0.92	62
	High	52	0.34	0.66	20
	Very high	2	0.03	1.27	2
Area 2	Very low	5	0.00	0.00	0
	Low	188	0.43	0.23	29
	Moderate	133	0.42	0.31	29
	High	66	0.59	0.90	41
	Very high	3	0.02	0.67	1

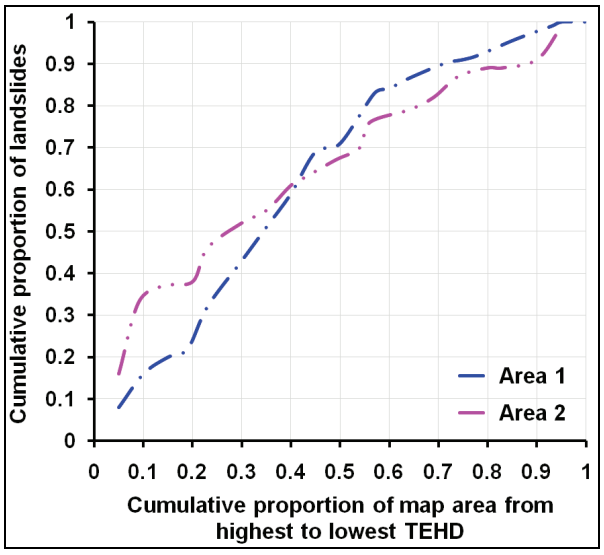

Fig. 2.4 Prediction rate curves of landslide susceptibility maps (BIS method).

2.3 Empirical method of landslide susceptibility mapping

Empirical weights of landslide factors can be obtained via various statistical and mathematical methods in a GIS by quantifying spatial associations between spatial factors and landslides. Either bivariate or multivariate methods can be used. Bivariate methods, such as the information value method (Yin and Yan, 1988), weights-of-evidence (Bonham-Carter, 1994), and evidential belief functions (Carranza and Hale, 2003; Carranza and Castro, 2006) are flexible to use and allow exploring the importance of individual factors in an interactive manner. Although, data-driven multivariate methods such as multiple discriminant analysis (Carrara et al., 1991), logistic regression (Mark and Ellen, 1995; Ayalew and Yamagishi, 2005) and artificial neural network (Lu and Rosenbaum, 2003; Kanungo et al., 2006) sometimes give better results than bivariate empirical methods, although; the interpretation of the contribution of each factor is less straightforward with the former. Given the objective of this study to verify the performance of specified LHEF ratings of factor classes, which represent an implicit bivariate relation between landslide occurrences and factors, the well-established WofE method (Bonham-Carter et al., 1989; van Westen, 2000; Carranza, 2004; Mathew et al., 2007; Thiery et al., 2007) was preferred over the other bivariate and multivariate empirical methods.

2.3.1. Comparison of WofE with LHEF ratings

According to the results of the WofE analysis (Table 2.5), landslides occur more frequently in phyllites/schist/quartzites in both case study areas. “Younger loose debris” has statistically significant positive spatial associations with landslide occurrences in Area 1. “Older well compacted debris” and “Gneisses” in either of the two case study areas have statistically significant negative spatial associations with landslide occurrences. Following the above quantified spatial associations, higher LHEF rating should be given to “phyllites/schists/quartzites” than to “weathered gneisses” in both the case study areas. Maximum LHEF rating for “younger loose debris” is appropriate in Area 1 but not in Area 2. Similarly, older and compacted debris material on slopes should be given the lowest LHEF rating in both the case study areas. During field surveys, it has also been observed that the landslide occurrences are comparatively lesser in “Gneiss” and “Older well compacted debris” than in “phyllites/schists/quartzites” and “younger loose material”, which corroborates the above WofE calculations. So, WofE calculated using quantified spatial associations between landslides and factors are more realistic than the subjectively-assigned LHEF ratings.

Table 2.5 *Wp* and related statistical parameters of factors (*C* and *Stud C*) based on the WofE method. *C* is the contrast defined by the difference between positive weight (*Wp*) and negative weight (*Wn*) of a factor class and Stud C is the studentised contrast defined by the ratio of contrast (*C*) to its standard deviation, calculated using variances of weights (Bonham-Carter et al., 1989).

Geofactors	Area 1			Area 2		
	C	Stud C	*Wp*	C	Stud C	*Wp*
Lithology						
Phyllite/Schist/Quartzites	0.79	9.2	0.78	0.98	10	1.02
Gneiss **	-0.97	-8.3	-0.98	-0.03	-0.3	0.01
Sheared gneiss	-1.11	-1.9	-1.12	0.62	2	0.66
Alluvial fill	0.69	4.3	0.68	?	?	-0.86
Older compacted debris	-1.19	-9.3	-1.20	-0.90	-8.2	-0.86
Younger loose debris	2.13	19.6	2.12	-0.29	-1	-0.25
Sandy soil	N.A	N.A	N.A	0.29	1.4	0.33
Clayey soil	N.A	N.A	N.A	0.59	3.5	0.63
Structure						
Type 1 (LHEF<0.8)	-0.05	-0.5	-0.06	-0.57	-6.1	-0.05
Type 2 (0.8≤ LHEF< 1)	-0.63	-3.7	-0.64	0.38	3.6	0.26
Type 3 (1≤LHEF<1.3)	0.24	2.7	0.22	0.47	5	0.20
Type 4 (1.3≤LHEF<1.6)	0.04	0.3	0.02	-0.56	-2.1	-0.47
Type 5 (LHEF≥1.6)	0.35	1	0.33	?	?	-0.47
Slope						
Very gentle	-0.57	-3.5	-0.58	0.10	1	0.06
Gentle	-0.06	-0.7	-0.07	0.07	0.6	0.03
Moderate	0.12	1.4	0.11	0.17	1.7	0.13
Steep	0.16	1.2	0.15	-3.60	-3.6	-3.63
Escarpment/cliff	1.10	4.5	1.09	?	?	-3.63
Relative relief						
Low	0.09	0.9	0.11	0.51	4.6	0.54
Medium	-0.30	-3.4	-0.29	-0.35	-3.7	-0.32
High	0.25	2.8	0.26	0.05	0.5	0.08
Landuse & land cover						
Agri/settlement	0.23	2.6	0.21	-0.48	-5	-0.52
Tea garden	-1.65	-10.6	-1.67	?	?	-1.78
Cinchona	N.A.	N.A.	N.A.	-0.69	-1.4	-0.74
Moderate forest	0.25	1.4	0.23	-0.71	-4.4	-0.75
Thick forest	0.60	6.8	0.58	-0.57	-1.7	-0.61
Sparse forest	0.00	0	-0.02	-1.74	-9.4	-1.78
Barren land	0.85	5.5	0.82	2.99	32.8	2.94
Hydrogeology						
Damp	-1.21	-7	-1.19	-0.79	-6.1	-0.74
Wet	-0.03	-0.2	0.00	-0.57	-6.2	-0.51
Dripping	1.94	15.8	1.96	1.48	16.2	1.53
Flowing	0.74	2.3	0.77	?	?	-0.74

N.A. – Not applicable because factor class is not mapped in that study area.
? - Unquantifiable spatial relationship.

In Area 1, steeper slopes generally have statistically significant increasing contrast values, starting from negative studentised contrast values in gentle slopes to highly positive studentised contrasts in escarpments and cliffs. This is in line with the fact that in Area 1 most landslides are rockslides, which occur on steep slopes in general. In Area 2, the pattern is different: there gentle to moderate slopes have statistically significant positive studentised contrast values, whereas steeper slopes have negative values, indicating the presence of large debris slides in lower slope classes. Therefore, the increasing trend of LHEF ratings with steeper slope classes is not always appropriate or is highly dependent on the type of landslides or failure mechanisms studied and on the use of the part of the landslide polygon (depletion or accumulation zone) for analysis.

Relative relief, the other topographic factor in the BIS method, does not show a consistent relation with landslides in both case study areas, as it is difficult to explain why the medium class has a negative spatial correlation while the other classes have a positive correlation. The increasing weights for higher internal relief as indicated in the LHEF rating in BIS is therefore not appropriate in both case study areas. Question should be raised whether this factor is useful to include in such an analysis, as it has also a large overlap and obvious conditional dependence with slope angle and size/area of the slope facet.

The weights and contrasts derived for the land-use and land-cover classes (Table 2.5) show large variations, between the two case study areas, and between the two methods used. Apart from the tea gardens, which show negative spatial associations with landslides, and the barren slopes, the contrast factors are reverse for all landuse types in both case study areas. According to the WofE calculations, in Area 1, maximum LHEF rating should be given to thick forest, followed by successively lower LHEF ratings to barren land, agriculture/settlement and moderate forest and lowest LHEF rating for tea garden. In Area 2, the highest LHEF is appropriate for barren land, but sparse forest must be given the lowest LHEF rating. The above analysis either points towards a complex causal relationship between landslides and land use in the study area which varies from an area to another or there could be no relation between the two. Landslides in such areas are perhaps more controlled by some other factors (e.g., lithology, slope etc.). Therefore, the relationship of land-use with rock slide is not direct and thus application of “land use and land cover” as a direct causal factor to rock slide needs further examination. Tea gardens in general ensure a better stability due to good land management practices, whereas other agricultural land or densely habitated land on moderate to steep slope can contain higher concentration of shallow debris slides depending on poor land-use practices.

As indicated earlier, the hydro-geological factor of the BIS method is difficult to include in the analysis. The classification as shown in Tables 2.1 and Table 2.5 is also dependent on the season in which the field data are collected, and the classes are not defined in a very scientific manner. Moreover, the recommended classes can barely be correctly mapped at medium scale (1:50,000) in field over a large area. According to WofE results, the class indicated as “dripping” has the most statistically significant positive spatial association with landslide occurrences in both areas, whereas the class indicated as “flowing” has only a positive but lower relation in Area 1 but a negative relation in Area 2. In Area 1 there is a relationship between landslides and the proximity to streams, which is lacking in Area 2, where

landslides occur more on gentle slopes and agricultural terraced lands. Thus, the weights derived from the WofE do not correspond with those from the BIS method for the hydro-geological factors, although, the former seems to represent some spatial association between landslides and specific factors, that could be genetically related. Perhaps more detailed and direct hydro-geological factors, derived from a digital elevation models, such as the wetness index (Beven and Kirby, 1979) are to be tested as potential predictors to different landslide types (see chapter 7).

2.3.2. WofE susceptibility maps and validation

To prepare the WofE-based landslide susceptibility maps, a final weight for each class of a factor is assigned by

$$WC_{Ji} = W_pC_{ji} + \Sigma W_nC_{ji} - W_nC_{ji} \quad (2.1)$$

where, WC_{ji} is the final weight of the j-th class of an i-th factor, W_pC_{ji} is the positive weight or W_p values of the j-th class of the i-th factor map and W_nC_{ji} is the negative weight or W_n values of the j-th class of an i-th factor.

The above formula (Eqn. 2.1) was applied to maximise the influence of positive weights of each factor class by simultaneously considering the sum of the negative weights of the rest of the factor classes of the same factor theme (Bonham-Carter et al., 1989). By applying the above conversion formula, highest positive weights were assigned only to the causal factor class whereas, other, insignificant factor classes or the factor classes having unquantifiable spatial relations (the factor class which contains no training landslide data) were assigned the maximum negative weight values. Multi-class weight maps of all layers of evidence were finally combined to derive the accumulated WofE for further susceptibility classification.

The final WofE maps of Area 1 and 2 were then spatially combined with the training landslide data and the success rate curves (also known as “goodness-of-model-fit”) were prepared (Fig 2.5) following the same method of constructing prediction rate curves for the BIS-susceptibility maps (Chung and Fabbri, 1999). The results indicate that 30% of the area with the highest weights contains 71% (Area 1) and 83% (Area 2) of cumulative landslide areas (Fig. 2.5). The different success rates in both case study areas indicate different slope failure mechanisms, which require different combinations of factors and segregation of landslide occurrences into different types. Using a randomly-selected landslide dataset as testing data which was not used in training the WofE models, prediction rate curves in both the areas were

prepared (Fig. 2.5). The available data of factors gave a better 'goodness-of-model-fit' and "prediction rate" in Area 2 than in Area 1 (Fig. 2.5).

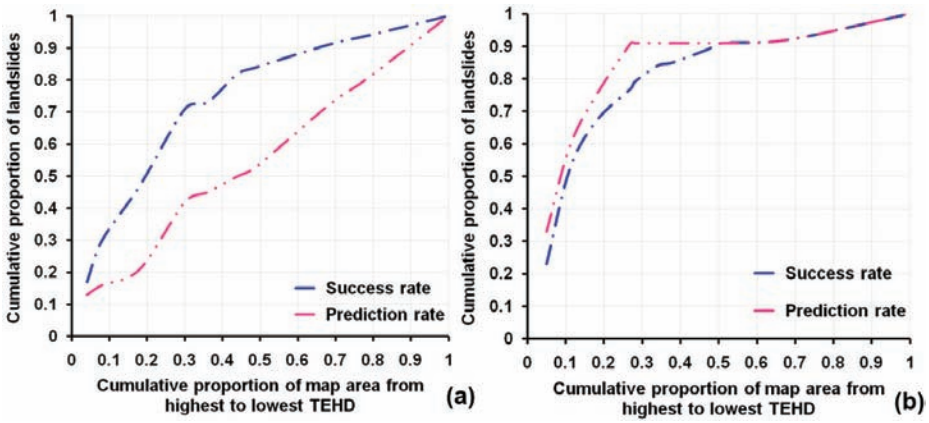

Fig. 2.5 Success and prediction rate curves of landslide susceptibility maps (WofE method) for (a) Area 1 and (b) Area 2.

Each of the WofE-based landslide susceptibility maps of the case study areas was then classified into five susceptibility classes (Fig. 2.2b and Fig. 2.3b) similar to the maps obtained via the BIS method. The class boundaries of WofE weights were determined according to the respective success rate curves of the two areas (Fig. 2.5) and considering the specified ranges of cumulative landslide area percent values (Table 2.6). In case of WofE landslide susceptibility maps, landslide density and percentage of total landslide area in each susceptibility class were also calculated considering the entire population of known landslide occurrences in each of the case study areas (Table 2.7). The "high" and "very high" susceptibility classes contain around 80% of the total landslide areas in Area 1 and around 83% of total landslide areas in Area 2 (Table 2.7). The landslide densities also sharply increase with increasing landslide susceptibility from "high susceptibility" to "very high susceptibility". These results indicate better models of spatial associations between factors and landslides as quantified by an empirical method (WofE) than those by an indirect heurist (e.g., BIS) method.

Table 2.6 WofE-based landslide susceptibility classes according to the steepness of success rate curves.

Landslide susceptibility	%-le break (Cummulative landslide area in success rate)	Range of weight values	
		Area 1 (TS78A/8)	Area 2 (TS78A/12)
Very low	100	≤-2.50	≤-1.81
Low	95	-1.71 to – 2.50	-1.35 to – 1.81
Moderate	90	-0.94 to -1.71	-0.87 to -1.35
High	85	1.31 to -0.94	1.43 to - 0.87
Very high	55	> 1.31	> 1.43

2.4 Predictive capabilities of BIS and WofE methods

To compare the results of WofE and BIS methods, both the success and prediction rates (Fig. 2.5) of WofE susceptibility maps are compared with the prediction rate curves of BIS susceptibility maps (Fig. 2.4). For Area 1, 30% of the map with highest weights according to the WofE method predicts 42% of the landslide areas, whereas the 30% of the map with highest TEHD values according to the BIS method also predict 42% of landslide areas. Whereas the success rate or 'goodness of model fit' of WofE in Area 1 is substantially higher (71%) (Fig. 2.5a) than the prediction rate of BIS susceptibility map (Fig. 2.4). In Area 2, 30% of the map with highest weights according to the WofE method predicts 90% of the landslide areas (Fig. 2.5b), whereas 30% of map with highest TEHD values according to the BIS method could predict only 52% of landslide areas, which is also substantially lower than the success rate (83%) of WofE susceptibility maps (Fig. 2.5b).

Excepting Area 1, both the prediction rate and success rate curves indicate that the landslide susceptibility maps created via the WofE method are better than the landslide susceptibility maps created via the BIS method. These demonstrate that the WofE method performs better than the BIS method both in "goodness-of-model-fit (success rate) and "prediction rate" analysis; although in both cases the prediction rates are not always equally high and not exceeding the corresponding success rate or prediction rate curves (e.g., Area 1). This inconsistency in validation results indicates that a) the factors specified by the BIS method (and the same which were used in the WofE method) are not the optimal spatial factors for prediction of landslide occurrences in either of the two case study areas, b) less-accurate and insufficient spatial representation of some of the spatial factors such as structure, hydro-geology, rock weathering and soil depth due to bias, uncertainty and scale constraints, and c) existing BIS guidelines do not allow selection of factors that are specific to different landslide types and failure mechanisms, and d) landslide inventory maps are most-probably incomplete since source data likely to have both temporal and spatial data gaps.

Table 2.7 Area, density, and percentage of landslides in different landslide susceptibility classes mapped in the study areas according to the WofE method.

Study area	Landslide susceptibility		Cross-validation		
	Class	Area covered (km^2)	Area (km^2) of known landslides	Landslide density	% total landslide area
Area 1	Very low	74	0.11	0.15	7
	Low	35	0.10	0.29	6
	Moderate	42	0.12	0.29	7
	High	95	0.52	0.55	31
	Very high	43	0.83	1.93	49
Area 2	Very low	169	0.07	0.04	5
	Low	61	0.09	0.15	6
	Moderate	43	0.08	0.18	6
	High	94	0.45	0.48	31
	Very high	27	0.75	2.78	52

2.5 Conclusions and recommendations

In this particular study, the performance of a specified-rating based landslide-independent knowledge-driven (heuristic) method (BIS) for landslide susceptibility mapping that is widely followed in India has been compared with an empirical method (WofE) in two adjacent case study areas, where the importance of the same factor classes is analyzed objectively through their spatial associations with landslide occurrences. The landslide susceptibility maps obtained via WofE show better success/prediction rates than those of the BIS landslide susceptibility maps in both case study areas. Due to different landslide types and related factor combinations in the two case study areas, the prediction rates varied substantially. The results show that landslide susceptibility mapping in complex environments like the Darjeeling Himalayas should not be done using pre-defined factors and specified weights, as in the BIS guidelines. In every area, experts should select those combinations of relevant factors only that best predict the occurrence of specific landslide types that occurred. A guideline for landslide susceptibility mapping at medium scales should therefore not specify factors and rating schemes based solely on subjective criteria but on the methods to be carried out iteratively and interactively to analyze the importance of the individual relevant factors using various empirical tools of spatial association analyses (see chapters 4 and 6). This could be combined with area specific knowledge on landslide types and causal mechanisms and a unique/effective way for quantitative validation of output susceptibility maps.

The results and inferences of this chapter lead to the importance of investigating landslide hazard analysis by first generating landslide inventory maps (chapter-3). Landslide inventory mapping is the most fundamental exercise in any landslide hazard prediction method because it allows us to develop knowledge about a) the past landslide types, failure mechanisms,

and conceptual knowledge about relations between existing landslides and causal factors, b) spatio-temporal evolution and activity of landslides, c) relation between existing landslides and triggering factors and d) frequency of occurrence of landslides having different magnitudes, which are essential inputs for determining spatial, temporal and magnitude predictions of landslide occurrence.

Chapter 3: Generating event-based landslide inventory maps

Landslide inventory maps store information on the spatio-temporal distribution of landslide occurrences and are usually linked to attributes with information on date of occurrence, types, failure mechanisms, area/volume, depth, etc. A special type of landslide inventory that displays the landslide occurrences that are caused by the same triggering event is also called an event-based landslide inventory or MORLE (Crozier, 2005). Generation of such event-based landslide inventory maps in perennially data-scarce environments, like the Indian Himalayas and their subsequent use for landslide hazard analysis is a challenging task. This chapter is based on two publications: (a) "*Generation of event - based landslide inventory maps in a data - scarce environment: case study around Kurseong, Darjeeling district, West Bengal, India*" (Ghosh et al., 2009b) and (b) "*Generating event-based landslide maps in a data-scarce Himalayan environment for estimating temporal and magnitude probabilities*" (Ghosh et al., 2011a). This chapter also describes how landslide inventory maps can be used to calculate the temporal and magnitude probabilities of future landslides.

3.1. Introduction

Incorporation of landslide hazard analysis into land use planning is important for proper mitigation of the impact of landslides. Whereas this has become a standard practice in developed countries, many developing countries still lack proper land use planning and zoning regulations, let alone analysis of landslide risk due to lack of detailed and reliable landslide hazard maps. In many cases, available landslide hazard maps are actually landslide susceptibility maps (e.g., Figs. 2.2 and 2.3) with qualitative levels of landslide proneness (e.g., Kanungo et al., 2006; Ghoshal et al., 2008; Gupta et al., 2008; Mathew et al., 2009), that cannot be used directly in the quantification of the possible impact of landslides. Conversion of landslide susceptibility maps into landslide hazard maps requires estimates of spatial, temporal and magnitude probabilities of landslides (Guzzetti et al., 1999; Glade et al., 2005; Fell et al., 2008; van Westen et al., 2008). Those probabilities can only be derived accurately through the generation and analysis of event-based landslide inventory maps.

Landslide inventory maps can be prepared through various methods, such as historical archive studies, interviews, detailed geomorphologic fieldwork, image interpretation and remote sensing techniques (Hansen, 1984; Wieczorek, 1984; Guzzetti et al., 2000; Cardinali et al., 2002; Galli et al.,

2008; van Westen et al., 2008; Martha et al., 2010). An event-based inventory is prepared soon after a prominent landslide-triggering event (e.g., rainfall, earthquake) to depict all slope failures that are due to that triggering event (Harp and Jibson, 1996; Guzzetti et al., 2004; Sorriso-Valvo et al., 2004). Due to lack of sufficient historical information on landslides or post-event field maps, air photos or satellite images from the past are often used as the main remote sensing source data for the generation of event-based landslide maps (Rib and Liang, 1978; Guzzetti et al., 2008).

The success of generating such event-based landslide inventory maps via stereoscopic interpretation of images/air-photos from different periods depends on several factors. Most importantly the availability of images of suitable quality and resolution, taken soon after a major landslide-triggering event, determines whether it is possible to extract individual event-based landslide maps. The characteristics of landslides may not be recognizable anymore in remote sensing imagery of later dates, as they may be obscured by vegetation re-growth or even by quick reactivation. If no images are available directly after a triggering event, it becomes difficult to make separate event-based inventories for triggering events that occurred between the dates of two available images. In addition, skills in image interpretation, which vary among individual persons, play an important role (Carrara, 1993), as well as the accuracy with which landslides are located on base maps (Malamud et al., 2004). Through time, multiple small slope failures may merge into larger landslides, which render detection of smaller landslides problematic and thereby introducing a bias in the frequency–size statistics of landslides. Accordingly, lack of spatial and temporal accuracy in landslide inventories, incompleteness of individual inventories and gaps in time between inventories are serious bottlenecks in determining temporal and magnitude probabilities of landslides and, therefore, pose difficulties in quantitative landslide hazard assessment (van Westen et al., 2006).

In this chapter, a work is presented on how to generate event-based landslide inventory maps for landslide-triggering events (e.g., rainfall) over a 40-year period (1968 to 2007) in a highly landslide-prone area (Fig. 1.1d) in Darjeeling Himalaya (India) based on available source data sets. In a data-scarce environment like India, source data for landslide inventory mapping are in general incomplete, and, there are data gaps for certain periods. Various source data also have different scales and resolutions. Notwithstanding such constraints, this study demonstrates how an event-based landslide database can be generated and used for estimating two important parameters (temporal and magnitude predictions) of landslide hazard.

3.2 Event based landslide inventory maps

3.2.1 Source data sets

The source data sets that were used in this study for landslide inventory mapping consisted of high-resolution satellite images, aerial photographs, topographic maps, old landslide inventory maps and reports of field investigations (Table 3.1). The oldest data set consists of topographic maps prepared by the Survey of India (SOI) in 1969, one year after a major landslide event that occurred between 2 and 4 October 1968, due to an high amount of rainfall of 1100 mm (Basu and De, 2003). During 1969, the SOI updated their topographic survey and prepared new 1:25,000 topographic maps, which included the locations of prominent and active landslides of the 1968-event. The next data set consists of 1:50,000 and 1:10,000 scale black-and-white stereo-air photos from 1980. The third data set is a field-based landslide inventory map from 1993 prepared by the Geological Survey of India (GSI) soon after a landslide event that occurred between 1 and 3 July 1993 (Sengupta, 1995). Unfortunately, this map covers only 56 km^2 in the south-eastern part of the study area. The fourth data set is another event-based landslide inventory map prepared by GSI after a landslide event that occurred between 6 and 8 July 1998 (Bhattacharya et al., 1998). This inventory map covers only a part of the area (~20 km^2) in the centre of the study area, and does not overlap with the previously-mentioned inventory map. For the period 2002 to 2006, three high-resolution Indian satellite images were used as source data (Table 3.1). The most recent data set is a detailed landslide inventory map prepared during this research through field surveys soon after a recent landslide event in 2007 (Table 3.1).

Table 3.1 Types, extent and period (DOA = date of acquisition) of source data and associated rainfall event-days for the landslide inventories (LI).

Source data (scale/resolution)	Extent (km^2)	DOA/period	Known rainfall event-days (24 days)	LI period
Topographic map (1:25,000)	90	1969-1970	2-4 October, 1968	LI68
B×W stereo airphotos (1:50000 and 1:10000)	90	1980	12 & 24 July, 1979	LI79
	90	1984	18 September, 1984	
	90	1985	18-19 October, 1985	
No source data available	90	1986	28 June, 1986	-
	90	1991	9-11 September, 1991	
Field-based landslide inventory map (1:25,000)	56	1993	1-3 July 1993	LI93
Field-based landslide inventory map (1:25,000)	20	1998	6-8 July 1998	LI98
IRS 1-D PAN image (5.8 m)	90	2002	Unknown	LI99-02
IRS P-6 LISS-4 MX (5.8 m)	90	2004	5-7 July 2003	LI03
IRS P5 Stereo Cartosat – 1 (2.5 m)	90	2006	Unknown	LI04-06
Field-based landslide inventory map (1:25,000)	90	2007	6-8 Sept., 2007	LI07

3.2.2 Methods of landslide inventory mapping

Because the source data sets vary in resolution, type and extent, different methods were adopted for extracting landslide information. For each period (Table 3.1; Fig. 3.1), a landslide inventory was made, and landslides were mapped as polygons, with a separation of their erosional and depositional area (preferably for large landslides). Each landslide was characterized by attributes such as movement type, material involved, activity, depth, failure mechanism, and date of occurrence (wherever possible), according to international standards (e.g., Varnes, 1978; UNESCO-WP/WLI, 1990; UNESCO-WP/WLI, 1993). A depth-to-failure surface of 5 m was considered as the main criterion to differentiate between deep-seated and shallow landslides. The source data of the 1968-event (topographic map sheets of 1969) contain no information on landslide types, depth and failure mechanisms. Thus, the 1980 airphotos were stereoscopically examined to characterize the 1968-landslides (LI68).

Stereoscopic interpretation of the 1:10,000 and 1:50,000 scale black-and-white stereo airphotos from 1980 was carried out using a mirror stereoscope, and landslide types were identified based on texture, tone of photo-elements, association, morphometry, depth and freshness of scarps. In addition, the airphotos from 1980 were used to map large scarps and depositional areas representing old/inactive landslides, which occurred prior to 1968 and thus, cannot be linked to any known landslide event. The landslides from the field-based inventory maps of 1993 and 1998 (LI93 and LI98) were converted to a base map, and additional non-spatial attributes, such as depth and failure mechanism, were interpreted from later images, although the extent of these two inventories did not cover the entire study area (Table 3.1).

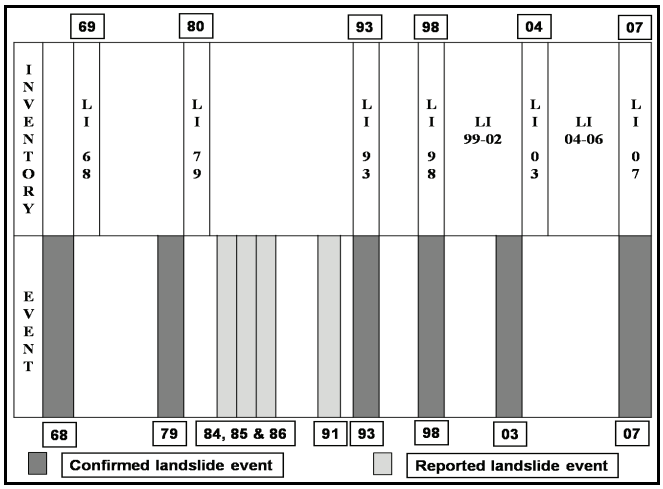

Fig. 3.1 Known landslide event-years and the generated landslide inventories (LI). Confirmed landslide events are the events having definite source data/maps; reported landslide events are known events but lack any source data/maps.

For subsequent periods (1999-2006), landslides were mapped from three high-resolution satellite images of 2002, 2004 and 2006 by digital stereo image interpretation with specialized software (Stereo-Analyst in ERDAS Imagine 9.x and ILWIS 3.3) using ortho-rectified images and a digital elevation model (DEM), derived from stereo Cartosat-I images of 2006 (Table 3.1). Within the above-mentioned period, only one major landslide event was known that occurred during the monsoon of 2003 (5-7 July, 2003) (Paul and Sarkar, 2003). The landslides for this event (LI03) were mapped mostly by comparing the images of 2002 and 2004 in conjunction with field data reported by Paul and Sarkar (2003). By comparing the landslides mapped for the period 1968 to 1998 with those in the image of 2002, an inventory of landslides that occurred between 1999 and 2002 (LI99-02) was generated. Unlike the other inventories (e.g., LI68 and LI93), this inventory lacks the exact date of the landslide-triggering event. Following a similar method, we compared further the landslides mapped from the images of 2004 and 2006 to generate another landslide inventory (LI04-06), which also lacks a specific landslide event-date. After a landslide event that occurred during the monsoon of 2007, all the associated landslides were mapped (LI07) by field surveys conducted during this research. In addition, some information and data about four landslide event years (1984, 1985, 1986 and 1991) were gathered from old geological reports and interviews with local people because no post-event landslide maps were available for those event years (These are indicated as reported landslide events in Fig. 3.1).

3.3 Analysis of landslide inventories

3.3.1 Landslide types and frequencies

The eight event-based landslide inventories were compared to examine variations in landslide characteristics (frequency, area, density, type and activity). For activity, the landslides associated with different events were spatially compared via buffer analysis in a GIS to identify the likely reactivated landslides. A buffer distance of 50 m was selected based on the field experiences and the scale of inventory mapping (1:25,000). Landslides from a later inventory were considered to be reactivated if they were located within 50 m of landslides from an earlier inventory; otherwise they were considered as new landslides.

The descriptive statistics for the eight event-based landslide inventories are presented in Table 3.2. The landslide density (number per km^2) varies through time, with the highest density in 1979 (6.2). The medians of areas of mapped landslides per event-based inventory vary between 519 m^2 (LI79)

and 3385 m^2 (LI68), excluding the large un-dated landslides that existed before 1968 (Table 3.2). The large landslides those are older than 1968 occupy about 21% of the study area and are mostly deep-seated rockslides with maximum area of 2.14 km^2. Since the inventory of pre-1968 landslides are not event-based, their density and dimension were not compared with those of the landslides in the eight event-based inventories between 1968 and 2007 (Table 3.2).

Between 1968 and 2007, shallow translational rockslides (hereafter denoted as Sh_rs; Fig. 3.2a) appear to be the most frequent slope movements (68%), followed by shallow translational debris slides (hereafter denoted as Db_rs; Fig. 3.2b) (29%) and deep-seated rockslides (hereafter denoted as Dp_rs; Fig. 3.2c-d) (3%). No analysis of Db_rs was made for LI98 because it contains only 31 debris slides that affected the railroad. The source map of LI98 did not cover any of the areas under natural slopes that were affected by 1998-event. Compared to the above two landslide types, the density frequency of Dp_rs is rather low, although they occupy larger areas (Table 3.2). Fig. 3.3 shows the overall landslide inventory for the study area, with indication of the most recent dates of landslide activity, and Fig. 3.4 illustrates the distributions of all landslide types that were mapped from the different source data sets.

Table 3.2 Summary statistics of landslides in individual event-based landslide inventory (NA = not available)

Landslide statistics	Pre-1968 slides	Event-based landslide inventory (LI)							
		LI68	LI79	LI93	LI98	LI99-02	LI03	LI04-06	LI07
Area of inventory (km^2)	90	90	90	56	20	90	90	90	90
Number of landslides	200	83	562	108	31	185	242	164	85
Landslide area (km^2)	9.5	0.49	0.64	0.5	0.05	0.84	1.18	0.65	0.11
Min. slide area (m^2)	192	776	45	372	185	271	221	45	42
Max. slide area (m^2)	2141500	70253	55815	40906	9573	79157	92155	119285	8265
Mean area (m^2)	101455	5986	1136	4634	1713	4525	4898	3985	1357
Median area (m^2)	20345	3385	519	2616	824	2301	1866	732	628
Number density(Nr/km^2)	2.2	0.9	6.2	1.9	1.6	2.1	2.7	1.8	0.9
Area density (%)	10	0.5	0.7	0.9	0.25	0.93	1.31	0.67	0.12
Shallow translational rock slides (Sh_rs)									
Total landslides (Nr)	0	59	374	86	NA	123	167	116	63
Landslide area (km^2)	0	0.22	0.32	0.28	NA	0.31	0.36	0.17	0.08
Shallow translational debris slides (Db_rs)									
Total landslides (Nr)	0	13	175	13	31	48	53	34	22
Landslide area (km^2)	0	0.04	0.12	0.05	0.05	0.16	0.17	0.04	0.03
Deep-seated rock slides (Dp_rs)									
Total landslides (Nr)	200	11	13	9	NA	14	22	14	0
Landslide area (km^2)	19	0.23	0.20	0.17	NA	0.37	0.65	0.44	0

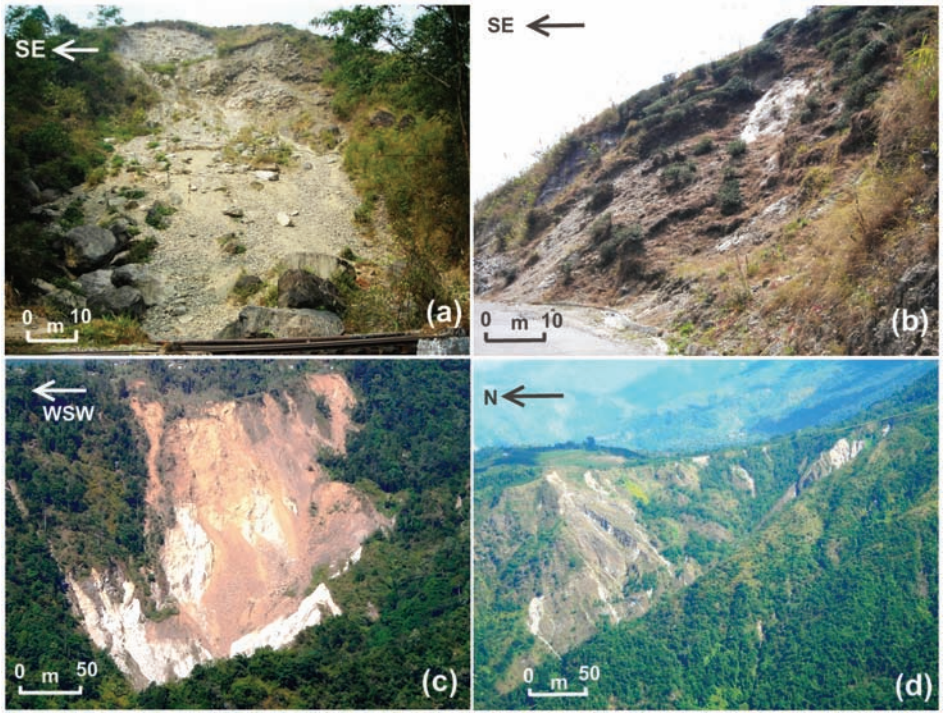

Fig. 3.2 Field photographs of recently active landslides. Examples of (a) a shallow translational rockslide (Sh_rs), (b) a shallow translational debris slide (Db_rs), (c) and (d) deep-seated rockslides (Dp_rs). Scale and directions shown in the photographs are approximate.

3.3.2. Temporal landslide activity

Table 3.3 shows the number and area of both reactivated and new landslides in each of the landslide inventories. For the inventory LI79, the analysis was done with respect to the LI68 inventory. Because some of the inventories (LI93 and LI98) do not cover the entire study area, it was considered that it is better to evaluate relative numbers (e.g., percentage of landslides) rather than the absolute numbers to understand the change in landslide activity. The inventory of 1979 (LI79) shows the highest percentage of reactivated landslides (90%). This is partly due to the effect of the large difference in the resolutions of source data from which the inventories were derived, as LI79 was obtained from 1:10,000 scale airphotos and LI68 from a generalized 1:25,000 scale topographic map. Similarly, the relative numbers of new landslides do not show a clear trend. There are years where the fraction of new landslides increases, periods when it seems constant, and followed again by periods of increase. LI03 is clearly an outlier, as all 185 landslides that were mapped in the previous event (LI99-02) were reactivated. The percentage of reactivated deep-seated rockslides is higher than the

percentage of reactivated shallow landslides, and, ranges from 54% (LI79) to 100% (LI03). On average, 61% of the 'new' landslides that occurred in the period from 1968 to 2007 were located either within or very close to the deep-seated large landslides that existed before 1968 (Figs. 3.3 and 3.4).

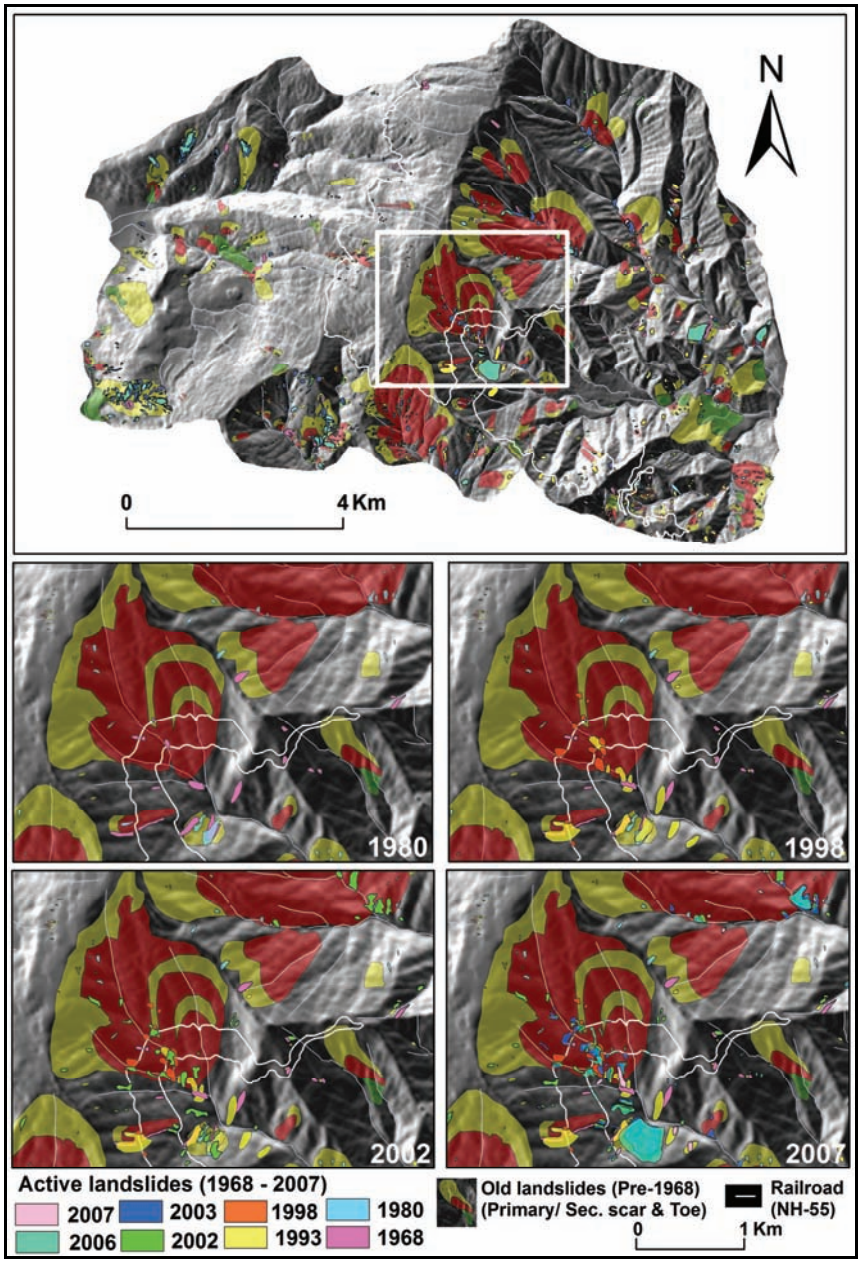

Fig. 3.3 Multi-temporal landslide inventory map of the study area indicating years of past landslide activity. The large un-dated landslides of pre-1968 are also shown.

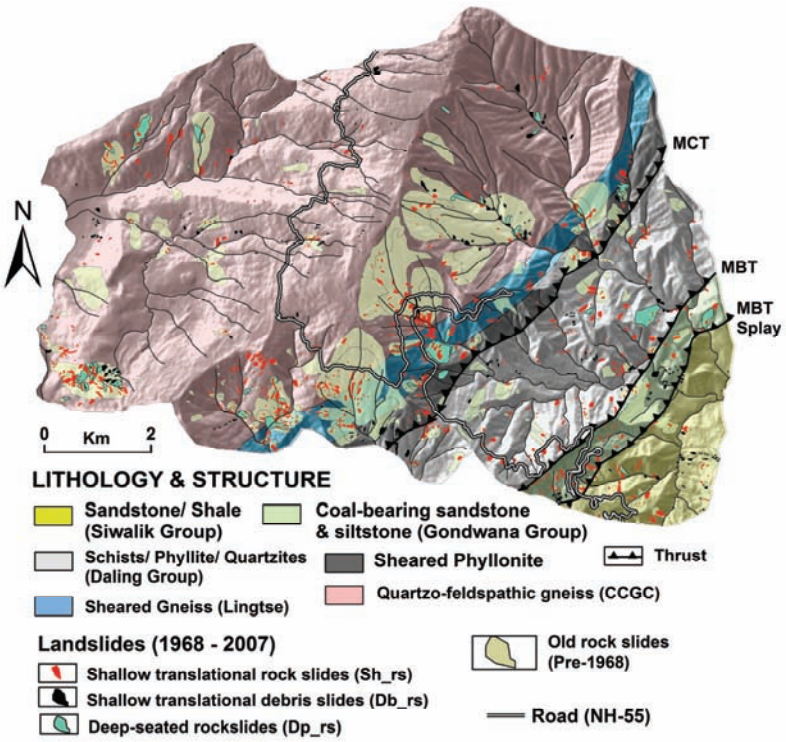

Fig. 3.4 Distribution of all landslide types mapped from eight different landslide inventory data sources. The large un-dated rockslides of pre-1968 are also shown.

Table 3.3 Frequency (Nr) and area of reactivated and new landslides in individual event-based landslide inventories (results of GIS-based buffer analysis). (NA = not mapped).

Landslide inventory (LI)	LI79	LI93	LI98	LI99-02	LI03	LI04-06	LI07
All landslides							
Number of landslides	562	108	31	185	242	164	85
Landslide area (km^2)	0.64	0.5	0.05	0.84	1.18	0.65	0.12
Reactivated (Nr)	55	60	13	76	185	98	53
New (Nr)	507	48	18	109	57	66	32
Reactivated area (km^2)	0.2	0.32	0.03	0.52	1.10	0.59	0.09
New area (km^2)	0.44	0.18	0.02	0.32	0.08	0.06	0.03
Shallow translational rockslides							
Number of landslides	374	86	NA	123	167	116	63
Landslide area (km^2)	0.32	0.28	NA	0.31	0.36	0.17	0.08
Reactivated (Nr)	42	44	NA	55	124	71	38
New (Nr)	332	42	NA	68	43	45	25
Reactivated area (km^2)	0.04	0.15	NA	0.17	0.30	0.14	0.05
New area (km^2)	0.28	0.13	NA	0.14	0.06	0.03	0.03
Shallow translational debris slides							
Number of landslides	175	13	31	48	53	34	22
Landslide area (km^2)	0.12	0.05	0.05	0.16	0.17	0.04	0.03
Reactivated (Nr)	6	9	13	12	30	14	15
New (Nr)	169	4	18	36	18	20	7
Reactivated area (km^2)	0.003	0.04	0.03	0.07	0.14	0.02	0.02
New area (km^2)	0.12	0.01	0.02	0.09	0.03	0.02	0.01
Deep-seated rockslides							
Number of landslides	13	9	NA	14	22	14	0
Landslide area (km^2)	0.20	0.17	NA	0.37	0.65	0.44	0
Reactivated (Nr)	7	7	NA	9	22	13	0
Reactivated area (km^2)	0.16	0.13	NA	0.29	0.65	0.43	0
New (Nr)	6	2	NA	5	0	1	0
New area (km^2)	0.04	0.04	NA	0.08	0	0.01	0

Further, landslide density within each terrain unit was calculated to study the changes in landslide activity (See Table 3.4). The map of terrain units was obtained via a semi-automatic technique by delineating ridge crests, streams and spur axes using a 10 m × 10 m digital elevation model (DEM) (cf. Carrara et al., 1991). Since both LI93 and LI98 inventories cover only small and separate parts of the study area (Table 3.2), they were merged into a single inventory for the purpose of this analysis. In view of mapping and digitization errors, terrain units with landslide density equal to or less than 2% are considered to be stable (Galli et al., 2008) or having "no landslides".

Table 3.4 Temporal trend of landslide activity in affected terrain units. There are 1001 terrain units in the study area.

Inventory year	Number of unstable terrain units			
	total	with new activity	with increased activity	with constant activity
Pre-1968	443	-	-	-
1968	66	-	-	-
1980	160	94	27	39
1998	206	46	56	104
2002	259	53	61	145
2004	293	34	106	153
2007	301	8	31	262

Fig. 3.5 illustrates variations in area-based landslide density per terrain unit during the last 40-year period (1968-2007). Table 3.4 lists the numbers of unstable terrain units in different periods derived from the above analysis. Initially, 44% of the terrain units (i.e., 443 out of 1001 terrain units) are covered by the large pre-1968 landslides. There is a steady increase of unstable terrain units from 1968 (66) to 2007 (301). About 68% (205) of these 301 unstable terrain units in 2007 are located on or very close to pre-1968 landslides (Fig. 3.5). The numbers of new terrain units affected by landslide activity decrease from 1980 (94) to 2007 (8) (Table 3.4), which clearly indicates the predominance of landslide reactivation in the study area. Terrain units with increasing landslide activity are mostly in 2004 (106) because of the landslide event that occurred in 2003, although, the numbers of terrain units with increasing landslide activity reduced to 31 in 2007. However, about 87% of the unstable terrain units in 2007 seem to have a constant landslide activity (because the absolute values of area based landslide density in such terrain units almost remained unchanged), as compared to those in the immediately preceding inventory.

3.4 Temporal probability estimation

Because of substantial gaps (e.g., 1969-1978, 1980-1992 and 1994-1997) in the available landslide inventories (Fig. 3.1) due to unavailability of source data, direct calculations of temporal probability of landslides using the frequencies of the known events could lead to an underestimated prediction. Instead, available information about the known days (or events) of landslides

(see Table 3.1) can be used to establish an empirical link with days (or events) of extreme rainfall (e.g., Gabet et al., 2004; Petley et al., 2007; Dahal and Hasegawa, 2008) assuming that such extreme rainfall events triggered the landslides. Unlike the methods of linking rainfall and landslides using bivariate linear relations between daily and antecedent rainfall amounts (Chleborad et al., 2006; Jaiswal and van Westen, 2009), a multivariate classification technique (discriminant analysis, hereafter denoted as DA) was used to predict landslide-triggering events. This latter method objectively facilitates capturing of possible non-linear relationship that exists between triggering rainfall events and various rainfall predictors, such as daily rainfall as well as a set of antecedent rainfall amounts. The frequencies of landslide events predicted via DA that were linked to triggering rainfalls were then used in Poisson distribution model to calculate the temporal probability of similar landslide events in the future.

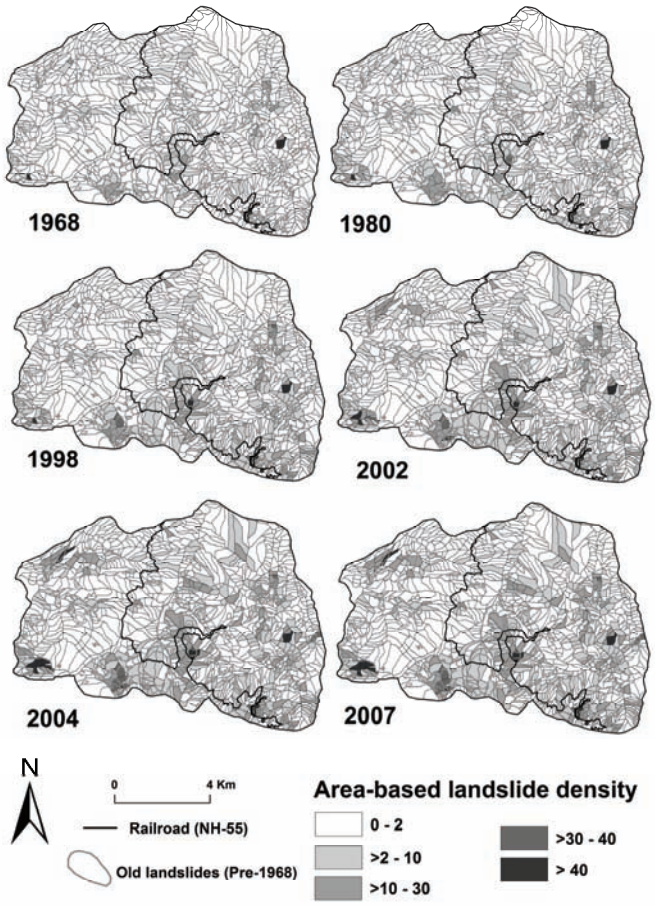

Fig. 3.5 Distribution of area-based landslide density per terrain unit (landslide area × 100/area of terrain unit) for the period from 1968 to 2007.

3.4.1 DA modelling for rainfall - landslide event relationships

The aim of DA was to define an empirical relationship between days with and without landslide events as response variable and daily variation in rainfall amounts as predictor variables. This analysis allows prediction of landslide event-days by using thresholds derived from the DA model. For the DA modelling, a rainfall station that is centrally located in the study area (Goomtee Tea Garden's rain gauge station; Fig. 1.1d) was selected and its daily rainfall data (in mm) for the same 40–year period of the landslide inventories (i.e., 1968–2007) were used. For DA, various rainfall indicators such as daily rainfall (DR) and different antecedent rainfall amounts (1, 2, 3, 5, 7 and 10-day antecedent rainfall, hereafter referred to as *DR*, AR_1, AR_2, AR_3, AR_5, AR_7 and AR_{10}, respectively) were used as predictors or explanatory variables (cf. Dai and Lee, 2001). As response or grouping variable, the known days (or events) of landslides (24 days) in the 40-year period were considered (see Table 3.1). To each of those 24 days of landslides, a Landslide Occurrence Score (LOS) of "1" was assigned. To all other days, a LOS of "0" was assigned. Because landslides in the study area were triggered only during monsoon rainfall, the rainfall data in the monsoon period (June to October) for each year were used in the analysis, which resulted in a data set of 6120 days. To calibrate the DA model, 4862 (or about 80%) of these 6120 days were randomly selected, of which only 20 days have LOS of 1. The other 1258 (or about 20%) days, of which 4 days have a LOS = 1, were kept aside for cross-validation of the DA model.

The DA model with seven rainfall predictors (*DR*, AR_1, AR_2, AR_3, AR_5, AR_7 and AR_{10}) resulted in a statistically significant discriminant function (Wilk's Lambda = 0.938 and significance level = 0.000), which was able to explain all the variances of the data in the model and successfully classified 80% of known landslide event-days (LOS = 1). The group centroids of the DA model have wide separation between the two response groups (LOS 0 = -0.017 and LOS 1 = 4.005) suggesting that the separation potential of the discriminant function between the two groups is strong. The highest coefficient value of the discriminant function pertains to daily rainfall (*DR*=0.849), followed by AR_1 (0.383), AR_2 (0.271) and AR_5 (-0.338) respectively, signifying their ability to classify the dichotomous response variable (i.e., LOS = 1 and LOS = 0). The predictors AR_3, AR_7 and AR_{10} are non-correlated with the discriminant function; and, therefore, contribute nothing to the model classification. The structure matrix of the discriminant function further reveals that both AR_7 (0.247) and AR_{10} (0.237) are sufficiently correlated with AR_5 (0.267) and the model statistics used in the DA model ("F to enter as 3.84" and "F to remove as 2.71") successfully resulted in the removal of

AR_7 and AR_{10} from the analysis. The variables or the predictors remaining at the final step of the DA are reasonably uncorrelated as depicted by the values of correlation in their structure matrix (DR = 0.886, AR_1 = 0.542, AR_2 = 0.480 and AR_5 = 0.267). Based on the results of above DA model, the following equation was derived to calculate the discriminant score (DS) for each case:

$$DS = -0.637 + (0.021DR) + (0.01AR_1) + (0.004AR_2) - (0.003AR_5) \quad (3.1)$$

The DA model successfully classified 80% (or 16) of the 20 known landslide event-days and 95.2% (4610) of the known non-landslide event-days (4842) in the calibration set, indicating that the overall success rate of the model is 95.15% (100*(4610+16)/4862) (Table 3.5). The validation of the DA model is obtained from the classification of cross-validation cases (1258) that were not used to calibrate the model. The DA model successfully classified 100% (four) known landslide event-days and 95.37% (1196 out of 1254) of the non-landslide event-days in the validation data set, which indicate that the overall prediction rate of the DA is 95.38% (Table 3.5).

Table 3.5 Classification results of DA model.

			Predicted		Total
			No landslide	Landslide	
Cases for model calibration	Original Count (days)	No landslide	4610	232	4842
		Landslide	4	16	20
Cases for model validation	Original Count (days)	No landslide	1196	58	1254
		Landslide	0	4	4

3.4.2 Prediction of landslide events using DA model results

The discriminant function scores (DS) derived from the DA model (Eq. 3.1) were used to identify thresholds to classify landslide event-years with varying degrees of severity by invoking similar concepts used in other analytical fields (cf. Altman, 1968; Rasmussen et al., 1985). Three different threshold DS values were used: 4, 10 and 20. A DS value of 4 was selected to separate years with no landslide events from those with landslide events. Years with a cumulative DS values between 4 and 10 were classified as “minor landslide event years”, those with DS values between 10 and 20 as “moderate landslide event years” and those with a DS values above 20 were designated as “major landslide event years”. These thresholds were subjectively determined by examining and comparing the cumulative DS values of the confirmed landslide events (e.g., LI93, LI03, LI68 etc.) with the severity and damage potential of the corresponding landslide events, as expressed by the landslide density in the terrain units and also from historical records. Fig. 3.6

shows that there are 30 predicted landslide event-years between 1968 and 2007 with cumulative *DS* values above the minimum threshold of 4. The LI68 event in Darjeeling Himalaya with *DS* value of 21.89 (Fig. 3.6) corresponds to the most severe landslide event-year (1968) within the analyzed period (Starkel and Basu, 2000) depicted both by the available data and model results. During that event, a very large number of landslides occurred throughout the entire Darjeeling Himalaya that destabilized the infrastructure and communication network in the region for more than a year. Another event confirmed in LI93 (*DS* = 4.36) was the least-severe event that occurred, causing a limited number of landslides in a few localized areas. Accordingly, in Fig. 3.6, 16 event-years classified as "minor", 10 event years as "moderate" and 4 event years as "major" based on available datasets that were input to DA to empirically define relationships between known landslide event days and different rainfall variables in the 40 year period (1968-2007). Among the confirmed events, LI93 was predicted as a "minor" landslide event, LI79, LI03 and LI07 as "moderate" landslide events and both LI68 and LI98 as "major" landslide events.

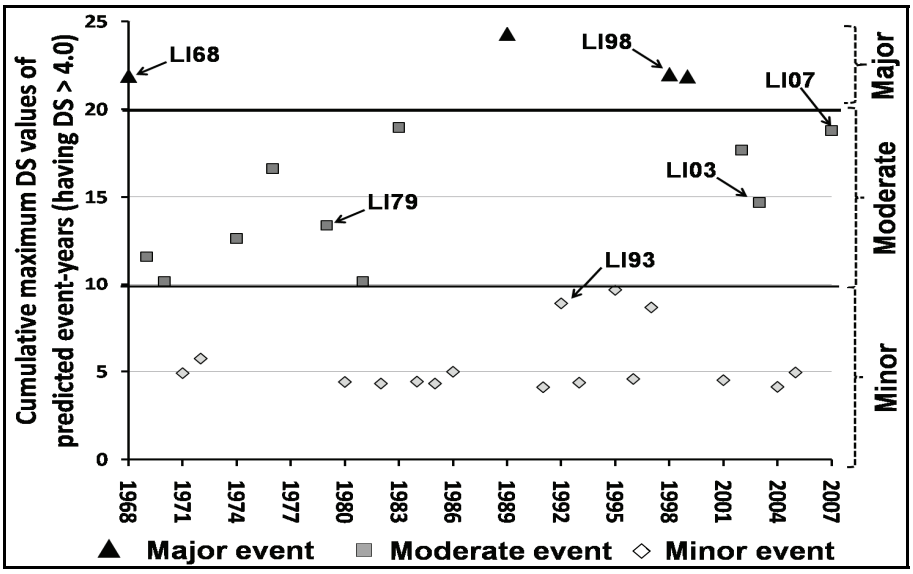

Fig. 3.6 Threshold cumulative discriminant scores (DS) for predicted "minor", "moderate" and "major" landslide events. The confirmed six events are shown and associated with corresponding inventory numbers to depict validity of model-derived severity classifications of known landslide events.

3.4.3 Calculation of exceedance probability

The mean recurrence interval (μ) of various predicted landslide events (Fig. 3.6 and Section 3.4.2.) can be determined by dividing the period of analysis (40 years, 1968-2007) with the number of predicted landslide event-years (major, moderate and minor). The estimated μ was then used to calculate the exceedance probability of landslide events by using the Poisson distribution model (Crovelli, 2000; Coe et al., 2004). In the Poisson distribution model, exceedance probability or probability of experiencing one or more landslide events during a period '*t*' can be estimated by the following equation.

$$P[N_L(t) \geq 1] = 1 - P[N_L(t) = 0] = 1 - e^{-\lambda t} = 1 - e^{-t/\mu} \quad (3.2)$$

where $P[N_L(t) \geq 1]$ is the exceedance probability or probability of occurrence of one or more landslide event in a period '*t*' and λ is the reciprocal of the mean recurrence interval (μ), that is, $\lambda = 1/\mu$.

Therefore, a graph of exceedance probability versus period (in years) (Fig. 3.7) can be used as an indication of the temporal probability of landslide events over 40 years. For example, within a 10-year period, the exceedance probability of "moderate" and "minor" predicted events are very high (0.91 and 0.98, respectively) compared to a "major" event (0.63).

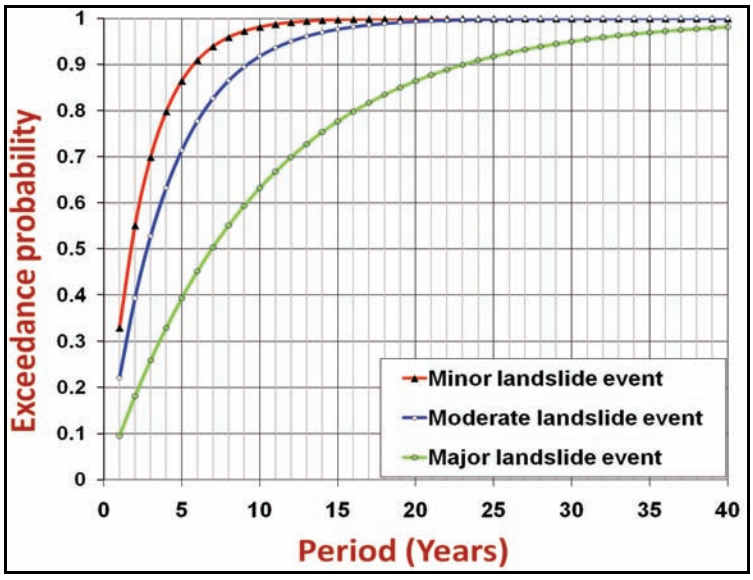

Fig. 3.7 Exceedance probability of predicted major, moderate and minor landslide events, resulting from the application of the Poisson distribution model.

3.5 Magnitude probability estimation

3.5.1 Landslide magnitude-frequency analysis

The quantitative estimation of the probability of occurrence of landslides of a given magnitude is a key issue for any regional landslide hazard analysis (Guzzetti et al., 1999; Malamud et al., 2004; Fell et al., 2008). Magnitude probabilities of landslides can be estimated after performing the magnitude-frequency analysis of the landslide inventory data. For estimating landslide magnitudes, the area of landslide (m^2) can be considered as a proxy (Aleotti, 2004; Dapporto et al., 2005; Guzzetti et al., 2005). Therefore, the frequency-size analysis of landslide area of all the eight event-based landslide inventories that were generated for the period 1968 to 2007 was carried out by calculating the probability density function (hereafter, denoted as pdf) of landslide area using the maximum likelihood estimation method (Fisher, 1922) assuming two standard distribution functions: (i) the Inverse-Gamma distribution function (Malamud et al., 2004), and (ii) the Double-Pareto distribution function (Stark and Hovius, 2001).

For each inventory, the raw probability density was calculated using the histogram estimation method and considering a logarithmic bin width. Starting from the estimated probability density functions, the corresponding cumulative distribution function (hereafter, denoted as cdf) were calculated to determine the possible magnitude probability of specific landslide sizes (or areas). The above estimation of landslide area (size)-frequency distribution was performed using a script developed in R (R Development Core Team, 2010), a free software environment for statistical computing and graphics (http://www.R-project.org) by Mauro Rossi of CNR-IRPI, Italy. The R package "bbmle" was used in the script to implement the maximum likelihood estimation method. For the said script, see Annexure I in the enclosed CD and also at the following toolbox of CNR-IRPI:
http://geomorphology.irpi.cnr.it/tools/stat-ls/estimation-of-probability-of-landslide-area/

3.5.2 Results and synthesis of magnitude-frequency analysis

The results of the magnitude-frequency analysis of landslide areas applied to eight event-based landslide inventories are shown in Figs. 3.8 to 3.10 and in Table 3.6. In Figs. 3.8 to 3.10, column A shows box plots demonstrating distributions of frequencies of landslide areas; column B shows estimates of the Inverse-Gamma pdfs and column D shows estimates of the Double Pareto pdfs. Columns C and E show the cdfs calculated from the corresponding Inverse-Gamma and the Double Pareto fitted distributions (Columns B and D)

respectively. Table 3.6 gives the related values for the exponent/slope of power-law tail (ρ or α) of the pdfs for medium to large landslides and the rollover points, where the distribution changes direction for smaller landslides (in m^2). The assumption in the analysis was that larger landslide events would show a higher value for the rollover point, whereas the slope of the right part of the curve (ρ or α), representing medium to large landslides would also be slightly steeper. From the data in Table 3.6 and Fig. 3.10, it can be concluded that the inventories show different values for the rollover points and for ρ or α. Except LI93, LI98 and LI07, the rest of the inventories can be satisfactorily described by both standard distribution functions available in the literature (Figs. 3.8 to 3.10). This implies that those inventories are more or less complete for landslide areas that are greater than the rollover sizes and, therefore, their respective cumulative probability estimates (cdfs in columns C and E) can be used for the estimation of the magnitude probability of different landslide events. However, of the eight inventories, only five inventories (LI68, LI93, LI98, LI03 and LI07) pertain to specific triggering events (Table 3.7). Inventory LI79 is made from very good source data. In fact, it is the only inventory for which large scale (1:10,000) stereo aerial photographs were available. However, it is the first inventory since 1968, and therefore the landslides that were mapped might have been produced by several triggering events between 1968 and 1979 (Figs. 3.1 and 3.6). Like LI79, the inventories LI99-02 and LI04-06 might also include landslides of several triggering events, as no spatial landslide source data was available for the intermediate years.

The cdfs shown in column C and E in Figs. 3.8 to 3.10 allow to determine the probability of landslides with an area smaller or larger than a particular size (e.g., area in m^2), which can be used as quantitative estimate for landslide size or magnitude probability (Guzzetti et al., 2005). For example, based on the LI68 event and the Inverse-Gamma fit of the landslide area-frequency data, the probabilities that a future landslide event of a similar magnitude would result in landslides >1000 m^2 and landslides >10,000 m^2 are 0.98 and 0.15 respectively (Fig. 3.8; Table 3.6). The same estimate, based on the Double Pareto fit of the LI68 data, gives somewhat similar probability values (0.95 and 0.12, respectively) (Fig. 3.8; Table 3.6). Table 3.6 presents the probability of future landslide sizes based on the magnitude-frequency analysis of each of the eight landslide inventories, for small (<1000 m^2) and large landslides (>10,000 m^2).

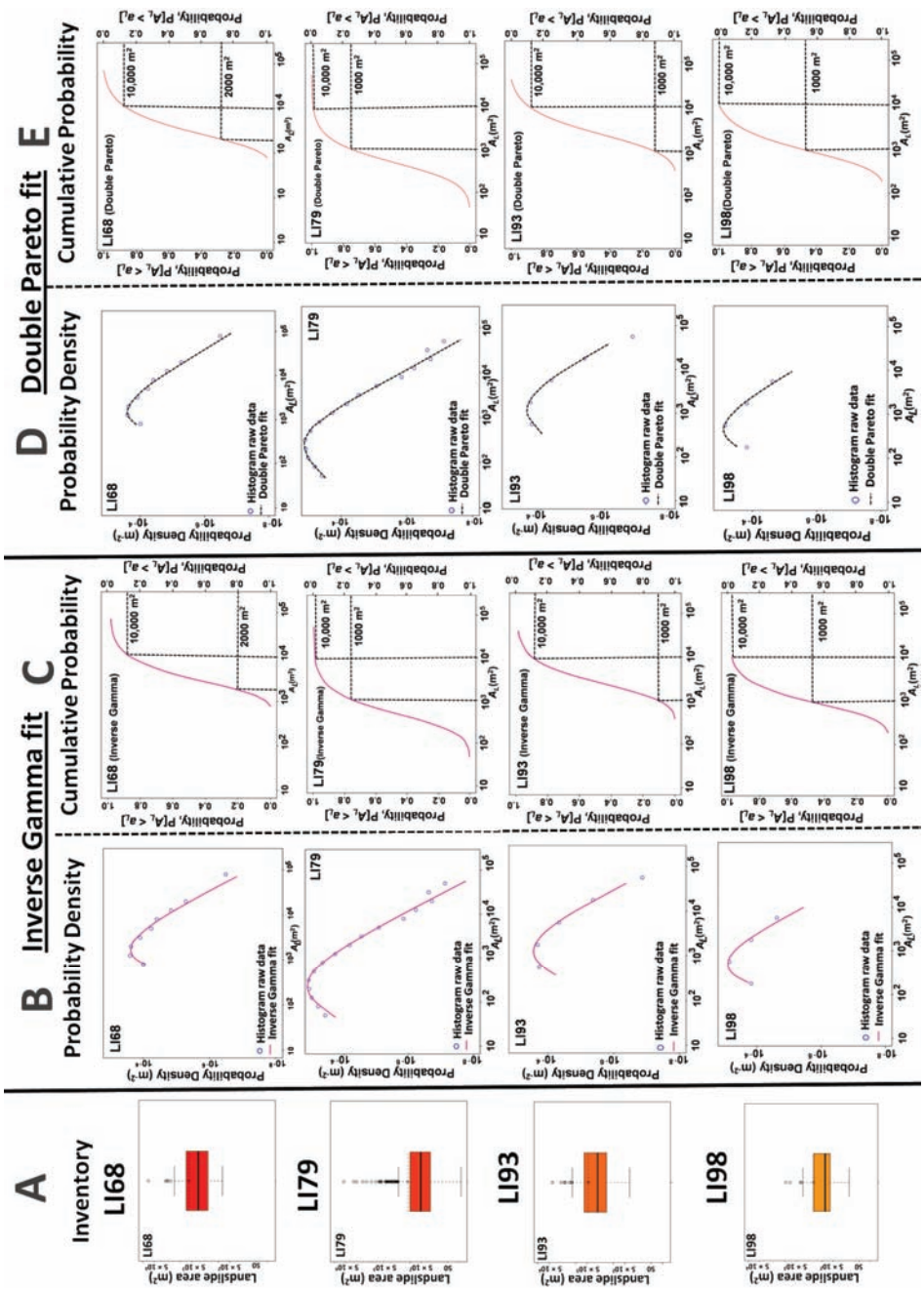

Fig. 3.8 Probability density function (pdfs) of landslide area (m2) for historic landslides of 1968-1998. (A) Box plots showing distributions of landslide area (m^2). (B) pdfs fitted with Inverse-Gamma distribution function of Malamud et al. (2004). (C) Probability estimates as per the fitted Inverse-Gamma distribution functions, (D) pdfs fitted with the Double Pareto distribution function of Stark and Hovius (2001). (E) Probability estimates as per the fitted Double Pareto distribution functions.

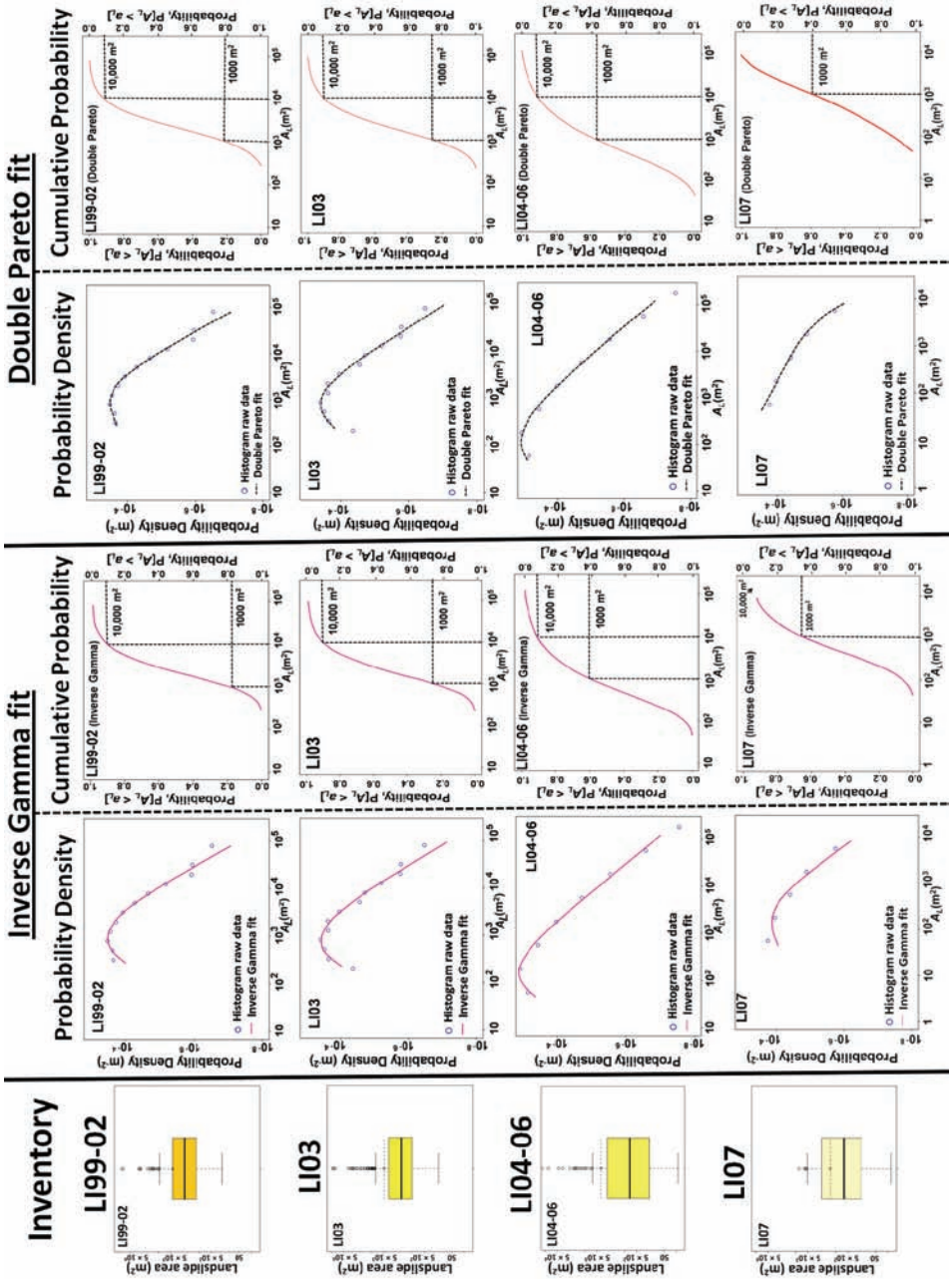

Fig. 3.9 Probability density function (pdfs) of landslide area (m2) for historic landslides of 1999-2007 and for all inventories together. (A) Box plots showing distributions of landslide area (m2). (B) pdfs fitted with Inverse-Gamma distribution function of Malamud et al. (2004). (C) Probability estimates as per the fitted Inverse-Gamma distribution functions, (D) pdfs fitted with the Double Pareto distribution function of Stark and Hovius (2001). (E) Probability estimates as per the fitted Double Pareto distribution functions.

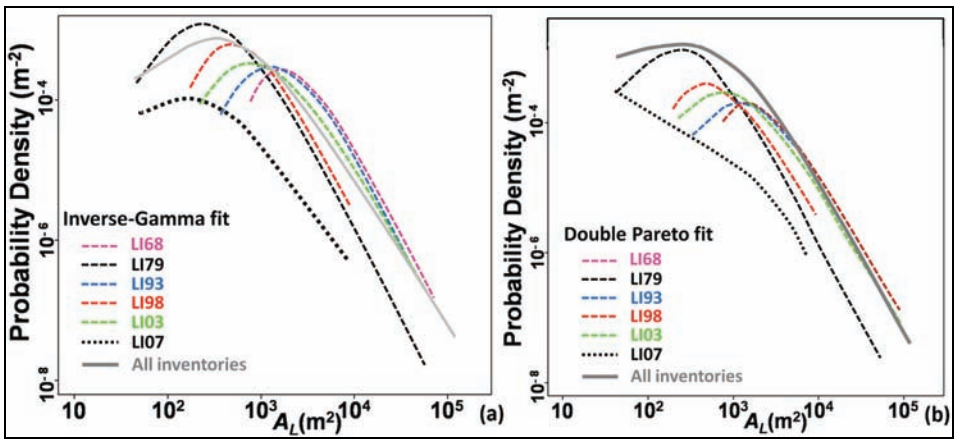

Fig. 3.10 Comparison of the pdfs of individual historic landslides that occurred in the period between 1968 and 2007: (a) using Inverse-Gamma fit and (b) using Double Pareto fit.

Table 3.6 Results of size-frequency analysis. The table also demonstrates examples of two magnitude probability estimates, $P[A_L<1000\ m^2]$: probability that a future landslide will have an area smaller than 1000 m^2 and $P[A_L>10{,}000\ m^2]$: probability that a future landslide will have area larger than 10,000 m^2 (Figs. 3.8 and 3.9); IG = Inverse-Gamma and DP = Double Pareto; ρ = power-law exponent or slope of the power-law tail (IG) and α = power-law exponent or slope of the power-law tail (DP); rollover (m^2) = area at which pdf changes direction for smaller landslides.

Inventory		LI68	LI79	LI93	LI98	LI99-02	LI03	LI04-06	LI07	All
Classification of event		Major	Mod.	Minor	Major	N.A.	Mod.	N.A.	Mod.	-
Min. area (m^2) – c (DP)		776	45	372	185	271	221	45	42	42
Max. area (m^2) – m (DP)		70253	55815	40906	9573	79157	92155	119285	8265	119285
Number		83	562	108	31	185	242	164	85	1460
I G	ρ	1.66	1.64	1.72	1.75	1.53	1.35	0.68	0.51	1.09
	Rollover (m^2)	1682	232	1269	496	918	770	143	-	300
	$P[A_L<1000\ m^2]$	0.02	0.75	0.12	0.48	0.18	0.28	0.61	0.68	0.50
	$P[A_L>10{,}000\ m^2]$	0.15	0.01	0.15	0.02	0.09	0.10	0.09	-	0.08
D P	α	1.27	1.49	1.34	1.28	1.47	1.22	0.69	1.97	1.17
	Rollover (m^2)	1500	241	1188	459	832	726	108	-	218
	$P[A_L<1000\ m^2]$	0.05	0.75	0.15	0.45	0.21	0.27	0.58	0.60	0.48
	$P[A_L>10{,}000\ m^2]$	0.12	0.01	0.15	0.0	0.1	0.10	0.1	-	0.08

The above magnitude-frequency estimates can be used to make an assessment of landslide size probabilities for the available landslide events. For major landslide events, such as LI68, the magnitude-frequency analysis indicates that the probability of landslides with sizes >10,000 m^2 is as high as 0.15. The rollover point of this curve is also the highest of all inventories (1682 m^2). However, values with a similar order of magnitude are obtained for LI93, which according to the classification in Fig. 3.6 was rated to be a minor triggering event. Despite the differences in the source data sets in terms of aerial and temporal coverages and resolutions (Table 3.7), the

frequency-size analysis using the eight inventories combined into a single inventory can depict a generalised magnitude-frequency distribution (Fig. 3.10) of landslides that occurred in the study area between 1968 and 2007. The results shown in Table 3.6 for the combined inventory (ρ or α ranging from 1.09 to 1.17 and rollover point from 218 to 300 m^2) are on the lower range of those reported by Malamud et al. (2004) and Stark and Hovius (2001). Therefore, given the problems involved in generation of the individual inventories, it is better to use the size probability values derived from the above combined inventory. Based on the Inverse-Gamma fit of the combined inventory, the probabilities of landslides areas of <1000 m^2 and >10,000 m^2 are 0.50 and 0.08 respectively, which, based on Double Pareto fit also gives similar probability values (0.48 and 0.08 respectively).

Table 3.7 Summary of problems associated with individual landslide inventories. (N.A. = Not applicable)

Inventory	Type of event	Triggering event	Explanation
LI68	Major	Single event	Data source is a topographic map, which is updated just after the 1968 landslide event. Many small landslides are not mapped.
LI79	Moderate	Combination of several triggering event	Amalgamation of several landslide events in the period between 1968 and 1979. Only source data consisting of detailed aerial photographs (1:10000), therefore many more smaller landslides could be mapped, as compared to the other inventories
LI93	Minor	Single event	The source data is a field map made after a triggering event, but it doesn't cover the entire study area.
LI98	Major	Single event	The source data is a field map made after a triggering event, but it doesn't cover the entire study area.
LI99-02	N.A.	Combination of several events	Amalgamation of several landslide events in the period between 1999 and 2002. Interpreted from satellite images.
LI03	Moderate	Single event	Interpreted from satellite images; Could represent a near-complete landslide inventory since its source data is bounded by other high-resolution satellite imagery at close intervals.
LI04-06	N.A.	Combination of several events	Amalgamation of several minor landslide events in the period between 2004 and 2006. Interpreted from satellite images.
LI07	Moderate	Single event	Field-based maps; no high-resolution remote sensing data available after the event.

3.6 Discussion

3.6.1 Incompleteness and data gaps in source data

For quantitative landslide hazard analysis, a quantitative estimation should be made for the spatial, temporal and magnitude probability of future landslide events. The reliability of such estimations depends on the completeness of event-based landslide inventories, which are only as good as the source data from which historical landslide information was extracted.

The results presented in this chapter about the analyses of temporal and magnitude probability indicates that several of the landslide inventories that were used, are not complete. Therefore, generating event-based landslide inventory maps is not a trivial task in areas where source data are of various resolutions and are constrained by irregular temporal gaps. When there is a large time gap between two data sources (e.g., LI68 and LI79), landslides triggered by several events are all mapped together. Therefore, the resulting landslide inventory contains too many landslides in relation to the last triggering event. This was the case for 1979-inventory (LI79), which, according to Fig. 3.6, actually contains the landslides caused by six moderate landslide events that perhaps occurred between 1968 and 1979. Unavailability of source data in the intermediate period thus makes it difficult to prove this phenomenon known as oversampling of landslides (van Westen et al., 2006). The quality of event-based landslide inventories also depends very much on the quality of input data. For instance, landslides caused by the major event of 1968 were mapped from an updated topographic map (1:25,000). However, this inventory was far from complete, and many small landslides were not included due to the relatively coarser resolution of the source map. Therefore, the 1968 landslide inventory (LI68) contains a much smaller number of smaller landslides than would be expected given the importance of the triggering event (Fig. 3.6) and damage history indicated in the literature (Mathur, 1982; Starkel and Basu, 2000). In contrast, the landslide inventory of 1979 (LI79), was made using large scale (1:10,000) aerial photographs, from which many smaller landslides could be mapped. Another common inconsistency observed was about the coverage of mapped area for field-based source data. Those maps rarely cover the entire portion of a large catchment area (Table 3.1) but they are mostly concentrated in areas accessible from a road and/or in areas where there are confirmed reports of damage to life and property (e.g., LI93, LI98). All the above constraints undermine the completeness of landslide inventory maps and, thereby, affect the correct estimation of the temporal and magnitude probability of future landslides.

3.6.2 Limitations in temporal probability estimation

Because the derived landslide inventory maps suffer from problems related to the quality and resolution of source data from which they were mapped, inconsistent landslide density estimates were often observed for different inventory maps. The higher landslide densities of LI79 (6.2) and LI03 (2.7) are thus, attributed to the ease in identification of smaller landslides (e.g., LI79, LI03, LI04-06) in high-resolution source data, so that smaller landslides with areas as small as 45 m^2 (LI79 and LI04-06) could even be mapped. In contrast, the LI68, which was derived from 1:25,000 scale topographic maps,

only contains landslides with areas larger than 776 m^2. Smaller landslides do not appear in the source data and, therefore, LI68 represents a landslide density (0.9) that is far too low with respect to the magnitude of the triggering event.

The above inconsistencies in landslide densities among the landslide inventories caused problems in the direct utilization of landslide density values for the estimation of temporal probability of landslides as proposed by Guzzetti et al. (2005) and other workers. Therefore, an indirect method was adapted for the estimation of temporal probability (cf. Dai and Lee, 2001) assuming rainfall as the only landslide trigger. Due to the paucity of any confirmed reports on earthquake-triggered landslides in the study area in the period of 1968-2007, analysis considering earthquakes as a triggering factor is not feasible. Although, it can be presumed that some of the very large un-dated old/inactive landslides of pre-1968 that have been mapped from 1:10,000 scale stereo air-photos (Figs. 3.3 and 3.4) could be earthquake-triggered. However, the importance of rainfall as a trigger is confirmed by Basu and De (2003) in the study area and in the adjacent Nepal Himalayas by Dahal and Hasegawa (2008) and Gabet et al. (2004). Thus, different rainfall amounts (daily rainfall and six antecedent rainfall amounts) were considered as predictors in modelling landslide event days using discriminant analysis. If there are landslide inventories with consistent landslide densities, it would have been better to apply a multinomial logistic regression using ranges of landslide density estimates as multiple response variables to estimate temporal probability of events linked to different levels of severity or magnitude. To overcome this problem, the discriminant score (*DS*) values derived from DA of the known landslide events were used in defining thresholds, assuming that some positive relation exists between *DS* values and severity of events (cf. Altman, 1968; Rasmussen et al., 1985). This allowed classification of three different magnitude classes of landslide events (major, moderate and minor) based on decreasing levels of cumulative *DS* values. Nevertheless, the over-prediction (232+58, see Table 3.5) of the landslide event-days by the DA models cannot be avoided since the source data of landslide inventory maps has significant data gaps (Fig. 3.1) between 1969 and 1978, 1979 and 1993 and 1993 and 1998 respectively and thus, any such over-prediction of model results is difficult to be proven/substantiated by the available landslide event database.

The recurrence intervals in 40 years (1968-2007) for each of the classified events can be used therefore, for the calculation of temporal probability of future similar landslide events using the Poisson's distribution model (Crovelli, 2000; Coe et al., 2004). The Poisson's distribution model indicates

a higher range of temporal probability values (Fig. 3.7) for each of the classified events (minor, moderate and major) which is quite significant for the study area and to some extent is corroborated by the reported and confirmed frequency of similar such landsliding events in the study area between 1968 and 2007. Although, it can also be argued that the period of analysis (i.e., 40-years) used in this study may not be sufficient enough to obtain for an optimal recurrence pattern of landslide events.

According to the proposed classification using *DS* values, the LI68 belongs to a "major" landslide event having a cumulative *DS* value of 21.89 (Fig. 3.6), which is supported by additional information about this event from literature (Starkel and Basu, 2000). However, the landslide density of LI68 is not the highest among eight inventories because of the earlier mentioned problems with the source data. In contrary, the inventory LI79 was classified as a "moderate" landslide event based on the rainfall analysis, but it shows the highest landslide density (6.2), perhaps due to mixing of landslides due to preceding events (Fig. 3.6). Compared to all the derived landslide inventories, the predicted "moderate" event, LI03 with a landslide density of 2.7, represents a more or less realistic situation since it was made from high-resolution source data (5.8 m multi-spectral satellite image, LISS-4), and is immediately preceded and followed by substantially complete landslide inventories, which were mapped from similar high-resolution source data. In terms of landslide damage, the 2003 landslide event (LI03) was considered to be one of the major damaging landslide events in the study area. Due to this event, in adjacent Mirik areas (immediately west of the study area), 25 people were killed and damages to roads and agricultural lands were profuse (Paul and Sarkar, 2003). Therefore, inadequacy in landslide inventory source data pose unavoidable inconsistencies and uncertainty in estimation of landslide hazard, which can further be examined and corroborated by the results of magnitude-frequency analysis (Figs. 3.8 to 3.10) that is required for magnitude predictions.

3.6.3 Limitations in magnitude probability estimation

Both the fitted Inverse-Gamma (Malamud et al., 2004) and Double Pareto (Stark and Hovius, 2001) probability density functions of all the inventories show power-law area-frequency distributions for medium to large landslides and a distinct exponential rollover for smaller landslides (excepting the Double Pareto fitted pdf of LI07). These indicate that the general nature of distribution of landslide area (m^2) is quite similar among all the landslide events in the study area. Due to the widely variable minimum landslide areas caused by the different qualities of the source data (42 m^2 in LI07 to 776 m^2 in LI68), rollover estimates vary between 45 m^2 for the Double Pareto fit of

LI98 and 1682 m^2 for the Inverse-Gamma fit for LI68 (Table 3.6). The widely variable rollover estimates observed in different event-based landslide inventories (Figs. 3.8 to 3.10) indicate that these could be used together with the steepness of slope in the power-law curve for medium to large landslide size (ρ or α) as an indication to separate distributions resulting from major, moderate and minor triggering events. It can be inferred further that the rollover phenomena is not always an artifact of censoring, whereby small landslides are simply not mapped (Guthrie and Evans, 2004) because the rollover was observed in almost all the inventories but at different rollover estimates. Nevertheless, it can be argued that the variable rollover changes observed in the present analysis could be due to the use of landslide inventory source data of variable resolutions, which, in turn, supports the connotations of Stark and Hovius (2001) that rollover changes can be attributed to survey resolution (Brardinoni and Church, 2004).

The results of size (area in m^2)-frequency analysis (Table 3.6) of the individual landslide inventory maps indicate wide variability of data as evidenced from variation in cumulative and non-cumulative power-law exponent or slope (α). For example, according to the Inverse-Gamma fit, the cumulative area-frequency power-law exponent (ρ) varies from 0.51 (LI07) to 1.75 (LI98) and the non-cumulative power-law exponent of the same (ρ +1) varies from 1.51 to 2.75. The lower limit of the above exponent matches with cumulative power-law exponent of 0.75 ± 0.30 as observed in the frequency-volume statistics of 1937 rock falls and rockslides in British Columbia (Hungr et al., 1999). Similarly, the upper limit of cumulative power-law exponent (ρ or α = 1.75) is quite comparable with the error estimate of 1.88 ± 0.30 as observed by Stark and Hovius (2001). According to Guzzetti et al. (2002), such variations in cumulative/non-cumulative power-law exponents (ρ or α) can be attributed to occurrence of landslides in different physiographic settings (lithology, geomorphology and geology). However, causes of such variations in a small study area (ca. 90 m^2), in the present research, could be different, such as subtle changes in the intensities of climatic triggers, which justifies the assumptions to link the results of magnitude-frequency analysis with the different types of predicted landslide events that are linked to variation in rainfall parameters acting as triggers.

Nevertheless, compared to all the inventories, the magnitude-frequency distributions of LI07 can be termed a distinct outlier (ρ = 0.51) (Table 3.6). The reason for this is difficult to explain because LI07 is the most-recent inventory prepared through field investigation immediately (within two months) after the event and contains most of the landslides trigged by that

particular event. Some inconsistencies and incompleteness in the fitting of magnitude-frequency distributions are also noticed for LI93 and LI98, both of which are old field-based landslide occurrence maps (Figs. 3.8 to 3.10). This could be due to comparison of pdfs of landslide inventories prepared using two different techniques of mapping and two distinct groups of source data – one through field-based mapping and another through employment of different remote sensing techniques using high resolution satellite imagery and air photos. Depending on spatial and spectral resolutions, the landslide inventory maps derived from the latter source data depict accurate spatial dimension of landslides, which facilitates correct estimation of landslide area. In contrast, the field-based landslide maps contain large number of smaller landslides having very high locational accuracy. However, due to scale constrains, spatial dimensions of these smaller landslides are in most cases exaggerated. Moreover, field-based inventory maps might lack landslide information in highly inaccessible areas. This invokes inaccuracies in estimation of landslide areas, which can be avoided if landslide polygon boundaries, identified through field investigations, are surveyed on large scale and later represented by down-scaling onto base maps, although, the same is generally a cost-prohibitive exercise on any medium to small scale (1;25,000 and smaller) landslide hazard analysis. Examples of the above inconsistencies in magnitude-frequency data in the literature are rather rare. Therefore, more studies comparing such types of inventories, being products of different mapping techniques and source data, are required to unravel this anomaly.

The landslides that occurred before 1968, for which no dates of occurrence are available, were not incorporated in the analysis of the temporal or magnitude frequency. These old landslides are generally large and cover a substantial part of the study area (Table 3.2 and Figs. 3.3 and 3.4). Because information about types and dates of triggering events associated with them is not available, quantitative estimation of the temporal and magnitude probability for these extreme events are not possible. As indicated earlier, it is expected that earthquakes could be important for triggering such very large landslide complexes in the area. Although, proximity of several active landslides (1968-2007) to these old, un-dated large rockslides (Fig. 3.4) warrants selection of the latter as a multivariate factor of susceptibility to different landsliding types (chapter 6).

3.7 Conclusions

The study presented in this chapter emphasizes the importance of generating event-based landslide inventory maps, directly after the occurrence of landslide triggering events. The use of ancillary data sources, with different quality, resolution and aerial coverage, creates problems in generating reliable and complete event-based landslide inventory maps. However, the estimation of temporal probability of triggering events in such a data-scarce environment can be attempted by identification of unknown events through statistical analysis using triggering rainfall variables as predictors and known landslide events as response variables. Using the recurrence interval of such unknown predicted events, temporal probability of similar events can be quantified. To estimate the probability of landslide magnitude, size-frequency analysis considering historic landslides is a valuable tool. However, inadequate information on past landslides makes it difficult for correct estimation. Both temporal and magnitude probability measures, when combined together with the estimates of spatial probability, can give a reasonable quantitative estimate of landslide hazard that is required to estimate further the landslide risk (see chapter 7).

Therefore, with the knowledge and inventories of historical landslides developed so far in the present study, subsequent studies on application of different empirical techniques of medium scale landslide susceptibility mapping were conducted, which are described in the succeeding chapters. The next chapter (chapter 4) deals with various techniques of exploratory spatial analyses to understand the mutual and/or exclusive control of regional faults/fractures and topography on various types of rockslides. This particular study is important to understand the role of regional structures and its relations with topography with respect to the rocksliding types that are predominant in the study area, which is located within an active fold-thrust belt in the Himalayas.

Chapter 4: Exploratory analysis of fault/ fracture and slope controls on rockslides

In a tectonically-active fold-thrust belt, regional faults/fractures have plausible genetic controls on rockslides but the extent of such controls on rocksliding of certain types could be spatially variable because the distribution of stress varies around the prominent regional tectonic structures and their subsidiary faults/fractures. Moreover, these linear features are actually planar structures in 3-D space and thus, their mutual geometric relations with topography likely influence rocksliding. This chapter is based on the ISI publication *"Spatial analysis of mutual fault/fracture and slope controls on rocksliding in Darjeeling Himalaya, India" (Ghosh and Carranza, 2010)* wherein mutual and/or exclusive controls of regional faults/fractures and topography on both shallow and deep-seated rocksliding are examined using various spatial analytical techniques.

4.1 Introduction

Several works on predictive mapping of landslide susceptibility consider proximity to linear geological structures as a spatial factor without regarding the types and orientations of such structures (e.g., Saha et al., 2002; Champati ray et al., 2007; Sharma and Kumar, 2008; Mathew et al., 2009). Implicit in this practice is the notion that every linear geological structure has equal weight of influence on the likelihood of landslide occurrence. However, a factor that is more important than proximity to linear geological structures is the geometric (and, thus, mutual) relationship between orientations of certain linear geological structures and orientations of certain slopes (Goodman and Bray, 1976; Hoek and Bray, 1981; Romana, 1985; Wagner et al., 1988). Thus, it can be hypothesized that using proximity to structures of certain types and trends, compared to using proximity to structures of different types and trends, is likely to yield better predictive maps of landslide susceptibility. Selection of sets of structures that are likely controls on landslides requires in-depth field studies, which apply more to predictive mapping of landslide susceptibility at site-specific scales (i.e., larger than 1:10,000) rather than at regional or medium scales (i.e., 1:25,000 or smaller). However, for regional- to medium-scale predictive mapping of landslide susceptibility, it can be hypothesized that analyses of the spatial pattern of landslides of certain types and their spatial association with certain types and trends of structures allow the selection of sets of structures that are likely controls on landslide occurrence.

In regional- to medium-scale predictive mapping of landslide susceptibility, landslides of certain types are usually depicted as point objects (Dai and Lee, 2002; Holm et al., 2004; Komac, 2006; Neuhäuser and Terhorst, 2007; Poli and Sterlacchini, 2007). For this study, landslide polygon centroids are used as landslide point objects. The spatial pattern (in terms of trends) of point objects can be studied via Fry analysis, which was developed originally for examining strain orientations in rocks (Fry, 1979). Fry analysis has not been applied to infer structural controls on landslides. The spatial association of point objects with linear features (e.g., faults/fractures) can be studied via distance distribution analysis, which is a bivariate empirical method for testing spatial dependency of a point process on another stochastic process (Berman, 1986). Distance distribution analysis has also not been applied to infer structural controls on landslides. Other bivariate empirical methods suitable for studying spatial associations between landslides (depicted as point objects) and linear features include density or proportion analysis (Süzen and Doyuran, 2004); frequency ratio (Lee and Dan, 2005), likelihood ratio (Chung, 2006) and weights-of-evidence (Neuhäuser and Terhorst, 2007). However, each of these latter bivariate techniques, unlike distance distribution analysis, has not been formalized originally for testing spatial dependency of a point process on another stochastic process.

In this study, Fry analysis and distance distribution analysis were applied to determine sets of faults/fractures, according to trends, that are likely involved in mutual fault/fracture and slope controls on rockslides. In addition, for representation and integration of spatial evidence layers of mutual fault/fracture and slope controls on rockslides, the data-driven evidential belief functions were applied, which have been developed for predictive mapping of mineral potential (Carranza, 2002; Carranza and Hale, 2003) and have been applied in predictive mapping of susceptibility to distal lahar-inundation (Carranza and Castro, 2006). These spatial analytical techniques were applied in the study area (Fig. 1.1) of Darjeeling Himalaya (India) to test the two hypotheses stated above in deriving a spatial model of mutual fault/fracture and slope controls on rockslide occurrence.

4.2 Structures in Himalayan FTB and rock slope failures

The Main Central Thrust (MCT) and Main Boundary Thrust (MBT) are major regional tectonic structures in the Himalayan fold-thrust belt (Figs. 1.1b and 1.1d). These ENE- to NE-trending thrusts and their associated fault/fracture systems are seismogenic (Dasgupta et al., 1987; Nandy and Dasgupta, 1991). Banerji et al. (1980) suggest that the study area and its surroundings

have been undergoing differential uplift along regional faults and local sub-vertical faults/fractures. Through air-photo interpretation and fieldwork in the area, several steeply-dipping faults/fractures (Fig. 4.1) have been mapped in this research. These fractures are not joints, but their dips and kinematics could be ascertained only at limited sites that have been visited during this research. Faults/fractures trending westerly-northwesterly and northeasterly are prevalent in the areas west of the MCT, whereas faults/fractures trending northeasterly are prevalent in the area east of the MCT (Fig. 4.2). Faults/fractures trending westerly-northwesterly are slightly more prevalent than northeasterly trending faults/fractures in the area <4 km west of the MCT, whereas northeasterly trending faults/fractures are slightly more prevalent than westerly-northwesterly trending faults/fractures in the area ≥4 km west of the MCT (Fig. 4.2). Northerly-northeasterly trending faults/fractures are more prevalent in the area <2.5 km east of the MCT than in the area ≥2.5 km east of the MCT (Fig. 4.2). Variations in trends of these faults/fractures in various parts of the area are likely due to variations in local stress fields with respect to the MCT and MBT (Pandey et al., 1999; Singh and Thakur, 2001; Joshi and Hayashi, 2008).

The likelihood of rock slope failures in the area is thus very high because of the fragile structural-topographical conditions of the active Himalayan FTB, and high precipitation (Shroder and Bishop, 1998). From the spatio-temporal inventory of landslides in the study area (Fig. 3.4), which were classified according to the classification of Varnes (1978), only the shallow translational rockslides (Sh_rs) and deep-seated rockslides (Dp_rs) were used. Compared to Sh_rs occurrences, Dp_rs occurrences are few and are mostly in the area west of the MCT (Fig. 4.1).

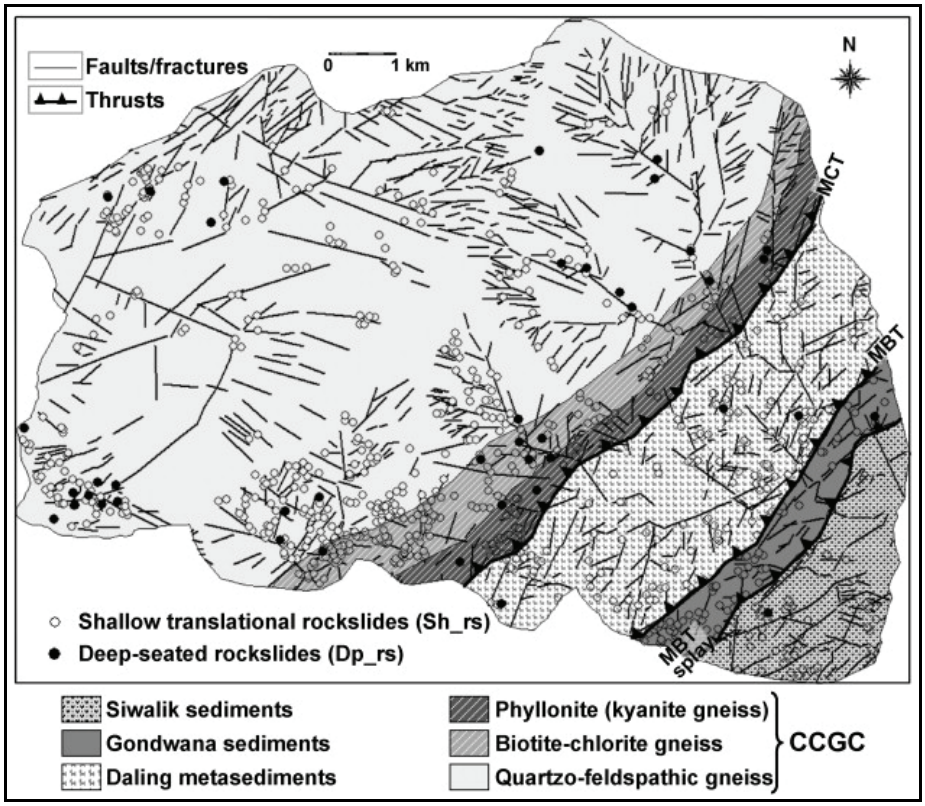

Fig. 4.1 Simplified geological map of the study area, mapped fault/fractures and locations of mapped rockslides (1968–2007). MCT = Main Central Thrust. MBT = Main Boundary Thrust. CCGC = Central Crystalline Gneissic Complex.

4.3 Spatial patterns of rockslides

4.3.1 Fry analysis of point geo-objects

Fry analysis (Fry, 1979) is a graphical method of spatial autocorrelation analysis of point objects (e.g., rockslides at a regional- to medium-scale). The method translates data points into so-called Fry plots. To understand the fry plot translations, let us consider a map of data points which is marked with parallel (N-S, E-W) reference lines. On a second but empty map, an origin is specified at the intersection of an N-S reference line and an E-W reference line. The origin in the second map is set on top of one data point in the first map, the reference lines in both maps are kept parallel, and positions of every data point are recorded in the second map. The origin in the second map is then set on top of a different data point in the first map, the reference lines in both maps are kept parallel, and positions of every data point are recorded again in the second map. The procedure is repeated until

every data point has been used as origin in the second map. For a number, n, data points, there are n^2-n number of translations called 'Fry points'.

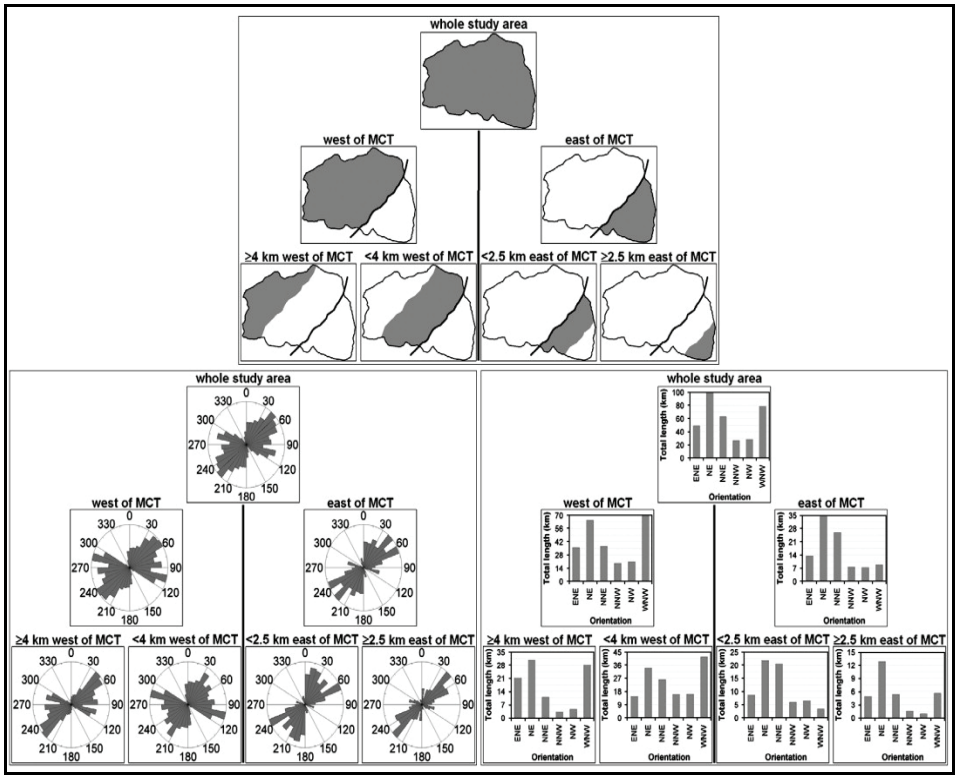

Fig. 4.2 The study area and sub-areas with respect to distance from the MCT (Main Central Thrust; Fig. 4.1) and corresponding trends and total lengths of faults/fractures.

Creation of Fry plots is not a routine function of any GIS software package. Although Fry plots can be created manually as described above, the procedure can be cumbersome especially with a large number of data points. There are software packages for creating graphics, including Fry plots and rose diagrams, to support geological analysis. The freeware DotProc package (http://www.kuskov.com) was used for this purpose. Coordinates of landslides stored in a GIS can be exported to DotProc. A DotProc output of Fry point coordinates can be imported back into a GIS in order to visualize the spatial pattern of Fry points and data points together.

Fry analysis not only reveals major trends but also enhances subtle trends in a set of points. It also allows recording of distances and trends between every pair of Fry points, which can be used to visualize trends in a point set. A rose diagram can be created to visualize trends between (a) all pairs of Fry points and (b) pairs of Fry points at certain distances from each other. The

former analysis may reveal major trends that are due either to regional geological processes or to the shape of an area, whereas the latter analysis may reveal subtle trends that are likely due to local geological processes. In order to infer structural controls on rockslide, it is instructive (a) to visualize trends of pairs of Fry points at certain distances from each other or (b) to use 2nd-order nearest neighbour Fry points as illustrated in Fig. 4.3. Compared to using 2nd-order nearest neighbour Fry points, using 1st-order nearest neighbour Fry points may not reveal trends reflecting local geological processes whereas using 3rd- or higher-order nearest neighbour Fry points tend to reveal trends reflecting either regional geological processes or the shape of the study area. The nth-order nearest neighbour (Fry) points can be determined via point pattern analysis (Boots and Getis, 1988).

4.3.2 Application of Fry analysis for rockslide occurrences

The Fry analysis was applied to each set of Dp_rs and Sh_rs occurrences in the whole study area. In addition, the Fry analysis of subsets of Dp_rs and Sh_rs was applied in (a) the areas west and east of the MCT, (b) sub-areas defined by certain distances toward west and east from the MCT and (c) areas defined by similar slope aspects. The rationale of Fry analysis of rockslides in (sub-)areas west and east of the MCT is based on the knowledge that (a) the MCT is a regional-scale tectonic control on structural and geomorphological developments in the area (Banerji et al., 1980; Acharya, 1989), (b) local stress fields vary with respect to major tectonic structures (Pandey et al., 1999; Singh and Thakur, 2001; Joshi and Hayashi, 2008) and (c) mechanisms for slope deformation vary with variations in distribution of stress (Di Luzio et al., 2004; Kinakin and Stead, 2005; Cadoppi et al., 2007). In the area east of the MCT, a separate analysis with respect to the MBT is unnecessary. That is because (a) the long axis of the Gondwana sediments, which is bounded by the MBT and its splay, is roughly located 2.5 km east of the MCT (Fig. 4.1) and (b) analysis in sub-areas east of the MCT allows interpretations with respect to the MBT.

The rationale of Fry analysis of rockslides in certain slope aspects can be explained with the aid of the hypothetical example shown in Fig. 4.3, in which slope aspect is generally toward NE and locations of landslides assume a northwesterly trend. If the hypothetical landslides are both structurally- and aspect-controlled, then it implies that controlling structures have northwesterly trends and northeasterly dip directions. Thus, if rockslides on slopes with similar aspects assume trends that make angles >45° with the slope aspects, then it can be deduced that those rockslides are both structurally- and aspect-controlled (e.g., Jaboyedoff et al., 2009).

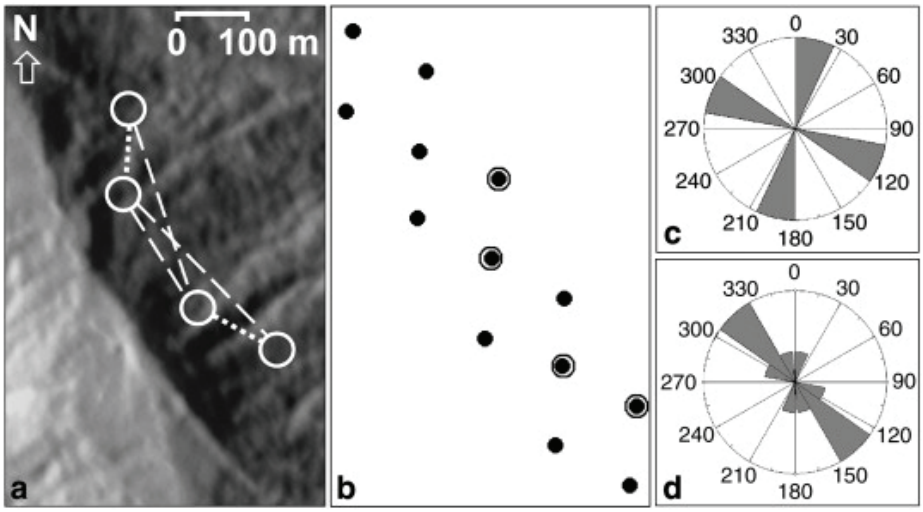

Fig. 4.3 Fry analysis of a hypothetical set of points. a) Hypothetical locations (open circles) of rockslides, showing 1st-order nearest neighbours connected by dotted lines and 2nd- order nearest neighbours connected by dashed lines. b) Fry points (black dots) of rockslide locations. c) Rose diagram of orientations of pairs of 1st-order nearest neighbour Fry points. d) Rose diagram of orientations of pairs of 2nd-order nearest neighbour Fry points. The rose diagram in d) depicts better the major orientation among the original points.

For the purpose of spatial analysis, topographic slopes were classified into 12 30°-interval classes of aspects (see Fig. 1.2c) and then Fry plots for each subset of rockslides per slope aspect class were created. For Fry analysis and spatial association analysis of fault/fracture controls, the faults/fractures were grouped into six 30°-interval classes of trends. Nevertheless, for space constraints, all the subsequent analyses pertaining to only Sh_rs are described in the following sections. For Dp_rs analyses, Annexure II in the enclosed CD can be consulted.

4.3.3 Spatial trends of shallow rockslides (Sh_rs)

The major WNW trend of all pairs of Sh_rs Fry points in the whole study area (Fig. 4.4a) is likely due to the WNW-elongation of the study area. All pairs of Sh_rs Fry points in the area west of the MCT show major trends varying between NE and ENE (Fig. 4.4b), which are partly due to either the main ENE trends of Himalayan thrusts or to the NE-elongation of the area west of the MCT. Major NE to NNE trends of all pairs of Sh_rs Fry points in the area east of the MCT (Fig. 4.4c) are likely artifacts of the NNE-elongation of that area. However, the mainly isotropic trends in pairs of 2nd-order nearest neighbor Sh_rs Fry points in the whole study area and in the areas west and east of the MCT (Fig. 4.4 insets) show subtle primary and secondary trends, suggesting controls on Sh_rs by certain linear geological structures.

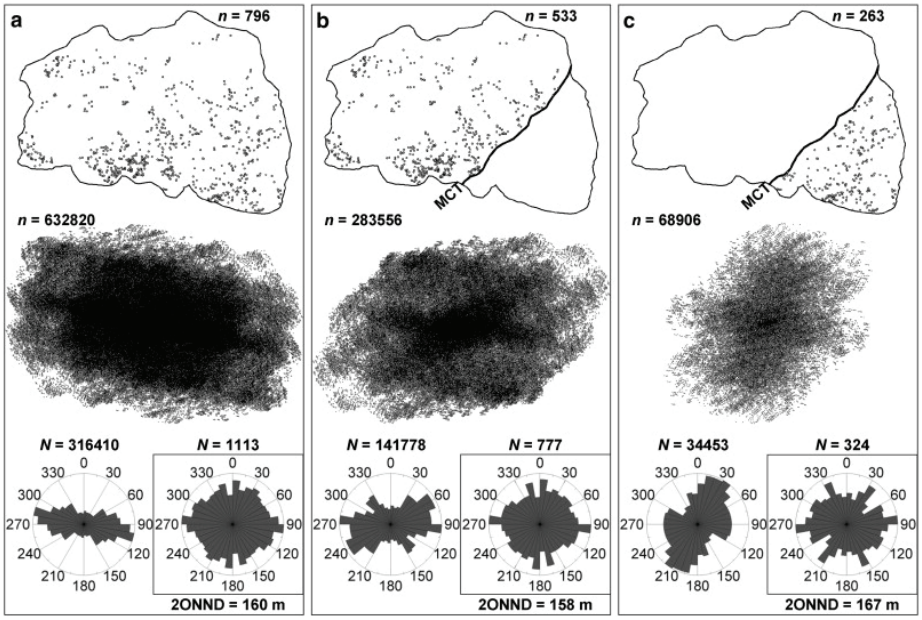

Fig. 4.4 Fry plots of Sh_rs, rose diagrams of relative frequencies of trends of all pairs of Fry points and, in insets, rose diagrams of relative frequencies of trends of pairs of 2nd-order nearest neighbour Sh_rs Fry points in a) the whole study area, b) the area west of the MCT (Main Central Thrust) and c) the area east of the MCT. *n* denotes number of Sh_rs locations or Fry points. N denotes number of pairs of Fry points. 2ONND means the 2nd-order nearest neighbour distance **used** to select Fry points for analysis.

The above-mentioned subtle primary and secondary trends (Fig. 4.4 insets) are quite consistent with trends deduced from the Fry analyses of Sh_rs in certain slope aspects (Table 4.1). Based on the trends of faults/fractures (Fig. 4.2) and the trends derived from Fry analyses (Fig. 4.4, Table 4.1), the following inferences can be made. In the whole study area, mutual controls on Sh_rs are due to (a) WNW-trending faults/fractures and SW-facing slopes, (b) NE-trending faults/fractures and NW- to WNW-facing slopes, and (c) SE- to SSE-facing slopes and ENE-trending structures that may not be faults/fractures. In the area west of the MCT, mutual controls on Sh_rs are due to (a) WNW-trending faults/fractures and SW-facing slopes, (b) NE-trending faults/fractures and either ESE- or WNW-facing slopes, (c) NNE-trending faults/fractures and SE-facing slopes, (d) ENE-trending faults/fractures and NNW-facing slopes, and (e) WSW-facing slopes and NNW-trending structures that may not be faults/fractures. In the area east of the MCT, mutual controls on Sh_rs are due to (a) ENE-trending faults/fractures and either SE- or SSW-facing slopes, (b) NNE-trending structures and mostly SSE-facing slopes, (c) WSW- to WNW-facing slopes

and NNW-trending structures that may not be faults/fractures, and (d) NNE-facing slopes and WNW-trending structures that may not be faults/fractures.

In the area <4 km (i.e., from <1 to <4 km) west of the MCT and in the area ≥4 km (i.e., from ≥7 to ≥4 km) west of the MCT, pairs of 2nd-order nearest neighbour Sh_rs Fry points show major and minor trends (Fig. 4.5) that are consistent with trends deduced from the Fry analyses of Sh_rs in certain slope aspects (Table 4.1). Based on the trends of mapped faults/fractures (Fig. 4.2) and trends derived from the Fry analyses (Fig. 4.5, Table 4.1), the following inferences can be made. In the area <4 km west of the MCT, mutual controls on Sh_rs are due to (a) NNE-trending faults/fractures and mostly SE-facing slopes, (b) NE-trending faults/fractures and ESE-facing slopes, (c) WNW-trending faults/fractures and SW-facing slopes and (d) ENE-tending faults/fractures and NNW-facing slopes. In the area ≥4 km west of the MCT, mutual controls on Sh_rs are due to (a) NNE-trending faults/fractures and SE-facing slopes, (b) NE-trending faults/fractures and SSE-facing slopes, (c) ENE-trending faults/fractures and NNW-facing slopes and (d) SSW- to WSW-facing slopes and NNW- to NW-trending structures that may not be faults/fractures.

In the area <2.5 km (i.e., from <1.0 to <2.5 km) east of the MCT and in the area ≥2.5 km (i.e., from ≥2.5 to ≥4.0 km) east of the MCT, pairs of 2nd-order nearest neighbor Sh_rs Fry points show major and minor trends (lower half of Fig. 4.5) that are mostly consistent with trends deduced from the Fry analyses of Sh_rs in certain slope aspects (Table 4.1). Based on the trends of mapped faults/fractures (Fig. 4.2) and the trends derived from the Fry analyses (lower half of Fig. 4.5, Table 4.1), the following inferences can be made. In the area <2.5 km east of the MCT, mutual controls on Sh_rs are due to (a) NNE-trending faults/fractures and ENE-facing slopes, (b) NE-trending faults/fractures and NW- to NNW-facing slopes, (c) ENE-trending faults/fractures and either SE- or SSW-facing slopes, (d) WNW-trending faults/fractures and either NNE- or SSE-facing slopes, (e) NNW-trending faults/fractures and WNW- to WSW-facing slopes and (f) NE-facing slopes and NW-trending structures that may not be faults/fractures. In the area ≥2.5 km east of the MCT, mutual controls on Sh_rs are due to (a) WNW-trending faults/fractures and either NE- or SW-facing slopes, (b) ENE-trending faults/fractures and SE- to SSE-facing slopes and (c) WSW-facing slopes and NNW-trending structures that may not be faults/fractures.

Table 4.1 Fry analyses of Sh_rs with respect to slope aspect in various parts of the study area. Analyses given are only for slope aspects coinciding with at least four Sh_rs and for average trends of 2nd-order nearest neighbor Fry points that make obtuse angles (i.e., >45°) with average slope aspects. [MCT = Main Central Thrust]

Slope aspect class	No. of *Sh_rs* per aspect class	Average aspect (°) at *Sh_rs*	Average 2nd-order nearest neighbor distance (m) among *Sh_rs*	Average trend (°) in pairs of 2nd-order nearest neighbor Fry points	Angle (°) between average aspect and average trend of 2nd-order nearest neighbor Fry points
In the whole study area:					
NNE	16	015	1629	285 (or WNW)	90
SE	115	136	346	080 (or ENE)	56
SSE	106	166	380	243 (or ENE)	77
SW	95	224	504	285 (or WNW)	61
WNW	49	282	469	235 (or NE)	47
NW	27	313	767	230 (or NE)	83
NNW	26	345	885	265 (or ENE)	80
In the area west of the MCT:					
ESE	63	107	360	055 (or NE)	52
SE	73	136	369	185 (or NNE)	49
SW	68	224	482	280 (or WNW)	61
WSW	43	256	563	345 (or NNW)	89
WNW	37	281	426	235 (or NE)	46
NNW	11	345	1110	265 (or ENE)	80
In the area ≤4 km west of the MCT:					
ESE	63	106	360	055 (or NE)	51
SE	57	135	387	187 (or NNE)	52
SW	48	223	486	285 (or WNW)	62
NW	4	312	1261	025 (or NNE)	73
NNW	4	349	2289	262 (or ENE)	87
In the area ≥4 km west of the MCT:					
SE	16	141	304	197 (or NNE)	56
SSE	18	166	256	235 (or NE)	69
SSW	19	198	798	142 (or NW)	56
SW	20	227	487	305 (or NW)	78
WSW	24	258	636	345 (or NNW)	82
NNW	7	344	1008	265 (or ENE)	79
In the area east of the MCT:					
NNE	10	028	1091	105 (or WNW)	77
ENE	27	074	598	005 (or NNE)	69
SE	43	137	381	085 (or ENE)	52
SSE	33	166	341	215 (or NE)	49
SSW	19	191	631	265 (or ENE)	74
WSW	11	257	1345	345 (or NNW)	88
WNW	12	282	603	352 (or NNW)	70
NW	14	315	920	235 (or NE)	80
In the area ≤2.5 km east of the MCT:					
NNE	8	013	1124	102 (or WNW)	89
NE	18	045	451	122 (or NW)	77
ENE	15	072	735	055 (or NNE)	67
SE	27	137	428	075 (or ENE)	62
SSE	21	167	475	117 (or WNW)	50
SSW	16	189	842	265 (or ENE)	76
WSW	7	259	1601	172 (or NNW)	87
WNW	9	280	715	345 (or NNW)	65
NW	12	316	785	235 (or NE)	81
NNW	11	340	871	045 (or NE)	65
In the area ≥2.5 km east of the MCT:					
NE	5	047	616	115 (or WNW)	68
SE	16	135	327	070 (or ENE)	65
SSE	9	162	390	075 (or ENE)	87
SW	7	224	600	285 (or WNW)	61
WSW	4	253	897	337 (or NNW)	84

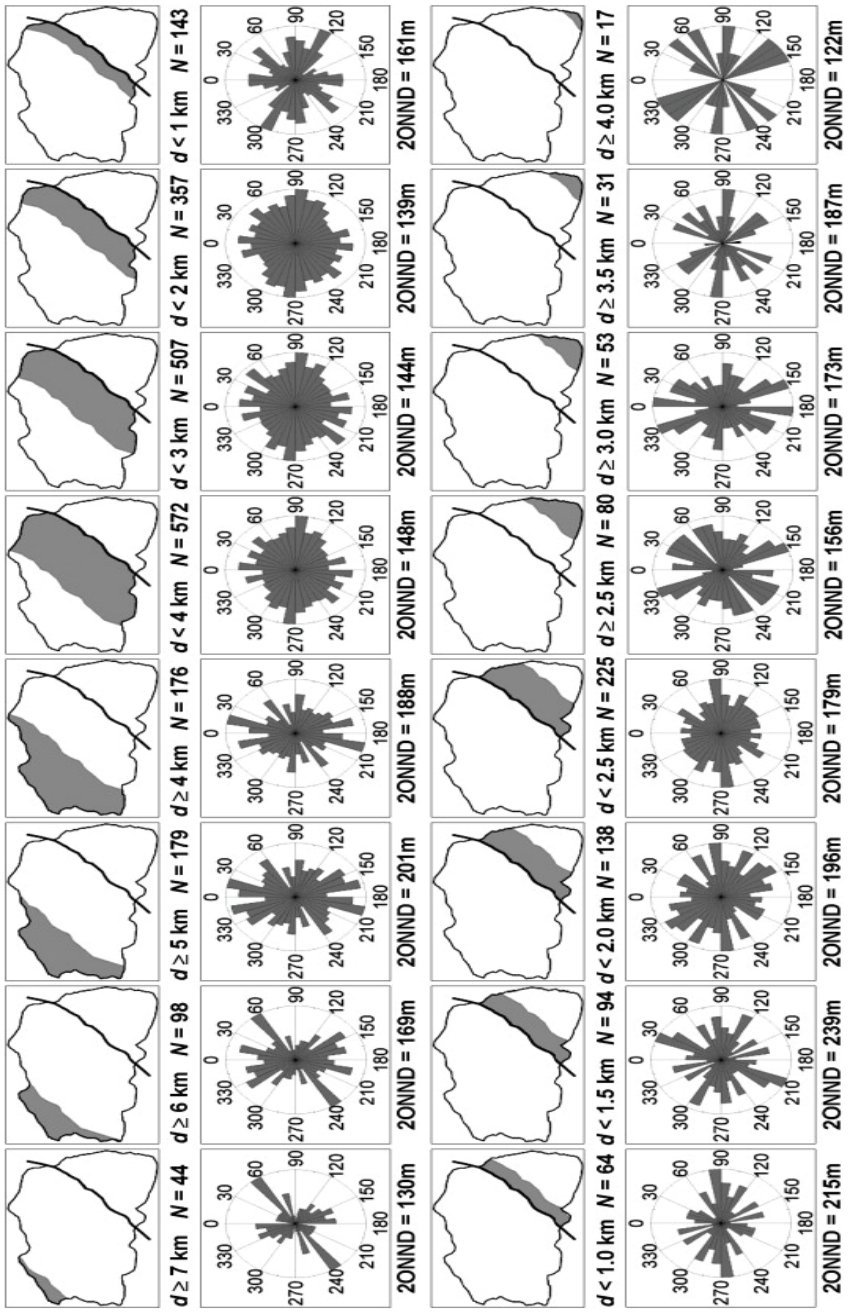

Fig. 4.5 Sub-areas (in grey) defined by distances (d) toward west and east from the Main Central Thrust and corresponding trends of N pairs of 2nd-order nearest neighbor Sh_rs Fry points. 2ONND means the average 2nd-order nearest neighbor distance used to select Fry points for analysis.

4.3.4 Synthesis of Fry analysis on structural and topographic controls on rockslides

Two major inferences can be made from Fry analyses of rockslides, with respect to the MCT and with respect to slope aspects, and relative frequencies of trends of mapped fault/fractures. Firstly, in some parts of the area, structures other than faults/fractures and some slope aspects provide mutual controls on rockslides. This inference plausibly pertains to rockslides in, for example, the area <4 km west of the MCT where pairs of 2nd-order nearest neighbor Sh_rs Fry points show a secondary NNW trend (Fig. 4.5), but there is paucity of NNW-trending faults/fractures in that area (Fig. 4.2). Secondly, in some parts of the area, only certain faults/fractures and only certain slope aspects provide mutual controls on rockslides. This inference is supported by knowledge that geometrical (and, thus, mutual) relationships between (certain) structural discontinuities in rocks and (certain) topographic slopes control slope failure (Goodman and Bray, 1976; Hoek and Bray, 1981; Romana, 1985; Wagner et al., 1988). However, the second inference reflects a caveat due to either the accuracy of the fault/fracture map or the sensitivity of Fry analysis to number of data points and shape of study area. Thus, there is a need to further investigate the second inference via spatial association analysis between rockslides and every set of faults/fractures and slope aspects in various parts of the area.

4.4 Spatial association of rockslides with fault/fractures and slope aspects

4.4.1 Distance distribution and proportion analysis

Methods for analysis of spatial association can be classified into two groups: (1) methods that are useful mainly in exploring plausible geological controls on landslide and (2) methods that lead directly to creation and integration of spatial evidence maps for predictive mapping of landslide susceptibility. The distance distribution method (Berman, 1986), which belongs to the first group, is applied here for exploring plausible structural controls on rockslide. In addition, a simple proportion analysis, which can be classified into either of the two groups of methods mentioned above, for determining which classes of slope aspects are associated spatially with rockslides were also applied.

Distance distribution analysis (Berman, 1986) compares (a) cumulative relative frequencies of distances from objects of a certain type to every location (hereafter denoted as $D(NL)$) and (b) cumulative relative frequencies of distances from the same objects to landslides of a certain type (hereafter

denoted as *D*(*L*)). The *D*(*NL*) is a probability density distribution of all locations in 'stable' slopes with respect to objects under study, whereas the *D*(*L*) is a probability density distribution of landslides with respect to the same objects. If the graph of *D*(*L*) follows closely the graph of *D*(*NL*), then landslides are randomly distributed with respect to objects under study. If the graph of *D*(*L*) plots above the graph of *D*(*NL*) (i.e., the difference of *D*(*L*)–*D*(*NL*) is positive), then landslides have positive spatial association with objects under study; otherwise, landslides have negative spatial association with objects under study. A positive *D-statistic* or *D*(*L*)–*D*(*NL*) difference represents the likelihood of landslide occurrence that is higher than would be expected due to chance as a function of distance to objects under study. Objects having strong positive spatial associations with landslides are of interest in predictive mapping of landslide susceptibility because proximity to such objects possibly represents a spatial control on landslide. The larger the *D*(*L*)–*D*(*NL*) difference, the stronger is the positive spatial association of landslides with objects under study. In a *D*(*L*)–*D*(*NL*) difference curve, the highest peak represents distance from the objects within which there is optimum positive spatial association between landslides and the objects under study. The ratio of the *D*(*L*)–*D*(*NL*) difference to the distance of optimum positive spatial association can be used in judging relative strength of positive spatial association between landslides and objects under study.

Proportion analysis determines (a) areal proportion of a slope aspect class ($PROP_a$) in an area under study and (b) proportion of rockslides within a slope aspect class ($PROP_{as}$) in the same area. If, for a slope aspect class, ratio $PROP_{as}$:$PROP_a$ is >1, then that slope aspect has positive spatial association with rockslides; otherwise, that slope aspect class has negative spatial association with rockslides.

The spatial association between rockslides and slope aspects was carried out to verify the distance distribution analyses of spatial association between rockslides and faults/fractures based on the same logic of Fry analysis of rockslides with respect to slope aspect as depicted in Fig. 4.3. That is, if rockslides are both structurally- and aspect-controlled, then it is likely that controlling structures are orientated at obtuse to right angles to aspects of controlling slopes, and vice versa. Thus, based on 30°-interval classes of trends, for rockslides on a WNW-facing slope, controlling structures possibly have NNW, NNE or NE trends. The frequency (or count) of possible trends of controlling structures interacting with controlling slope aspects can be used as an index of consistency between the analyses of spatial association between rockslides and faults/fractures and between rockslides and slope aspects. Consistent analyses would imply that only certain faults/fractures

and only certain slope aspects provide mutual controls on rockslide occurrence in certain parts of the area. Inconsistent analyses would imply that certain geological structures other than faults/fractures and certain slope aspects provide mutual controls on rockslide occurrence in certain parts of the area.

4.4.2 Spatial association of Sh_rs with faults/fractures and slope aspects

Occurrences of Sh_rs in the whole study area commonly have positive spatial associations with NNE-trending faults/fractures have (Fig. 4.6). However, the relative strength of positive spatial association of Sh_rs with NNE-trending faults/fractures varies in different parts of the area with respect to the MCT (Table 4.2). In the area <4 km west of the MCT, Sh_rs occurrences also have positive spatial associations with WNW- and NNW-trending faults/fractures. In the area ≥2.5 km east of the MCT, Sh_rs occurrences also have positive, albeit very weak, spatial association with NW-trending faults/fractures. The difference of *D(L)–D(NL)* within distances of optimum positive spatial association between Sh_rs and faults/fractures suggest that, on average, there is at least 0.15 higher likelihood of Sh_rs occurrence than would be expected due to chance, but Sh_rs occurrences are located mostly within 500 m (i.e., mean ≈ 285 m, std. dev. ≈ 215 m) of the positively associated sets of faults/fractures. In addition, the trends of the sets of faults/fractures found to have positive spatial associations with Sh_rs in the areas west of the MCT (Table 4.2) are consistent with the major trends of Sh_rs Fry points in those areas (Figs. 4.4b-c, Fig. 4.5), but they are inconsistent with the major trends of 2nd-order nearest neighbor Sh_rs Fry points with respect to slope aspects (Table 4.1). Thus, the analyses imply that (a) some sets of faults/fractures having positive spatial associations with Sh_rs are located away from Sh_rs occurrences and (b) geological structures other than faults/fractures possibly interact with slope aspects to influence Sh_rs occurrence.

Occurrences of Sh_rs are associated mostly with southerly- and easterly-facing slopes (Table 4.3). It is difficult to judge if the frequencies of trends of structures possibly interacting with slope aspects having positive spatial associations with Sh_rs (Table 4.2) and the relative strengths of positive spatial associations of each set of faults/fractures with Sh_rs (Table 4.2) are consistent or not. That is because mainly NNE-trending faults/fractures are found to have positive spatial association with Sh_rs (Table 4.2). However, structural trends deduced from the proportion analyses (Table 4.3) are mostly consistent with major trends derived from Fry analyses with respect to slope aspects (Table 4.1), which are mostly inconsistent with trends derived from distance distribution analyses (Table 4.2). Thus, inconsistencies

between frequencies of trends of structures possibly interacting with slope aspects having positive spatial associations with Sh_rs (Table 4.3) and relative strengths of positive spatial associations of each set of faults/fractures with Sh_rs (Table 4.2) imply that, if Sh_rs occurrences in the study area are both structurally- and aspect-controlled, then the controlling structures mostly trend NNE and some of these structures may not be faults/fractures.

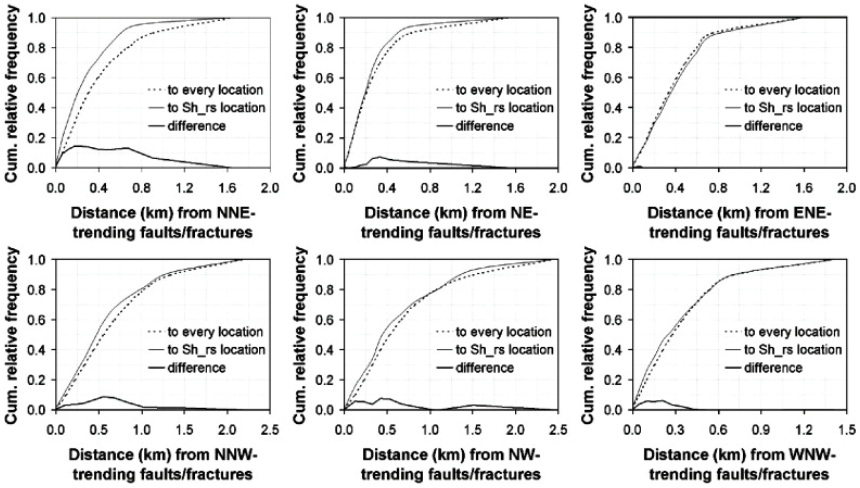

Fig. 4.6 Graphs of cumulative relative frequency of distances from individual sets of faults/fractures to every locations of Sh_rs.

Table 4.2 Sets of faults/fractures arranged in order of decreasing relative strength of positive spatial association (as indicated by values of ($D(L)$–$D(NL)$)/distance) with Sh_rs occurrence in various parts of the study area. $D(NL)$= cumulative relative frequency distribution of distances to every location per area. $D(L)$= cumulative relative frequency distribution of distances to every Sh_rs location per area. [MCT = Main Central Thrust].

Sets of faults/fractures according to trends	Distance (m) of optimum positive spatial association with *Sh_rs*	$D(L) - D(NL)$ at optimum distance	Ratio of $(D(L) - D(NL))$ to optimum distance
In the whole study area:			
NNE	170	0.1425	0.0008
In the area west of the MCT:			
WNW	130	0.1115	0.0009
NNW	495	0.1770	0.0004
NNE	625	0.1808	0.0003
In the area ≤4 km west of the MCT:			
WNW	125	0.1624	0.0013
NNW	475	0.1527	0.0003
NNE	560	0.1491	0.0003
In the area ≥4 km west of the MCT:			
NNE	190	0.1948	0.0010
In the area east of the MCT:			
NNE	70	0.1027	0.0015
In the area ≤2.5 km east of the MCT:			
NNE	65	0.0936	0.0014
In the area ≥2.5 km east of the MCT:			
NNE	95	0.1823	0.0019
NW	450	0.1729	0.0004

Table 4.3 Slope aspects arranged in decreasing positive spatial association with Sh_rs and trends of structures possibly interacting with slope aspect to influence Sh_rs occurrence. PROPas:PROPa is ratio of proportion of Sh_rs within a slope aspect class in an area to areal proportion of a slope aspect class in the same area. [MCT = Main Central Thrust].

Slope aspect class	$PROP_{as}$: $PROP_a$	Trends of structures possibly interacting with slope aspects to influence *Sh_rs* occurrence	Frequency of trends of structures possibly interacting with slope aspects
In the whole study area:			
SE	1.5932	ENE, NE, NNE	
ESE	1.4093	NE, NNE, NNW	ENE – 3; NE – 3;
SSE	1.2698	WNW, ENE, NE	NNE – 3;
ENE	1.2266	NNE, NNW, NW	NNW – 3; NW – 3; WNW
SSW	1.1927	ENE, WNW, NW	– 3
SW	1.0845	WNW, NW, NNW	
In the area west of the MCT:			
ESE	1.5908	NE, NNE, NNW	
SE	1.5393	ENE, NE, NNE	NE – 4; NNE – 3; ENE –
ENE	1.3696	NNE, NNW, NW	3;
SSW	1.3499	ENE, WNW, NW	NNW – 3; WNW – 3; NW
SSE	1.2349	WNW, ENE, NE	– 2
SW	1.1105	WNW, NW, NNW	
In the area ≤4 km west of the MCT:			
ESE	1.4142	NE, NNE, NNW	
SSW	1.3116	WNW, NW, NNW	NE – 4; NNE – 3;
ENE	1.1894	NNE, NNW, NW	ENE – 3;
SE	1.1549	ENE, NE, NNE	NNW – 3; WNW – 3; NW
SW	1.1150	WNW, NW, NNW	– 2
SSE	1.0576	WNW, ENE, NE	
In the area ≥4 km west of the MCT:			
SE	3.0779	ENE, NE, NNE	ENE – 3; WNW – 3;
SSE	1.6256	WNW, ENE, NE	NE – 3;
SSW	1.3673	ENE, WNW, NW	NNE – 2; NNW – 2;
SW	1.1973	WNW, NW, NNW	NW – 2
WSW	1.1909	NW, NNW, NNE	
In the area east of the MCT:			
SE	1.6688	ENE, NE, NNE	NE – 3; ENE – 2;
SSE	1.4645	WNW, ENE, NE	NNE – 2;
SW	1.0709	WNW, NW, NNW	NNW – 2; WNW – 2; NW
ESE	1.0603	NE, NNE, NNW	– 1
In the area ≤2.5 km east of the MCT:			
SE	1.5429	ENE, NE, NNE	NE – 4; NNE – 3;
SSE	1.4964	WNW, ENE, NE	ENE – 3;
NW	1.2308	NNE, NE, ENE	NNW – 2; WNW – 2; NW
SW	1.0581	WNW, NW, NNW	– 1
WNW	1.0293	NNW, NNE, NE	
In the area ≥2.5 km east of the MCT:			
SE	1.9139	ENE, NE, NNE	NE – 3; NNW – 3;
ENE	1.3917	NNE, NNW, NW	ENE – 2;
SSE	1.3889	WNW, ENE, NE	NNE – 2; NW – 2; WNW
ESE	1.3100	NE, NNE, NNW	– 2
SW	1.1232	WNW, NW, NNW	

4.4.3 Synthesis of spatial association analyses

The analyses of spatial associations of rockslides with every set of faults/fractures and every set of slope aspects suggest that, in certain parts of the area, rockslide occurrence is controlled by either only certain faults/fractures or only certain slope aspects. This deduction is supported by analyses that some sets of faults/fractures have positive, albeit weak, spatial associations with rockslides, and the latter are located, on average, at least 400 m away from the former (Table 4.2). The foregoing inferences based on

the spatial association analyses can be examined further by considering consistencies and inconsistencies between Fry analyses of Sh_rs with respect to slope aspects and analyses of spatial associations Sh_rs with slope aspects and each set of faults/fractures (Table 4.4). For the synthesised results of Dp_rs, Annexure II in the enclosed CD may be consulted.

Thus, to interpret the analyses summarized in Table 4.4, the following considerations were made (Fig. 4.7). Firstly, consistent structural trends derived from analyses of spatial associations of rockslides with slope aspects and faults/fractures are considered to imply mutual controls on rockslide by certain faults/fractures and associated slope aspects. Secondly, consistent structural trends derived only from Fry analyses of rockslides with respect to slope aspect and from analyses of spatial associations between rockslides and slope aspects are considered to imply mutual controls on rockslide by certain slope aspects and structures that may not be faults/fractures. Finally, inconsistent structural trends derived from analyses of spatial associations between rockslides and slope aspects and from Fry analyses of rockslides with respect to slope aspect and analyses of spatial associations between rockslides and faults/fractures are considered to imply lack of mutual controls on rockslide by structures of deduced trends and certain slope aspects. Thus, only the interpretations of the analyses according to the first consideration, with respect to mutual fault/fracture and slope aspect controls on rockslide, are explained below.

The analyses summarized in Table 4.4 imply the following. In the whole study area, mutual controls on Sh_rs are due to NNE-trending faults/fractures and SE-facing slopes. In the area west of the MCT, particularly in the area <4 km west of the MCT, mutual controls on Sh_rs are due to WNW, NNW- and NNE-trending faults/fractures and associated slope aspects. In the area ≥4 km west of the MCT, mutual controls on Sh_rs are due to NNE-trending faults/fractures and either SE- or WSW-facing slopes. In the area either <2.5 km or ≥2.5 km east of the MCT, mutual controls on Sh_rs are due to SE-, NW- and WNW-facing slopes and NNE-trending faults/fractures. In addition, in the area ≥2.5 km east of the MCT, mutual controls on Sh_rs are due to NW-trending faults/fractures and SW-facing slopes.

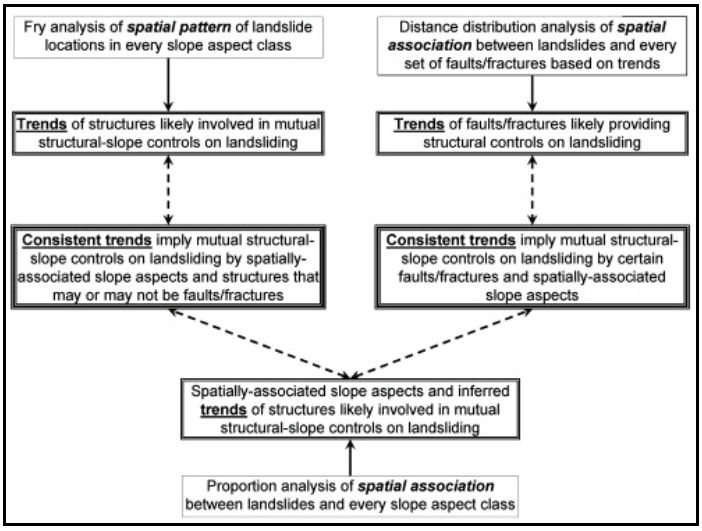

Fig. 4.7 Diagram of strategy to synthesize results of spatial analyses in order to determine which sets of faults/fractures (based on trends) and which classes of slope aspects are likely involved in mutual fault/fracture and slope aspect controls on rocksliding in the study area. Single-end arrows represent analysis–result processes, whereas double-end arrows represent comparing/synthesizing of results of different analyses.

Table 4.4 Summary of Fry analyses of Sh_rs with respect to slope aspects and analyses of spatial associations of Sh_rs with slope aspects and faults/fractures. Trends in bold are consistent analyses of spatial associations of Sh_rs with slope aspects and faults/fractures. Trends in italics are consistent Fry analyses of Sh_rs with respect to slope aspects and analyses of spatial associations of Sh_rs with slope aspects. [MCT = Main Central Thrust]

Area	Spatially associated aspects containing ≥4 *Sh_rs* (Tables 4.1 and 4.3)	Trends of controlling structures based on pairs of 2nd-order nearest neighbor *Sh_rs* Fry points with respect to slope aspect (Table 4.1)	Frequency of trends of structures possibly interacting with spatially associated slope aspects containing ≥4 *Sh_rs* (Table 4.3)	Trends of faults/fractures spatially associated with *Sh_rs* (Table 4.2)
Whole study area	SE, SSE, SW	*ENE*, *WNW*	*ENE* – 2; *WNW* – 2; NE – 2; NW – 1; NNW – 1; **NNE** – 1	**NNE**
West of MCT	ESE, SE, SW	*NE*, *NNE*, *WNW*	*NE* – 2; ***NNE*** – 2; **NNW** – 2; ***WNW*** – 1; NW – 1; ENE – 1	**WNW**, **NNW**, **NNE**
<4 km west of MCT	ESE, SE, SW	*NE*, *NNE*, *WNW*	*NE* – 2; ***NNE*** – 2; **NNW** – 2; ***WNW*** – 1; NW – 1; ENE – 1	**WNW**, **NNW**, **NNE**
≥4 km west of MCT	SE, SSE, SSW, SW, WSW	*NNE*, *NE*, *NW*, *NNW*	*NW* – 3; ENE – 3; *NE* – 2; ***NNE*** – 2; *NNW* – 2; WNW – 2	**NNE**
East of MCT	SE, SSE	*ENE*, *NE*	*ENE* – 2; *NE* – 2; **NNE** – 1; WNW – 1	**NNE**
<2.5 km east of MCT	SE, SSE, NW, WNW	*ENE*, *WNW*, *NNW*, *NE*	*NE* – 4; *ENE* – 3; **NNE** – 3; *NNW* – 1; *WNW* – 1	**NNE**
≥2.5 km east of MCT	SE, SSE, SW	*ENE*, *WNW*	*ENE* – 2; *WNW* – 2; NE – 2; **NNE** – 1; NNW – 1; **NW** – 1	**NNE**, **NW**

In order to verify the foregoing interpretations, proportion analyses were performed and it was observed that, in various parts of the area, varying degrees of positive spatial associations exist between Sh_rs and above-mentioned slope aspects containing each set of above-mentioned faults/fractures. Thus, only certain faults/fractures and only certain slope aspects provide mutual controls on rockslide occurrence in certain parts of the area. This means that it is trivial to use all sets of faults/fractures as a single spatial factor of rockslide. Accordingly, the spatial analyses must be considered in the way spatial factor maps are created for each set of faults/fractures. Similar nature of results was also observed for deep-seated rockslides (Dp_rs) (see Annexure II in the enclosed CD).

4.5 Spatial modelling of mutual fault/fracture and slope controls on rockslides

4.5.1 Conceptual framework

The foregoing spatial analyses suggest that the study area can be divided into the three domains, in which only certain sets of faults/fractures and certain slope aspects provide mutual controls on rockslide occurrence: (A) the area ≥4 km west of the MCT; (B) the area <4 km west of the MCT; and (c) the area east of the MCT. However, instead of using 4-km distance from the MCT, the major southwesterly-plunging ridge (see Fig. 1.2c) can be used as a divider because southerly- and easterly-facing slopes located east of this ridge mostly receive heavy monsoon precipitation coming usually from the south. By using the ridge, along which the mean distance from the MCT is ca. 3.5 km, instead of the 4-km line from the MCT to divide the area west of the MCT into two domains, 11 Sh_rs occurrences in the area <4 km west of the MCT become part of domain A (Fig. 4.8). However, by perfunctorily re-doing the analyses, no significant differences between the results for domains A and B and those for areas ≥4 km and <4 km west of the MCT, were observed respectively. Thus, the interpretations in areas ≥4 km and <4 km west of the MCT also apply, respectively, in domains A and B.

The spatial analyses summarized in Table 4.4 are interpreted as follows. In domain A, Sh_rs is controlled mutually by NNE-trending faults/fractures and either SE- or WSW-facing slopes. In domain B, Sh_rs is controlled mutually by (a) WNW-trending faults/fractures and SW-facing slopes and (b) NNW-trending faults/fractures and either ESE- or SW-facing slopes. In domain C, Sh_rs is controlled mutually by (a) NNE-trending faults/fractures and SE-, NW- and WNW-facing slopes and (b) NW-trending faults/fractures and SW-facing slopes. These interpretations serve as framework for predictive mapping of rockslide susceptibility.

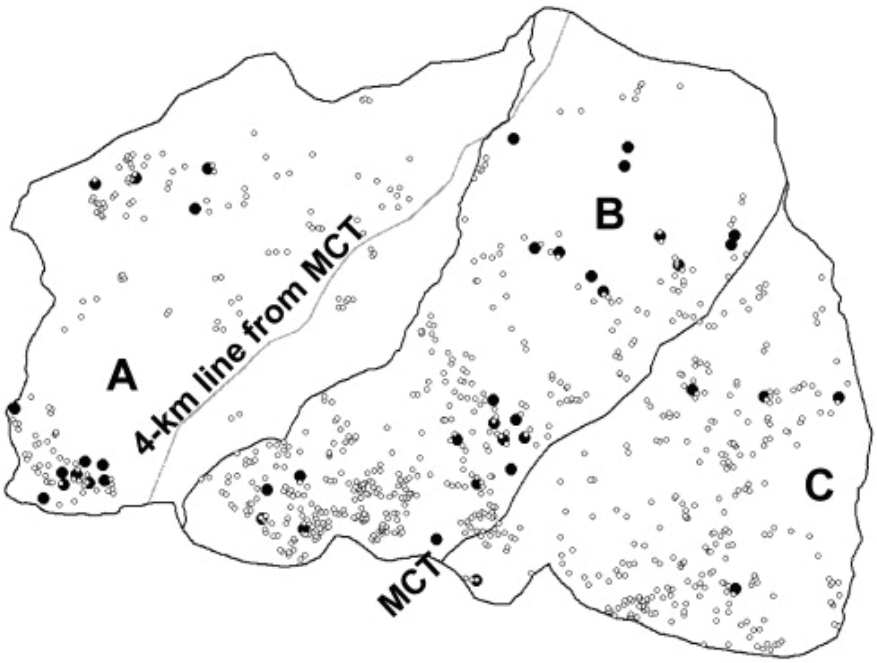

Fig. 4.8 Spatial domains in the study areas based on spatial analyses of mutual fault/fracture and slope controls on rockslide occurrence. The boundary between domains A and B is the major southwesterly-plunging ridge west of the MCT (Main Central Thrust) (cf. Fig. 1.2c), whereas the boundary between domains B and C is the MCT (cf. Fig. 4.1). Large filled circles and small unfilled circles are locations of, respectively, Dp_rs and Sh_rs.

The spatial analyses suggest that NNE-, WNW-, NNW- and NW-trending faults/fractures must be used as separate map layers in modelling mutual fault/fracture and slope aspect controls on Sh_rs in the area. However, separating classes of slope aspects into individual map layers is illogical. That is because, whereas faults/fractures represent discrete structural processes that influence variations in local stress fields within and between domains, slope aspects, like topographic elevations from which they are calculated, actually represent continuous fields even if they are discretized into a number of classes to facilitate spatial analysis. Therefore, the same layer of 12 classes of slope aspects was used (Fig. 1.2c).

Following the slope failure criteria based on orientations of geological structures and orientations of topographic slopes (Goodman and Bray, 1976), it is important to use, in addition to slope aspects and trends of faults/fractures, inclinations (or dips) of faults/fractures and slopes in modelling mutual fault/fracture and slope aspect controls on rockslide in the area. As spatially-distributed dip data for the mapped faults/fractures are not available, slope inclinations were only used further in modelling of mutual

fault/fracture and slope controls on rockslide. For this purpose, slope inclinations were discretized into narrow classes of 5º-intervals and, for the same reason that separate classes of slope aspects into individual map layers were not made; a single map layer of classes of slope inclinations was used.

4.5.2 Evidential belief modelling

Predictive modelling of landslide susceptibility requires representation and integration of relevant spatial factor maps or layers of spatial evidence. The Dempster-Shafer theory of evidential belief (Dempster, 1967; Shafer, 1976) provides a concept for assigning probabilities or degrees of belief to any evidence used in evaluating a proposition. Dempster's (1967; 1968) work on the generalization of Bayesian lower and upper probabilities is the basis for the theory of evidential belief. Shafer (1976) then defined two evidential belief functions (EBFs), belief and plausibility, to represent lower and upper probabilities, respectively, that a proposition is valid based on given evidence. Chung and Fabbri (1993) described the representation of geosciences information for data integration based on the Dempster-Shafer theory of evidential belief. An et al. (1994) demonstrated the representation of uncertainty in integrating mineral exploration data by using EBFs. Recently, Carranza and Castro (2006) demonstrated the application of EBFs for predictive mapping of susceptibility to distal lahar-inundation in Mount Pinatubo (Philippines).

The mathematical formalism of the EBFs is complex (Dempster, 1967; Shafer, 1976). The following explanations, for their application to create and integrate spatial factor maps representing controls on rockslide, are simplified and informal. With respect to a proposition (e.g., rockslide occurrence), three EBFs are estimated for an evidence (e.g., NNE-facing slopes), namely, belief (hereafter called *Bel*), disbelief (hereafter called *Dis*) and uncertainty (hereafter called *Unc*), each of which falls in the range [0,1]. The *Bel* is lower degree of belief in given evidence with respect to a proposition. The *Dis* is degree of disbelief in given evidence with respect to a proposition. The *Unc* is 'ignorance' or 'doubt' for given evidence with respect to a proposition. The sum of *Bel* and *Unc* (called plausibility) is upper degree of belief in given evidence with respect to a proposition. The sum of *Bel*+*Unc*+*Dis* for given evidence with respect to a proposition is equal to 1 (i.e., maximum probability). The *Unc* influences the relation between *Bel* and *Dis*. If *Unc*=0 (i.e., complete knowledge about given evidence), then *Bel*+*Dis*=1 and the relation between *Bel* and *Dis* is binary (i.e., *Bel=1−Dis* or *Dis=1−Bel*), as in the theory of probability. If *Unc*=1 (i.e., complete ignorance or doubt about given evidence), then *Bel* and *Dis* are both equal to zero. That is because; if there is complete uncertainty, then there can be

neither belief nor disbelief. Usually, however, *Unc* is neither equal to zero nor equal to one. If 0<*Unc*<1, then *Bel*=1–*Dis*–*Unc* or *Dis*=1–*Bel*–*Unc*. This means that, because some uncertainty is usually present, the relation between *Bel* and *Dis* is usually not binary. Thus, for every proposition, one should estimate not only *Bel* but also *Dis* and *Unc* for any evidence.

Estimation of EBFs of evidence with respect to certain propositions has traditionally been knowledge-driven (i.e., based on expert opinion), which is subjective because (a) no two experts will have the same opinion about an evidence for a certain proposition and (b) differentiating between and, thus, estimating disbelief and uncertainty is conceptually difficult. However, Carranza (2002) and Carranza and Hale (2003) have derived and proposed equations for GIS-based data-driven estimation of EBFs of evidence for mineral potential. Here, the GIS-based data-driven method of estimating EBFs was adopted to create and integrate maps of EBFs representing fault/fracture and slope controls on rockslide in the area.

Suppose that in a study area (or a spatial domain) T, comprising $N(T)$ total number of unit cells or pixels, there are a number of known rockslides, R, of a certain type occurring in $N(R)$ number of pixels (Fig. 4.9). Suppose further that maps of X_i ($i=1,2,\ldots,n$) spatial factors, each with a number of C_{ji} ($j=1,2,\ldots,m$) classes, are given. Each of the jth C_{ji} class of X_i spatial factor has $N(C_{ji})$ number of pixels. The sum of $N(C_{ji})$ number of pixels in every X_i map is equal to $N(T)$. By overlaying a map of R on each spatial factor map, the number of C_{ji} pixels coinciding with R pixels [i.e., $N(C_{ji} \cap R)$] is determined, from which the number of *Cji* pixels not overlapping with R pixels [i.e., $N(C_{ji}) - N(C_{ji} \cap R)$] is derived. The values of $N(T)$, $N(R)$, $N(C_{ji})$ and $N(C_{ji} \cap R)$ are the ones used in data-driven estimation of the EBFs.

$Bel_{C_{ji}}$ for the jth C_{ji} ($j=1,2,\ldots,m$) class of X_i ($i=1,2,\ldots,n$) spatial factor with respect to R is estimated as:

$$Bel_{C_{ji}} = W_{C_{ji}R} \Big/ \sum_{j=1}^{m} W_{C_{ji}R} \,, \tag{4.1a}$$

where, $$W_{C_{ji}R} = \frac{N(C_{ji} \cap R)}{N(C_{ij})} \Big/ \frac{N(R) - N(C_{ji} \cap R)}{N(T) - N(C_{ji})} \tag{4.1b}$$

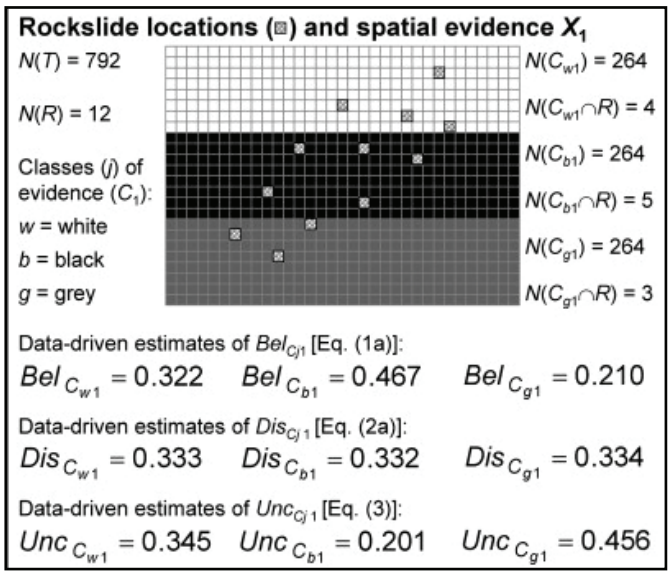

Fig. 4.9 Hypothetical data of rockslide (R) locations and a map of spatial evidence (C_1) with three classes (C_{j1}) (j=grey scale) for illustration of data-driven estimates of $Bel_{C_{ji}}$ [Eq. (4.1a)], $Dis_{C_{ji}}$ [Eq. (4.2a)] and $Unc_{C_{ji}}$ [Eq. (4.3)] (adapted from Carranza, 2008). The area (T) is discretized into a number of equal-area unit cells $N(T)$. The number of unit cells with rockslides $N(R)$ is determined. Each evidential class occupies a number of unit cells $N(C_{ji})$.The numbers of class evidence unit cells with rockslides $N(C_{ji} \cap R)$ are determined via map overlay operation. The values of $N(T)$, $N(R)$, $N(C_{ji})$ and $N(C_{ji} \cap R)$ are used in data-driven estimations of the EBFs [Eqs. (4.1a), (4.2a) and (4.3)]. See text for further explanation.

The composite numerator in Eq. (4.1b) is conditional probability that R exists given presence of C_{ji}. The composite denominator in Eq. (4.1b) is conditional probability that R exists given absence of C_{ji}. Thus, the $W_{C_{ji}R}$ is relative weight of every C_{ji} in terms of R being more present than absent in C_{ji} as may be expected due to chance. Accordingly, in every X_i spatial factor map, $Bel_{C_{ji}}$ is relative strength of spatial association of C_{ji} with R compared to the relative strengths of spatial associations of all other classes C_{ji} with R.

$Dis_{C_{ji}}$ for the jth C_{ji} (j=1,2,…,m) class of X_i (i=1,2,…,n) spatial factor with respect to R is estimated as:

$$Dis_{C_{ji}} = W_{C_{ji}\overline{R}} \Big/ \sum_{j=1}^{m} W_{C_{ji}\overline{R}} \,, \qquad (4.2a)$$

where $W_{C_{ji}\overline{R}} = \dfrac{N(C_{ji}) - N(C_{ji} \cap R)}{N(C_{ji})} \Big/ \dfrac{N(T) - N(R) - [N(C_{ji}) - N(C_{ji} \cap R)]}{N(T) - N(C_{ji})}$ (4.2b)

and $\overline{R}$ means non-rockslide pixels. The composite numerator in Eq. (4.2b) is conditional probability that R does not exist given presence of C_{ji}. The composite denominator in Eq. (4.2b) is conditional probability that R does not exist given absence of C_{ji}. Thus, $W_{C_{ji}\overline{R}}$ is relative weight of C_{ji} in terms of R being more absent than present in C_{ji} as may be expected due to chance. Accordingly, in every X_i spatial factor map, $Dis_{C_{ji}}$ is relative strength of the spatial association of C_{ji} with $\overline{R}$ (but not with R) compared to the relative strengths of spatial associations of all other classes C_{ji} with $\overline{R}$.

There are two outcomes if, in every X_i spatial factor map, the relative strengths of spatial associations of all classes C_{ji} with R and $\overline{R}$ are considered. First, the values of either $Bel_{C_{ji}}$ or $Dis_{C_{ji}}$ estimated according to Eqs. (4.1a) and (4.2a), respectively, are constrained to the unit range [0,1], which is consistent with the concept of probability. Second, the sum of the values of $Bel_{C\,ji}$ and $Dis_{C\,ji}$ is less than 1, which allows modelling of $Unc_{C_{ji}}$ as:

$$Unc_{C_{ji}} = 1 - \left(W_{C_{ji}R} \Big/ \sum_{j=1}^{m} W_{C_{ji}R} \right) - \left(W_{C_{ji}\overline{R}} \Big/ \sum_{j=1}^{m} W_{C_{ji}\overline{R}} \right) = 1 - Bel_{C_{ji}} - Dis_{C_{ji}} \qquad (4.3)$$

In applying the foregoing equations for data-driven estimation of EBFs, one must take note of a result that $W_{C_{ji}R} = 0$ [Eq. (4.1b)]. This means that $N(C_{ji} \cap R) = 0$, which results in $Bel_{C_{ji}} = 0$ [Eq. (1a)]. If $W_{C_{ji}R} = 0$, the corresponding estimate of $W_{C_{ji}\overline{R}} \neq 0$ [since $N(C_{ji}) - [N(C_{ji} \cap R)] \neq 0$; Eq. (4.2b)] must be discarded and replaced with 0. By doing so, the corresponding $Dis_{C_{ji}} = 0$ and the corresponding $Unc_{C_{ji}} = 1$, which are based on the logic that, if there is no belief, then there is also no disbelief but there is only uncertainty.

Maps of EBFs of spatial factor map X_1 can be combined with maps of EBFs of spatial factor map X_2 according to Dempster's (1968) rule of combination. The formulas for combining EBFs of two spatial factor maps (X_1, X_2) are (cf. An et al., 1994):

$$Bel_{X_1X_2} = \left(Bel_{X_1}Bel_{X_2} + Bel_{X_1}Unc_{X_2} + Bel_{X_2}Unc_{X_1}\right)/\beta \qquad (4.4)$$

$$Dis_{X_1X_2} = \left(Dis_{X_1}Dis_{X_2} + Dis_{X_1}Unc_{X_2} + Dis_{X_2}Unc_{X_1}\right)/\beta \quad (4.5)$$

$$Unc_{X_1X_2} = \left(Unc_{X_1}Unc_{X_2}\right)/\beta \quad (4.6)$$

where $\beta = 1 - Bel_{X_1}Dis_{X_2} - Dis_{X_1}Bel_{X_2}$, which ensures that $Bel+Dis+Unc=1$. Thus, only maps of EBF of two spatial factors are combined each time. Other maps of EBFs representing spatial factors $X_3,\ldots,X_i$ are combined one after another by repeated applications of Eqs. (4.4) to (4.6). Note that Eqs. (4.4) and (4.5) are both commutative and associative, meaning that their application results in a map of integrated *Bel* and integrated *Dis*, respectively, in which the output values are controlled by high values of *Bel* and *Dis* associated with certain classes in either of two input maps. In contrast, Eq. (4.6) is associative, meaning that its application results in a map of integrated *Unc* in which the output values are controlled by low values of *Unc* associated with certain classes in either of two input maps. Thus, the Dempster's (1968) rule of combination is suitable in combining data of spatial factors providing mutual controls on certain phenomena. In addition, because Eqs. (4.4) to (4.6) are all associative, any order of combining maps of EBFs of spatial factors $X_1,\ldots X_i$ (i.e., not necessarily that X_1 and X_2 are combined first, and so on) does not affect the final output.

4.5.2.1 Spatial modelling using EBFs

In applying the method of EBFs to test the model (or proposition) of mutual fault/fracture and slope controls on rockslide, the inventory rockslides were divided into two subsets – one training subset for estimation and integration of EBFs of various spatial factors and one testing subset for cross-validation of the integrated maps of EBFs of spatial factors. This scheme of model testing did not work well for Dp_rs because there are only 42 Dp_rs occurrences (Ghosh et al., 2009b), and the training subset consists of 28 Dp_rs in 1968 to 2003 while the testing subset consists of 14 Dp_rs in 2004 to 2006. However, the scheme of model testing worked well for Sh_rs because there are 796 Sh_rs (Ghosh et al., 2009b), and the training subset consists of 740 Sh_rs in 1968 to 2006 while the testing subset consists of 56 Sh_rs in 2007. Thus, below only the results for modelling of mutual fault/fracture and slope controls on Sh_rs are discussed.

For each set of pre-selected faults/fractures, a spatial factor map based on 5-percentile intervals of distance from faults/fractures is created. Then EBFs of every fault/fracture distance class with respect to rockslides in each domain are estimated. In addition, according to the conceptual framework discussed above based on the spatial analyses, in a domain where a set of faults/fracture is likely not involved in mutual fault/fracture and slope

controls on rockslide, all classes of distance to such set of fault/fracture values of *Bel*=0, *Dis*=0 and *Unc*=1 are assigned. This means that, in a domain where a set of faults/fracture is likely not involved in mutual fault/fracture and slope controls on rockslide, the influence of that set of faults/fractures are modeled to be uncertain. For example, the spatial analyses suggest that NNE-trending faults/fractures are likely involved mutual fault/fracture and slope aspect controls on Sh_rs in domains A and C, but not in domain B. Thus, in domains A and C the EBFs of individual classes of distance to NNE-trending faults are calculated with respect to Sh_rs in those domains, whereas in domain B the EBFs of all classes of distances to NNE-trending faults/fractures are assigned a *Bel* of 0, a *Dis* of 0 and an *Unc* of 1 (Fig. 4.10). In conformity with the spatial association analyses given in Table 4.2, Fig. 4.10 shows that areas proximal to NNE-trending faults/fractures in domains A and C have values of *Bel* and *Unc* that are, respectively, higher and lower than those of areas distal to such set of faults/fractures, although variations in values of *Dis* in areas proximal and distal to such set of faults/fractures are very minor. Nevertheless, below the effect of assigning a *Bel* of 0, a *Dis* of 0 and an *Unc* of 1 in modelling the influence of a set of faults/fractures that is likely not involved in mutual fault/fracture and slope controls on rockslide is revisited below.

For classes of slope aspects and slope inclinations, EBFs are not estimated per domain but in the whole study area. That is because, in addition to the reason stated above for not separating classes of slope aspects and slope inclinations into individual map layers, each pre-selected set of faults/fractures could possibly interact, albeit locally in a domain, with slope aspects other than those found to have positive spatial associations with rockslides. This follows the earlier assumption of this study that controlling structures and slope aspects are orientated at obtuse to right angles to each other. The EBFs of slope aspects with respect to Sh_rs in the area are shown in Fig. 4.10. In conformity with the relative strengths of quantified positive spatial associations between slope aspects and Sh_rs (Table 4.3), southerly- to easterly-facing slopes have values of *Bel*, *Dis* and *Unc* that are, respectively, higher, and lower and lower than those of other slope aspects. The EBFs of slope inclinations (Figs. 4.10-4.11) show that Sh_rs occurrences are associated mostly with slope inclinations between 30º and 50º. Whereas the maps of EBFs of slope aspects suggest broad areas where Sh_rs could possibly occur, the maps of EBFs of slope inclinations suggest restricted areas where Sh_rs could possibly occur. Thus, integration of maps of EBFs of slope inclinations is important in modelling mutual fault/fracture and slope controls on rockslide.

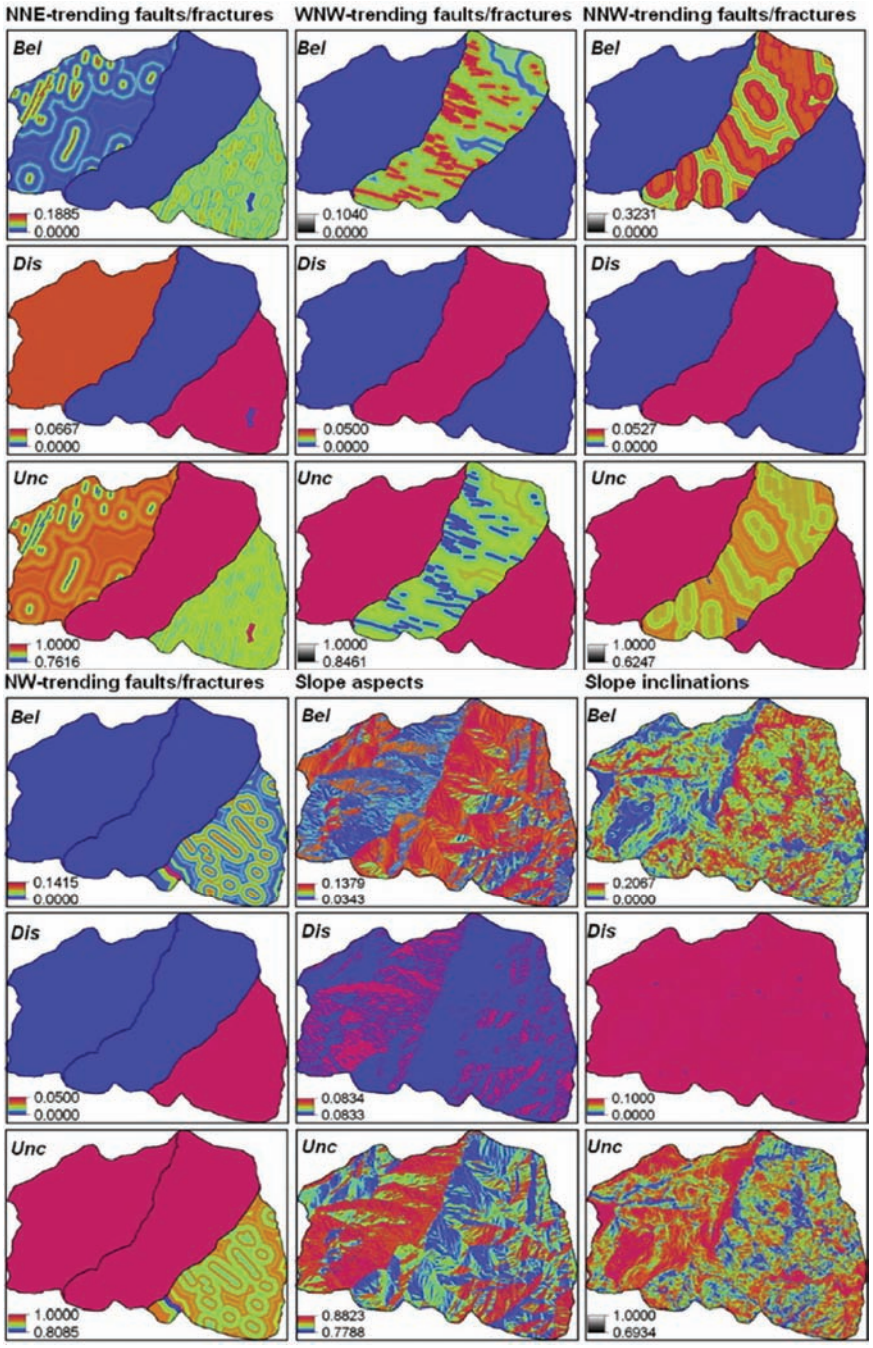

Fig. 4.10 Evidential belief functions of classes of distances to individual sets of faults/fractures with respect to Sh_rs occurrence in every domain (Fig. 4.8), and evidential belief functions of slope aspects and slope inclinations with respect to Sh_rs occurrence in the whole study area.

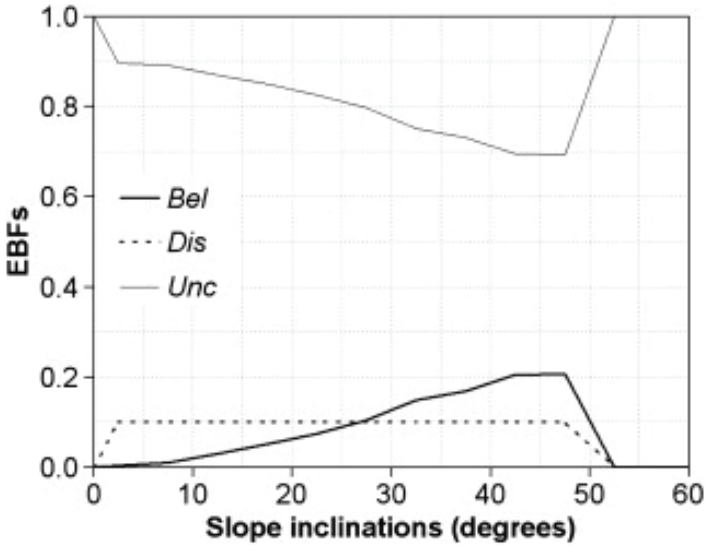

Fig. 4.11 Variation of EBFs of slope inclinations with respect to Sh_rs occurrences in the study area.

To determine the effect of assigning a *Bel* of 0, a *Dis* of 0 and an *Unc* of 1 in modelling the influence of a set of faults/fracture that is possibly not involved in mutual fault/fracture and slope controls on rockslide, the maps of integrated EBFs of slope aspects and distances to NNE-trending faults/fractures (Fig. 4.10a) can be examined. The maps show that there is higher *Bel*, higher *Dis* and lower *Unc* for Sh_rs in domains A and C than in domain B, but in many parts of domain A there is lower *Bel* for Sh_rs than in domain B. Subtraction of the EBFs of slope aspects from the integrated EBFs of slope aspects and distances to NNE-trending faults/fractures results in maps (Fig. 4.12b) with (a) positive values of *Bel*, positive values of *Dis* and negative values of *Unc* in domains A and C and (b) null values for *Bel*, *Dis* and *Unc* in domain B. The former results suggest that, in domains A and C, the presence of NNE-trending faults/fractures in certain slope aspects increases the likelihood and uncertainty of Sh_rs , whereas the latter results illustrate that, in domain B, the integrated EBFs of slope aspects and distances to NNE-trending faults/fractures are all due to the EBFs of slope aspects. Thus, assigning a *Bel* of 0, a *Dis* of 0 and an *Unc* of 1 to all classes of distances to a set of faults/fracture that is likely not involved in mutual fault/fracture and slope controls on rockslide is satisfactory for representing EBFs of a set of non-controlling faults/fractures. It has a null effect that does not interfere with modelling of mutual fault/fracture and slope controls on rockslide. This means that if an area is divided into domains, in which only certain faults/fractures are likely involved in mutual fault/fracture and slope

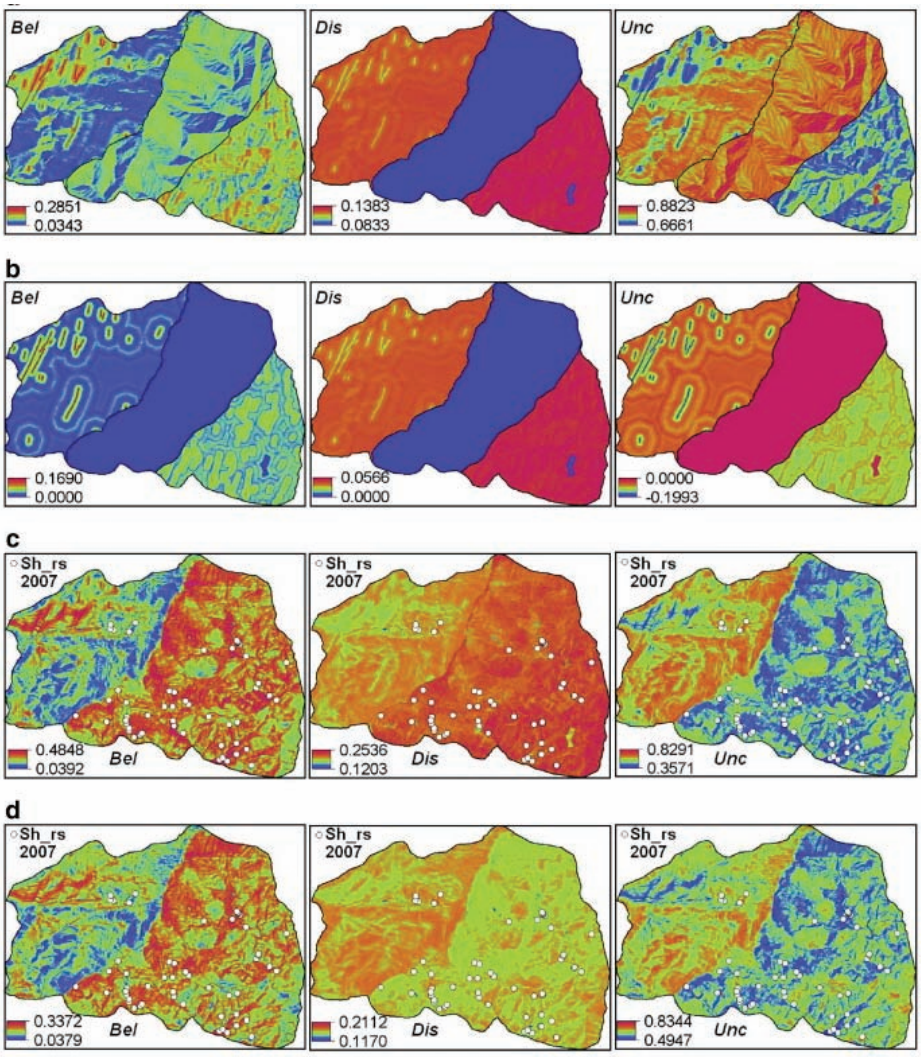

Fig. 4.12 Models of mutual controls on Sh_rs occurrence by faults/fractures and slope aspects. a) Integrated EBFs of slope aspects and classes of distances to NNE-trending faults/fractures. b) Contributions of EBFs of distances to NNE-trending faults/fractures to the model in a). c) Model-1 of Sh_rs occurrence based on a training subset of 1969–2006 Sh_rs occurrences, slopes and only sets of faults/fractures spatially associated with whole set of Sh_rs occurrences. d) Model-2 of Sh_rs occurrence based on a training subset of 1969–2006 Sh_rs occurrences, slopes and all sets of faults/fractures. The testing subset of 2007 Sh_rs occurrences illustrates the predictive capability of Model-1 and Model-2 (text for discussion).

controls on rockslide, maps of EBFs of a set of spatial features can be created even although such spatial features influence rockslide only in some domains. This means further that (a) it is unnecessary to model mutual fault/fracture and slope controls on rockslide per domain by creating and integrating

evidence maps of only controlling spatial features per domain, but (b) it is certainly trivial to create and integrate evidence maps of spatial features that are not likely involved in mutual fault/fracture and slope controls on rockslide in all domains.

The outputs of integrating all the maps of EBFs in Fig. 4.10 show that several parts of domains B and C have high *Bel* and low *Unc* but high *Dis* for Sh_rs, whereas mainly the northwestern parts of domain A have high *Bel*, low *Dis* and low *Unc* for Sh_rs (Fig. 4.12c). The high *Dis* for Sh_rs in many parts of domains B and C imply that mutual fault/fracture and slope controls are alone inadequate for Sh_rs occurrence in those domains, whereas low *Dis* for Sh_rs in the northwestern parts of domain A implies that mutual fault/fracture and slope controls strongly influence Sh_rs occurrence in that domain. Even so, high *Bel* and low *Unc* for Sh_rs in many parts of domains B and C, compared to the high *Bel* and low *Unc* for Sh_rs in the northwestern parts of domain A, show that many areas east of the major SW-plunging ridge, where the MCT and MBT are located, are more prone to Sh_rs than many areas west of the ridge.

4.5.2.2 Model evaluation

In order to provide an empirical proof to the two hypotheses put forward in Section 4.1, another model of Sh_rs occurrence (Fig. 4.12d) was derived by creating maps of EBFs of classes of distances to all faults/fractures and integrating those maps with maps of EBFs of slope aspects and those of slope inclinations. The model derived by using only sets of faults/fractures that are spatially associated with Sh_rs (hereafter called Model-1; Fig. 4.12c) and the model derived by using all faults/fractures (hereafter called Model-2; Fig. 4.12d) are strongly similar, except that the latter does not show sharp contrast between values of *Dis* east and west of the major southerly-plunging ridge and it does not reflect the strong influence of NNE-trending faults/fractures in the northwestern parts of the area.

To examine further the differences between the two models, the cross-validation technique proposed by Chung and Fabbri (1999) was applied. By using cumulative decreasing values of integrated *Bel* of each model, the cumulative increasing proportions of rockslide-prone areas were defined, from which the cumulative increasing proportions of training Sh_rs, testing Sh_rs and Dp_rs were determined (Fig. 4.13). Proportions of training Sh_rs and testing Sh_rs are also known as success- and prediction-rates, respectively. In addition, the average of each EBF in cumulative increasing proportions of rockslide-prone areas was also determined.

The graphs in Fig. 4.13 show that Model-1 has a prediction-rate curve that fluctuates below and above but closely follows its success-rate curve, whereas Model-2 has a prediction-rate curve that is mainly below its success-rate curve (Fig. 4.13). This means that the testing Sh_rs occurrences have a better spatial association with Model-1 than with Model-2. However, the graphs in Fig. 4.13 show that, in the whole study area, Model-1 has higher *Dis* than Model-2. This implies that (a) mutual fault/fracture and slope controls are alone inadequate to influence Sh_rs occurrence in every portion of the area and (b) any of the other sets of faults/fractures that were not used in Model-1 possibly interacts with certain slopes to influence Sh_rs occurrence albeit at local places within the study area. Nevertheless, the graphs in Fig. 4.13 show that, in the 40% most Sh_rs-prone portions of the area, Model-1 is superior to Model-2 because it has (a) higher success-rates (with maximum difference of 7% success-rate within the 25% most Sh_rs-prone portions of the area), (b) higher prediction-rates (with the maximum difference of the 16% prediction-rate within the 20% most Sh_rs-prone portions of the area), (c) higher *Bel* for Sh_rs, and (d) lower *Unc* for Sh_rs. Thus, the graphs in Fig. 4.13 support the two hypotheses that were put forward in Section 4.1.

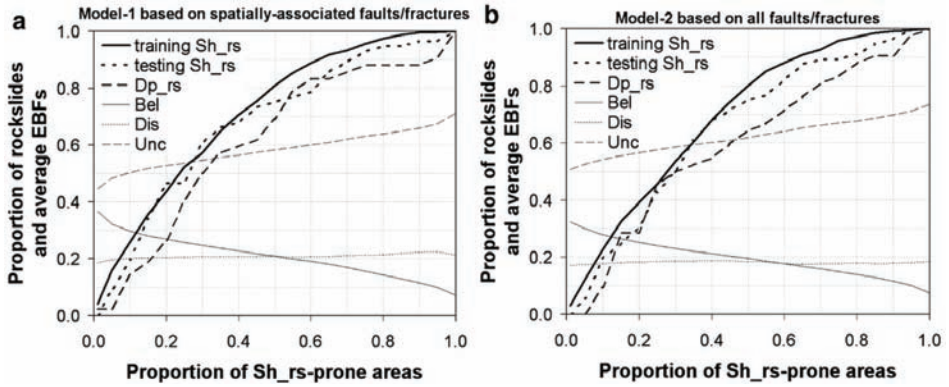

Fig. 4.13 Goodness-of-fit of models of Sh_rs occurrence with training and testing subsets of Sh_rs and with Dp_rs. a) Model-1 derived by using slope aspects, slope inclinations and sets of faults/fractures having positive spatial associations with Sh_rs occurrences (Fig. 4.14c). b) Model-2 derived by using slope aspects, slope inclinations and all faults/fractures (Fig. 4.14d).

4.6 Discussion

In spite of the slope failure criteria based on orientations of geological structures and topographic slopes (Goodman and Bray, 1976), many previous works on mapping landslide susceptibility in the Darjeeling district (e.g., Kanungo et al., 2006; Gupta et al., 2008) and elsewhere (e.g., Saha et al., 2002; Champati ray et al., 2007; Sharma and Kumar, 2008; Mathew et

al., 2009) simply considered proximity to geological lineaments as a spatial factor of landslide susceptibility without regard to types and orientations of lineaments.

In this study, the two hypotheses that were put forward in Section 4.1 are supported by the results of cross-validation of the model derived by using only sets of faults/fractures that are associated spatially with rockslides and the model derived by using all faults/fractures (section 4.5.2.1; Figs. 4.12c-d and 4.13). Thus, (1) using proximity to faults/fractures of certain trends, compared to using proximity to all faults/fractures, yields a better predictive map of rockslide susceptibility, and (2) analyses of the spatial pattern of certain types of slope failures and their spatial association with certain types and trends of geological structures allow the determination of which sets of structures likely control rocksliding.

Applications of spatial analytical techniques to select sets of geological lineaments, based on the trends that are individually good spatial evidence of slope failure at regional-scales, have not yet been reported in the literature. The criterion for good spatial evidence of slope failure is essentially based on positive spatial association (or correlation) between certain geological lineaments and slope failures. Recently, Antinao and Gosse (2009) showed that spatial correlation between rockslides and geological structures can be determined by comparing a variogram of rockslide density with a variogram of geological structure density. However, creating a map of object density is sensitive to the choice of unit area.

In this study, the methods applied do not require a choice of unit area – Fry analysis (Fry, 1979) and distance distribution analysis (Berman, 1986) – in order to select sets of faults/fractures, based on the trends that plausibly control rocksliding. These methods have not been used yet in studies of landslide controls, but they have been employed in studies of mineralization controls. Fry analysis has been applied to deduce trends of structures controlling mineralization (Vearncombe and Vearncombe, 1999; Carranza, 2008; Carranza, 2009) and geothermal fields (Carranza et al., 2008a). Distance distribution analysis has been applied to quantify spatial associations between mineral deposits and geological features (Bonham-Carter, 1985; Carranza and Hale, 2003; Carranza et al., 2008b). As shown in this study, as well as in Carranza et al. (2008b; 2009), Fry analysis and distance distribution analysis may show more-or-less inconsistent trends of possibly controlling structures as described in Sections 4.3.3 and 4.4.2. That is because Fry analysis is a technique to determine trends in a set of point objects, whereas distance distribution analysis is a technique to analyze

spatial association between a set of point objects and a set of linear objects. However, with the aid of proportion analysis of spatial association between rockslides and slope aspects (Fig. 4.7), consistency between Fry analyses and distance distribution analyses can be synthesized into coherent interpretations about which set of faults/fractures and which classes of slope aspects are likely involved in mutual fault/fracture and slope controls on rockslide (Table 4.4).

The spatial analyses of subsets of rockslides in various parts of the study area, with respect to the MCT, imply that only certain sets of faults/fractures are likely involved in mutual fault/fracture and slope controls on rockslide in certain parts of the area. This finding conforms to knowledge that (a) major tectonic structures likely act as regional-scale tectonic control on geomorphic processes in a study area (Banerji et al., 1980; Acharya, 1989), (b) local stress fields vary with respect to major tectonic structures (Pandey et al., 1999; Singh and Thakur, 2001; Joshi and Hayashi, 2008), and (c) mechanisms for slope deformation can vary with variations in the distributions of stress (Di Luzio et al., 2004; Kinakin and Stead, 2005; Cadoppi et al., 2007). Therefore, variations in spatial distribution of geological structures certainly influence variations in spatial pattern of rockslides (Roering et al., 2005). Accordingly, based on the spatial analyses, the area can be divided into three domains for predictive mapping of rockslide susceptibility.

In predictive mapping of rockslide susceptibility, EBFs were applied (Dempster, 1967; 1968; Shafer, 1976) to create layers of spatial evidence of rockslide occurrence. EBFs have not yet been used in regional-scale predictive mapping of landslide susceptibility, but they have been used in predictive mapping of susceptibility to distal lahar-inundation (Carranza and Castro, 2006). In this study it was shown that, by using EBFs, a layer of evidence can be created for faults/fractures even although they are associated spatially with rockslides in only certain domains but not in every domain. This is achieved by estimating EBFs of proximity to faults/fractures in domains where they are associated spatially with rockslides and by assigning EBFs of proximity to faults/fractures only to uncertainty in domains where they are not associated spatially with rockslides. Thus, by applying EBFs, it is feasible to simultaneously derive an integrated model of mutual fault/fracture and slope controls on rockslide for all domains. This can also be achieved by application of weights-of-evidence whereby faults/fractures are considered as missing evidence in domains where they are not associated spatially with rockslides (Bonham-Carter et al., 1989; Carranza, 2004). However, in this study EBFs were applied instead of weights-of-evidence

because the latter is hampered by conditional dependence among evidence whereas EBFs are not (Walley, 1987) and in this study the objective was to model conditionally dependent or mutual fault/fracture and slope controls on rockslide.

In general, slope failure occurs when the shear stress acting on that slope exceeds the shear strength of the materials on that slope. Faults/fractures and slopes are only among the various factors that could contribute to both increase in shear stress acting on slopes and decrease of shear strength of slope materials. As the spatial analyses suggest, structures other than faults/fractures are likely involved in mutual fault/fracture and slope controls on rockslide in certain parts of the area. Therefore, the model of mutual fault/fracture and slope controls on rockslide for shallow translational rockslide (Fig. 4.12c) only represents one plausible multivariate factor of slope failure. It can be used further, however, as an input map in probabilistic predictive mapping of susceptibility to shallow translational rockslide occurrence.

4.7 Conclusions

Fry analysis, distance distribution analysis and proportion analysis are complementary and supplementary exploratory methods that can be used in conjunction with one another in order to determine mutual fault/fracture and slope controls on rockslide. Results of applications of these spatial analytical techniques suggest that, in different parts of the study area, rocksliding is controlled mutually by certain sets of faults/fractures and certain slope aspects. Application of the Dempster–Shafer theory of belief is satisfactory for creating a layer of spatial evidence for every set of faults/fractures in the study area even although such a set is only likely involved in mutual fault/fracture and slope controls on rockslide for deep-seated rockslide occurrence in some, but not in all, parts of the area. However, it is trivial to create and integrate spatial evidence layers for sets of faults/fractures that are not spatially associated with rockslides anywhere in the study area. A model of mutual fault/fracture and slope controls on rockslide is not a final multivariate factor of slope failure but it can be used as an input in probabilistic predictive modelling of slope failure susceptibility.

The weakness of the model of mutual fault/fracture and slope controls on rockslide relates to lack of dip data for faults/fractures. Considering mainly the poor accessibility of the rugged terrains in the area, obtaining thorough and spatially distributed dip data for regional faults/fractures is a non-trivial task. When such data become available, the model of mutual fault/fracture and slope controls on rockslide obtained in this study must be updated and

revised accordingly. In that case, proper methods for the interpolation of 3D structural orientation data (De Kemp, 1998; Günther, 2003) must be used to create 2D maps of structural orientations (i.e., trends and dips) for deterministic spatial analysis of mutual structural and slope controls on slope failure. A similar study taken up in this research is described in detail in the next chapter (chapter 5) where rock slope failure modes (e.g., planar, wedge, topple) are modelled using spatially distributed rock discontinuity orientation data. Therefore, if strike/dip data for faults/fractures are available, it is more apt to perform similar kinematic analysis of slope failure (Gokceoglu et al., 2000; Jaboyedoff et al., 2004; Ghosh et al., 2010). Nevertheless, the analyses discussed in this chapter (chapter 4) are useful for first-pass regional-scale exploratory assessment of slope failure susceptibility.

Chapter 5: Rock slope instability analysis using structural orientations

One of the major factors governing the stability of rock slopes is the directional anisotropy of planar structural discontinuities (e.g., foliations, bedding plane and joints) in rocks (Romana, 1985; Selby, 1993; Orr, 1996; Hack et al., 2003; Sitar et al., 2005; Pantelidis, 2009) and their mutual kinematic relationships with topography. The presence of such structural discontinuities in rocks thus contributes to both an increase in shear stress acting on slopes and decrease of shear strength of slope materials. Therefore, to model rock slope instability in a GIS, spatial modelling of 3-D structural orientation data onto a 2-D continuous structural surface is necessary. This is not a trivial task because rock discontinuity orientation data are generally sparse over a large area due to poor exposure conditions and inaccessibility. This is especially true in a structurally-complex terrain like the Himalayas. This chapter is based on the publication "*Rock slope instability assessment using spatially distributed structural orientation data in Darjeeling Himalaya (India)*" (Ghosh et al., 2010), wherein methods for spatial modelling of different rock slope failure modes using spatially distributed rock discontinuity orientations, its shear strength parameters and topography data are examined and discussed.

5.1 Introduction

The geometrical relationships of structural discontinuities (e.g., bedding, foliation, joints etc.) in rocks with topographic slopes define different modes of rock slope failures (plane, wedge or topple) (Goodman and Bray, 1976; Hoek and Bray, 1981; Matheson, 1983; Cruden, 1989; Roy and Mandal, 2009). The mode of such discontinuity-controlled rock slope failure is also governed by the shear strength of structural discontinuities, which can be represented by their residual friction angles (Φ'_d). Data of Φ'_d may be derived through an empirical relationship with observed discontinuity-condition parameters available in the literature (Serafim and Pereira, 1983). Discontinuity-controlled rock slope instability occurs in either natural or man-made ('engineered') rock slopes. This study is mainly concerned with the spatial analysis of instability of natural rock slopes.

Despite applications of the principles of different rock slope failure modes to spatial analysis of rock slope instability at various mapping scales have been reported in the literature (e.g., Wagner et al., 1988; Anbalagan, 1992; Carrara, 1999; Gupta et al., 1999; Guzzetti et al., 1999; Jaboyedoff et al., 2004; Park et al., 2005), very few attempts actually exist to incorporate

spatially distributed data of structural discontinuity orientations in GIS-based rock slope instability assessment (e.g., Meentemeyer and Moody, 2000; Günther, 2003; Günther et al., 2004). That is because modelling of the spatial distribution of structural discontinuity orientations is complex and is not commonly realized in a 2-D GIS. Relative success has been achieved by using structural discontinuity orientation data in rock slope instability assessments at detailed to large scales (i.e., larger than 1:25,000) (Wagner et al., 1988; Günther et al., 2004; Günther and Thiel, 2009). However, using data of structural discontinuity orientations in rock slope instability assessment at medium to small scales (i.e., 1:25,000 or smaller) is even more challenging because such data are usually sparse due to, for example, poor rock exposures, thick vegetation and/or overburden cover and, inaccessibility of the terrain.

For application in spatial rock slope instability assessment, point observations of 3-D orientations of structural discontinuities in rocks must be regionalized (i.e., interpolated) into a continuous 2-D surface model of orientations of a certain type of geological structures. This surface model is here referred to as a Digital Structural Model (or, DStM). In structurally complex terrains, the accuracy of a DStM depends on observation scale, data density, distribution and availability of suitable structural constraints such as trace-lines of major faults and fold axes. However, structural orientation data cannot be interpolated directly to create a DStM. For example, interpolation of azimuth data points of 330º and 30º can erroneously result in values about 150º (Meentemeyer and Moody, 2000; Günther, 2003). De Kemp (1998; 1999) proposed a concept for interpolation of structural orientation data by decomposing the unit vectors into three linear cosine components that can be used for 3-D interpolation. Günther (2003) followed this approach for 2-D constrained interpolation of each of the three cosine components and then integrated the results in order to derive DStMs for azimuths and for dips of a certain type of geological structures. Nevertheless, in complex structural terrains like the Himalayas, irregularity and scarcity of spatially distributed structural orientation data as well as lack of structural constraints make DStM generation through conventional 2-D interpolation very problematic (Günther, 2003). In situations of data scarcity in large areas, deriving discrete directional information on individual rock discontinuity sets for suitable mapping units using vector statistical considerations (Wallbrecher, 1986; Swan and Sandilands, 1995) may be an alternative (Günther and Thiel, 2009).

In this study, application of suitable techniques for regionalization of point data of 3-D orientations of structural discontinuities in rocks in order to

create DStMs at two different spatial scales is discussed in detail. The DStMs are realized together with DEM-derived terrain properties in order to (a) assess rock slope instability, (b) test the kinematical possibility of different modes of rock slope failures and (c) interpret their respective causal failure mechanisms. This study also compares the modeled rock slope instabilities and their respective failure mechanisms with prevalent rock slope failures (both shallow and deep-seated) that were observed and mapped (Fig. 5.1) in the study area. These techniques were first applied to a small area (Area A in Fig. 5.2) with a relatively high density and quite good distribution of structural data observation points. Then, the same techniques were applied to a larger area (Area B in Fig. 5.2) with relatively scarce and poor distribution of structural data observation points. The results of application of the methods in both test areas were evaluated by quantifying the spatial association between the instability maps and the available rockslide occurrence maps.

5.2 Input data

5.2.1 Field-based 3-D orientation data of rock discontinuities

The dip (azimuth normal) directions and dip values of rock discontinuities that were used for this study were measured in the field at 315 accessible locations. These measurements are for 315 foliation/bedding (hereafter denoted as, Fol) planes and 514 joint surfaces (Fig. 5.2). Via cluster analysis, the joint orientation data were divided into four sets, namely J1 (southwesterly-dipping joints), J2 (southeasterly-dipping joints), J3 (northwesterly-dipping joints) and J4 (northeasterly-dipping joints). Thus, including Fol, five sets of data on structural discontinuity orientations were used in this study.

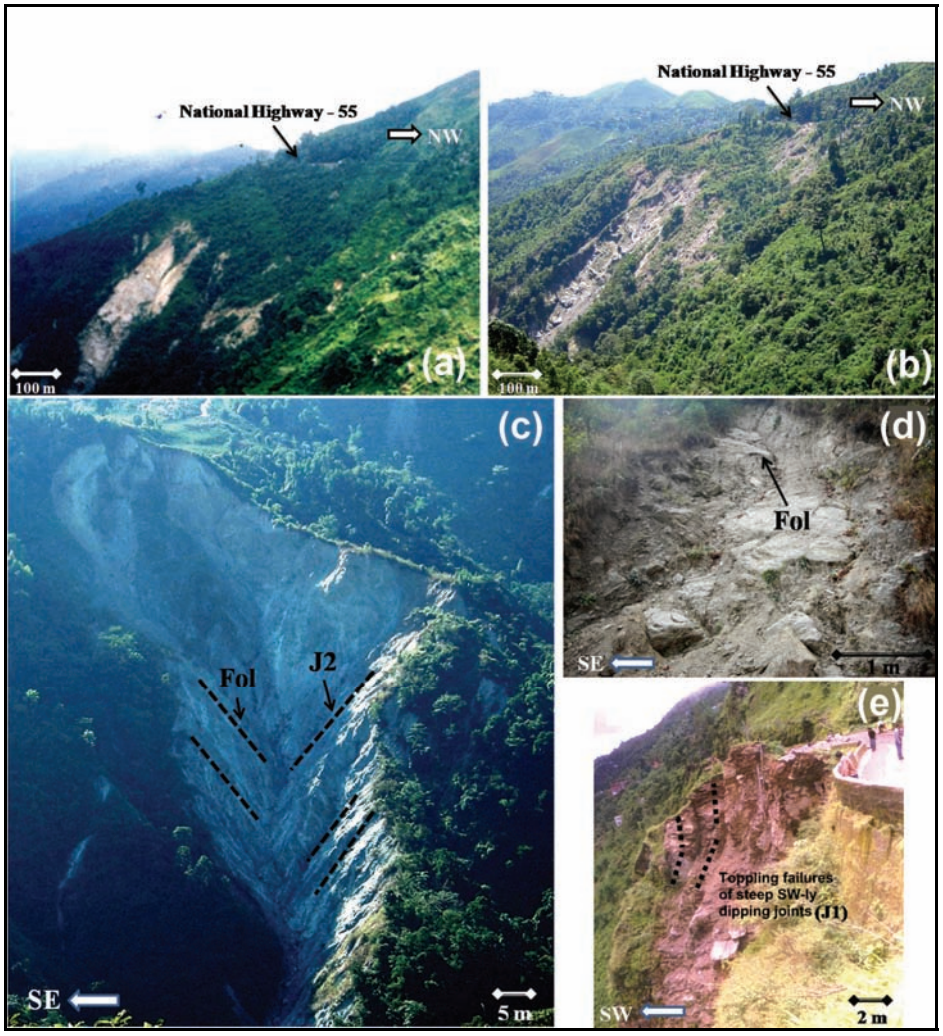

Fig. 5.1 Different rockslides in the study area that occurred between 1968 and 2007 (see Chapter 3 and Ghosh et al., 2009b). (a) and (b) Retrogression of a deep-seated rock wedge slide. Photo in (a) taken in 2001, and photo in (b) of the same rockslide was taken in 2008. (c) A deep-seated rock wedge (W_Fol_J2) within Daling metasediments. (d) Plane failure (P_Fol) along foliation surface (Fol) in sheared phyllonitic rocks. (e) Toppling (T_J1) caused by steeply-dipping southwest (SW)-dipping joints (J1) within quartzo-feldspathic gneiss.

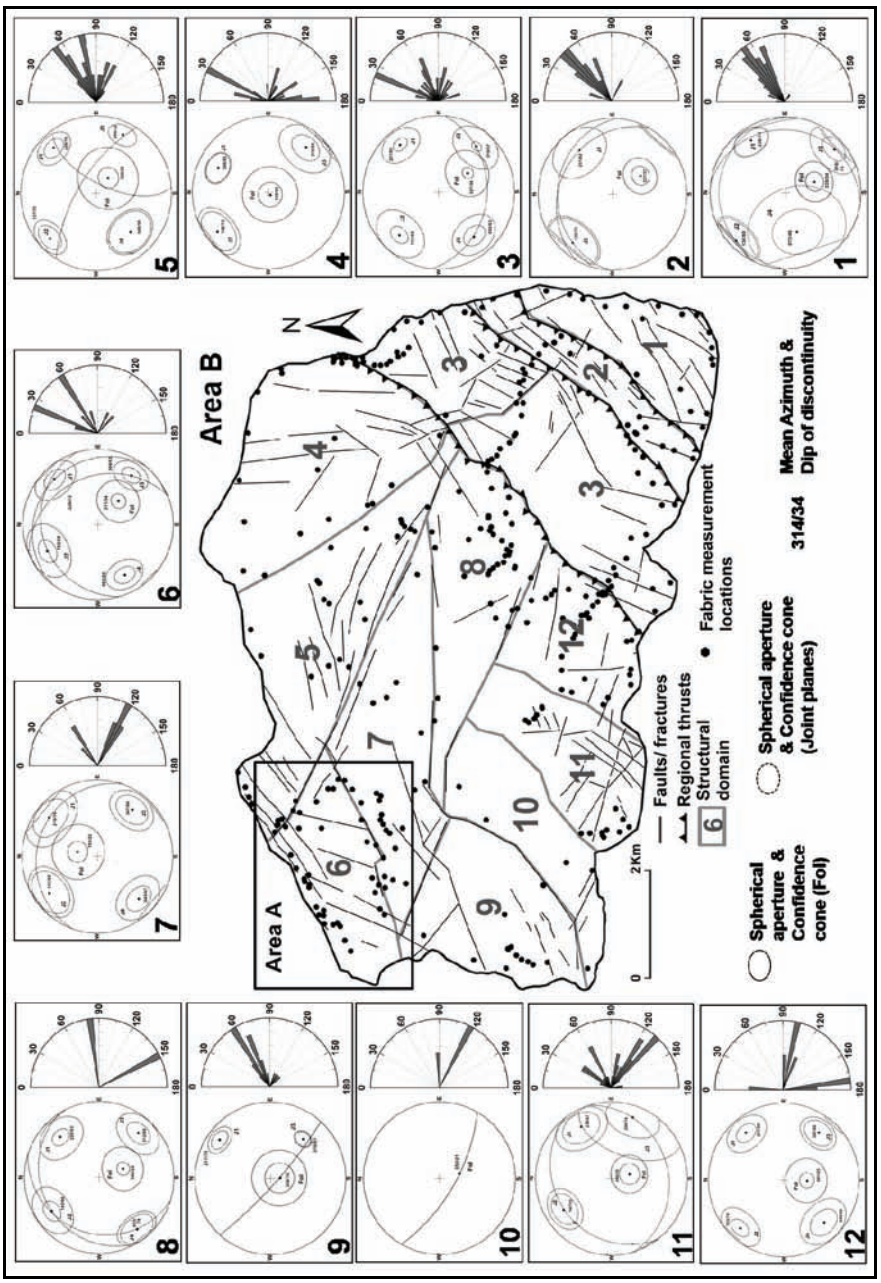

Fig. 5.2 Map of Area A and Area B showing locations of fabric (orientation) measurements, mapped thrusts/faults/fractures and boundaries of 12 interpreted structural domains. Also shown for individual domains are equal-area projection nets and uni-directional rose plots (5º-intervals of strike directions) of faults/fractures. For each domain, Table 5.4 for vector statistics (mean orientation, spherical aperture and confidence cone) of measured fabric orientations of each discontinuity set and Table 5.3 for strikes of the mapped faults/fractures.

In order to visualize the variability in structural discontinuity orientations, the poles-to-planes of each of the five structural orientation data sets were plotted in a synoptic fabric diagram (Fig. 5.3), which indicates respective mean vector discontinuity orientation in each data set together with the respective vector statistical parameters such as confidence cone, spherical aperture and eigenvectors (Wallbrecher, 1986).

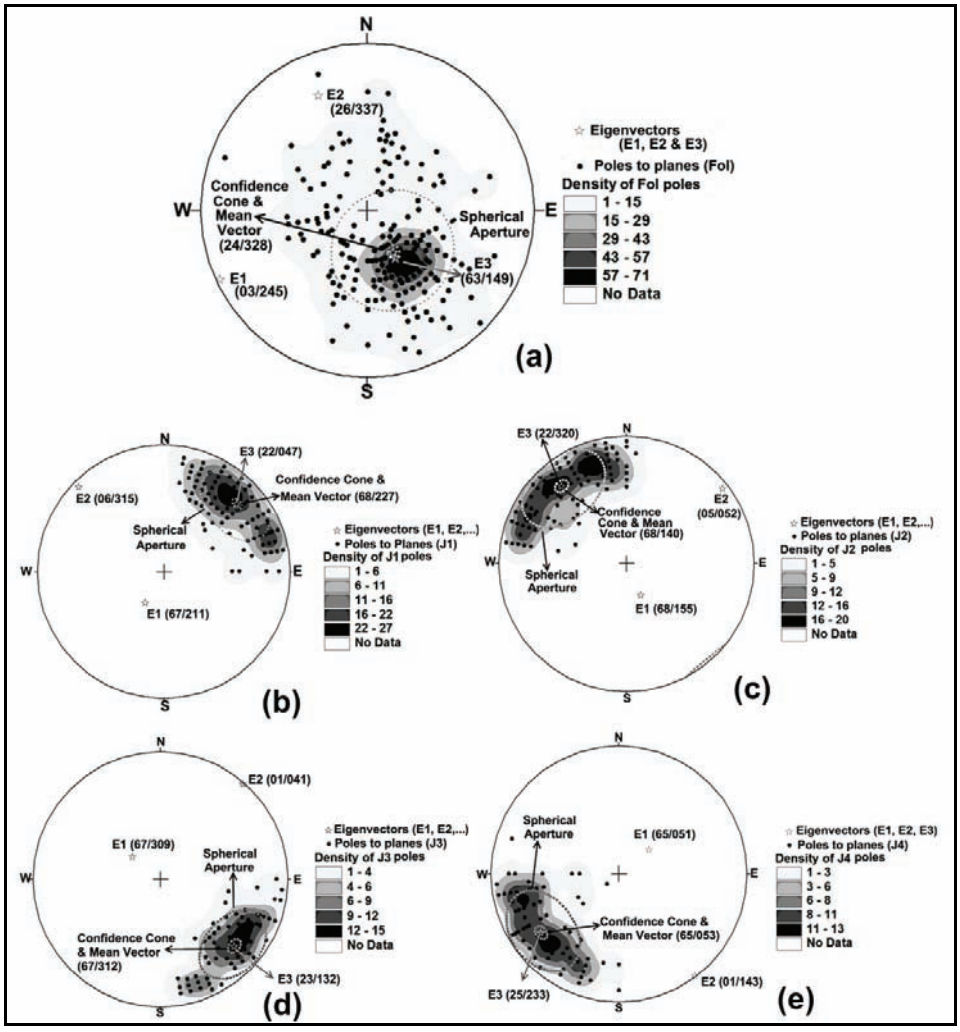

Fig. 5.3 Synoptic fabric plots of poles to five measured discontinuity planes in an equal area projection (Schmidt's projection, lower hemisphere) along with the plot of mean vectors, confidential cones and spherical apertures and eigenvectors for (a) foliation plane (Fol), (b) joint set J1, (c) joint set J2, (d) joint set J3 and (e) joint set J4.

Each of the structural discontinuity orientation data set shows a high degree of conformity of measurements (75-87%), very small confidential cones (3–4º), and reasonable spherical apertures (21–30º). The azimuth/dip orientation of mean vectors of Fol, J1, J2, J3 and J4 data sets are 328º/24º, 227º/68º, 140º/68º, 312º/67º and 053º/65º, respectively (Table 5.1, Fig. 5.3). At some of the 315 accessible locations, the presence of major thrusts and faults that have been compiled from old geological maps (Mallet, 1875; Acharya and Ray, 1977) and some of the linear structural features that have been interpreted from stereo-pairs of 1:10,000 scale aerial photographs (Fig. 5.2) were confirmed during field studies. The confirmed mapped traces of major thrusts/faults/fractures were then used as primary structural constraints for generating DStMs of structural orientation data for each set of structural discontinuities.

Table 5.1 Vector statistics of measured discontinuity orientations (in the entire study area – Area B).

Discont. set	Data (Nr)	Mean orientation (azimuth/dip)	Conf. cone	Spherical aperture	Eigenvectors (azimuth/dip)			Degree of Conform.	*K value of Woodcock, 1977*
					E1	E2	E3		
Fol	315	328°/24°	3°	30°	245°/03°	337°/26°	149°/63°	74.52%	0.27
J1	166	227°/68°	3°	22°	211°/67°	315°/06°	047°/22°	86.06%	0.56
J2	158	140°/68°	4°	25°	155°/68°	052°/05°	320°/22°	82.52%	0.79
J3	92	312°/67°	4°	21°	309°/67°	041°/01°	132°/23°	86.8%	0.84
J4	98	053°/65°	4°	24°	051°/65°	143°/01°	233°/25°	83.57%	0.56

5.2.2 Spatially distributed shear strength (Φ'_d) parameters

Following the guidelines of Bieniawski (1989) for rock mass rating (RMR) classification, data for joint condition parameters (i.e., spacing, length/persistence, infilling, roughness, separation and weathering condition) were collected at 240 of the 315 accessible locations in the field. In general, it has been observed that the joints have average spacing of <40 cm, persistency of up to 1-3 m or more and are smooth to rough planar. The walls of the observed joints vary from un-weathered to weathered and generally do not exhibit perceptible separation. Minor infilling (<1 mm) of crushed silty materials are present in slightly open joint walls. In all the four joint sets (J1, J2, J3 and J4), no significant variations in joint-condition properties were observed. Using the measured joint condition parameters, the values of Φ'_d at each of the 240 locations were empirically estimated according to the empirical relation of Serafim and Pereira (1983) are empirically estimated. The empirically-derived values of Φ'_d vary between 22º and 36º. After performing spatial autocorrelation analysis on the empirically derived Φ'_d values, inverse distance weighting (IDW) interpolation with a power of 2 and a minimum of 15 data points within a

search radius of 5 km was applied. During training of interpolation, a jack-knife (or omit one data point) approach was followed in order to derive the best-fit surface model of Φ'_d (i.e., interpolation was performed 240 times, each time with 239 data points and each surface model was cross-validated with the respective single data point omitted in the analysis). The best obtained surface model of empirically-derived values of Φ'_d (Fig. 5.4) has a root mean square error of 4 for interpolation data points and a squared difference of 0 for all the cross-validation data points. This best surface model of empirically-derived values of Φ'_d (Fig. 5.4) was used as a spatially distributed shearing strength parameter of discontinuity, instead of using a single arbitrary global value of Φ'_d as proposed by Aksoy and Ercanoglu (2007), in testing the kinematical possibility of specific modes of rock slope failures in the test areas.

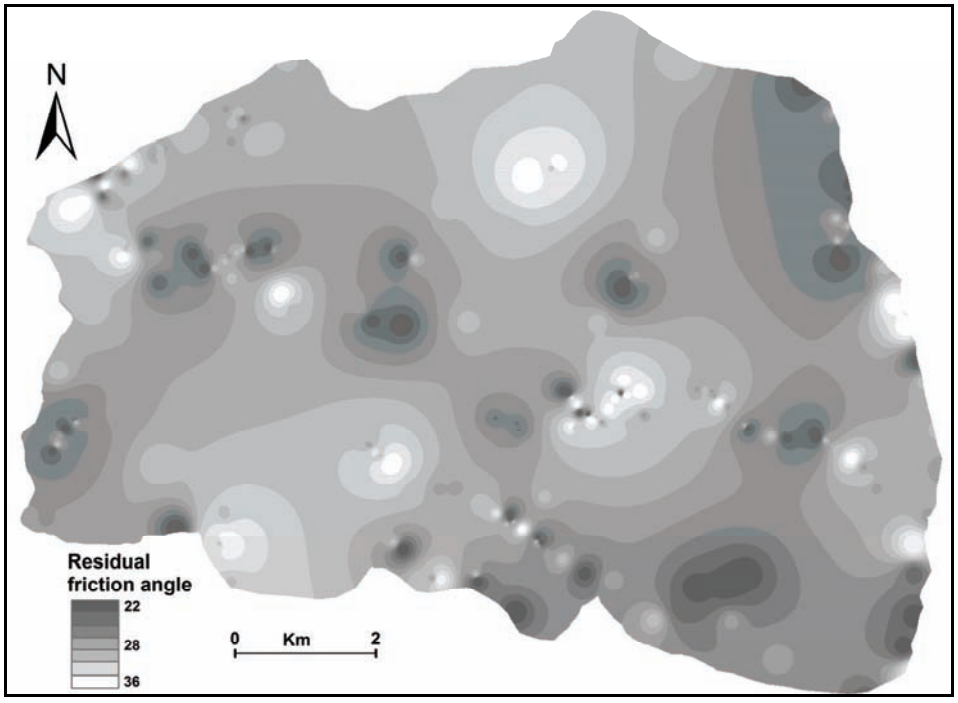

Fig. 5.4 Map of interpolated residual friction angles (Φ'_d) of structural discontinuities.

5.2.3 Digital topographic data

For topographic data, the 10 m × 10 m pixel resolution 'CartoDEM' that was prepared through photogrammetric techniques (in the LPS suite of ERDAS Imagine 9.2) using stereo-images of 2.5 m resolution IRS P5 Cartosat-1 satellite data of 2006 has been used. In order to generate a high-precision

CartoDEM, the stereo Cartosat images were otho-rectified by using 16 ground control points (GCPs) measured through differential GPS in the field. For geo-referencing, the WGS 84 as datum was used and the ortho-rectified maps were projected using UTM (Zone 45N) projection parameters. From the CartoDEM, raster maps of slope and aspect were derived using ArcGIS 9.3. These maps were used as topographic inputs for both test areas (Area A and Area B; Fig. 5.2).

5.3 Spatial modelling of structural discontinuity orientations

Considering the differences in density and distribution of structural discontinuity orientation data and the differences in amount of structural constraints in areas A and B (Fig. 5.2), different regionalization techniques in order to create DStMs for the two areas were employed. In Area A, where point data of structural discontinuity orientations are quite dense and well-distributed, regionalization of such data involved interpolation. In contrast, in Area B (i.e., the whole study area), where point data of structural discontinuity orientations are quite sparse and poorly-distributed, regionalization of such data involved generalization.

5.3.1 DStM generation in Area A

For Area A, the technique proposed by Günther (2003) was followed to interpolate 3-D orientation or fabric measurements for individual types (or sets) of structural discontinues in rocks at every observation point. The interpolation process (Günther, 2003) involved (a) decomposition of orientation data (i.e., unit vectors having only directions) into three linear cosine components (cos(α), cos(β) and cos(χ); see De Kemp (1998) for details) followed by separate interpolation of each cosine component and (b) conversion of the interpolated linear cosine components into rasters (i.e., DStMs) of azimuth and dip. Mapped structural constraints (major faults/thrusts) were incorporated as barriers (i.e., linear features known to interrupt the resulting surface geometry) into the interpolation process. The IDW interpolation was used because it does not produce pixel values out of the input data range, which is important for the interpolation of unit vector components since values of either cos(α) or cos(β) must be in the [-1,+1] range and values of cos(χ) must be in the [0,1] range. In IDW interpolation a power of 2 was used so as to give stronger weights to pixels of and close to the original input data than pixels farther away and a jack-knife approach was followed to derive the best-fit DStMs of azimuth and dip for each set of structural discontinuities in rocks.

Fig. 5.5 shows the DStMs for azimuth and dip of FoI, whereas Table 5.2 shows the vector statistics of measured orientation data and the interpolated values in DStMs. The averages of interpolated FoI orientations are closely similar to the averages of measured FoI orientations (Table 5.2). Both poles-to-planes projections of measured and interpolated FoI orientations are aligned to steep great circles with π-poles of 250º/17º and 243º/13º, respectively (Fig. 5.5b). The fabric shape of the original FoI data is closely resembled by the DStMs of FoI, as indicated by their nearly identical spherical apertures, great circle alignments and near-similar eigenvector orientations and magnitudes (Fig. 5.5, Table 5.2). In the raster maps of interpolated FoI orientations (Figs. 5.5c and 5.5d), abrupt changes of FoI orientations at the breaklines seem to be artifacts but they actually represent near-real ground situations. In the interpolation process, the breaklines acted as interpolation 'barriers' so that fabric orientations are offset along the thrusts/faults (e.g., the nearly E-W trending fault passing through a valley in Figure 5.5), which has also been observed during fieldwork. The same technique was applied to the orientation data of each of the four joint sets, J1 to J4. For each of the joint sets, the means of interpolated values in the DStMs are much more closely similar to the means of the measured data, as indicated by the smaller spherical apertures and fabric shape eccentricities derived from the eigenvectors (Table 5.2). In general, a good fit of vectorial orientation between the measured data and the interpolated values is observed for all the five structural discontinuity sets.

Table 5.2 Vector statistics of measured discontinuity orientations and interpolated discontinuity orientations in DStMs.

Discontinuity set	Data (Nr)	Mean orientation (azimuth/dip)	Conf. cone	Spherical aperture	Eigenvectors (azimuth/dip)			Great circle align.	Small circle align.
					E1	E2	E3		
FoI (Measured)	63	291°/22°	8°	34°	250°/17°	346°/18°	120°/64°	54%	-
FoI (Interpolated)	90349	295°/20°	0°	32°	243°/13°	338°/22°	125°/64°	77%	-
J1 (Measured)	30	225°/71°	7°	22°	207°/70°	313°/05°	045°/19°	47%	17%
J1 (Interpolated)	86618	220°/67°	0°	14°	257°/62°	136°/15°	040°/23°	14%	50%
J2 (Measured)	35	146°/66°	8°	27°	158°/66°	058°/04°	326°/24°	42%	27%
J2 (Interpolated)	86620	148°/67°	0°	14°	181°/63°	064°/13°	328°/23°	14%	50%
J3 (Measured)	14	313°/66°	11°	22°	328°/65°	226°/06°	133°/25°	32%	30%
J3 (Interpolated)	89836	311°/68°	0°	16°	266°/60°	033°/19°	131°/22°	19%	40%
J4 (Measured)	28	057°/65°	8°	23°	054°/65°	147°/01°	238°/25°	44%	18%
J4 (Interpolated	75187	058°/66°	0°	13°	061°/66°	329°/01°	238°/24°	26%	25%

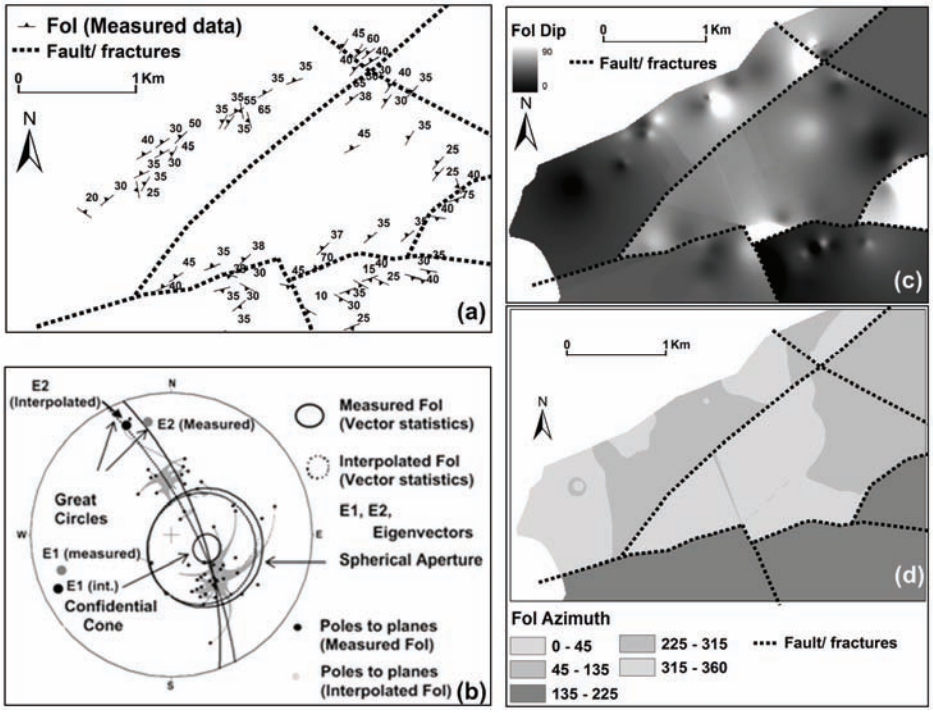

Fig. 5.5 Distribution of orientation data for foliation (FoI), their respective DStMs and equal area projection nets of measured data and interpolated values of FoI in Area A. (a) Locations of measured orientation data for foliation (FoI). (b) Plot of 'poles-to-plane' (showing spherical apertures, confidence cones, eigenvectors and great circles) of measured FoI orientations and their respective interpolated orientations in DStMs. (c) DStM of FoI dip. (d) DStM of FoI azimuth. Table 5.2 for vector statistics of measured and interpolated orientation data.

5.3.2 DStM generation in Area B

The whole study area (Area B) was subdivided into 12 structural domains in terms of presence of major thrusts/faults as natural structural boundaries, predominant strike (or azimuth) of faults/fractures and fracture density (Fig. 5.2). Where traces of the major thrusts/faults are not confirmed during fieldwork, the structural domains were demarcated based on changes in the dominant strike maxima of mapped fault/fracture systems and on differences in fracture densities (Fig. 5.2, Table 5.3). Spatial distribution of fracture density was modeled via interpolation of density of mapped traces of faults/fractures and thrusts considering 500 m as search radius. The purpose of subdividing the whole study area into structural domains was to create smaller structurally-unique areas of influence for regionalization of structural orientation data. Subsequently, in each structural domain, structural discontinuity orientations were regionalized by computing and using the mean integer values of measured orientations of each set of structural

discontinuities (Fol, J1, J2, J3 and J4) in order to create two raster grids (one for azimuth, one for dip).

Table 5.3 Attributes of photo-interpreted lineaments (faults/fractures) in individual structural domains (Fig. 5.2).

Domain	Nr. of lineaments	Strike maxima of lineaments	Lineament density (mean)	Principal basis for delineation of domain boundary
1	22	055°	2.74	Thrust boundary, lineament density
2	24	045°	3.78	Thrust boundary, lineament density
3	40	023°	2.28	Thrust boundary, strike maxima of lineaments, lineament density
4	19	024°	1.47	Strike maxima of lineaments, lineament density
5	21	055° and 080°	1.99	Strike maxima of lineaments, lineament density
6	18	023° and 055°	2.20	Strike maxima of lineaments, lineament density
7	22	115°	1.51	Strike maxima of lineaments, lineament density
8	11	085° and 155°	0.99	Fracture density, lineament density
9	19	057°	1.54	Strike maxima of lineaments, lineament density
10	9	120°	0.85	Strike maxima of lineaments, lineament density
11	29	135°	2.31	Strike maxima of lineaments, lineament density
12	12	100° and 170°	1.48	Thrust boundary, strike maxima of lineaments, lineament density

5.4 Kinematical testing of rock slope instability

5.4.1 Identification of modes of rock slope failure

By using the raster maps of DStMs, Φ'_d values, slopes and aspects, the kinematical possibility of a certain mode of discontinuity-controlled rock slope failure (plane, wedge and topple) can be tested for every pixel in the map (Günther, 2003). In principle, plane failure is kinematically possible if the dip of a controlling structural discontinuity is steeper than the residual friction angle of discontinuity (Φ'_d) and shallower than the apparent inclination of the slope with aspect the same as or similar to the dip direction of the structural discontinuity (Fig. 5.6a). Wedge failure is kinematically possible if the above condition for plane failure is met by the cutting line or wedge axis between two structural discontinuity surfaces (Fig. 5.6b). Plane topple is kinematically possible if a nearly vertical structural discontinuity strikes sub-parallel to a nearly vertical slope with aspect the same as or similar to the dip direction of the structural discontinuity (Fig. 5.6c). Wedge topple is kinematically possible if nearly vertical cutting lines or wedge axes between two structural discontinuity surfaces strike sub-parallel to a nearly vertical slope with aspect the same as or similar to the plunge direction of the cutting lines or wedge axes (Jaboyedoff et al., 2009). For any failure mode, the controlling structural discontinuity or cutting line(s) may either dip/plunge into the slope

with β≤90º (Goodman and Bray, 1976) or out of the slope with β >90º (Cruden, 1989), where β is the inclination of the discontinuity or cutting line measured from the dip direction of the slope normal.

Based on raster maps of DStMs, Φ'_d values, slopes and aspects, the foregoing criteria for kinematical possibility of certain modes of rock slope failure were evaluated in the SlopeMap module of the RSS-GIS software by applying the following conditions at every pixel in the maps:

$$\Phi'_d \le \beta \le \theta' \quad \text{(for plane and wedge sliding); and} \tag{5.1}$$

$$\theta' \ge (\Phi'_d + (90^\circ - \beta)) \quad \text{(for plane and wedge topple),} \tag{5.2}$$

Where θ' is the apparent dip/inclination of the topography with aspect the same as or similar to the dip direction of the controlling structural discontinuity or the plunge direction of the controlling cutting line(s). If any of the above relations is true for a pixel, SlopeMap after executing the above map calculation algorithms in ArcVIEW 3.x, returns a value of 1 for that pixel, meaning that a particular failure mode is kinematically possible; otherwise, SlopeMap returns a "null" value for that pixel, meaning that a particular failure mode is kinematically impossible (Günther, 2003). The returned values for every pixel where one or more failure modes are kinematically possible were then aggregated through linear map combination in a GIS so that rock slope instability according to one or more failure mode can be assessed for every pixel.

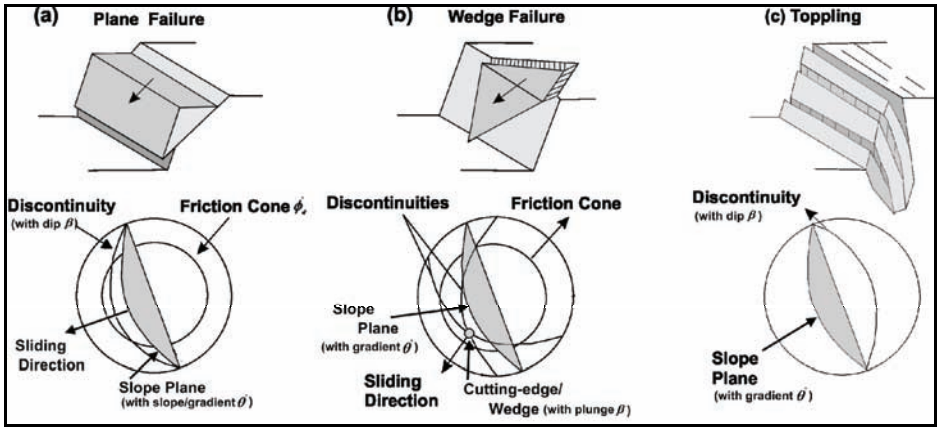

Fig. 5.6 Modes of different rock slope failures (after Goodman and Bray, 1976; Hoek and Bray, 1981).

5.4.2 Rock slope instability in Area A

The DStMs for each of the five sets of structural discontinuities and their 10 mutual cutting lines, the raster map of Φ'_d values, and raster maps of slope and aspect derived from the 10-m resolution CartoDEM were used to identify 10 m $\times$ 10 m pixels where certain modes of rock slope failures are kinematically possible. Theoretically, the five sets of structural discontinuities and their 10 cutting lines can result in 30 possible failure mechanisms, meaning failure modes due to one or more set of structural discontinuities. In Area A, the analysis resulted in 22 out of 30 possible failure mechanisms (Fig. 5.7), which includes all possible failure modes.

For possibility of plane failure mode, bedding plane/foliation (P_Fol) provides the highest contribution of 74% to rock slope instability, followed by joint set J3 (P_J3) with 22% contribution. Of the 10 possible wedge rock failures, prominent contributions to rock slope instability are due to failure mechanisms W_J1_J4 (40%), W_J2_J3 (29%) and W_Fol_J1 (19%). Only eight of 15 possible topple mechanisms (both plane and wedge topples) could possibly result in topple failures, and prominent contributions to rock slope instability are provided by plane topple mechanisms T_J2 (45%) and T_J3 (34%). Wedge topple mechanisms are comparatively less possible than the plane topples, because among the 10 possible wedge topple mechanisms, only four wedge topples involving the four joint sets are kinematically possible. Mostly cutting-lines between joints with steep plunges (i.e., >70º) contribute to wedge topples, which are relatively a rare possibility in the study area. Due to the kinematic possibility of multiple failure modes, some areas prone to rocksliding can have the possibility of multiple failure mechanisms and multiple failure modes.

Thus, the analysis was extended by presenting a map of failure mode count for every pixel in order to identify pixels where multiple failure modes and multiple failure mechanisms are kinematically possible (Fig. 5.7d). The result shown in Fig. 5.7d suggests that there is possibility for any mode of rock slope failure in 17% of Area A (1.5 km^2), in 70% of which there is possibility for at least one failure mode and in 30% of which there is possibility for multiple failure modes. In the 17% of Area A mapped as unstable slopes, wedge failure is kinematically possible in about 55% of those unstable slopes, topple failure is kinematically possible in about 37% of those unstable slopes and plane failure is kinematically possible in about 8% of those unstable slopes. For plane failure, none of the unstable pixels has more than one plane failure mechanism, but for wedge failure, about 10% of the unstable pixels have more one than one wedge failure mechanism. For topple failure, about

21% of the unstable pixels has more than one topple failure mechanisms. The above model results pertaining to the aerial contributions of different failure modes and their respective failure mechanisms in a tabular form can be perused in Annexure III (see the enclosed CD).

While validating the modelled results, it was observed that all the mapped prominent retrogressive deep-seated rockslides (Dp_rs) and 39 out of the 52 mapped shallow translational rockslides (Sh_rs) coincide with pixels modeled to be unstable for certain modes of rock slope failure (Fig. 5.7). The synoptic analysis of kinematical possibility for certain modes of rocks slope failure (Figure 5.7d) suggest that extensive portions of the terrain in Area A are possibly unstable although no rockslides have been mapped in those portions for the period 1968-2007. However, a large proportion of the areas of 'old and inactive' landslides of pre-1968 coincide with those possibly unstable slopes where no rockslides in the last four decades have been mapped.

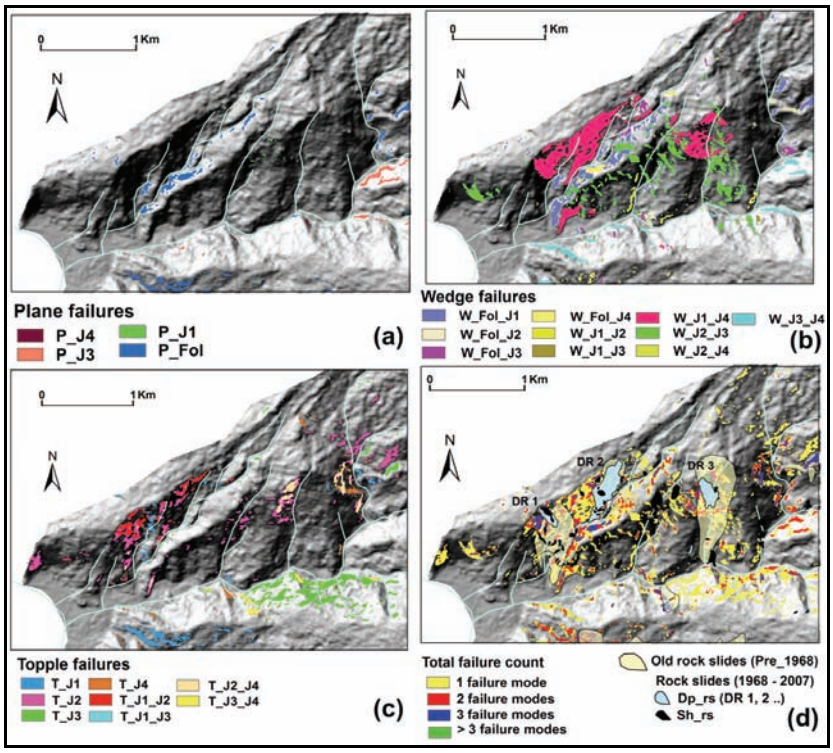

Fig. 5.7 Unstable slopes in Area A [based on CartoDEM of 2006, interpolated map of residual friction angles of discontinuities (Fig. 5.4), and DStMs of orientation data according to different failure modes and discontinuity-controlled failure mechanisms in Area A (see Annexure III). (a) Slopes where plane failure is kinematically possible. (b) Slopes where wedge failure is kinematically possible. (c) Slopes where topple failure is kinematically possible. (d) Slopes where at least one failure mode is kinematically possible.

5.4.3 Rock slope instability in Area B

The same procedure performed for the rock slope instability assessment in Area A was also performed in Area B to identify 10 m × 10 m pixels in the entire study area where certain modes of rock slope failures are kinematically possible and their respective discontinuity-controlled failure mechanisms. For Area B, the DStMs prepared for the structural domains, the raster map of Φ'_d values, and raster maps of slope and aspect derived from the 10-m resolution CartoDEM of 2006 were used. The results presented in Table 5.6 and Fig. 5.8 can be summarized as follows. There is possibility for any mode of rock slope failure in about 6.5% of Area B (5.9 km^2). In the 6.5% of Area B mapped as unstable slopes, wedge failure is kinematically possible in about 60% of those unstable slopes, topple failure is kinematically possible in 28% of those unstable slopes and plane failure is kinematically possible in 12% of those unstable slopes.

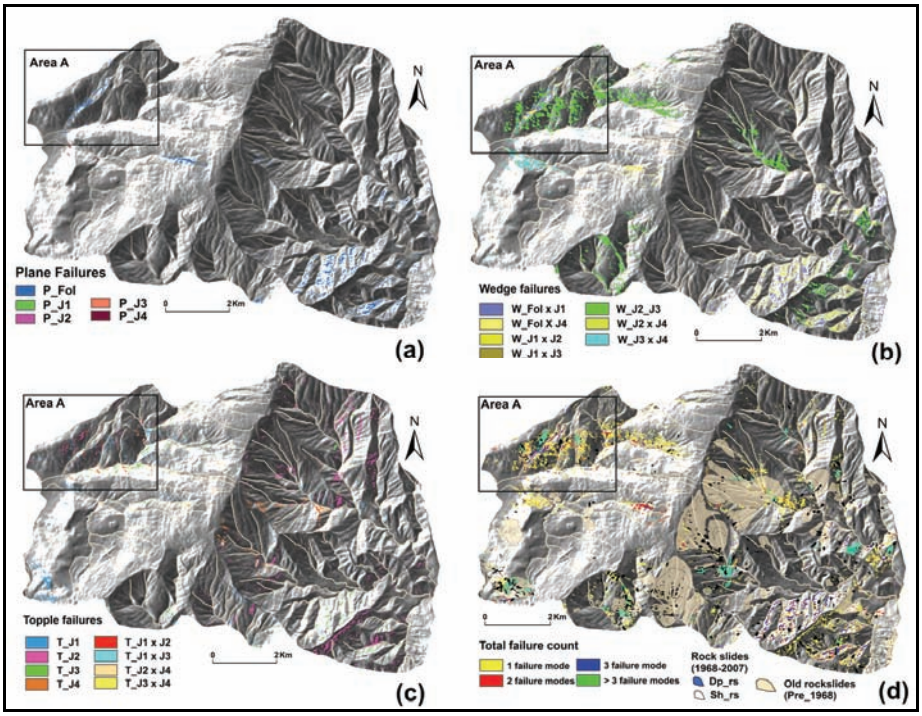

Fig. 5.8 Unstable slopes in Area B based on CartoDEM, interpolated map of residual friction angles of discontinuities (Figure 5.4), and DStMs of orientation data according to different failure modes and discontinuity-controlled failure mechanisms in Area B (see Annexure III for details). Maps showing kinematic possibility of (a) plane failures, (b) wedge failures, (c) topple failure, and (d) Slopes where at least one failure mode is kinematically possible.

For possibility of plane failure mode, failure mechanism P_Fol provides the highest contribution of about 96% to rock slope instability. Of the six identified possible wedge failure mechanisms, prominent contributions to rock slope instability are provided by failure mechanisms W_J2_J3 (52%), W_Fol_J1 (24%) and W_Fol_J4 (23%). Only eight of the 15 possible topple failure mechanisms could possibly result in topple failures, and the most prominent contribution to rock slope instability is provided by T_J2 (52%). Combining all failure modes together results in about 78% unstable slopes where only one failure mechanism is kinematically possible and in about 22% unstable slopes where more than one failure mechanisms are kinematically possible.

5.4.4 Evaluation of rock slope instability maps

The GIS-based methodology for rock slope instability assessment described in this Chapter follows deterministic approach to landslide susceptibility modelling, but it considers only the geometrical relationships between topographic slopes and structural discontinuities in rocks to assess binary kinematical possibility of certain modes of slope failures. The rock slope instability assessment maps, therefore, do not represent spatially-varying degrees of likelihood or probability of rockslide occurrence based on a set of known (training) occurrences of rockslides and various causal factors or explanatory variables of rockslides. In addition, according to the discussion in the first two paragraphs in the introduction section of this Chapter (Section 5.1) and according to the relationships of variables depicted in Eqs. 5.1 and 5.2, which form the bases of the kinematical testing of slope failure, each of the rock slope instability maps is actually a map of multivariate factors (or multi-evidence) contributing to both increase in shear stress acting on slopes and decrease of shear strength of slope materials. Because there are several other factors of rockslide occurrence (see next chapter), each of the rock slope instability maps derived from the study presented here is therefore, not a prediction (e.g., probabilistic) map of rockslide occurrence, although they can be used as inputs to predictive mapping of rockslide occurrence (see details in next chapter). Accordingly, the cross-validation method proposed by Chung and Fabbri (1999) using another set of known (testing) landslide occurrences is not suitable for evaluating the rock slope instability assessment maps. Thus, direct application of the area-based cross-validation method of Chung and Fabbri (1999), using both sets of Dp_rs and Sh_rs as testing rockslides, results in somewhat poor prediction rates of at most 46% in Area A and at most 33% in Area B. Proper evaluation of the slope instability models like those proposed in this study involves application of comprehensive spatial datasets containing information about slope instabilities locations of open cracks, release places, and actual failure

initiation locations, but not the entire landslide areas. Unfortunately, such required spatial datasets are currently unavailable.

An alternative way to test the efficacy of a rock slope instability factor (or evidence) map as a predictor of rockslide occurrence is to characterize and quantify the spatial association of that factor (or evidence) map with a rockslide occurrence map. A positive spatial association between a factor (or evidence) map and a landslide occurrence map implies that the factor map is a good predictor of the landslide occurrence map; otherwise, the factor map is a poor predictor of the landslide occurrence map.

Given that any of our rock slope instability maps (*f*) is binary and any of rockslide occurrence maps (*s*) is also binary, we can quantify the spatial correlation between *f* and *s* by calculating Yule's coefficient (Y_c) as follows (Fleiss, 1991; Bonham-Carter, 1994):

$$Y_c = \frac{\sqrt{M_{fs}/M_{\bar{f}s}} - \sqrt{M_{f\bar{s}}/M_{\bar{f}\bar{s}}}}{\sqrt{M_{fs}/M_{\bar{f}s}} + \sqrt{M_{f\bar{s}}/M_{\bar{f}\bar{s}}}} \tag{5.3}$$

where M_{fs} is area of 'positive match' where both factor and landslides are present, $M_{\bar{f}s}$ is area of 'mismatch' where factor is absent but landslides are present, $M_{f\bar{s}}$ is also area of 'mismatch' where factor is present but landslides are absent and $M_{\bar{f}\bar{s}}$ is area of 'negative match' where both factor and landslides are absent. The Y_c ranges in values between -1 and +1, just like the Pearson correlation coefficient. A negative Y_c means negative spatial association, whereas a positive Y_c means positive spatial association. Note that the value of Y_c is based on areal proportions, which are also the bases in spatial conditional probability calculations (Bonham-Carter, 1994). Therefore, in probabilistic terms, a positive Y_c implies that a factor of slope instability increases the likelihood of landslide occurrence, whereas a negative Y_c implies that a factor of slope instability decreases the likelihood of landslide occurrence.

The values of Y_c for each map of slope failure mode (Figs. 5.7a-c and 5.8a-c) calculated against the maps of Sh_rs and Dp_rs are given in Table 5.7. Following the *t*-test for significance of a correlation coefficient and based on *N* total number of pixels in each of the two test areas, the calculated values of Y_c in Table 5.4 are all significant at 99.9% level. In either Area A or Area B, unstable slopes for plane failure mode have mainly negative spatial associations with known rockslides, implying that, because Y_c is related to

conditional probability, occurrence of either Sh_rs or Dp_rs in identified unstable slopes for plane failure mode is unlikely. Likewise, in either Area A or Area B, unstable slopes for wedge and topple failure modes have positive spatial associations with either Sh_rs or Dp_rs, implying that, because Y_C is related to conditional probability, occurrence of either Sh_rs or Dp_rs in identified unstable slopes for either wedge or topple failure mode is likely. The results also show that unstable slopes have stronger spatial associations with Dp_rs than with Sh_rs, implying that the different sets of structural discontinuities provide stronger structural controls on Dp_rs occurrence than on Sh_rs occurrence. These evaluations of the results are consistent with our field observations of the rockslides in either Area A or Area B.

Table 5.4 Yule's coefficients of unstable slopes with known rockslides in Areas A and B.

Area	Unstable slopes	Sh_rs	Dp_rs
A	Plane failure slopes	-0.047	-0.114
	Wedge failure slopes	0.266	0.450
	Topple failure slopes	0.189	0.322
	All unstable slopes	0.215	0.387
B	Plane failure slopes	0.083	-0.122
	Wedge failure slopes	0.179	0.205
	Topple failure slopes	0.244	0.308
	All unstable slopes	0.216	0.258

5.5 Discussion

The ability of the techniques for spatial assessment of discontinuity-controlled rock slope instability discussed in this chapter to characterize the complexity of a structural setting at certain observation scales depend on density and spatial distribution of available point orientation data of structural discontinuities in rocks. Consequently, the quantity and quality of available point orientation data of structural discontinuities in rocks influence (a) the choice of approach to regionalization of those data into continuous DStMs (or digital structural models) and, consequently, (b) the accuracy of the DStMs. For rock slope instability assessment in small areas (e.g., Area A) where there might be high density and good spatial distribution of point orientation data of structural discontinuities in rocks, spatial interpolation is never completely devoid of any artifact or uncertainty. The DStM does not always replicate local structural variations due to incomplete data as a consequence of poor exposure conditions, thick vegetation and/or overburden cover and poor accessibility in rugged terrains. For rock slope instability assessment in large areas (e.g., Area B), where there might be low density and poor spatial distribution of point orientation data of structural discontinuities in rocks, subdividing the area into smaller structurally-unique domains according to certain structural criteria is intuitive. However, using the mean of point

orientation data of structural discontinuities in every structural domain in order to regionalize such data is an unavoidable oversimplification that could render the results to be meaningless. Nevertheless, if in Area B (or in similar large areas) there is high density and good spatial distribution of point orientation data of structural discontinuities in rocks, then delineation of structural domains must still be adopted but the point orientation data must be interpolated as in Area A. Alternatively, probabilistic assessment of discontinuity orientations may be derived from vector statistics of point orientation data, although the main drawback of this is still the validity of a-priori assumption of structural homogeneity. The techniques for creation of DStMs described in this study assume that, in every pixel, discontinuity orientation is invariant. This assumption explicitly oversimplifies our rock slope instability assessments whereas in natural conditions it can be observed that structural discontinuities often either disappear or change in orientation very rapidly. Accurate modelling of such natural conditions, on medium- to small scale however, might be extremely difficult to achieve especially in geo-environments like the Himalayan Fold-thrust belt, where rocks suffer multiple phases of both ductile and brittle deformations.

Regionalization by interpolation of empirically-derived shearing strengths of structural discontinuities (Günther and Thiel, 2009), determined on the basis of proxy joint-condition attributes, also incurs spatial uncertainties that could adversely affect results of rock slope instability assessments. An ideal approach is to obtain large number of in-situ or laboratory test data of shear strength of structural discontinuities at several representative locations in a study area. Obtaining such data for large areas, however, is too costly and extremely time-consuming and, thus, cannot be applied either for timely assessment of rock slope instability. Because carrying out comprehensive geotechnical testing of rock samples for a large study area is also beyond the scope of the present research, an interpolated map of proxy data for shearing strength of joints in rocks was thus, used. This, nonetheless, allowed to (a) perform rock slope instability assessments according to several possible rock slope failure mechanisms, (b) obtain spatially distributed patterns of kinematically possible discontinuity-controlled slope failure mechanisms in a large area and in a small area and (c) perform multi-temporal analysis of slope instability in a small area.

In both the two test areas (Area A and B), wedge failure is the predominant failure mode followed by toppling and then plane failure, which are consistent with field observations. For wedge failures in both test areas, failure mechanisms W_J2_J3, W_J1_J4 and W_Fol_J1 are the most prominent, which make sense because the respective cutting lines of those structural

discontinuities have shallow plunges and, thus, have the maximum possibility of being daylighted in moderate to steep slopes. Where the cutting lines of W_J2_J3, W_J1_J4 and W_Fol_J1 have plunges that are steeper than the residual friction angles, they increase the kinematical possibility of slope failure. According to Woodcock's (1977), a method of representing fabric shapes of structural orientation data is to plot the ratios of normalized eigenvalues (s_1, s_2 *and* s_3) of an orientation vector in a *log-log* paper. *K* is the ratio of $\ln(s_1/s_2)$ to $\ln(s_2/s_3)$ of such orientation vector that represents the gradient of the straight-line radiating from the origin of the *log-log* plot. If the *k*-value is less than 1, then it indicates oblate orientation tensors describing girdle distributions, whereas *k* values more than 1 represents clusters, which are obtained for all sets of model cutting lines except for Fol_J3 and Fol_J4 (k=1.8 and k=2.4 respectively, indicating clustered distributions). This suggests that most wedge failure mechanisms in the study area predicted by the proposed modelling approach produce wedges sliding in widely distributed directions, with the exception of the aforementioned failure mechanisms resulting in wedges mostly sliding to N (Fol_J3, azimuth 1°) and NNW (Fol_J4, azimuth 336°) directions. For topple failures in both test areas, it was found that kinematical possibility of topple failure is not due to shallow-dipping foliation planes alone but due to wedges formed by foliation planes and all sets of joint planes. This finding is realistic because topple failure is likely to occur only in the presence of steeply-dipping structural discontinuities and steeply-plunging cutting lines of at least two types of structural discontinuities (Goodman and Bray, 1976). Thus, in both test areas slope failure is kinematically possible due to steeply-dipping discontinuity surfaces such as J1, J2 and J3, and steeply-plunging cutting lines such as those of T_J1_J2. For plane failures, the failure mechanism involving foliation planes (P_Fol) are the most prominent, which makes sense because foliations in both two test areas are shallow-dipping and, thus, are likely to be daylighted. The realistic findings from the above analyses of kinematical possibility of slope failure indicate the efficacy of the techniques that were applied for slope instability assessments at two different spatial scales, which allow meaningful insights into different possible failure mechanisms that are involved in both shallow translational rockslides and deep-seated rockslides in the entire study area. For example, it seems that, in either of the two test areas, particular sets of structural discontinuities in rocks provide scale-invariant roles in slope instability. Thus, a quantitative assessment of the scale-invariant role of structural discontinuities in slope instability would be a motivation for future study.

Although, rockslides are complex phenomena, the present study considered only one vital factor of rock slope instability. This factor is the geometric

relationship between topography, residual friction angles and orientations of structural discontinuities. This consideration was motivated by the belief that many rockslides within the entire study area are discontinuity-controlled because the Himalayan Fold-thrust belt is a tectonically active area, although this motivation does not ignore the fact that many devastating landslide events within the entire study area were triggered by high amounts of rainfall. Therefore, an attempt can be made to develop scenario-based maps of slope instability by using some arbitrary uniform boundary conditions and assumptions of some global saturation conditions (see for details in Annexure III in the enclosed CD). It is acknowledged here that the scenario-based assessment of slope instability is hampered by the fact that a spatially distributed model of groundwater table response to recharge is not available. Therefore, it is acknowledged further that the global assumption of a highly pessimistic scenario (i.e., full saturation) is highly likely only in mostly southerly-facing slopes of the study area because these slopes mostly receive significant amounts of monsoon precipitation coming usually from the south. In addition, although it is plausible that some landslides events within the entire study area were earthquake-triggered, the lack of suitable source data precludes development of scenario-based maps based on a spatially distributed model of dynamic loading due to earthquake triggering. This could, nevertheless, be an important parameter for actual slope instability conditions in a tectonically active geo-environment like the Himalayan Fold-thrust belt. Thus, this could be another motivation for future research.

It is further important to state here that there could be other factors, which are influencing rockslides in the study area such as changing discontinuity conditions, weathering, local slope saturations, and permeability contrasts. Therefore, further investigation of rock mass and discontinuity properties, methods on their regionalization, and incorporation of such information into similar stability models will definitely improve the methods further. In addition, a quantitative multivariate assessment of structural evidence layers could also be an important issue for future research.

Finally, although the techniques applied in this study follow deterministic approaches to landslide susceptibility modelling, uncertainties in the input data (DEM derivates, structural models, discontinuity shear strengths) have not been considered and probabilistic analyses of slope instability have not been performed (e.g., Hack et al., 2003; Jaboyedoff et al., 2004; Park et al., 2005). Therefore, the slope instability maps (Figs. 5.7, and 5.8) only indicate binary kinematical possibility of rock slope failure(s). Incorporation of uncertainty analysis of both input data and output information as well as probabilistic analysis in a methodology for rock slope instability assessment

would, therefore, certainly be a major motivation for the physically-based rock slope failure modelling. Nevertheless, the evaluations of the slope instability maps (Figs. 5.7 and 5.8), which are actually maps of multivariate factors (or evidence) contributing to both increase in shear stress acting on slopes and decrease of shear strength of slope materials but they are not prediction maps of rockslide occurrence, consistently indicate that, in both test areas, structural discontinuities are more important controls on deep-seated rockslides than on shallow translational rockslides. These results are realistic and, therefore, suggest that the different techniques adapted in Area A and in Area B in order to assess discontinuity-controlled rock slope instability are non-trivial and could, therefore, be adapted in data-poor situations.

5.6 Conclusions

- Spatial assessment of rock slope instability relies heavily on density and spatial distribution of point orientation data of structural discontinuities in rocks.
    - o For small areas where there is usually high density and good spatial distribution of point orientation data of structural discontinuities, good digital structural models can be obtained via spatial interpolation with structural breaklines.
    - o For large areas where there is usually low density and poor spatial distribution of point orientation data of structural discontinuities, good digital structural models can be obtained by subdividing the area into structural domains according to meaningful structural criteria and by using the mean of point orientation data in every structural domain.

- An interpolated map of empirically-derived residual friction angles (Φ'_d) is a useful proxy for a spatially distributed map of shearing strengths of structural discontinuities, which is an important explanatory variable of rock slope instability.

- Within the entire study area
    - o individual sets of structural discontinuities (i.e., foliation planes and joint sets) in rocks seem to provide scale-invariant roles in rock slope instability,
    - o the predominant mode of slope failure is wedge failure, followed by topple failure and by plane failure,

  - structural discontinuities are more important controls on deep-seated rockslides than on shallow translational rockslides.

- The different techniques adapted in this study in order to assess discontinuity-controlled rock slope instability could be adopted and/or adapted in data-poor situations.

- The slope instability maps obtained in this study are actually maps of multivariate factors contributing to both increase in shear stress acting on slopes and decrease of shear strength of slope materials. They can be used as input maps in probabilistic predictive modelling of landslide susceptibility as shown in the next chapter (chapter 6).

Chapter 6: Selecting and weighting of spatial factors of landslide susceptibility

Susceptibility mapping to landslides of a certain type requires integration of only the appropriate spatial factors as input maps. Appropriate spatial factors can be selected by quantifying spatial associations of individual spatial factors with landslides of different types using various empirical spatial association analyses. In addition, susceptibility mapping to landslides is dependent on determination and use of weights of every spatial factor with respect to the other spatial factor in relation to the landslide types under study. Accordingly, this chapter describes "*Selecting and weighting spatial predictors for empirical modelling of landslide susceptibility in Darjeeling Himalayas (India)*" (Ghosh et al., 2011b), wherein a two-stage bivariate empirical analysis is proposed to quantify spatial associations of individual spatial factors with landsliding of a certain type in order to select the appropriate spatial factors (e.g., slope, aspect, geomorphology, lithology, etc.), which are then weighted by empirically determining the inter-predictor relationships via the analytical hierarchy process (AHP).

6.1 Introduction

Previous assessments of landslide susceptibility in the Himalayas were mainly based on mapping of morphodynamic processes and related landforms. Their main objective was to understand slope processes for estimating their threat to socio-economic resources (Kienholz et al., 1983; Peters and Mool, 1983; Vuichard, 1986; Zimmermann et al., 1986; Shroder, 1998). The potential sites of such slope instability in the Himalayas are mostly controlled by geomorphology, lithology and structure. With the advent of statistical/mathematical spatial data analysis using GIS, more recent studies of landslide hazards aim to incorporate the vast amount of empirical data obtained thus far in spatial prediction of landslide susceptibility (Gupta and Joshi, 1990; Pachauri et al., 1998; Gupta et al., 1999; Saha et al., 2002; Kanungo et al., 2006).

Predictive modelling of susceptibility to landsliding of type L (S_L) aims to make estimate at every location in a study area based on known landslide occurrences. The analysis thus assumes that spatial factors of past landslides are relevant to the occurrence of future landslides. Thus, S_L can be defined as a function of relevant spatial factors Xi ($i = 1, 2,\ldots,n$):

$$S_L = f(X_1,\ldots,X_n), \tag{6.1}$$

If a study area is partitioned into square unit cells (or pixels) for estimating local SL and Xi is categorized into classes C_{ji} (j = 1, 2,…,m), S_L can be defined as:

$$S_L = f(aC_{ji}, \ldots, aC_{mn}) \quad (6.2)$$

where for example, aC_{ji} represents predictor weights (i.e., degree of spatial associations) of C_{ji} attributes of Xi spatial factor (or map) with respect to the known occurrences of L-type landslides.

Published literature indicates that empirical analysis for predictive modelling of S_L can be achieved by either bivariate or multivariate analysis. Whereas spatial associations of known landslide occurrences with factors of landslide susceptibility and the inter-relationships among the factors are complex and likely non-linear, methods of bivariate analysis typically model those relationships as linear. In contrast, multivariate analysis, especially those with non-linear functions, are more often employed in predictive modelling of S_L for two main reasons. One is that multivariate analysis can model complex associations of spatial variables. The other is that multivariate analysis can simultaneously and automatically select predictors based on the spatial input data. However, some of the predictors selected may not represent genetic processes of landslides being studied (Baeza and Corominas, 2001; van Westen et al., 2008) because of purely statistical or mathematical assumptions used in the multivariate analysis (e.g., independence among predictors with respect to target variables).

There are two other likely reasons why methods of bivariate analysis are less often employed in predictive modelling of S_L. One is that the function f in bivariate analysis mainly describes spatial associations of individual Xi factor with known landslides but not the relative importance of each factor. The other is the lack of methodology to select predictors and simultaneously assign predictor weights.

The objective of this study was to propose a methodology involving bivariate analysis to select and weight predictors for predictive modelling of S_L. This methodology involves two stages: 1) quantifying spatial associations between individual spatial factors and landslides via bivariate analysis, and 2) using the quantified spatial associations in an analytical hierarchy process (AHP; (Saaty, 1977) to weight predictors. The proposed methodology is applied to the landslide-prone Darjeeling Himalayas (India) using the weighted multi-class index overlay in a GIS (Bonham-Carter, 1994), for medium- to regional-scale predictive modelling of S_L. We also showed that the predictors

selected and weighted via our proposed methodology are more realistic compared to predictors selected and weighted via a method of multivariate analysis (i.e., logistic regression).

6.2 Data

Shallow translational landslides are nearly planar failures in the upper few meters of slope materials (regolith including weathered bedrock and unconsolidated scree/colluvium). The failure plane usually corresponds to a pre-existing discontinuity within regolith or to the interface between regolith and bedrock (Fig. 3.2a-b). The frequency of such landslides is generally high in areas with high precipitation rates and/or storm frequencies (Zaruba and Mencl, 1969; Rogers and Selby, 1980), as in the study area (Starkel and Basu, 2000; Starkel, 2004). Shallow landslides occur when the shearing stress along the failure plane exceeds the shearing strength of rock/debris mass (Varnes, 1978). This can be affected by the physical state of slope such as slope gradient, shape, and aspect; orientation of planar/linear discontinuities in rock mass; lithology and degree of weathering; depth to failure surface; hydrology, and land use/cover. Based on this assumption, we included various factors for the GIS-based analysis of susceptibility to shallow landsliding (Table 6.1).

Raster maps of slope, aspect, elevation and curvature were prepared from a 10 m digital elevation model (DEM). This DEM was prepared photogrammetrically using the LPS suite of ERDAS Imagine 9·2 and stereo images of 2·5 m resolution from the IRS (Indian Remote Sensing) P5 Cartosat-1 satellite of 2006. The images were ortho-rectified using 16 ground control points (GCPs) measured with DGPS using the WGS 84 datum and the UTM-45N projection. The computed aspect values ranging from 0° to 359° were discretized into 12 classes using 30° intervals whereas; gradient/slope (^{o}) per each pixel was directly used as a continuous field data. The curvature values ranging from -23.87 to 25 were also discretized into 10 percentile intervals. Negative and positive curvature values represent concave and convex upward slopes, respectively.

Table 6.1 Data source, methods of preparation/mapping of spatial factors of shallow landslides. Sh_rs = shallow translational rockslides. Db_rs = shallow translational debris slides.

Generic factor theme	Specific factor	Source data, scale or spatial resolution and method of mapping of factor	Landslide type	
			Directly related	Indirectly related
Topography/ morphometry	Slope Aspect Curvature	DEM of 10 m × 10 m pixel resolution; automated mapping in GIS.	Sh_rs, Db_rs	-
Lithology or slope material	Rock and soil type	Field data, information from existing geological maps (1:10,000 -1:50,000 scales)	Sh_rs, Db_rs	-
Depth to bedrock	Soil/overburden thickness	Estimated using field data from 400 sites and linked to lithology map	Db_rs	-
Structure	Distance to major thrusts	Compiled from 1:50,000 and 1:25,000 geological maps; interpreted from high spatial resolution satellite imagery and stereo air-photos (1:50,000 and 1:10,000); ground-truthing in the field.	Sh_rs,	Db_rs
	Distance to faults/fractures	Interpreted from stereo-pairs of 1:10,000 and 50,000 B×W air-photos with limited ground-truthing in the field.	Sh_rs,	Db_rs
	Distance to kinematically unstable slopes	Determined using field data of rock discontinuity orientations and DEM-derived slope and aspect maps (Ghosh et al., in press)	Sh_rs,	Db_rs
Land-use/ land-cover	Land-use/ land-cover	Interpreted from 1:10,000 and 1:50,000 B×W air-photos and multispectral IRS LISS 4 MX imagery (5.8 m spatial resolution) with limited ground-truthing in the field.	Sh_rs, Db_rs	-
Old rockslides	Distance to old rockslides (pre-1968)	Mapped from stereo interpretation of 1:10,000 scale B×W stereo air-photos of 1980.	Sh_rs, Db_rs	-
Hydrology	Contributing area upslope	DEM of 10 m × 10 m pixel resolution	Sh_rs, Db_rs	-
	Wetness index	DEM of 10 m × 10 m pixel resolution		
	Drainage density	DEM of 10 m × 10 m pixel resolution; digitized streams from 1:25000 topographic maps.		
	Distance to streams	DEM of 10 m × 10 m pixel resolution; digitized streams from 1:25000 topographic maps.		

Despite limited access in the rugged terrain and limited rock exposures, site-specific data of slope materials at 315 locations were collected (Ghosh et al., 2010). Fieldwork was conducted from December to March in 2007, 2008 and 2009 to collect data on landslides including locations, extents, rock and soil types, rock discontinuity types and orientations, soil depth, and weathering degrees. Most visited sites were along roads and footpaths and are reasonably spread over the study area. Incorporating the above field data with the available information and geological maps (Banerji et al., 1980; Acharya, 1989; Searle and Szulc, 2005; Ghoshal et al., 2008), interpretative maps of lithology and soil/overburden thickness were prepared. The lithology map represents 13 different rock types and the soil/overburden thickness map has five classes (Figs. 6.1c & 6.1e). The distribution of soil/overburden thickness is controlled by topography and erosion processes. Therefore, it is related to slope morphometry (Dietrich et al., 1986; DeRose et al., 1991). Using landforms as proxies (e.g., Taylor and Eggleton, 2001), a subjective soil/overburden thickness map was first prepared, since those proxies can easily be mapped on 1:25,000 scales using remote sensing data. Then the base map was modified using thickness data obtained in the field.

The geomorphic features were mapped through visual interpretation of stereo pairs of high-resolution (2.5 m) Cartosat-1 images of Indian Remote Sensing (IRS) Satellite (P5), multispectral LISS 4 images of IRS P6 (5.8 m resolution) draped on the DEM, and stereo pairs of 1:50,000 and 1:10,000 panchromatic air-photos. The results were checked during field investigations. Thirteen different geomorphic landforms were mapped (Fig. 6.1f), which are linked to various geomorphic processes.

The steeply-dipping faults/fractures were also mapped through fieldwork and air-photo interpretation. The mapped faults/fractures were segregated into six 30°-interval classes of trends (NNE to NNW). It is likely that faults/fractures of different trends reflect local stress fields and have unequal controls on landslides (Ghosh and Carranza, 2010). Although the local-scale structural data such as slickensides, mylonitised and cataclastic zones etc., were collected in field, the effects of such structures on rocksliding in the Himalayas are too localized (Weidinger et al., 1996; 2006), for the mapping scale (1:25,000) in this study. Nevertheless, through a separate study, the discontinuity-controlled kinematically unstable slopes were modeled and mapped using deterministic testing of the geometrical relationships between topographic slopes and structural discontinuities in rocks (Ghosh et al., 2010), that were used as a spatial factor in this study.

Concerning hydrological parameters, the digitized perennial streams were classified using Strahler's (1957) ordering system. The 2nd to 4th order perennial streams (Fig. 6.2a) were only considered because field observations show that 1st order streams cause only limited erosion including shallow landslides. From the DEM, maps of upslope contributing area (Mark, 1988) and the wetness index (Beven and Kirby, 1979) were also derived (Fig. 6.2b-c). The study area was also subdivided into different sub-catchments by delineating ridge crests, boundaries of high order streams and spur axes using the DEM and adapting the semi-automatic method of Carrara et al. (1991) and then drainage density for each sub-catchment was calculated and used as another hydrologic spatial factor (Fig. 6.2d).

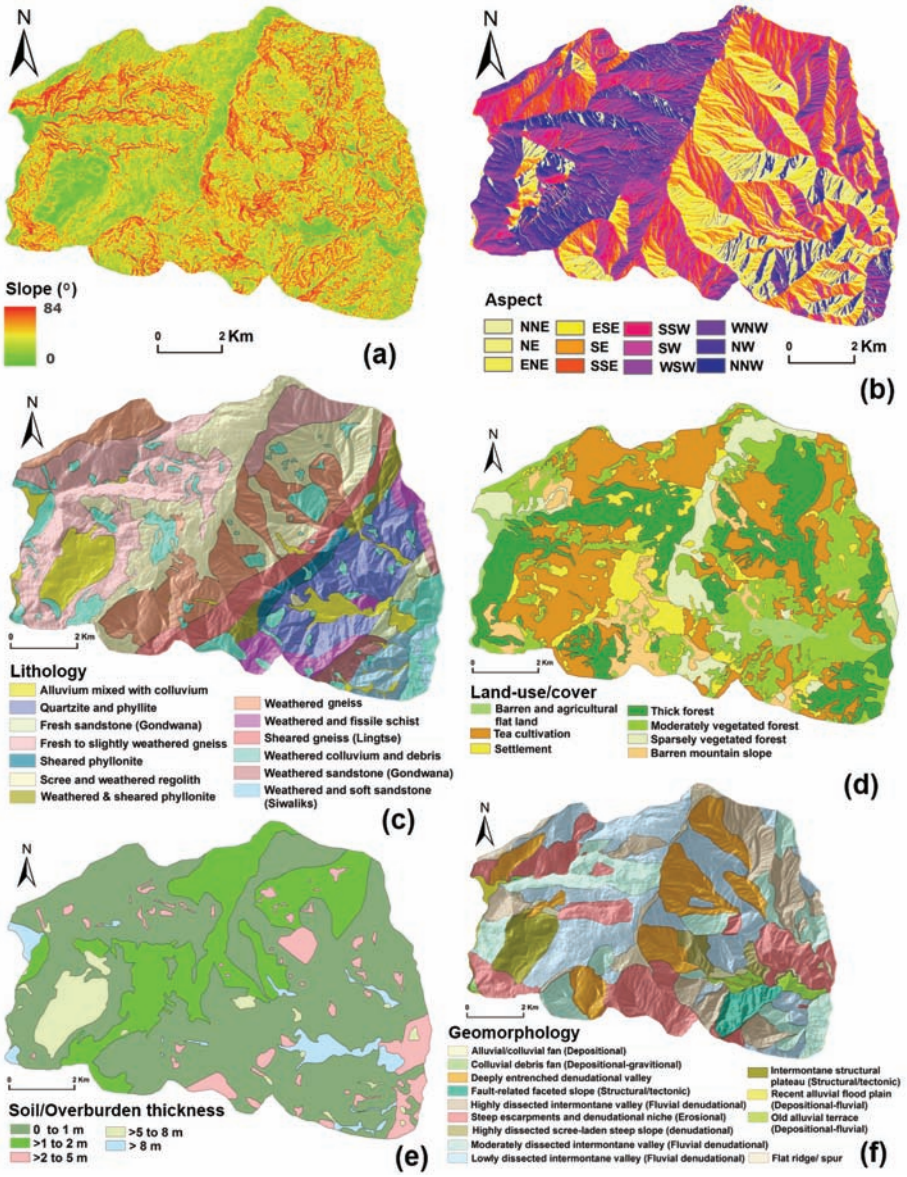

Fig. 6.1 Maps of some relevant spatial factors of susceptibility to shallow landslides. (a) Slope grid. (b) Aspect grid showing 30°-interval aspect classes. (c) Lithology (slope material). (d) Land-use/cover. (e) Soil/Overburden depth. (f) Geomorphology.

The land use/cover map for 2004–2006 was prepared through visual interpretation of multispectral LISS 4 images and fused images of LISS 4 and Cartosat 1 and later the interpretations were confirmed during field investigations. The seven different land use/cover classes were identified (Fig. 6.1d) and calibrated for investigating the period 1968–2003. Because

the aim of the present study was not to depict temporal changes of landslides due to changes in land use/cover (e.g., Kienholz et al., 1983), land use/cover maps for the older period were not created.

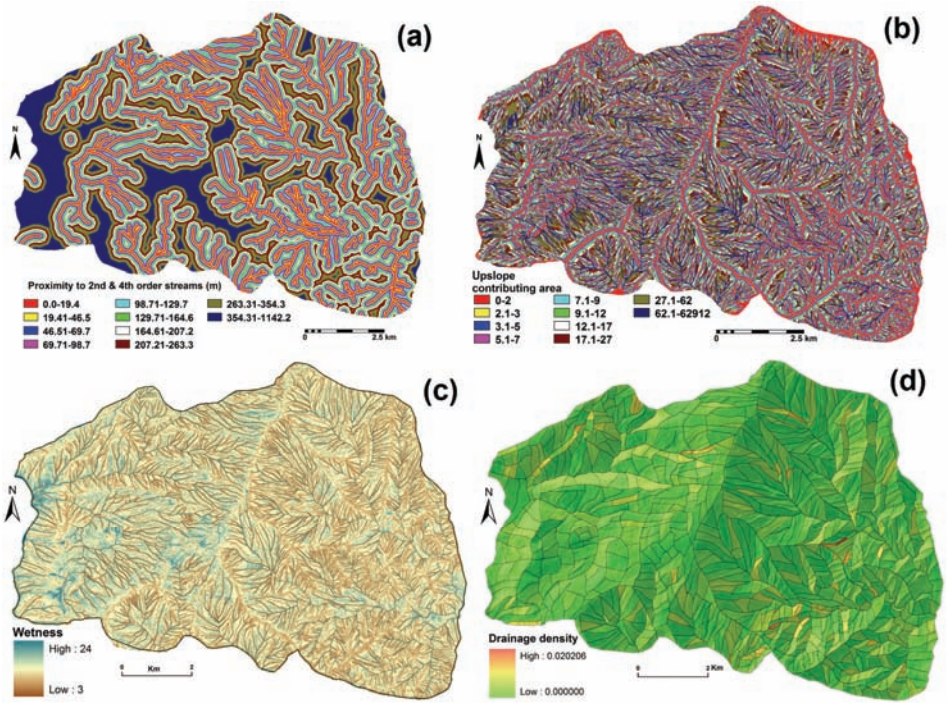

Fig. 6.2 Various hydrological factor maps of shallow landsliding. (a) Proximity to 2nd – 4th order streams. (b) Upslope contributing area. (c) Wetness index. (d) Drainage density.

Landslide inventory mapping for the past 40 years (1968-2007) indicates that there are three major types of landslides in the study area (Fig. 3.2) - deep-seated rockslides (hereafter denoted as Dp_rs), shallow translational rockslides (hereafter denoted as Sh_rs) and shallow translational debris slides (hereafter denoted as Db_rs) – having varied spatial and temporal occurrences (Table 3.2). Due to their predominance in the study area, Sh_rs and Db_rs occurrences were used in this study for model calibration, whereas, Dp_rs occurrences were used as validation samples.

6.3 Analytical methods

For predictive modelling of S_L, it is important to select and use only the good predictors, which are spatial factors that exhibit positive spatial associations with existing landslides of the type studied. After selection of such predictors, the next step is to objectively determine their inter-predictor weights and

then combine the selected predictors with their weights in a suitable susceptibility model.

6.3.1 Spatial association analysis for categorical spatial factors

For each class of a categorical factor, the Yule's coefficient (Y_c) (see Eq. 5.3; chapter 5) was used to quantify its spatial association with known occurrence of shallow landslides. Based on calculated values of Y_c for every factor, a Landslide Occurrence Favourability Score (*LOFS*) was calculated per factor class (Table 6.2):

$$LOFS_{categorical} = \begin{cases} 0 & for \quad Y_c \leq 0 \\ Y_c / Y_{c_{max}} & for \quad Y_c > 0 \end{cases}, \tag{6.3}$$

which numerically represents relative significance of every factor class in terms of susceptibility to occurrence of a particular landslide type in the range of probability values [0,1].

6.3.2 Spatial association analysis for continuous spatial factors

The concept of distance distribution analysis (or DDA) for measuring the spatial association between a set of point geo-objects of interest and another set of spatial geo-objects by Berman (1977; 1986) has been introduced and described in section 4.4.1. Instead of point geo-objects of interest, the DDA can also be used for polygonal spatial geo-objects. To determine, if landslides as polygonal objects are associated spatially with a set of spatial features, the graph of $D(L)$ is compared with graph of $D(NL)$ by calculating D statistic (see section 4.4.1).

Table 6.2 Yule's coefficients (Yc) and Landslide Occurrence Favourability Score (LOFS) of every categorical factor class with respect to Sh_rs and/or Db_rs.

Factor	Factor class	Sh_rs		Db_rs	
		Y_C	*LOFS*	Y_C	*LOFS*
Aspect	NNE	-0.112	0	-0.201	0
	NE	-0.060	0	-0.151	0
	ENE	0.081	0.68	-0.210	0
	ESE	0.119	1.00	-0.028	0
	SE	0.061	0.52	0.040	0.22
	SSE	0.043	0.36	0.042	0.24
	SSW	0.055	0.46	0.178	1.00
	SW	0.041	0.34	0.107	0.60
	WSW	-0.096	0	0.068	0.38
	WNW	-0.128	0	-0.047	0
	NW	-0.177	0	-0.228	0
	NNW	-0.073	0	-0.175	0
Lithology (slope material)	Scree and weathered regolith (SCR)	-0.803	0	0.044	0.09
	Alluvium mixed with colluvium (COLUALU)	-0.529	0	0.144	0.28
	Weathered colluvium and debris (WRCOLU)	-0.464	0	0.522	1.00
	Sheared phyllonite (SHPH)	0.010	0.03	-1.000	0
	Fresh gneiss (FRGN)	-0.047	0	-0.521	0
	Quartzite and phyllite (FRCSCH)	0.044	0.13	-0.624	0
	Fresh sandstone (Gondwana) (FRGOND)	0.142	0.41	-1.000	0
	Weathered gneiss (WRGN)	0.162	0.47	-0.211	0
	Weathered sheared phyllonite (WRSHPH)	0.221	0.64	-0.695	0
	Weathered and soft sandstone (Siwaliks) (WRSIWA)	0.234	0.68	-0.093	0
	Weathered schists and phyllite (WRSCH)	0.142	0.41	-1.000	0
	Weathered and sheared gneiss (Lingtse) (WRSHGN)	0.287	0.84	-0.277	0
	Weathered sandstone (Gondwana) (WRGOND)	0.344	1.00	-0.544	0
Geomorphology	Intermontane plateau (structural/tectonic) (PLATEAU)	-0.834	0	-1.000	0
	Recent alluvial flood plain (depositional - fluvial) (ALU)	-1.000	0	-0.114	0
	Colluvial debris fan (depositional - gravitational) (FAN)	-1.000	0	-1.000	0
	Lowly dissected intermontane valley (fluvial/denudational) (LDISVAL)	-0.485	0	-0.467	0
	Old alluvial terrace (depositional-fluvial) (TERRACE)	-0.091	0	0.300	0.71
	Flat ridge (RIDGE)	-0.476	0	-0.723	0
	Mod. dissected intermontane valley (fluvial/denudational) (MDISVAL)	-0.245	0	-0.057	0
	Highly dissected intermontane valley (fluvial/denudational) (HDISVAL)	0.006	0.02	-0.192	0
	Scree-laden highly dissected steep slope (denudational) (SCHDISVAL)	0.018	0.07	0.218	0.52
	Alluvial/colluvial terrace and fan (depositional) (ALCLFAN)	0.096	0.36	0.421	1.00
	Fault-related faceted slope (structural/tectonic) (FACET)	-0.168	0.00	-0.586	0
	Steep escarpments and denudational niches (ENTRVAL)	0.265	1.00	0.169	0.40
	Deeply entrenched denudational valley (DEEP)	0.247	0.93	0.232	0.55

Land-use/land-cover	Barren and agricultural flat lands (AGRI)	-0.530	0	0.182	0.84
	Tea cultivation (TEA)	-0.422	0	-0.243	0
	Settlement (SET)	-0.149	0	-0.209	0
	Thick forest (TF)	0.034	0.09	-0.026	0
	Moderately vegetated forest (MF)	0.022	0.06	0.045	0.21
	Sparsely vegetated forest (SPF)	0.156	0.42	0.196	0.90
	Barren mountain slope (BARREN)	0.374	1	0.217	1
Depth to bedrock (m)	0 – 1	-	-	-0.420	0
	1 – 2	-	-	-0.114	0
	2 – 5	-	-	0.404	0.96
	5 – 8	-	-	0.423	1.00
	>8	-	-	0.274	0.65
Curvature	(-) 23.87 to (-) 2.2	0.156	1	0.133	1
	(-) 2.2 to (-) 1.3	0.059	0.38	0.038	0.29
	(-) 1.3 to (-) 0.7	0.003	0.02	0.025	0.19
	(-) 0.7 to (-) 0.3	-0.053	0	-0.071	0
	(-) 0.3 to 0.0	-0.074	0	-0.046	0
	0.0 - 0.3	-0.103	0	-0.067	0
	0.3 - 0.7	-0.061	0	-0.064	0
	0.7-1.3	-0.082	0	-0.041	0
	1.3 - 2.2	-0.013	0	-0.002	0
	2.2 - 25.1	0.068	0.44	0.031	0.23

DDA is appropriate for quantifying spatial associations of landslides of certain type (e.g., rockslides) with spatial objects like regional thrusts, faults/fractures, 2nd–4th order streams, proximity to kinematically unstable slopes and old rockslides of pre-1968, etc. However, instead of distance to spatial objects, DDA can be adapted to quantify spatial associations of landslide polygons of a certain type with continuous field data like elevation, slope inclination, wetness index, contributing area upslope, etc. In DDA, the distance to spatial features or the value of continuous field data that corresponds with the highest positive D (or D_{max}) represents distance to spatial features or continuous field data with which landslides of a certain type have strongest positive spatial association. A *LOFS* for every distance to spatial features or continuous field data is thus defined as:

$$LOFS_{continuous} = \begin{matrix} 0 & for & D \leq 0 \\ D/D_{\max} & for & D > 0 \end{matrix} \quad (6.4)$$

6.3.3 Weighting of predictors

Individual spatial factors can have different degrees of spatial associations with landslides of the type studied. That is intuitive because every spatial factor has a different degree of influence (or weight) on landslide occurrence. However, as landsliding is due to an inter-play of multiple factors, predictive mapping of landslide susceptibility (S_L) requires analysis of inter-predictor weights. This analysis can benefit from expert/generic knowledge of causal factors of landslides. However, expert knowledge is subjective and landslide experts are likely to assign different weights to every landslide factor. This section describes how analysis of inter-predictor weights can be made more

objective by applying analytical hierarchy process or AHP (Saaty, 1977), whereby pairwise analysis of predictor weights are performed based on the results of quantified spatial associations of individual spatial factors with landslides of the type studied. To determine the relative importance of every predictor of either landslide types (Sh_rs or Db_rs), a predictor rating (*PR*) for every spatial factor (e.g., for Sh_rs, Table 6.3) based on their spatial association with each landslide type, thus:

$$PR = \left|SA_{\max} - SA_{\min}\right| \Big/ \left|SA_{\max} - SA_{\min}\right|_{\min}, \quad (6.5)$$

where SA is index of spatial association (either Y_c or D) of a spatial factor with a set of landslide type. For each factor the absolute difference between the maximum and minimum SA values is calculated, which is then divided by the lowest absolute difference of all the factors (Table 6.3). By pairwise comparison of PR values of every predictor of landslide occurrence and by using the 9-point pairwise rating scale in AHP (see Saaty, 1977 for details), a matrix of pairwise ratings of relative importance of every predictor can be obtained (Table 6.4). Thus, for example, as predictors of susceptibility to occurrence of Sh_rs, lithology and geomorphology are equally important and are 6× more important than slope or the latter is 1/6× less important than the former (Table 6.4).

Table 6.3 Ratings of predictors (PR) based on indices of spatial associations (SA) of spatial factors with landslide occurrences (for example only the spatial factors of Sh_rs are shown). Value in bold is $\left|SA_{\max} - SA_{\min}\right|_{\min}$

Predictors of Sh_rs occurrence	*SA* (Y_C or *D*)		$\lvert SA_{max} - SA_{min}\rvert$	*PR* (Eq. (6.8))
	min	max		
Lithology/slope material (***L***)	-0.803	0.344	1.147	23
Geomorphology (***G***)	-1.000	0.265	1.265	25
Land-use/land-cover (***LC***)	-0.530	0.374	0.904	18
Aspect (***A***)	-0.177	0.119	0.296	6
Slope (***S***)	0	0.28	0.28	6
Elevation (***E***)	0	0.13	0.13	3
Proximity to NE-trending faults/fractures (***NE***)	0	0.13	0.13	3
Proximity to NNE-trending faults/fractures (***NNE***)	0	0.16	0.16	3
Proximity to regional MCT/MBT (***RT***)	0	0.24	0.24	5
Proximity to NNW-trending faults/fractures (***NNW***)	0	0.11	0.11	2
Proximity to NW-trending faults/fractures (***NW***)	0	0.15	0.15	3
Proximity to WNW-trending faults/fractures (***WNW***)	0	0.06	0.06	1
Proximity to ENE-trending faults/fractures (***ENE***)	0	0.05	0.05	1
Presence of and proximity to kinematically unstable slopes (***KUS***)	0	0.25	0.25	5
Proximity to 2nd–4th order streams (***ST***)	0	0.09	0.09	2
Proximity to road (***R***)	0	0.06	0.06	1
Upslope contributing area (***UC***)	0	0.13	0.13	3
Curvature (***C***)	-0.103	0.156	0.259	5
Wetness (***W***)	0	0.05	0.05	1
Drainage density (***DR***)	0	0.08	0.08	2
Presence of and proximity to old rockslides (pre-1968) (***OSL***)	0	0.4	0.4	8

After obtaining a matrix of pairwise ratings of relative importance of every predictor, the next step is to estimate the eigenvectors of the matrix (Boroushaki and Malczewski, 2008). Reasonable estimates of eigenvectors of the pairwise rating matrix can be obtained by normalizing the pairwise ratings down each column. That is, for example in Table 6.4, each pairwise importance rating in a column is divided by the sum of pairwise importance ratings in that column. This procedure is repeated for all columns in the matrix of pairwise importance ratings to obtain the eigenvectors of the matrix (Table 6.5). Then, a fractional predictor weight is obtained by averaging the eigenvectors across a row (Table 6.5). The sum of fractional predictor weights is approximately equal to 1, which reflects approximately 100% of the explained variances of the eigenvectors of the matrix. Each of the fractional predictor weights can be converted into an integer predictor weight by dividing each of the fractional predictor weights by the smallest fractional predictor weight and then by rounding-off decimals of every quotient to nearest ones (Table 6.5). Note that each of predictor weight in Table 6.5 relates to aC_{ji} in Eq. (6.2).

The consistency of predictors weights derived via the AHP must be checked first by determining the consistency of the matrix of pairwise importance ratings, which was obtained through interpretation of relative importance of every predictor. A matrix is consistent if every value across each row is a multiple of every other value in the other rows. This is not the case of the matrix in Table 6.4, signifying that some degree of inconsistency exists among the pairwise importance ratings assigned to predictors of Sh_rs occurrence. The consistency of an $n \times n$ matrix (n = number of predictors) of pairwise importance ratings is determined by estimating consistency vectors (CV) of pairwise importance ratings, which are used to determine the consistency index (CI) and consistency ratio (CR) of that matrix. Details of procedures to estimate CV, CI and CR are not described here, but readers are referred to Saaty (1977) or Carranza (Carranza, 2008) for details. The CR is the ratio of CI to random inconsistency index (RI) of an n×n matrix of randomly generated pairwise importance ratings (Saaty, 1977). A CR of >0.1 (i.e., >10% of RI) indicates that a pairwise comparison matrix has a level of inconsistency that is unacceptable, meaning that pairwise importance ratings must be re-evaluated to obtain usable (i.e., meaningful) predictor weights. The results in Table 6.6 show that (a) inconsistencies among pairwise ratings of predictors of susceptibility to occurrence of Sh_rs (Table 6.4) are minor and (b) estimated fractional (or integer) weights of predictors of susceptibility to occurrence of Sh_rs (Table 6.5) are consistent.

Table 6.4 Matrix of pairwise ratings of relative importance of predictors of susceptibility to Sh_rs occurrence based on pairwise comparison of *PR* values (Table 6.3). A value of >1 means that a predictor in the first column is 'more important' than a predictor in the first row, whereas a value of <1 that means a predictor in the first column is 'less important' than a predictor in the first row. For explanations of predictor symbols, see caption of Table 6.3

Predictors	*L*	*G*	*LC*	*KUS*	*A*	*S*	*RT*	*E*	*NE*	*NNE*	*NW*	*U*	*O*	*ST*	*NNW*	*WNW*	*ENE*	*R*	*C*	*W*	*DR*
L	1	1	3	8	8	8	8	9	9	9	9	9	7	9	9	9	9	9	8	9	9
G	1	1	4	8	8	8	8	9	9	9	9	9	7	9	9	9	9	9	8	9	9
LC	1/3	1/4	1	7	7	7	7	8	8	8	8	8	8	9	9	9	9	9	7	9	9
KUS	1/8	1/8	1/7	1	1	1	1	5	5	5	5	5	1/2	6	6	7	7	7	1	7	6
A	1/8	1/8	1/7	1	1	1	1	5	5	5	5	5	1	6	6	8	8	8	1	8	6
S	1/8	1/8	1/7	1	1	1	1	5	5	5	5	5	1	6	6	8	8	8	1	8	6
RT	1/8	1/8	1/7	1	1	1	1	5	5	5	5	5	1/2	6	6	7	7	7	1	7	5
E	1/9	1/9	1/8	1/5	1/5	1/5	1/5	1	1	1	1	1	1/5	3	3	5	5	5	1/5	5	3
NE	1/9	1/9	1/8	1/5	1/5	1/5	1/5	1	1	1	1	1	1/5	3	3	5	5	5	1/5	5	3
NNE	1/9	1/9	1/8	1/5	1/5	1/5	1/5	1	1	1	1	1	1/5	3	3	5	5	5	1/5	5	3
NW	1/9	1/9	1/8	1/5	1/5	1/5	1/5	1	1	1	1	1	1/5	3	3	5	5	5	1/5	5	3
U	1/9	1/9	1/8	1/5	1/5	1/5	1/5	1	1	1	1	1	1/5	3	3	5	5	5	1/5	5	3
O	1/7	1/7	1/8	2	1	1	2	5	5	5	5	5	1	6	6	7	7	7	2	7	6
ST	1/9	1/9	1/9	1/6	1/6	1/6	1/6	1/3	1/3	1/3	1/3	1/3	1/6	1	1	1	1	1	1/6	1	1
NNW	1/9	1/9	1/9	1/6	1/6	1/6	1/6	1/3	1/3	1/3	1/3	1/3	1/6	1	1	1	1	1	1/6	1	1
WNW	1/9	1/9	1/9	1/7	1/8	1/8	1/7	1/5	1/5	1/5	1/5	1/5	1/7	1	1	1	1	1	1/7	1	1
ENE	1/9	1/9	1/9	1/7	1/8	1/8	1/7	1/5	1/5	1/5	1/5	1/5	1/7	1	1	1	1	1	1/7	1	1
R	1/9	1/9	1/9	1/7	1/8	1/8	1/7	1/5	1/5	1/5	1/5	1/5	1/7	1	1	1	1	1	1/5	1	1
C	1/8	1/8	1/7	1	1	1	1	5	5	5	5	5	1/2	6	6	7	7	5	1	7	5
W	1/9	1/9	1/9	1/7	1/8	1/8	1/7	1/5	1/5	1/5	1/5	1/5	1/7	1	1	1	1	1	1/7	1	1
DR	1/9	1/9	1/9	1/6	1/6	1/6	1/5	1/3	1/3	1/3	1/3	1/3	1/6	1	1	1	1	1	1/5	1	1
Sum	4.43	4.35	10.24	32.07	31	31	32.10	62.8	62.8	62.8	62.8	62.8	28.57	85	85	103	103	101	32.16	103	83

Table 6.5 Estimated eigenvectors of pairwise rating matrix (Table 6.4) and weights of predictors of susceptibility to Sh_rs occurrence. For explanation of predictor symbols, see Table 6.3. The selected predictors and their corresponding integer weights are marked with bold fonts.

Predictors	*L*	*G*	*LC*	*KUS*	*A*	*S*	*RT*	*E*	*NE*	*NNE*	*NW*	*U*	*O*	*ST*	*NNW*	*WNW*	*ENE*	*R*	*C*	*W*	*D*	Row sum	Fractional weight (row sum/$n_{predictor}$)	Integer weight
L	0.23	0.23	0.29	0.25	0.26	0.26	0.25	0.14	0.14	0.14	0.14	0.14	0.25	0.11	0.11	0.09	0.09	0.09	0.25	0.09	0.11	0.23	0.17	**20**
G	0.23	0.23	0.39	0.25	0.26	0.26	0.25	0.14	0.14	0.14	0.14	0.14	0.25	0.11	0.11	0.09	0.09	0.09	0.25	0.09	0.11	0.23	0.18	**21**
LC	0.08	0.06	0.10	0.22	0.23	0.23	0.22	0.13	0.13	0.13	0.13	0.13	0.28	0.11	0.11	0.09	0.09	0.09	0.22	0.09	0.11	0.08	0.14	**16**
KUS	0.03	0.03	0.01	0.03	0.03	0.03	0.03	0.08	0.08	0.08	0.08	0.08	0.02	0.07	0.07	0.07	0.07	0.07	0.03	0.07	0.07	0.03	0.05	**6**
A	0.03	0.03	0.01	0.03	0.03	0.03	0.03	0.08	0.08	0.08	0.08	0.08	0.04	0.07	0.07	0.08	0.08	0.08	0.03	0.08	0.07	0.03	0.06	**7**
S	0.03	0.03	0.01	0.03	0.03	0.03	0.03	0.08	0.08	0.08	0.08	0.08	0.04	0.07	0.07	0.08	0.08	0.08	0.03	0.08	0.07	0.03	0.06	**7**
RT	0.03	0.03	0.01	0.03	0.03	0.03	0.03	0.08	0.08	0.08	0.08	0.08	0.02	0.07	0.07	0.07	0.07	0.07	0.03	0.07	0.06	0.03	0.05	**6**
E	0.03	0.03	0.01	0.01	0.01	0.01	0.01	0.02	0.02	0.02	0.02	0.02	0.01	0.04	0.04	0.05	0.05	0.05	0.01	0.05	0.04	0.03	0.02	**3**
NE	0.03	0.03	0.01	0.01	0.01	0.01	0.01	0.02	0.02	0.02	0.02	0.02	0.01	0.04	0.04	0.05	0.05	0.05	0.01	0.05	0.04	0.03	0.02	**3**
NNE	0.03	0.03	0.01	0.01	0.01	0.01	0.01	0.02	0.02	0.02	0.02	0.02	0.01	0.04	0.04	0.05	0.05	0.05	0.01	0.05	0.04	0.03	0.02	**3**
NW	0.03	0.03	0.01	0.01	0.01	0.01	0.01	0.02	0.02	0.02	0.02	0.02	0.01	0.04	0.04	0.05	0.05	0.05	0.01	0.05	0.04	0.03	0.02	**3**
UC	0.03	0.03	0.01	0.01	0.01	0.01	0.01	0.02	0.02	0.02	0.02	0.02	0.01	0.04	0.04	0.05	0.05	0.05	0.01	0.05	0.04	0.03	0.02	**3**
OSL	0.03	0.03	0.01	0.06	0.03	0.03	0.06	0.08	0.08	0.08	0.08	0.08	0.04	0.07	0.07	0.07	0.07	0.07	0.06	0.07	0.07	0.03	0.06	**7**
ST	0.03	0.03	0.01	0.01	0.01	0.01	0.01	0.01	0.01	0.01	0.01	0.01	0.01	0.01	0.01	0.01	0.01	0.01	0.01	0.01	0.01	0.03	0.01	1
NNW	0.03	0.03	0.01	0.01	0.01	0.01	0.01	0.01	0.01	0.01	0.01	0.01	0.01	0.01	0.01	0.01	0.01	0.01	0.01	0.01	0.01	0.03	0.01	1
WNW	0.03	0.03	0.01	0.00	0.00	0.00	0.00	0.00	0.00	0.00	0.00	0.00	0.01	0.01	0.01	0.01	0.01	0.01	0.00	0.01	0.01	0.03	0.01	1
ENE	0.03	0.03	0.01	0.00	0.00	0.00	0.00	0.00	0.00	0.00	0.00	0.00	0.01	0.01	0.01	0.01	0.01	0.01	0.00	0.01	0.01	0.03	0.01	1
R	0.03	0.03	0.01	0.00	0.00	0.00	0.00	0.00	0.00	0.00	0.00	0.00	0.01	0.01	0.01	0.01	0.01	0.01	0.01	0.01	0.01	0.03	0.01	1
C	0.03	0.03	0.01	0.03	0.03	0.03	0.03	0.08	0.08	0.08	0.08	0.08	0.02	0.07	0.07	0.07	0.07	0.05	0.03	0.07	0.06	0.03	0.05	**6**
W	0.03	0.03	0.01	0.00	0.00	0.00	0.00	0.00	0.00	0.00	0.00	0.00	0.01	0.01	0.01	0.01	0.01	0.01	0.00	0.01	0.01	0.03	0.01	1
DR	0.03	0.03	0.01	0.01	0.01	0.01	0.01	0.01	0.01	0.01	0.01	0.01	0.01	0.01	0.01	0.01	0.01	0.01	0.01	0.01	0.01	0.03	0.01	1

Table 6.6 Estimation of consistency vector (CV), consistency index (CI) and consistency ratio (CR) for judgment of consistency of pairwise importance ratings of predictors (Table 6.4). Cell value per predictor is product of eigenvector and corresponding fractional predictor weight (Table 6.5). For explanation of predictor symbols, see Table 6.3.

Predictors	*L*	*G*	*LC*	*KUS*	*A*	*S*	*RT*	*E*	*NE*	*NNE*	*NW*	*U*	*O*	*ST*	*NNW*	*WNW*	*ENE*	*R*	*C*	*W*	*D*	Row sum	CV
L	0.17	0.18	0.42	0.43	0.45	0.45	0.43	0.21	0.21	0.21	0.21	0.21	0.42	0.08	0.08	0.08	0.08	0.08	0.42	0.08	0.08	4.96	28.57
G	0.17	0.18	0.56	0.43	0.45	0.45	0.43	0.21	0.21	0.21	0.21	0.21	0.42	0.08	0.08	0.08	0.08	0.08	0.42	0.08	0.08	5.10	28.61
LC	0.06	0.04	0.14	0.38	0.40	0.40	0.37	0.18	0.18	0.18	0.18	0.18	0.48	0.08	0.08	0.08	0.08	0.08	0.37	0.08	0.08	4.10	29.46
KUS	0.02	0.02	0.02	0.05	0.06	0.06	0.05	0.11	0.11	0.11	0.11	0.11	0.03	0.06	0.06	0.06	0.06	0.06	0.05	0.06	0.06	1.35	25.01
A	0.02	0.02	0.02	0.05	0.06	0.06	0.05	0.11	0.11	0.11	0.11	0.11	0.06	0.06	0.06	0.07	0.07	0.07	0.05	0.07	0.06	1.41	24.95
S	0.02	0.02	0.02	0.05	0.06	0.06	0.05	0.11	0.11	0.11	0.11	0.11	0.06	0.06	0.06	0.07	0.07	0.07	0.05	0.07	0.06	1.41	24.95
RT	0.02	0.02	0.02	0.05	0.06	0.06	0.05	0.11	0.11	0.11	0.11	0.11	0.03	0.06	0.06	0.06	0.06	0.06	0.05	0.06	0.05	1.34	25.10
E	0.02	0.02	0.02	0.01	0.01	0.01	0.01	0.02	0.02	0.02	0.02	0.02	0.01	0.03	0.03	0.04	0.04	0.04	0.01	0.04	0.03	0.49	21.39
NE	0.02	0.02	0.02	0.01	0.01	0.01	0.01	0.02	0.02	0.02	0.02	0.02	0.01	0.03	0.03	0.04	0.04	0.04	0.01	0.04	0.03	0.49	21.39
NNE	0.02	0.02	0.02	0.01	0.01	0.01	0.01	0.02	0.02	0.02	0.02	0.02	0.01	0.03	0.03	0.04	0.04	0.04	0.01	0.04	0.03	0.49	21.39
NW	0.02	0.02	0.02	0.01	0.01	0.01	0.01	0.02	0.02	0.02	0.02	0.02	0.01	0.03	0.03	0.04	0.04	0.04	0.01	0.04	0.03	0.49	21.39
UC	0.02	0.02	0.02	0.01	0.01	0.01	0.01	0.02	0.02	0.02	0.02	0.02	0.01	0.03	0.03	0.04	0.04	0.04	0.01	0.04	0.03	0.49	21.39
OSL	0.02	0.03	0.02	0.11	0.06	0.06	0.11	0.11	0.11	0.11	0.11	0.11	0.06	0.06	0.06	0.06	0.06	0.06	0.10	0.06	0.06	1.54	25.91
ST	0.02	0.02	0.02	0.01	0.01	0.01	0.01	0.01	0.01	0.01	0.01	0.01	0.01	0.01	0.01	0.01	0.01	0.01	0.01	0.01	0.01	0.21	22.67
NNW	0.02	0.02	0.02	0.01	0.01	0.01	0.01	0.01	0.01	0.01	0.01	0.01	0.01	0.01	0.01	0.01	0.01	0.01	0.01	0.01	0.01	0.21	22.67
WNW	0.02	0.02	0.02	0.01	0.01	0.01	0.01	0.00	0.00	0.00	0.00	0.00	0.01	0.01	0.01	0.01	0.01	0.01	0.01	0.01	0.01	0.18	21.77
ENE	0.02	0.02	0.02	0.01	0.01	0.01	0.01	0.00	0.00	0.00	0.00	0.00	0.01	0.01	0.01	0.01	0.01	0.01	0.01	0.01	0.01	0.18	21.77
R	0.02	0.02	0.02	0.01	0.01	0.01	0.01	0.00	0.00	0.00	0.00	0.00	0.01	0.01	0.01	0.01	0.01	0.01	0.01	0.01	0.01	0.19	21.91
C	0.02	0.02	0.02	0.05	0.06	0.06	0.05	0.11	0.11	0.11	0.11	0.11	0.03	0.06	0.06	0.06	0.06	0.04	0.05	0.06	0.05	1.32	25.23
W	0.02	0.02	0.02	0.01	0.01	0.01	0.01	0.00	0.00	0.00	0.00	0.00	0.01	0.01	0.01	0.01	0.01	0.01	0.01	0.01	0.01	0.18	21.77
DR	0.02	0.02	0.02	0.01	0.01	0.01	0.01	0.01	0.01	0.01	0.01	0.01	0.01	0.01	0.01	0.01	0.01	0.01	0.01	0.01	0.01	0.21	22.80
Total CV																							500.12
λ = mean CV = $CV_{total}/n_{predictor}$ = 500.12/21 = 23.82 Consistency index (CI) = $(\lambda - n_{predictor})/(n_{predictor} - 1)$ = (23.82–21)/(21–1) = 0.1407																							
Random inconsistency index (RI) for 21×21 matrix (see Saaty,1977) = 1.49 Consistency ratio (CR) = CI/RI = 0.1407/1.49 = 0.09																							

6.4 Predictive models of landslide susceptibility

6.4.1 Weighted multi-class index overlay model using pre-selected predictors

Based on the spatial association analyses and the derived integer predictor weights derived via AHP (Tables 6.3–6.7), 14 out of 21 identified spatial factors of shallow translational landslides can be used as predictors of susceptibility to Sh_rs occurrence in the study area (Table 6.7). Likewise, 12 out 22 identified spatial factors of shallow translational debris slides can be used as predictors of susceptibility to Db_rs occurrence in the study area (Table 6.7).

Table 6.7 Generic factors of shallow translational landslides and selected predictors of susceptibility to Sh_rs and Db_rs occurrence in the study area. Numerical values in bold within brackets are AHP integer weights of the selected predictors of susceptibility to the occurrence of Sh_rs and Db_rs (For Sh_rs, also Table 6.5).

Factor theme	Factor	Predictors of susceptibility to shallow translational landsliding	
		Sh_rs	Db_rs
Lithology/geo-morphology	Lithology	Lithology **(20)**	Lithology **(15)**
	Geomorphology	Geomorphology **(21)**	Geomorphology **(15)**
	Soil/overburden thickness	-	Soil/overburden thickness **(11)**
Land-use/ land-cover	Land-cover	Land-use/land-cover **(16)**	Land-use/land-cover **(8)**
	Proximity to road	-	-
Topography/ morphometry	Slope	Slope **(7)**	Slope **(2)**
	Aspect	Aspect **(7)**	Aspect **(7)**
	Elevation	Elevation **(3)**	Elevation **(3)**
	Curvature	Curvature **(6)**	-
Geological structures	Presence of and proximity to kinematically unstable slopes	Presence of and proximity to kinematically unstable slopes **(6)**	-
	Proximity to NE-trending faults/fractures	Proximity to NE-trending faults/fractures **(3)**	-
	Proximity to NNE-trending faults/fractures	Proximity to NNE-trending faults/fractures **(3)**	-
	Proximity to NNW-trending faults/fractures	-	Proximity to NNW-trending faults/fractures **(3)**
	Proximity to NW-trending faults/fractures	Proximity to NW-trending faults/fractures **(3)**	-
	Proximity to ENE-trending faults/fractures	-	-
	Proximity to WNW-trending faults/fractures	-	Proximity to WNW-trending faults/fractures **(3)**
	Proximity to major thrusts (MCT/MBT)	Proximity to major thrusts (MCT/MBT) **(6)**	Proximity to major thrusts (MCT/MBT) **(3)**
Hydrology	Proximity to 2nd–4th order streams	-	Proximity to 2nd–4th order streams **(3)**
	Wetness index	-	-
	Upslope contributing area	Upslope contributing area **(3)**	-
	Drainage density	-	-
Old rockslides (pre-1968)	Presence of and proximity to old rockslides (pre-1968)	Presence of and proximity to old rockslides (pre-1968) **(7)**	Presence of and proximity to old rockslides (pre-1968) **(4)**

To integrate the selected predictors of each type of shallow landsliding, the weighted multi-class index overlay method (Bonham-Carter, 1994) was applied. In each of the *i*-th (*i* = 1,…,*n* number of) predictor maps, each of the *j*-th (*j* = 1,…,*k* number of) predictor classes is assigned a *LOFS* obtained via spatial association analysis (Eq. (6.3) and Eq. (8)). Every *i*-th predictor map is assigned an integer predictor weight, W_i, obtained via AHP (e.g., Table 5). Weighted predictor maps are then combined using the following equation, which calculates an average weighted score ($\overline{S}$) for every location (Bonham-Carter, 1994):

$$\overline{S} = \sum_i^n (LOFS_{ji} \times W_i) \Big/ \sum_i^n W_i \ . \qquad (6.6)$$

The output map of $\overline{S}$ is a predictive model of susceptibility to occurrence of each type of shallow translational landslides under examination in the area. Note that, in Eq. (6.9), the product of $LOFS_{ji} \times W_i$ represents in aC_{ji} in Eq. (6.2). To show the usefulness of the proposed methodology, three different models – Model-1 (using selected and weighted spatial predictors), Model-2 (using selected but un-weighted spatial predictors) and Model-3 (using all relevant spatial factors as predictors with their respective weights) of susceptibility to occurrence of Sh_rs and to occurrence of Db_rs are developed (Fig. 6.3).

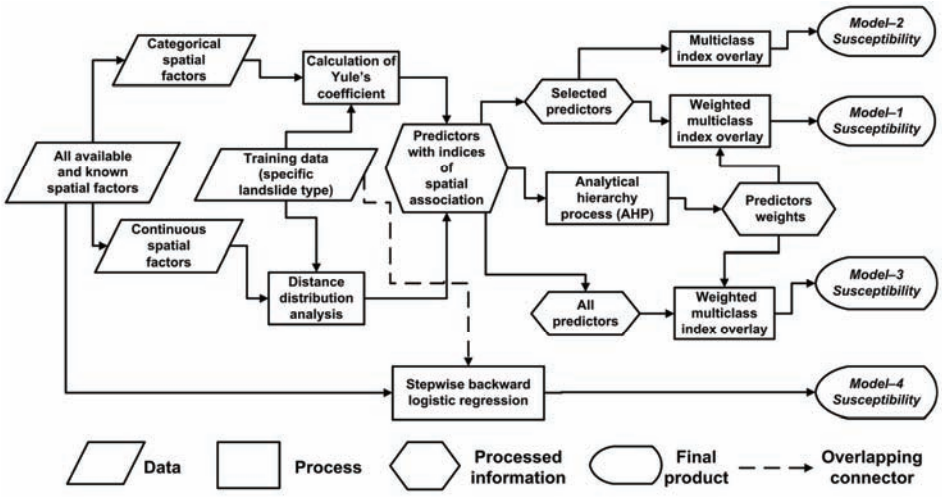

Fig. 6.3 Schematic flow diagram showing data, processes and steps for developing 4 different models of susceptibility to shallow landsliding.

6.4.2 Logistic regression model using all identified/mapped spatial factors

Logistic regression (LR) is a method for multivariate analysis of spatial association between target and predictor variables. LR was used to derive predictive maps (Model-4) of susceptibility to Sh_rs and to Db_rs occurrence because it is appropriate when the target variable is dichotomous (e.g., landslide occurrence score, LOS, depicting presence or absence of landslide). The LR predictive model of susceptibility to shallow translational landslide occurrence can be defined as (Hosmer and Lomeshow, 2000):

$$\overline{LOS_i} = 1 \Big/ \left(1 + e^{-\left(b_0 + b_{M1}M_{1i} + b_{M2}M_{2i} + \ldots + b_{Mn}M_{ni}\right)}\right) \quad (6.7)$$

where $\overline{LOS_i}$ is predicted landslide occurrence score or the probability of landslide occurrence at every i-th pixel, b_0 is a constant, b is coefficient of individual predictor variables (M_{1i}, M_{2i}, … , M_{ni}) representing different spatial factors. Note that b_{M1}, for example, represents aC_{ji} in Eq. (6.2).

To calibrate the LR model (Model-4), the centroids (each of 10 m × 10 m pixel size) of 1968–2003 shallow landslides polygons (584 for Sh_rs and 206 for Db_rs) were used as landslide-bearing grid-cells because, among locations mapped within a landslide, they have the least uncertainty of being within a landslide (Dai and Lee, 2002). To each landslide-polygon centroid, *LOS* = 1 was assigned. For un-biased selection of non-landslide locations (each assigned *LOS* = 0), three criteria (Carranza, 2008) were examined. First, the number of non-landslide locations (*LOS* = 0) is equal to the number of landslide locations (*LOS* = 1) because LR is optimal if equal number of 'zeros' and 'ones' are used (Schill et al., 1993). Second, non-landslide locations are sufficiently distal to landslide locations so that dissimilar multivariate spatial data signatures are obtained for locations with LOS of 0 and 1. Third, in contrast to landslide locations, which usually exhibit clustered distribution, non-landslide locations must be randomly-distributed. To satisfy the second criterion, a point pattern analysis (Boots and Getis, 1988) applied to the landslide-polygon centroids reveals that that non-landslide locations are to be selected at least 200 m away from existing landslides. To satisfy the third criterion, a point pattern analysis (Boots and Getis, 1988) was further applied to the randomly-selected non-landslide locations to evaluate the degree of spatial randomness of non-landslide locations for both landslide types.

For representation of predictors based on categorical factors (e.g., aspect, geology, geomorphology etc.), dummy binary values were assigned

according to the method of data representation proposed by Chung et al. (1995). Since some of the factor maps represent distances to objects (e.g., faults/fractures, streams, old rockslides, kinematically unstable slopes) and each having ten percentile proximity classes, representing them as ten different categories/classes per factor results in a large number of predictor variables that increases the chances of redundancy in LR. Thus, the number of classes of those proximity factor maps was reduced to three ('low', 'moderate' and 'high'). The distance limits for the 3-class proximity maps are based on our field observations about their spatial associations with certain spatial features (Table 6.9). For predictors based on continuous field data (e.g., slope, elevation, upslope area contributing, wetness index), map values are directly used as input to LR.

Backward stepwise approach to LR was applied, which starts with all input predictors and ends with only statistically significant predictors that contribute to the prediction or classification. In order to compare statistically significant predictors with those selected via bivariate spatial association analyses, in the backward stepwise LR model, b_0 was forced to zero. However, because LR coefficients are non-linear weights, they cannot be compared with predictor weights derived via the linear methods of bivariate spatial association analyses.

6.4.3 Model evaluation

Each of the four predictive S_L models (Model-1 to Model-4) was evaluated by calculating and graphing of success and prediction rates (Chung and Fabbri, 1999) based on the calibration landslides of 1968–2003 and validation landslides of 2004–2007, respectively. Each of the models was also evaluated by calculating and graphing of prediction rates against a different type of landslides (e.g., Sh_rs predictive model versus Db_rs) to test some degree of similarity in landsliding processes, but not to indicate that predictive model of susceptibility to a particular landslide type would predict occurrences of another landslide type. Further, the performance of all predictive S_L models were evaluated by calculating and graphing of receiver operating characteristics (ROC) (Fawcett, 2006; Frattini et al., 2010). Since both of the above methods for empirical model evaluation (success and prediction rates; ROC) are cutoff-independent, they are suitable for evaluating the performance of predictive models that use arbitrary selection of classification cutoffs (e.g., in LR model, by default cutoff used as 0.5) (Frattini et al., 2010).

6.5 Results

6.5.1 Spatial association analysis for categorical spatial factors

The results of the spatial association analyses for categorical spatial factors are presented in Table 6.2. For slope aspect, the south-facing slopes have positive spatial associations with both types of shallow landslides. This is because in the study area the south-facing slopes compared to north-facing slopes, have steeper inclinations and receive higher amounts of rainfall coming from the south during monsoons. Due to the tectonic setting of the Himalayan thrust fronts, south-facing slopes exhibit more landslide activity (Fig. 3.4). Slope aspect is, thus, an important predictor of susceptibility to shallow translational landsliding in the area.

Compared to slopes with convex profiles (with positive curvature values), those with concave ones (negative curvature values) have a higher degree of positive spatial association for both types of shallow landslides because landslides in the areas are characterized by depletion zones upslope and accumulation areas down slope (Fig. 3.2).

Lithological units with weathered bedrock and less-competent clastic rocks have strong positive spatial associations with shallow rockslides (Sh_rs) but have negative spatial associations with shallow debris slides (Db_rs) (Table 6.2). For weathered colluvium/debris and scree/weathered regolith the situation is reverse (Table 6.2). Lithology is, thus, an important predictor of susceptibility to occurrence of both types of shallow landslides in the area (e.g., Peters and Mool, 1983; Anbalagan, 1992; Weidinger et al., 1996; Weidinger, 2007).

Landforms like deeply entrenched valleys, steep scarps, highly dissected intermontane valleys and denudational niches have strong positive spatial associations with Sh (Table 6.2). Strong positive spatial associations of alluvial/colluvial terraces and fans with shallow rockslides are due to the fact that the accumulation zones are located on these gentler slopes. Alluvial/colluvial terraces and fans, old terrace deposits, deeply entrenched valleys and scree-laden highly dissected steep slopes also have strong positive spatial associations with shallow debris slides (Db_rs) (Table 6.2). Strong positive spatial associations of deeply entrenched valleys, steep escarpments and denudational niches with Db are due to the presence of debris of old rockslides (Anbalagan, 1992; Shroder and Bishop, 1998; Weidinger and Korup, 2009; Korup et al., 2010). Geomorphology is, thus, an

important predictor of susceptibility to occurrence of both types of shallow translational landslides in the area (e.g., Burbank et al., 1996; Wesnousky et al., 1999; Gabet et al., 2010).

Moderately to sparsely vegetated forests and barren slopes have positive spatial associations with both types of shallow landslides (Table 6.2). That is because lack of vegetation reduces the shear strength of slope materials, facilitates penetration of surface runoff and increases hydrostatic pressure in slope material (Swanson and Dyrness, 1975; Wu and Swanston, 1980; Ives and Messerli, 1989). Barren and agricultural lands also have positive spatial associations with shallow debris slides (Db_rs). This is due to fact that compared to Sh_rs, Db_rs occurs at gentle to flatter slopes. Thus, land use/cover forms an important predictor of susceptibility to occurrence of both types of shallow translational landslides in the area (e.g., Peters and Mool, 1983; Begueria, 2006).

Areas with soil/overburden thickness larger than 2 m have strong positive spatial associations with debris slides (Db_rs), whereas those with thin soil cover have negative spatial associations with Db_rs (Table 6.2) whereas those areas are related to rockslides. Therefore, soil/overburden thickness is an important predictor of susceptibility to occurrence of shallow debris slides in the area (Anbalagan, 1992; Ghoshal et al., 2008; Ghosh et al., 2009a).

6.5.2 Spatial association analysis for continuous spatial factors

Fig. 6.4 presents some examples of the results of the distance distribution analysis (DDA) using continuous spatial factors. Most shallow landslides (of both Sh_rs and Db_rs types) are present on 22º–34º slopes, where there is a 24–28% higher likelihood of Sh occurrence (Fig. 6.4a) and 10–11% higher likelihood of Db_rs occurrence (Fig. 6.4b). DDA analysis further indicates that most rockslides occurred at elevations between 532 m and 1532 m, where there is an 11–13% higher likelihood of Sh occurrence whereas most debris slides are present between 590 m and 1260 m, where there is a 6–11% higher likelihood of Db occurrences. The fact that most debris slides are present at relatively lower elevations than most rockslides suggests that the former are likely developed within the accumulation zones that are present down slope of the depletion zones of rockslides.

The regional thrusts such as MCT and MBT have positive spatial associations with either type of shallow landslides (Figs. 6.4c-d). Within 2400 m of these regional thrusts, there is at least 24% higher likelihood of Sh_rs (Fig. 6.4c). Within 1600 m of those regional thrusts, there is at least 20% higher

likelihood of Db_rs (Fig. 6.4d). These results are meaningful because, in a structurally complex terrain like the Himalayan FTB, proximity to regional discontinuities such as MCT and MBT are inherent structural controls on landslides. Thus, proximity to MCT/MBT can be used as a predictor of susceptibility to occurrence of either Sh_rs or Db_rs in the area (Anbalagan, 1992; Gupta, 2005; Anbarasu et al., 2010; Ghosh and Carranza, 2010).

The spatial association analyses of proximity to different faults/fractures show that NNE-, NE- and NW-trending faults/fractures have strong positive spatial associations with shallow rockslides (Sh_rs), whereas NNW-, WNW- and NW-trending faults/fractures have strong positive spatial associations with shallow debris slides (Db_rs) (e.g., Figs. 6.4e-f). The strong positive spatial associations of Sh_rs with NNE- and NE-trending faults/fractures can be explained by the presence of several sympathetic faults/fractures sub-parallel to the general NE trend of MCT and MBT, which are inherent structural controls on geomorphic processes in the area. The strong positive spatial association of Sh_rs with NW-trending faults/fractures is likely due to some prominent NW-trending faults/fractures that form oblique angles with the MCT and MBT. The positive spatial association of Db_rs with northwesterly trending faults/fractures can be explained by the fact that many Db_rs are the products of landslide reactivation as they occur at the toes of the shallow rockslide occurrences (Anbalagan, 1992; Shroder, 1998; Weidinger and Korup, 2009), which are associated spatially with NW-trending faults/fractures. Thus, different sets of faults/fractures, according to their trends, have different degrees of spatial association with the landslides under study (Ghosh and Carranza, 2010).

Within 150 m of 2nd–4th order streams, there is only 9% higher likelihood of Sh_rs whereas within 70 m of 2nd–4th order streams, there is about 19% higher likelihood of Db_rs occurrence than would be expected due to chance (Figs. 6.4g-h). These results are consistent with earlier results that most Db_rs are present at relatively lower elevations than most Sh_rs and are more proximal to 2nd–4th order streams. Although, compared to the proximity to streams, other hydrologic factors such as wetness index, contributing area upslope and drainage density have weak spatial associations with both types of shallow landslides.

Some rockslides (Sh_rs) and debris slides (Db_rs) in the area occurred along or close to the national highway (NH-55) and railway track as well as along other roads. However, the results of spatial association analysis show that occurrences of either Sh_rs or Db_rs mainly have weak positive spatial associations with roads because we had to consider the entire map area for

the present spatial association analysis. Although, it never rules out the fact that proximity to road cuts in mountainous terrain increases the susceptibility to landsliding.

Within old rockslides and within 90 m and 155 m of those spatial features, 72% of Sh_rs and 65% of Db_rs are present, respectively, and there exists chances of 42% higher likelihood of Sh_rs and 25% higher likelihood of Db_rs. Similarly, kinematically unstable slopes have strong positive spatial association with either Sh_rs or Db_rs. Within kinematically unstable slopes and within 100 m of those spatial features, about 84% of Sh are present and there exists chances of 24% higher likelihood of Sh_rs. Within kinematically unstable slopes and within 137 m of those spatial features, about 87% of Db_rs are present and there exists chances of 17% higher likelihood of Db_rs. Therefore, presence of and proximity to either old rockslides or kinematically unstable slopes are good predictors of susceptibility to shallow translational landsliding in the area.

For consulting the illustrations related to the results of DDA of other continuous spatial factors, Annexure IV in the enclosed CD may be perused.

6.5.3 Weighting of spatial factors

Table 6.3 shows the results of quantified spatial association in the form of predictor rating (PR) of all the predictors used for determination of pairwise ratings of relative importance (Table 6.4) using the 9-point pairwise rating scale in AHP (see Saaty, 1977 for details). The fractional weights for all the identified 22 spatial factors are obtained (Table 6.5), the sum of which equals to 1 explaining that approximately 100% of the explained variances are satisfied in the AHP pairwise importance rating matrix prepared by using PR. The integer weights of the important and selected predictors of susceptibility to both Sh_rs and Db_rs obtained using AHP as shown in Tables 6.4 & 6.5. The consistency ratio of AHP weights obtained so far, was below 0.1 (Table 6.6), indicating that (a) inconsistencies among pairwise ratings of predictors of susceptibility to occurrence of Sh_rs and Db_rs are minor and (b) estimated fractional (or integer) weights of predictors of susceptibility to occurrence of either Sh_rs or Db_rs are consistent.

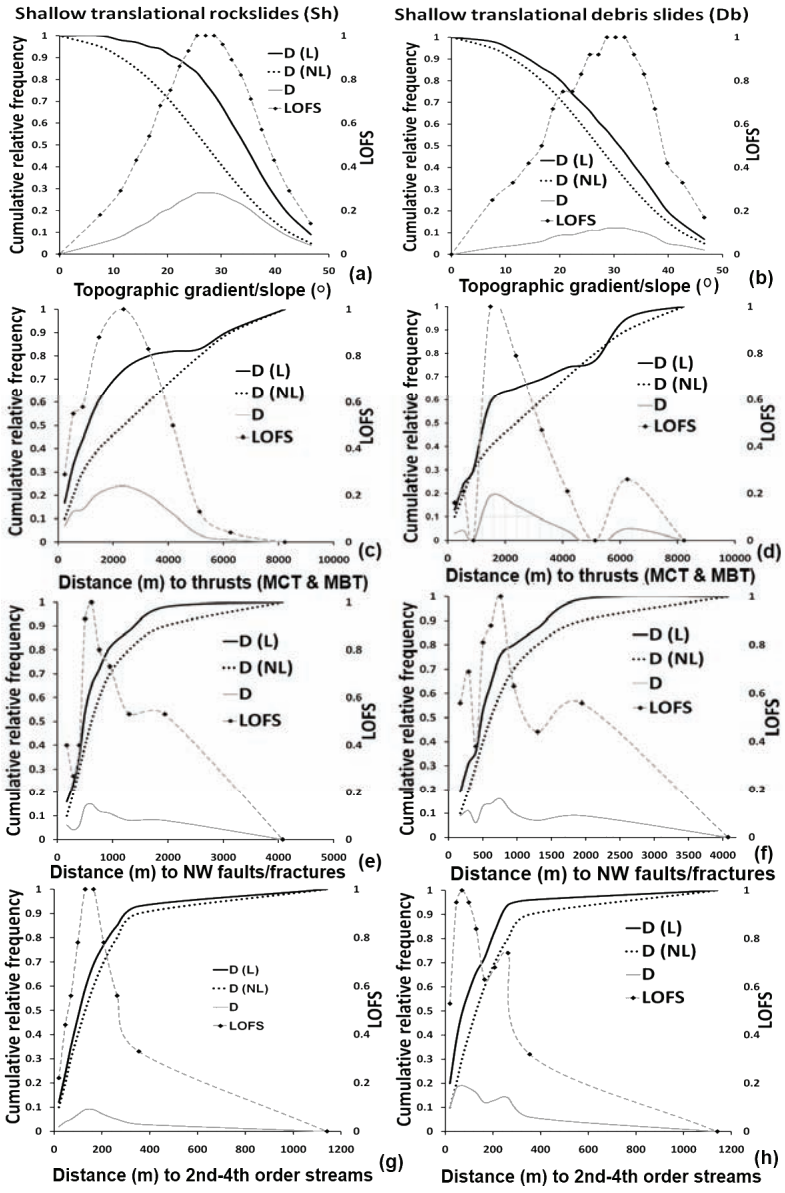

Fig. 6.4 Cumulative relative frequencies of topographic gradient/slope and distances from major thrusts, faults/fractures and other linear features at Sh and Db locations and at non-landslide locations. (a) Spatial association of topographic gradient/slope at Sh and non-Sh locations. (b) Spatial association of topographic gradient/slope with Db and non-Db locations. (c) Spatial association of MCT and MBT with Sh and non-Sh locations. (d) Spatial association of MCT and MBT with Db and non-Db locations. (e) Spatial association of NW-trending faults/fractures with Sh and non-Sh locations. (f) Spatial association of NW-trending faults/fractures with Db and non-Db locations. (g) Spatial association of 2nd–4th order streams with Sh and non-Sh locations. (h) Spatial association of 2nd–4th order stream with Db and non-Db locations.

6.5.4 Predictive modelling of susceptibility

6.5.4.1 Predictive models of susceptibility to shallow translational rockslides (Sh_rs)

Model-1 of susceptibility to Sh_rs occurrence (i.e., based on 14 selected and weighted predictors; Table 6.7) has 79% success rate (Fig. 6.5a) and 91% prediction rate (Fig. 6.5c) based on 30% of the study area with the highest values of $\overline{S}$. *Model-1* has a prediction rate of 89% against Dp_rs occurrences in 30% of the study area with highest values of $\overline{S}$ (Fig. 6.5e), suggesting that the 14 selected and weighted predictors of Sh_rs are relevant for predictive modelling of susceptibility to occurrence of deep-seated rockslides. However, *Model-1* has a poor prediction rate (54%, based on 30% of the study area with highest values of $\overline{S}$) against Db_rs occurrences (Fig. 6.5g), indicating that the spatial factors of Sh_rs occurrence and their inter-predictor weights are strongly different from those of Db_rs occurrence. This illustrates that predictive modelling of S_L must be specific to a landslide type, or that landslides of strongly different types must not be used for predictive modelling of S_L.

Model-2 of susceptibility to Sh_rs occurrence (i.e., based on 14 selected but un-weighted predictors) has 71% success rate (Fig. 6.5a) and 83% prediction rate (Fig. 6.5c) based on 30% of the study area with highest values of $\overline{S}$. Model-2 has a prediction rate 64% against Dp_rs occurrences in 30% of the study area with highest values of $\overline{S}$ (Fig. 6.5e). Thus, Model-2 does not outperform Model-1, indicating that different degrees of influence of individual spatial factors on landslide occurrence must be quantified for predictive modelling of S_L. Model-3 has 77% success rate (Fig. 6.5a) and 90% prediction rate (Fig. 6.5c) against calibration and validation Sh_rs, respectively, and 87% prediction rate against Dp_rs (Fig. 6.5e) based on 30% of the study area with highest values of $\overline{S}$. Thus, Model-3 does not outperform Model-1, indicating that using all identifiable spatial factors of landslide occurrence undermines predictive modelling of S_L.

Model-4 of susceptibility to Sh_rs occurrence has an overall 92.6% goodness-of-fit with calibration Sh_rs (Table 6.8). Out of 69 input predictors, 45 predictors contribute significantly to Model-4 (Table 6.9). Based on 30% of the study area with the highest values of $\overline{LOS_i}$, Model-4 has, compared to Model-1, a higher success rate (87%, Fig. 6.5a) against calibration Sh_rs, but has a slightly lower prediction rate (89%, Fig. 6.5c) against validation

Sh_rs and a substantially lower prediction rate (79%, Fig. 6.5e) against Dp_rs. These results indicate that LR modelling of S_L allows better goodness-of-fit between predictors and calibration landslides but does guarantee higher prediction rates against validation landslides. Moreover, compared to Model-1, Model-4 has very poor prediction rate (34%) against Db_rs, indicating further that predictive modelling of S_L must be specific to a landslide type.

Table 6.8 Results of model calibration of Model-4 (LR) for susceptibility to Sh_rs and Db_rs

Model performance					
Observed			Predicted LOS (Slide_1968-2003)		
			0	1	% Correct
Model-4 (Sh_rs)	LOS (Slide 1968-2003)	0	524	60	89.7
		1	43	541	92.6
		Overall (%)			91.2
Observed			Predicted LOS (Slide_1968-2003)		
			0	1	% Correct
Model-4 (Db_rs)	LOS (Slide 1968-2003)	0	178	28	86.4
		1	27	179	86.9
		Overall %			86.7

The results of ROC analyses (Figs. 6.5b,d,f,h) are statistically significant and show low levels of estimated model error. The lower ROC areas for Model-2 (0.762) and Model-3 (0.598), compared to Model-1 (0.802) (Fig. 6.5b), show that predictive modelling of S_L based on selected and weighted predictors (Model-1) results in higher sensitivity (true positive rate) than based on selected but un-weighted predictors (Model-2) and on all identifiable spatial factors (Model-3). ROC analyses based on validation Sh_rs (Fig. 6.5d) and on Dp_rs (Fig. 6.5f), indicate that the sensitivities or true positive rates of Model-1 and Model-4 are much higher than those of Model-2 and Model-3. With respect to Dp_rs, the ROC areas for Model-2 (0.743) and Model-3 (0.527), compared to that of Model-1 (0.855), suggest that the predictors used to derive Model-1 would be useful in predictive modelling of susceptibility to Dp_rs occurrence in the area. The ROC analyses of Model-1, Model-2 and Model-3 with respect to Db_rs occurrences show low sensitivities, suggesting that Db_rs is strongly dissimilar to Sh_rs and Dp_rs and that predictive modelling of susceptibility to Db_rs occurrence will not benefit from using predictors of susceptibility to either Sh_rs or Dp_rs occurrence.

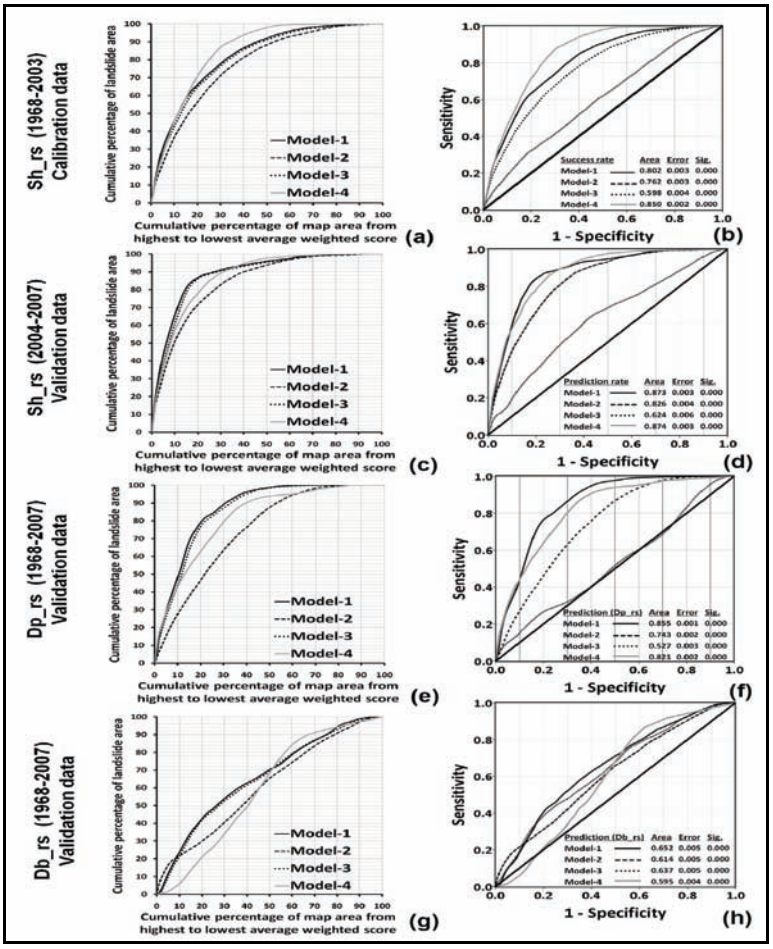

Fig. 6.5 Success rate, prediction rate and ROC curves for different predictive models (Model-1 to Model-4) of susceptibility to shallow rocksliding. The validation and goodness-of-model-fitting curves were calculated based on (a-b) calibration Sh_rs (1968-2003), (c-d) validation Sh_rs (2004-2007), (e-f) validation deep-seated rockslides of 1968-2007 (Dp_rs) and (g-h) validation shallow debris slides of 1968-2007 (Db_rs). The plots in (a) represent success rate curves of four predictive models and the plots in (c), (e) and (g) represent prediction rate curves for four predictive models. The corresponding ROC curves are shown at (b), (d), (f) and (h) respectively.

Tables 6.7 and 6.9 illustrate the inconsistencies among the predictors selected to derive Model-1 and Model-4 of susceptibility to Sh_rs occurrence. For slope aspect, LR modelling selected and assigned highest weight for NNE-facing slopes, whereas our field observations and bivariate spatial association analysis indicate that this particular aspect class exhibits negative spatial association with Sh_rs. For lithology, LR modelling selected 11 out of 13 input predictors, whereas bivariate spatial association analyses indicate three predictors consisting of mainly weathered lithology (i.e., WRSHGN, WRSIWA,

and WRSHPH). For geomorphology, LR modelling selected HDISVAL, LDISVAL, MDISVAL and RIDGE (Table 6.9), but the bivariate spatial association analyses show that these spatial factors lack spatial association with Sh_rs. Nevertheless, LR modelling and bivariate spatial association analyses resulted in selection of similar predictors such as slope, elevation, land-use/land-cover, proximity to old rockslides (pre-1968) and proximity to some sets of structures. However, unlike the proposed methodology (i.e., Model-1), LR modelling (Model-4) did not select proximity to kinematically unstable slopes as a predictor of susceptibility to Sh_rs occurrence.

Finally, by classifying the output $\overline{S}$ values in Model-1 into four categories – very high, high, moderate and low – based on the difference between prediction and success rate curves (Fig. 6.6a), the qualitative Sh_rs susceptibility map (Fig. 6.6b) was prepared. Areas with very high and high susceptibility to Sh_rs occurrence based on Model-1 contain 79% of 1968–2003 Sh_rs (calibration set) and 91 % of 2004–2007 Sh_rs (validation set). Areas with very high and high susceptibility to Sh_rs occurrence contain 90% of Dp_rs in the area, suggesting that the predictors to Sh_rs are equally relevant to Dp_rs occurrence in the area. Similarly, by classifying the output $\overline{LOS}_i$ values in Model-4 into four classes based on the difference between the prediction and success rate curves (Fig. 6.6c), we prepared a qualitative Sh_rs susceptibility map (Fig. 6.6d). Areas with very high and high susceptibility to Sh_rs occurrence based on Model-4 contain 87% of calibration Sh_rs, 89% of validation Sh_rs and 79% of Dp_rs occurrences in the area.

6.5.4.2 Predictive models of susceptibility to shallow translational debris slides (Db_rs)

Model-1 of susceptibility to Db_rs occurrence (i.e., based on 12 selected and weighted predictors; Table 6.7) has 84% success rate (Fig. 6.7a) and 95% prediction rate (Fig. 6.7c) based on 30% of the study area with highest values of $\overline{S}$. Model-1 has poor prediction rates of 68% and 54% against Dp_rs occurrences (Fig. 6.7e) and Sh_rs occurrences (Fig. 6.7g) based on 30% of the study area with highest values of $\overline{S}$, indicating that the spatial factors of susceptibility to Db_rs occurrence are strongly different from those of Dp_rs and Sh_rs occurrences. This illustrates that predictive modelling of S_L must be specific to a landslide type, or that landslides of strongly different types must not be used for predictive modelling of S_L.

Model-2 of susceptibility to Db_rs occurrence (i.e., based on 12 selected but un-weighted predictors) has 82% success rate (Fig. 6.7a) and 95%

prediction rate (Fig. 6.7c) based on 30% of the study area with highest values of $\overline{S}$. Thus, Model-2 does not outperform Model-1, indicating that different degrees of influence of individual spatial factors on landslide occurrence must be quantified for predictive modelling of S_L. Model-3 has 84% success rate (Fig. 6.7a) and 96% prediction rate (Fig. 6.7c) against calibration and validation Sh_rs, respectively, and 64% prediction rate against Dp_rs (Fig. 6.7e) based on 30% of the study area with highest values of $\overline{S}$. Thus, Model-3 does not outperform Model-1, indicating that using all identifiable spatial factors of landslide occurrence undermines predictive modelling of S_L.

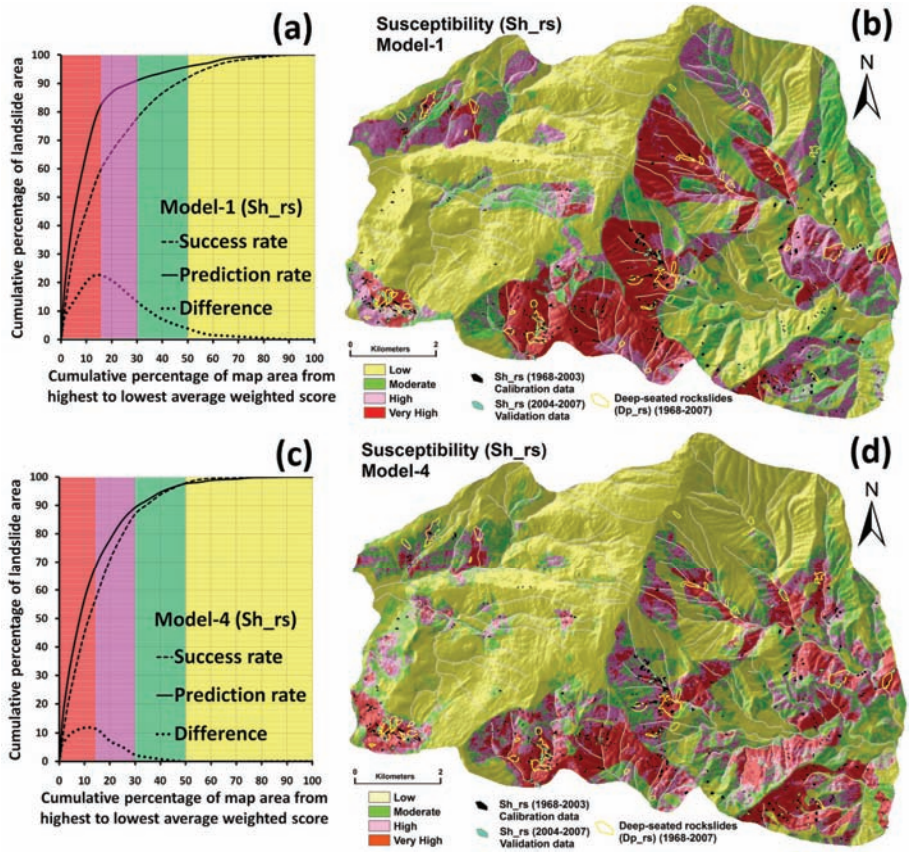

Fig. 6.6 Predictive Model-1 (based on 14 selected and weighted predictors) and Model-4 (backward stepwise LR) of susceptibility to occurrence of Sh_rs. (a) Success and prediction rate curves of Model-1. (b) Map of classified susceptibility to occurrence of Sh_rs obtained via Model-1. (c) Success and prediction rate curves of Model-4 (backward stepwise LR). (d) Map of classified susceptibility to occurrence of Sh_rs obtained via Model-4.

Table 6.9 Generic factors of shallow translational landslides and selected predictors of susceptibility to Sh_rs and Db_rs occurrence in the study area. (For Sh_rs, also Table 6.5).

Predictor variables			*Model-4* (Sh_rs)	*Model-4* (Db_rs)
Description		Code	*b*	*b*
Drainage density		Drndens	-168.64	(-)353.66
Elevation		Elvn	-0.004	-
Slope		Slope	0.067	-
Aspect		NNE	4.447	-
		NEAST	3.116	-
		ENE	2.592	-
		ESE	2.661	-
		SE	3.618	-
		SSE	2.715	-
		SSW	2.767	1.731
		SW	3.549	-
		WSW	3.190	-
		WNW	3.955	-
		NW	3.640	-
		NNW	2.290	-
Proximity to structures	0–200 m of ENE-trending faults/fractures	LENE	0.636	-
	0–200 m of NE-trending faults/fractures	LNE	-0.676	-
	0–200 m of NNE-trending faults/fractures	LNNE	-	(-)1.321
	201–500 m of NNE-trending faults/fractures	MNNE	-0.461	(-)0.915
	0–200 m of NNW-trending faults/fractures	LNNW	0.788	-
	201–500 m of NNW-trending faults/fractures	MNNW	0.773	-
	0–200 m of NW-trending faults/fractures	LNW	0.712	-
	0–200 m of WNW-trending faults/fractures	LWNW	-	1.356
	201–500 m of WNW-trending faults/fractures	MWNW	-	0.839
	201–500 m of major thrusts	MTH	1.518	-
Geomorphology	Steep escarpments and denudational niches	ENTRVAL	-1.872	(-)2.643
	Flat ridge	RIDGE	-2.149	(-)3.234
	Highly dissected intermontane valley	HDISVAL	-1.629	(-)2.286
	Intermontane Plateau	PLATEAU	-	(-)24.103
	Lowly dissected intermontane valley	LDISVAL	-2.859	(-)3.656
	Moderately dissected intermontane valley	MDISVAL	-2.762	-
Land-cover/ land-use	Barren and agricultural flat lands	AGRI	-1.808	-
	Barren mountain slope	BARREN	1.386	-
	Moderately vegetated forest	MF	-	0.902
	Sparsely vegetated forest	SPF	0.852	-
	Tea cultivation	TEA	-0.926	-
Lithology	Alluvium mixed with colluvium	COLUALU	-5.662	2.356
	Quartzite and phyllite	FRCSCH	-2.340	(-)2.660
	Fresh sandstone (Gondwana)	FRGOND	-3.412	-
	Fresh gneiss	FRGN	-2.981	(-)2.127
	Sheared gneiss (Lingtse)	SHGN	-3.991	-
	Scree and weathered regolith	SCR	-6.170	-
	Weathered gneiss	WRGN	-1.149	-
	Weathered schists and phyllite	WRSCH	-2.216	-
	Weathered sheared phyllonite	WRSHPH	-	(-)20.522
	Weathered colluvium and debris	WRCOLU	-4.958	3.022
	Weathered sandstone (Gondwana)	WRGOND	2.562	-
2nd–4th order streams	0–50 m of 2nd–4th order streams	LSTRM	-	1.040
Proximity to road	0–50 m of road	LRD	1.071	-
	51–100 m of road	MRD	1.106	-
Presence and proximity to old rockslides (pre-1968)	0–50 m of old rockslides	LOLDSLD	2.841	-
	51–100 m of old rockslides	MOLDSLD	1.35	-
Depth to bedrock	Low (0–1 m)	LD	-	1.314

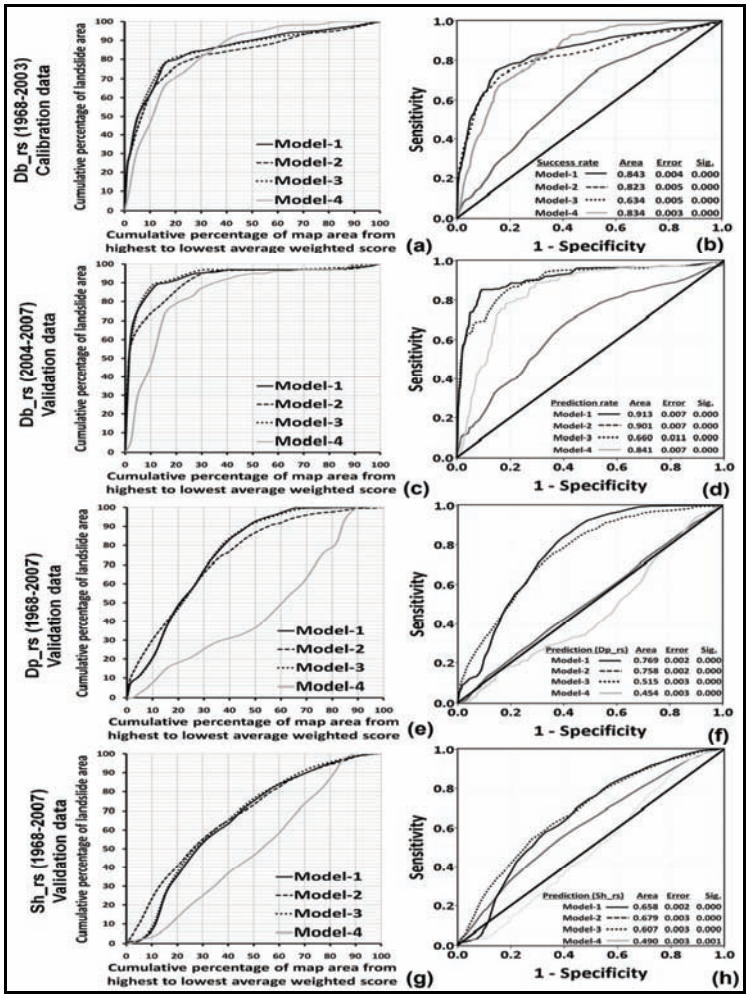

Fig. 6.7 Success rate, prediction rate and ROC curves for different predictive models (Model-1 to Model-4) of susceptibility to shallow debris sliding. The validation and goodness-of-model-fitting curves were calculated based on (a-b) calibration Db_rs (1968-2003), (c-d) validation Db_rs (2004-2007), (e-f) validation deep-seated rockslides of 1968-2007 (Dp_rs) and (g-h) validation shallow rock slides of 1968-2007 (Sh_rs). The corresponding ROC curves are shown in (b), (d), (f) and (h) respectively.

Model-4 of susceptibility to Db_rs occurrence has an overall 86.7% goodness-of-fit with calibration Db_rs (Table 6.8). Out of 72 input predictors, 19 predictors contribute significantly to Model-4 (Table 6.9). Based on 30% of the study area with the highest values of $\overline{LOS_i}$, Model-4 has, compared to Model-1, a slightly lower success rate (81%, Fig. 6.7a) against calibration Db_rs and a much lower prediction rate (86%, Fig. 6.7c) against validation Db_rs and an extremely lower prediction rate (~25%, Fig. 6.7e) against Dp_rs. These results indicate that LR modelling of S_L provides for satisfactory

goodness-of-fit between predictors and calibration landslides but does less satisfactory prediction rates against validation landslides. Moreover, compared to Model-1, Model-4 has also has lower prediction rates against validation Dp_rs and Sh_rs occurrences, indicating further that predictive modelling of SL must be specific to a landslide type.

The results of ROC analyses Fig. 6.7 are statistically significant and show low levels of estimated model error. The lower ROC areas for Model-2 and Model-3, compared to Model-1 (Figs. 6.7b,d), show that predictive modelling of S_L based on selected and weighted predictors (Model-1) results in higher sensitivities (true positive rates) than those based on selected but un-weighted predictors (Model-2) and on all identifiable spatial factors (Model-3). Results of ROC analyses based on validation Db_rs show that the sensitivity or true positive rate of Model-4 is slightly lower than that of Model-1 (Fig. 6.7b and Fig. 6.7d). This goes to show that, with respect to Db_rs, our proposed methodology for selection and weighting of predictors outperforms the LR algorithm for selection and weighting of predictors. Figs. 6.7f and 6.7h further show that the four predictive models of susceptibility to Db_rs have low ROC areas with respect to landslides of dissimilar types (Dp_rs and Sh_rs). This illustrates that predictive modelling of S_L must be specific to a landslide type, or that landslides of strongly different types must not be used for predictive modelling of S_L.

Tables 6.7 and 6.9 illustrate the inconsistencies among the predictors selected to derive Model-1 and Model-4 of susceptibility to Db_rs occurrence. For slope aspect, LR modelling selected only SSW-facing slopes, whereas bivariate spatial association analyses indicate that Db_rs occurrences have positive spatial associations with SW-, SSW-, SE- and SSE-facing slopes. For geomorphology, LR modelling did not select old terraces, screes and scarps, although these units exhibit positive spatial associations with Db_rs occurrence. For land-use/land-cover, LR modelling did not select agricultural areas, sparse forests and barren slopes although these units exhibit positive spatial associations with Db_rs occurrence. LR modelling shows that proximity to WNW-trending faults/fractures is the main structural factor of Db_rs occurrence, but our proposed methodology of selecting and weighting predictors based on bivariate spatial association analysis shows that proximity to NNW- and NW-trending faults/fractures are also important structural factors of Db_rs occurrence. Nevertheless, LR modelling and bivariate spatial association analyses were more-or-less consistent in terms of selecting lithology as predictor and in terms of not selecting elevation and proximity to old rockslides (pre-1968) as predictors of Db_rs occurrence. However, it can be observed that predictors selected in LR modelling of

susceptibility to Db_rs occurrence are less realistic than those selected via bivariate spatial association analysis.

Finally, by classifying the output $\overline{S}$ values in Model-1 into four categories – very high, high, moderate and low – based on the difference between prediction and success rate curves (Fig. 6.8a), the qualitative Db_rs susceptibility map (Fig. 6.8b) was prepared. Areas with very high and high susceptibility to Db_rs occurrence based on Model-1 contain 78% of 1968–2003 Db_rs (calibration set) and 90 % of 2004–2007 Db_rs (validation set). Similarly, by classifying the output $\overline{LOS}_i$ values in *Model-4* into four classes based on the difference between the prediction and success rate curves (Fig. 6.8c); a qualitative Db_rs susceptibility map was prepared (Fig. 6.8d). Areas with very high and high susceptibility to Sh_rs occurrence based on Model-4 contain 71% of calibration Db_rs and 80% of validation Db_rs in the area.

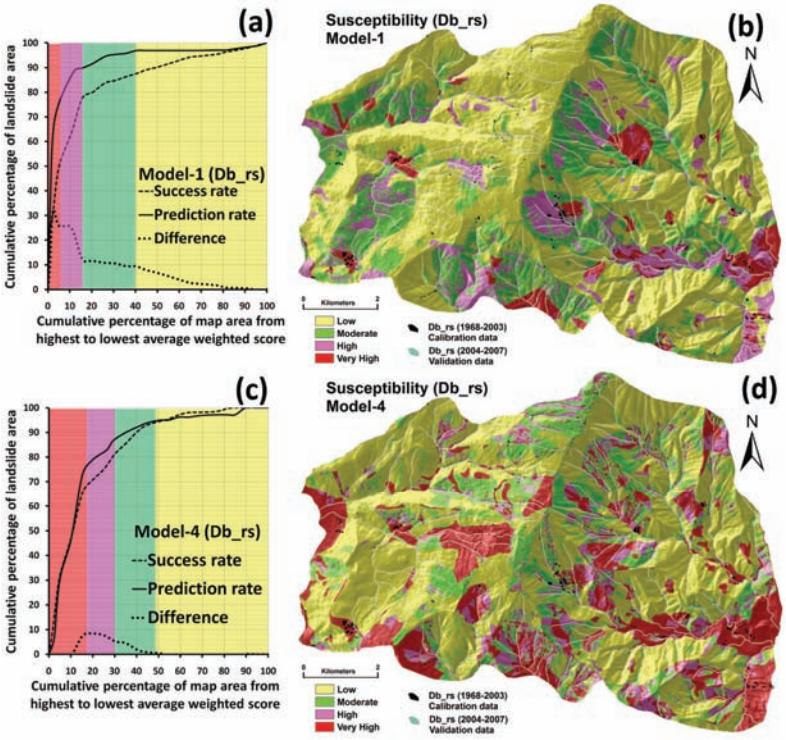

Fig. 6.8 Predictive Model-1 (based on 12 selected and weighted predictors) and Model-4 (backward stepwise LR) of susceptibility to occurrence of Db_rs. (a) Success and prediction rate curves of Model-1. (b) Map of classified susceptibility to occurrence of Db_rs obtained via Model-1. (c) Success and prediction rate curves of Model-4 (backward stepwise LR). (d) Map of classified susceptibility to occurrence of Db_rs obtained via Model-4.

6.6 Discussion

Predictive modelling of susceptibility to landsliding of a certain type involves the empirical selection and assignment of weights to appropriate predictors (Guzzetti et al., 2005; van Westen et al., 2008; Van Den Eeckhaut et al., 2009). That is because susceptibility to landsliding is a function of two types of spatial associations: (1) spatial associations of individual spatial factors with known occurrences of landslides of a certain type; and (2) relative importance of every spatial factor with respect to other spatial factors in relation to those known landslide occurrences.

6.6.1 Modelling of predictor-target spatial associations

For quantifying spatial associations between predictor and target variables, in this study, (a) Yule's coefficient to evaluate spatial associations between landslide occurrences and discrete field factors (e.g., lithology, aspect, etc.) and the (b) distance distribution analysis to evaluate spatial association between landslide occurrences and continuous field factors (e.g., slope, elevation, etc.) were used. Both of these objectives can also be achieved by calculating likelihood functions (Fisher, 1922; Pratt, 1976), weights-of-evidence (Good, 1950; Bonham-Carter, 1994) and evidential belief functions (Dempster, 1967; Shafer, 1976). These methods of bivariate analysis measure predictor-target spatial associations in probabilistic terms and have been used in predictive modelling of susceptibility to certain types of natural hazards (Lee and Choi, 2004; Carranza and Castro, 2006; Ghosh and Carranza, 2010; Regmi et al., 2010). Other methods of bivariate analysis for measuring predictor-target spatial associations with probabilistic interpretations involve calculating landslide frequency or density analysis per predictor class (Ayalew and Yamagishi, 2005; Yalcin, 2008; Blahut et al., 2010). Here, in this research the Yule's coefficient and the distance distribution analysis were introduced because, to the best of the existing knowledge, they have not been applied in predictive modelling of landslide susceptibility.

The predictor-target spatial associations quantified by the Yule's coefficient and the distance distribution analysis also have probabilistic interpretations. Note that the value of Y_C (Eq. (5.3)) is based on areal proportions, which are also the bases of spatial conditional probability calculations (Bonham-Carter, 1994). Note also that the D-statistic in distance distribution analysis is equivalent to the spatial contrast (W+–W–) in weights-of-evidence analysis (Good, 1950; Bonham-Carter, 1994), which is based on the Bayesian theory of probability (Bayes, 1764). Therefore, in probabilistic terms, a positive value of Y_C or D implies that a spatial factor class increases the likelihood of

landslide occurrence of a particular type, whereas a negative of Y_C or D implies that a spatial factor class decreases the likelihood of landslide occurrence of a particular type. Accordingly, maps with relevant spatial factor classes found to have positive spatial associations with known landslide occurrences of a certain type are considered predictors in predictive modelling of susceptibility to occurrence of that type of landslide.

It can be argued that quantified positive factor-landslide spatial associations, regardless of which method of bivariate analysis is applied, may not necessarily imply genetic associations between spatial factors and landslides. That is because, at local-scales, landslides are dynamic objects whereas spatial factors or features considered in the analysis represent static objects. However, the methods of bivariate analysis used here and discussed above have been used in predictive mapping of mineral prospectivity (Bonham-Carter, 1994; Pan and Harris, 2000), wherein the target (mineral deposit occurrence) and predictor variables considered all represent static objects and the results of spatial association analyses are given district- to regional-scale genetic predictor-target interpretations (Carranza, 2009). Nevertheless, in the present study, comparisons of site-specific observations of landslides vis-à-vis quantified positive regional-scale spatial associations between certain factor classes and landslides suggest genetic links between some spatial factors and landslide occurrence. One example is that shallow translational rockslides in the area occur on and have positive spatial associations with weathered bedrock but they do not occur on and, thus, have negative spatial associations with alluvial/colluvial deposits (Table 6.2). Another example is that shallow translational rockslides in the area have positive spatial association with MCT/MBT, which is likely real because previous works in the area and elsewhere show the following. The MCT/MBT are regional-scale tectonic controls on structural and geomorphological developments in the area (Banerji et al., 1980; Acharya, 1989), local stress fields vary with respect to major tectonic structures (Pandey et al., 1999; Singh and Thakur, 2001; Joshi and Hayashi, 2008) and mechanisms for slope deformation are influenced by variations in distribution of stress (Di Luzio et al., 2004; Kinakin and Stead, 2005; Cadoppi et al., 2007). Therefore, the results of the bivariate analyses of spatial associations presented in this work are intuitive and instructive, if not, realistic. In contrast, some of the factor-landslide spatial associations quantified through logistic regression analysis (Table 7) are less intuitive and instructive.

6.6.2 Pairwise modelling of predictor-target relationships

Various relevant spatial factors are involved in landsliding and individual relevant spatial factors have different degrees of influence of landsliding. Assignment of meaningful weights to individual predictors, to portray the relative importance of every spatial factor with respect to other spatial factors in relation to known landslide occurrences, is a highly subjective exercise. It may involve a trial-and-error procedure, even in the case when expert knowledge is available especially from different experts. The difficulty of the exercise lies in deciding objectively and simultaneously how much more important or how much less important is one predictor compared to every other predictor. This difficulty is alleviated here with the application of the analytical hierarchy process (Saaty, 1977). In this process, the quantified spatial associations between landslides and individual predictors were used as bases, by converting them into predictor ratings (Eq. (6.5)), because somehow they suggest genetic links between some spatial factors and landslide occurrence. Expert knowledge is, nonetheless, essential in this process because quantified factor-landslide spatial associations may not necessarily imply genetic associations between spatial factors and landslides.

Because expert knowledge is subjective, it is considered non-instructive to describe here how precisely the pairwise comparison matrix were obtained so that readers may be able to replicate the process. The only guide for objectivity is to obtain a consistent pairwise comparison matrix (Saaty, 1977) using the results of the proposed spatial association analyses (Table 6.3). A matrix is consistent if every value across each row in a pairwise comparison matrix is a multiple of every other value in the other rows. We observe, however, that this may not be the case always with the pairwise importance matrix (Table 6.5), illustrating the subjectivity (or inconsistency) introduced by applying expert knowledge in the pairwise comparison process. Nevertheless, the analytical hierarchy process provides for quantifying and determining whether inconsistencies in a pairwise comparison matrix are within acceptable limits (Table 6.6).

Because the analytical hierarchy process involves simultaneous use of three variables (i.e., two predictors, one target), it constitutes a semi-multivariate analysis. In fact, analytical hierarchy process is a form of principal component analysis, wherein loadings on individual variables in a component reflect their degrees of association in that component. Thus, the methodology proposed here above actually endeavours to emulate multivariate analysis in modelling of predictor-target relationships and predictor-predictor relationships with respect to targets. That is because, for example, in stepwise multiple

regression, predictor-target relationships are evaluated in a number of steps until a final model is obtained consisting of only predictors that contribute significantly to the prediction of the target variable. The logistic regression analysis was chosen for comparing the performance of the proposed methodology. The consistency among predictors derived through logistic regression and the proposed methodology constitutes a basis to describe the efficacy of the proposed methodology. However, describing that further in terms of magnitude of predictor weights is irrelevant because logistic regression coefficients are non-linear weights whereas predictor weights derived through methods of bivariate spatial association are linear weights.

6.6.3 Integration of predictors and evaluation of susceptibility maps

The weighted multi-class index overlay (Eq. (6.6)) was used to integrate individual predictors because it allows to model susceptibility to landsliding of a certain type as a function of the two types of spatial associations described in Eq. (6.1) and in the first paragraph of this discussion section. This objective can neither be achieved by application of weights-of-evidence modelling (Bonham-Carter, 1994) nor evidential belief modelling (Carranza and Castro, 2006). That is because these two predictor integration modelling techniques accommodate only predictor class weights (e.g., F_{ji} in Eq. (6.6)), which represent overall spatial associations of individual predictors with the target, but they do not accommodate predictor weights (e.g., W_i in Eq. (6.6)), which represent relative importance of every predictor with respect to other predictors in relation to the target.

If weights-of-evidence or evidential belief modelling were applied, the results would have been more similar to Model-2 (i.e., using selected but un-weighted predictors) and less similar to Model-3 (i.e., using all relevant spatial factors as predictors with their respective weights). As shown above, Model-1 (i.e., using selected but un-weighted predictors) outperforms Model-2 and Model-3, regardless of the type of landslides being examined. This goes to show two things: (1) the importance of selecting predictors and assigning weights to predictors; and (2) the advantage of the weighted multi-class index overlay modelling technique over weights-of-evidence and evidential belief modelling techniques. The latter is supported by the following facts. Weights-of-evidence modelling is disadvantaged by the assumption of conditional independence among predictors with respect to target (Bonham-Carter, 1994), whereas weighted multi-class index overlay modelling is not based on such assumption. Evidential belief modelling is disadvantaged by the estimation of not one but three types of predictor class weights (Dempster, 1967; Shafer, 1976; Carranza and Castro, 2006),

whereas weighted multi-class index overlay modelling involves estimation of only one type of predictor class weights. Compared to weights-of-evidence, evidential belief and logistic regression modelling techniques, the main disadvantages of weighted multi-class index overlay modelling are: (a) it relies on methods of bivariate analysis for estimation of predictor class weights; and (2) it does not represent prediction uncertainty. Here, a map of prediction uncertainty associated with the logistic regression modelling was not shown because it cannot be used anyway to compare with the results of the proposed methodology.

Comparisons of the performance of the Model-4 (logistic regression model) with those of Model-1 show that the main weakness of the proposed methodology is in achieving a good fit between predictors and target (or success rate of prediction against calibration data). That, nevertheless, is a common weakness of bivariate analysis compared to multivariate analysis because the inter-play of multiple factors in landsliding is complex and requires, indeed, methods that can model it simultaneously. However, strong similarity in success and prediction rates between the two models indicates strong similarity in the spatial pattern of the classified susceptibility maps, which are also evident from visual inspection of these two susceptibility maps (e.g., Fig. 6.6b and Fig. 6.6d). The fact that prediction rate is higher than success rate in case of Model-1, compared to Model-4, means that in the former case the validation landslides have very strong spatial association with the predictions based on the training landslides. This means further that validation landslides and training landslides have strongly similar spatial characteristics, which result very satisfactory prediction results (Carranza et al., 2008b). Thus, Model-4 only outperforms Model-1 by 8% with respect to success-rate against shallow translational rockslides, but Model-1 outperforms Model-2 and Model-3. This indicates the major improvement in predictive modelling of landslide susceptibility that can be derived from our proposed methodology. Although our study area has limited extension, the strong similarity of geo-environmental settings and types of failure mechanisms in various parts of the Himalayan region (Anbalagan, 1992; Anbalagan and Singh, 1996; Ghoshal et al., 2008; Mathew et al., 2009), the methodology proposed here would be applicable in many parts of the region.

6.7 Conclusions

The application of the proposed methodology for selecting and weighting predictors of landslide susceptibility in the Darjeeling Himalayas (India) highlights the following findings.

- Not all relevant spatial factors of susceptibility to landsliding of a certain type, as identified theoretically and heuristically, can be used as predictors of landslide susceptibility.
- Methods for bivariate spatial association analysis, such as Yule's coefficients and distance distribution analysis are (a) instructive for defining empirical relationships between landslides and spatial factors and (b) useful for selection and weighting of spatial predictors of susceptibility to landsliding.
- Results of quantified bivariate spatial associations between landslides and spatial factors are useful empirical metrics because they help to reduce subjectivity of expert knowledge that is applied in the analysis of inter-predictor weights via analytical hierarchy process.
- Predictive maps of landslide susceptibility based on all possible predictors and on selected but un-weighted predictors do not outperform those based on selected and weighted spatial predictors.
- In the study area, predictors selected and weighted via the proposed methodology are more realistic than those obtained via logistic regression modelling. Because this may not necessarily be the case in other areas, further testing of the proposed methodology elsewhere is warranted.
- Predictive modelling of landslide susceptibility via a method of multivariate analysis, like logistic regression, is likely to result in high success-rates but not necessarily high prediction-rates.
- The results of the study demonstrate the usefulness of the proposed 2-stage methodology for selecting and weighting of spatial predictors for predictive modelling of landslide susceptibility.

After obtaining a satisfactory predictive map of landslide susceptibility, the next step is to use this map to prepare a landslide hazard and risk map (chapter 7).

Chapter 7: Integrating spatial, temporal and magnitude probability for medium-scale landslide hazard and risk estimation

Predictive mapping of landslides is the first step in quantitative hazard and risk assessment which is required for determining priorities of the society engaged in mitigating this hazard. This chapter presents a method for using the results of the predictive modelling described in chapter 6 in combination with event-based landslide inventories (chapter 3) for quantitative landslide hazard and risk analysis that can be applied at a medium scale to objectively determine various losses due to different plausible landslide hazard scenarios. This chapter is based on a paper on "*Integrating spatial, temporal and magnitude probability for medium scale landslide hazard and risk analysis in Darjeeling Himalayas*" (Ghosh et al., Submitted in Landslides).

7.1 Introduction

Quantitative landslide hazard and risk analysis requires the availability of sufficient historical landslide information in order to estimate the spatial, temporal and magnitude probabilities (Cruden, 1997; Einstein, 1997; Malamud et al., 2004; Fell et al., 2008; Zêzere et al., 2008; Salvati et al., 2010).

In most cases, however, information on past landslides is scarce which acts as a serious deterrent in correctly predicting landslide hazard scenarios and thereby impedes subsequent quantitative risk assessment. Thus, it has compelled many landslide scientists to rely more on susceptibility maps to do a qualitative/semi-quantitative landslide hazard and risk assessment (Anbalagan and Singh, 1996; Rautela and Lakhera, 2000; Kanungo et al., 2008) in areas where historic information on landslides is lacking. In literature, not much research on medium-scale (1:25,000) landslide hazard and risk estimation in a data-scarce environment is available, where varying levels of uncertainties that are expected to propagate in quantitative landslide hazard and risk assessment are shown.

In order to address the above issue this study was undertaken because, quantitative estimation of landslide hazard and risk (a) renders a standardized and quantifiable way to express the expected impact of landslides, and, (b) facilitates a more objective way to allocate or prioritize resources for mitigation by administrators. The hazard and risk assessment was undertaken in the study area (Fig. 1.1d), making use of the results of the steps presented in the earlier chapters. The chapter starts with a brief

recapitulation of the required data sets, followed by a description of the method applied and a presentation of the results.

7.2 Source data sets and information

Estimation of landslide hazard and risk starts with the predictive mapping of landslide susceptibility, which was presented in the previous chapter. The two landslide susceptibility maps (Figs. 6.6b and 6.8b) are used in the present study to calculate the impacts of rockslides and debris slides respectively in different hazard scenarios. To determine landslide events of certain magnitudes, a frequency-magnitude analysis is required, which has been carried out in this research via an empirical analysis between triggering factors (e.g., rainfall) and the known landslide event-days. For that particular study, daily rainfall data of the past 40 years (1968-2007) and 24 confirmed landslide event days were used (section 3.4).

For elements at risk, building and demographic data at the level of settlement units (hereafter, denoted as SU) were collected from the local village or administrative authorities, municipalities and census. For spatial representation of this data in the form of settlement units, a land-use/land-cover map prepared from high-resolution satellite imagery (5 m resolution IRS P6 MX image of 2004) was combined with the census blocks and village maps to make a settlement unit map containing 236 SUs (Fig. 7.1). Information on the number of buildings and population for each village block (locally known as “mouza”) obtained from the reports of the “Rural Household Survey (RHS), 2006” were integrated with the SU map. Each SU therefore, contains attribute information on the total number of buildings, type of dwelling structure and population and its related demographic details including number of children, employed people etc. (Fig. 7.1a and 7.1b; Table 7.1). For areas within the town of Kurseong, the same was obtained both from the census and municipality records. As this study focuses on medium scale analysis (1:25,000), the SUs are the basic units for loss estimation. Apart from the settlement units, spatial maps of major road networks were also used to calculate the likelihood of direct losses along roads in different hazard scenarios (Fig. 7.1c).

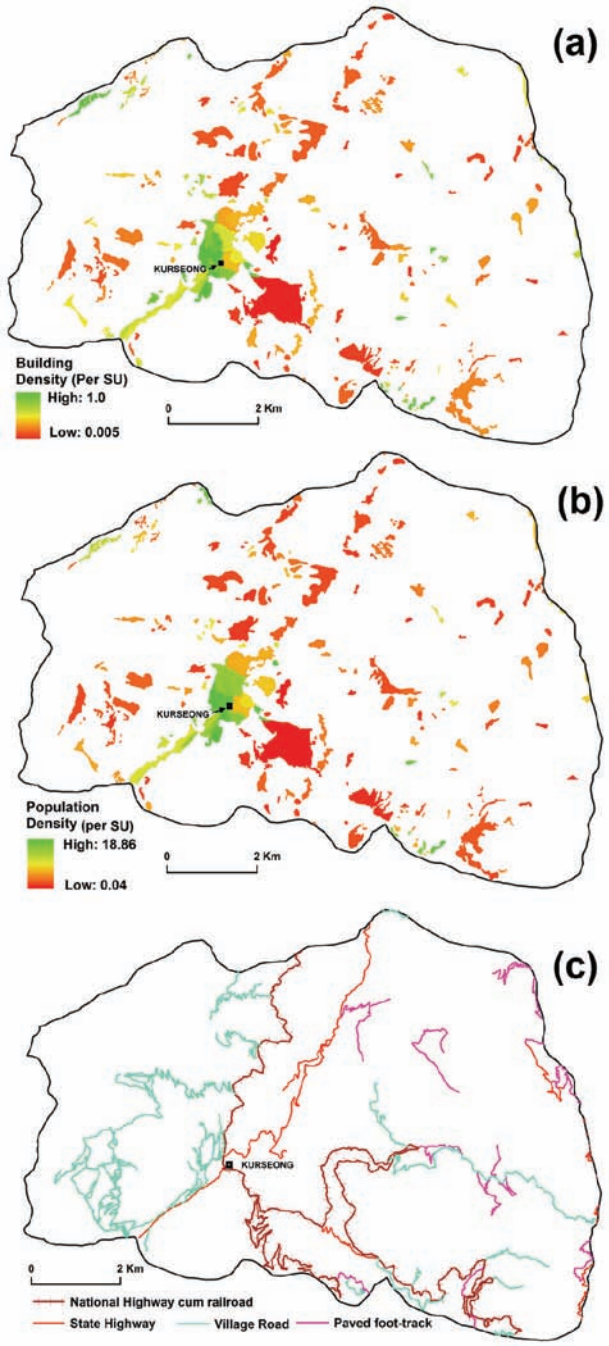

Fig. 7.1 Map showing major elements-at-risks of the study area. (a) Distribution showing building density (No/100 m^2), (b) distribution showing population density (No/100 m^2) and (c) major road networks.

Table 7.1. Details of different elements-at-risk used to calculate expected losses.

Details of elements-at-risk data	
Number of Settlement Units (SUs)	236
Total number of buildings	13736
Density of buildings (maximum)	0.005 (Nos./m^2)
Density of buildings (Minimum)	1.0 (Nos./m^2)
Total number of RCC buildings	1945
Total number of Concrete buildings	5208
Total number of squatter buildings	6583
Total population	76126
Population density (maximum) per SU	18.86 per 100 m^2
Population density (minimum) per SU	0.051 per 100 m^2
Population density (Average for the entire study area)	0.08 per 100 m^2
Population density in urban area (Average)	2.12 per 100 m^2
Population density in rural area (Average)	0.04 per 100 m^2
Total length (km.) of major roads	162 km

Source: Census of India, 2001 and Rural Household Survey (RHS), 2006

7.3 Landslide hazard and risk estimation methods

Landslide risk expresses the likelihood of losses arising from an event of certain magnitude within a given period of time and area (Lee and Jones, 2004). Therefore, the first step is to characterize landslide events with varying degrees of severity or magnitudes and determine their respective recurrence intervals. This is done using the event-based landslide inventories presented in Chapter 3 (section 3.4).

7.3.1 Prediction of landslide events and hazard scenarios

The temporal prediction of landslide events depends on the analysis of past event data and analysis of their return periods (RP) from which, the annual probability (AP) can be estimated (AP=1/RP). Due to gaps in the source data sets (e.g., 1969-1978, 1980-1992 etc.; see Fig. 3.1), the event-based landslide inventories available for the study area, could not be used directly to calculate the return periods. Moreover, these inventories were not complete and therefore cannot provide complete information about landslide events and their varying levels of magnitudes (i.e., severity of events in terms of landslide numbers, density, damage potentials etc.) that have occurred in the gap period. Although, the historic data gives a good indication of the importance of landslide triggering events (e.g., landslides that occurred in 1968, 1998, 2003 etc.), still they are not exhaustive as other triggering events might have occurred for which the landslide inventories are not available. Therefore, to model the unknown events, a relationship between landslide events and triggering rainfall was established. The landslides between 1968 and 2007 mostly occurred in the monsoon period (June-October), when precipitation is very high (between 2500 mm and 3600 mm), and accounting for 80-85% of the total annual precipitation (Starkel and Basu, 2000; Starkel, 2004; Soja and Starkel, 2007). Therefore a

stepwise discriminant analysis (DA) model was used to establish a quantified relationship between landslide events and triggering rainfall (section 3.4).

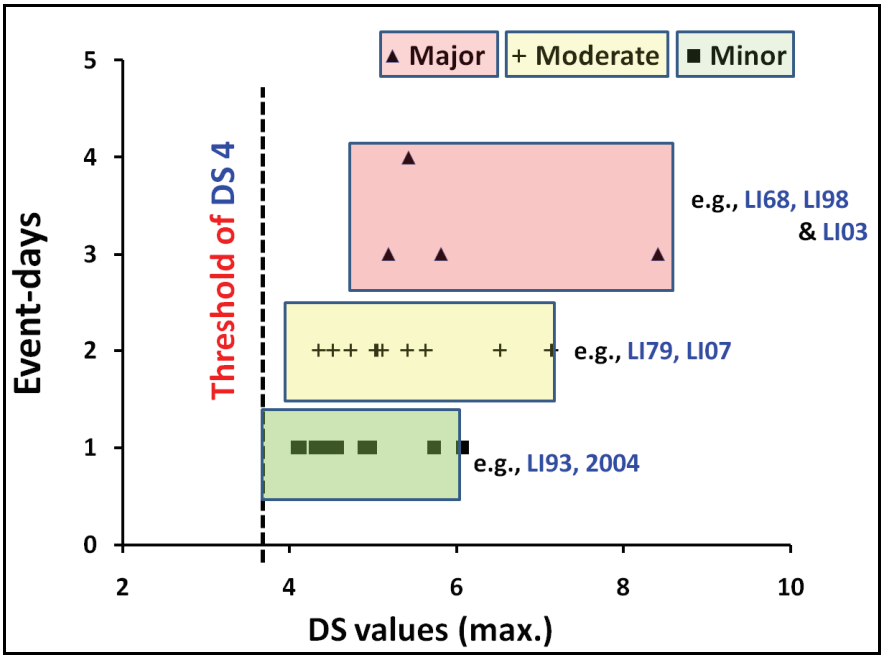

Fig. 7.2 Predicted landslide events with different magnitudes. The discriminant scores (DS) presented in chapter 3 are plotted against the number of landslide triggering event-days for minor, moderate and major events. Also the known landslide inventories that matched/correlated with different magnitude classes are also shown (see also Fig. 3.1 for the nomenclature of the inventories (e.g. LI68) used in this illustration).

The DA model (see section 3.4), predicted 30 landslide event-years based on a subjectively-derived threshold discriminant score (DS) of 4.0. Based on increased DS values and the number of predicted landslide event-days per year, landslide events were classified into three classes: minor, moderate and major events (Fig. 7.2), with increasing levels of magnitude expressed as landslide density. The basic assumptions are that the severity of landslide events will increase with increasing DS values and with the increasing number of predicted landslide event-days per event year. For example, major landslide events (e.g., LI68, LI03 in Fig. 7.2) have at least three landslide event-days per year and high DS values. Based on the above criteria, 16 minor, 10 moderate and 4 major landslide events were predicted (See also Fig. 3.6 in section 3.4.). Therefore the return periods of events were assumed ranging between 3-5 years for minor events, 4-10 years for moderate ones and 20-50 years for major events. These ranges of values were assumed, considering the number of occurrences of both confirmed/known and model-predicted landslide events together for the

entire period of analysis (40 years). The ranges of return periods or annual probabilities express the level of uncertainty in temporal probability.

The identification of landslide events of certain magnitudes also facilitates the correlation of predicted events with the existing landslide inventories of 1968-2007, which are required for the estimation of the spatial probability of landslides. The spatial probability (P_s) of a pixel to have a future landslide can be calculated as:

$$P_s = L_{S_i} / S_i \quad (7.1)$$

Where, L_{S_i} is the total landslide area in a susceptibility class i, S_i is total area of the susceptibility class i.

The spatial probability can be calculated for different landslide magnitude scenarios indicated as major, moderate and minor events as shown in Fig.7.2. The known landslide inventories that are representative for the respective magnitude classes were used to calculate the spatial probability. The variation in landslide densities per magnitude class was considered by evaluating the landslide densities of all known events that are classified in a particular magnitude class. So for instance, for major events, the landslide densities of the inventories LI68, LI98 and LI03 were used, and the range of densities reflects the level of uncertainty in the spatial probability. Therefore, a combination of the range of temporal probabilities with the range of spatial probabilities resulted in 12 different landslide hazard scenarios that were taken into account (Fig. 7.3).

7.3.2 Landslide risk estimation

The 12 landslide hazard scenarios (Fig. 7.3) were used to calculate specific risks. Specific risks to elements-at-risks (e.g., buildings) were calculated per mapping unit (i.e., the settlement unit or SU) containing many individual elements at risks (e.g., buildings) through an exposure-based approach adapted from the method of rock fall hazards proposed by Lee and Jones (2004; see page 349-351). The method for calculating loss per SU (L_{SU}) is illustrated in Eq. 7.2 and Fig. 7.4.

$$L_{SU} = Cell_{aff_{SU}} * P_{Cell_{Occ}} \quad (7.2)$$

where, $Cell_{aff_{SU}} = P_s * N_{Cell_{SU}}$; $P_{Cell_{Occ}} = N_{Elm} / N_{Cell_{SU}}$; $Cell_{aff_{SU}}$ is the number of cells affected in a SU, P_S is the spatial probability according to Eq. 7.1,

$N_{Cell_{SU}}$ is the total number of cells/pixels in a SU, $P_{Cell_{Occ}}$ is the probability of cells occupied by an elements at risk (e.g. buildings) in a SU and N_{Elm} is the total number of elements-at-risk (e.g., buildings) within a SU.

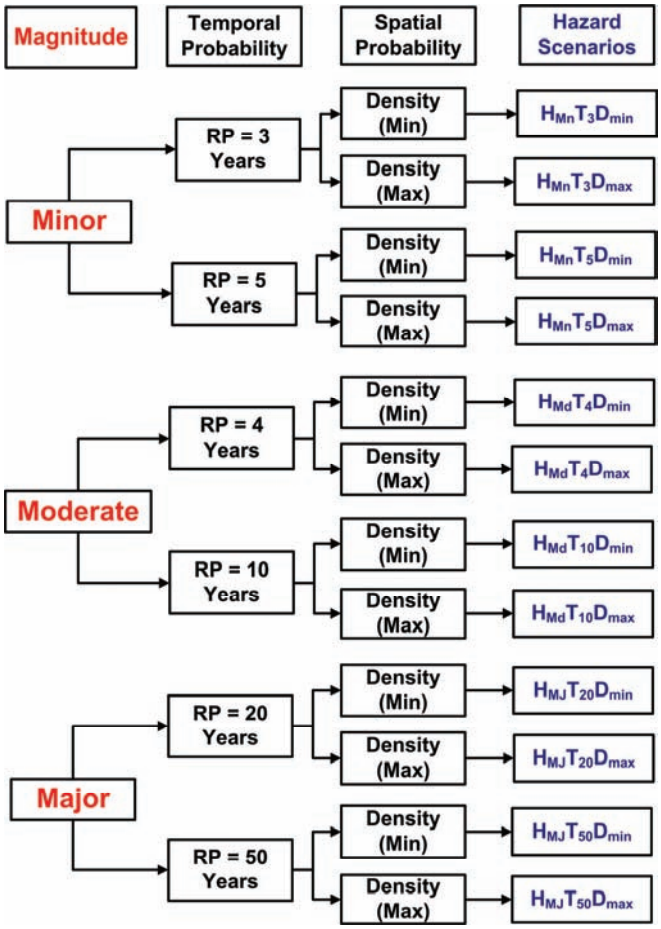

Fig. 7.3 Different possible landslide hazard scenarios based on minimum and maximum temporal and spatial probabilities of landslide events of certain magnitudes. The abbreviation used for each hazard scenario (e.g., HMJT20Dmin) can be read as H = Hazard; MJ (subscript) = Major event; Md (subscript) = Moderate event; Mn (subscript) = Minor event; T with RP value in subscript signifies different temporal probabilities (e.g. T_{20}); D_{max} and D_{min} signifies ranges of spatial probability that has been calculated by using landside distribution maps of maximum and minimum landslide densities respectively using Eq. 7.1.

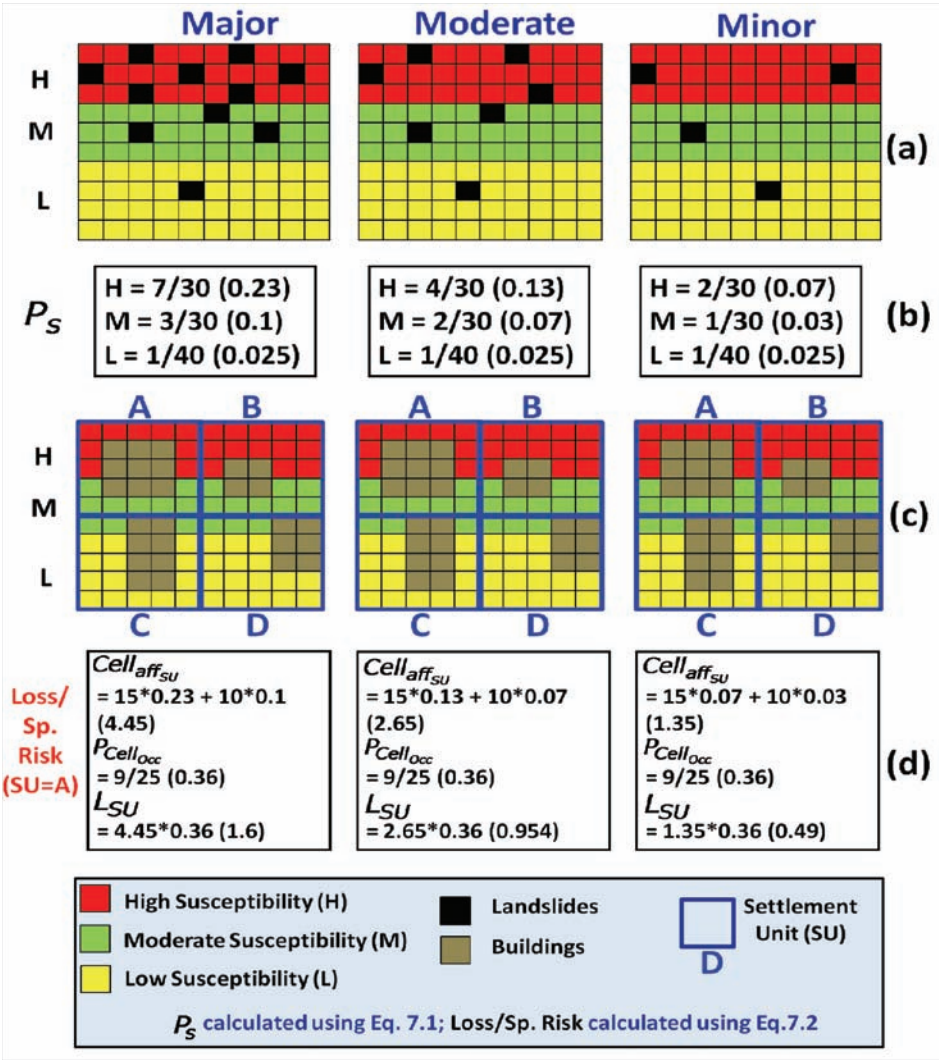

Fig. 7.4 A schematic diagram illustrating in stages, how building losses can be calculated in a settlement unit (e.g. A) in combination with susceptibility units (High, Moderate, Low) through exposure-based modelling. (a) and (b) illustrate different susceptibility zones (H, M, L) and the method how spatial probabilities are calculated following Eq. 7.1 using distribution of landslides of different magnitudes (major, moderate and minor). (c) and (d) illustrate how building losses are calculated in a settlement unit (A) following Eq. 7.2 in three magnitude scenarios. For abbreviations at (d), please refer to the explanations given in Eq. 7.2.

Fig. 7.4 demonstrates two steps to arrive at the loss calculation. The first step is to calculate the number of cells per SU ($Cell_{aff_{SU}}$) that are likely to be affected by landslides given a triggering event of a certain magnitude. The $Cell_{aff_{SU}}$ is a function of the spatial probability (P_S) that depends on the

landslide susceptibility map and also on the specific landslide distribution maps that have been identified for events of different magnitudes. The spatial probability is not calculated separately for each SU but is calculated for each class of the susceptibility map. Therefore, the proportion of cells within a SU likely to be affected ($Cell_{aff_{SU}}$ in Fig. 7.4) that actually have elements-at-risk depends on its spatial exposure with different susceptibility classes. Therefore, by overlaying SU map with the susceptibility map in a GIS (Fig. 7.4c), the number of cells affected per settlement unit can be calculated (Fig. 7.4d). As a building foot print map is not available, it is assumed that there is a uniform distribution of buildings within the settlement unit. Therefore, the number of buildings affected can be calculated by multiplying the number of cells affected ($Cell_{aff_{SU}}$) by the probability of cells occupied ($P_{Cell_{Occ}}$) by buildings in a settlement unit (Eq. 7.2 and Figs. 7.4c-d). It is important to mention here that the vulnerability of the elements at risk is not considered, and therefore, the results actually indicate the number of elements-at-risk likely to be affected. Given the uncertainty of the data and the medium scale of analysis, it is not possible to use vulnerability curves and express the losses as number of elements-at-risk destroyed. By adding the results for all 236 different settlement units (SU), the total loss due to a particular hazard scenario can be calculated and the corresponding losses due to the event of different magnitudes can be plotted in a standard risk curve against the temporal probability of occurrence of the hazard scenarios. The same method can also be followed to calculate the expected losses to roads, population etc.

Since the number of people living in a building during day-time and night-time varies a lot, the estimation of people likely to be affected should be based separately on day-time and night-time population. The day-time population is calculated on the basis of the number of unemployed people, housewives and small children. For the night-time population, a proportion of 2% of the total population was excluded from the total inhabitants assuming that they are staying away from their homes due to some personal work. The likely number of people affected by landslides can then be graphically presented by adopting the standard Frequency-Number (F-N) curves used to represent societal risk, in which the frequency of events (F) that likely affect N people can be plotted along the Y-axis against the number of affected people (N) on the X-axis on log-log scales. The frequency of events (N) is represented by P_L which is the annual probability of the landslide event to occur, which in this case has a range with a minimum and maximum values depending of landslide events of different magnitudes. The temporal spatial probability of a person or group of person based on their respective exposure

in day and night time is taken into account when estimating the number of people (N) likely to be affected, by multiplying the number of affected buildings by the average number of people per building (both during day and night time) in each settlement unit, for landslide events of different magnitudes. The vulnerability of a person or a group of person at risk is also assumed here as 1, since the aim is only to represent the number of people likely to be affected, and not the number of people injured or killed.

The expected losses can also be represented in a map, by considering a certain period of time, instead of annualized losses. For instance the probability that an event with a given return period (RP) is likely to occur within a 50-year period (T_{50}) can be calculated using the following expression:

$$T_{50} = \left(1 - (1 - 1/RP)^{50}\right) \quad (7.3)$$

To express the number of buildings or persons affected by landslides during a period of 50-years, we can multiply T_{50} by the respective specific losses for each return period and integrate the losses for all return periods with their respective T_{50} values. The cumulative expected losses can also be expressed annually. These annualized loss values are calculated as the “area under the risk curve”.

7.4 Results of hazard and risk estimation

7.4.1 Landslide hazard estimation

Following Eq. 7.1, the spatial probability of landslide occurrence can be estimated for the three magnitude classes (major, moderate and minor) using both the minimum and maximum landslide density values of the known landslide inventories. This resulted in spatial probability for six different hazard scenarios and for two types of landslides (rockslides and debris slides). The results are presented in Tables 7.2 and 7.3. for different susceptibility zones (low to very high) which are required to convert the susceptibility zones into hazard zones. Examples of specific landslide hazard maps related to major landsliding event are shown in Fig. 7.5., where the ranges of spatial probabilities (minimum-maximum) for each susceptibility class are shown.

In Tables 7.2.-7.3., a hazard scenario (H_{Ext}) has been added, which represents a hypothetical situation of an extreme landslide event caused by an earthquake occurring in the direct vicinity of the study area. For

calculating the spatial probability of this extreme event, the inventory of large un-dated landslides of pre-1968 was used to calculate the landslide density. The purpose of modelling such an extreme event is relevant because the study area falls within an active Fold-thrust-belt of the Himalayas and is highly earthquake-prone (BIS, 2002). However, data is lacking to make a more detailed analysis of return periods of earthquakes in relation to earthquake-triggered landslide inventories. Based on expert judgement a range between 300 and 500 years was assumed for the return period of such an extreme scenario.

Table 7.2 Spatial probabilities for different hazard scenarios for rockslides. The spatial probabilities were calculated according to Eq. 7.1.

Landslide event		Susceptibility class			
		Low	Moderate	High	Very high
	Total pixel	429865	150612	158050	155198
Minor	H_{MnDmin}	9.538E-05	3.785E-04	9.491E-04	1.186E-03
	H_{MnDmax}	6.141E-04	9.827E-04	2.360E-03	2.713E-03
Moderate	H_{MdDmin}	1.605E-04	5.312E-04	7.276E-04	3.808E-03
	H_{MdDmax}	8.305E-04	3.592E-03	5.688E-03	8.815E-03
Major	H_{MJDmin}	7.770E-04	4.289E-03	5.878E-03	1.713E-02
	H_{MJDmax}	5.234E-04	3.214E-03	9.794E-03	5.041E-02
Extreme	H_{Ext}	1.117E-01	2.241E-01	2.352E-01	4.506E-01

Table 7.3 Spatial probabilities for different hazard scenarios for debris slides. The spatial probabilities were calculated according to Eq. 7.1

Landslide event		Susceptibility class			
		Low	Moderate	High	Very high
	Total pixel	513049	226781	104730	49166
Minor	H_{MnDmin}	3.898E-05	1.980E-04	1.910E-05	2.156E-03
	H_{MnDmax}	5.068E-05	2.999E-04	1.136E-03	5.919E-03
Moderate	H_{MdDmin}	1.169E-05	1.499E-04	9.071E-04	3.763E-03
	H_{MdDmax}	3.177E-04	7.805E-04	2.444E-03	1.277E-02
Major	H_{MJDmin}	3.411E-04	1.102E-04	6.111E-04	3.315E-03
	H_{MJDmax}	4.542E-04	1.755E-03	3.819E-03	1.452E-02

7.4.2 Landslide risk estimation

7.4.2.1 Expected losses to buildings and population

Based on the exposure analysis presented in Fig.7.4, the ranges of buildings likely to be affected for minor, moderate, major and extreme events were calculated. Depending on the variation in spatial probability due to the variation in landslide densities of the event-based landslide inventories linked to a certain magnitude of triggering events, a range of expected loss values was analyzed. The results given in Table 7.4 show that the number of affected buildings is generally higher for rockslides than for debris slides. In case of an extreme event the number of affected buildings is much higher (2194), compared to any of the other scenarios, due to fact that a nearby

earthquake scenario can trigger many more landslides than any of the rainfall-triggered ones that occurred in the last 40 years (1968-2007).

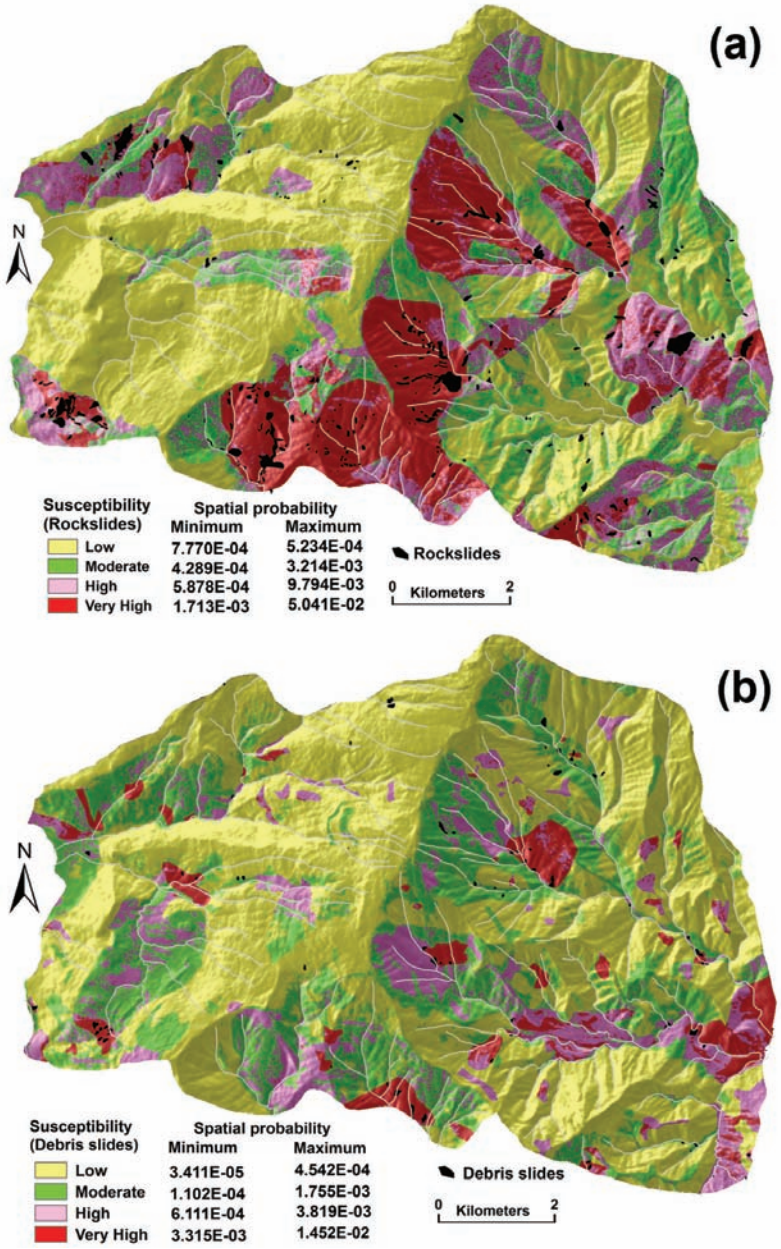

Fig. 7.5 Examples of landslide hazard maps showing the ranges of spatial probabilities of occurrence of landslides (see Tables 7.2 and 7.3) for major landsliding events to (a) rockslides and (b) debris slides in the case of a major landslide triggering event (rainfall related).

Table 7.4 Number of buildings likely to be affected for different landslide hazard scenarios. Also the range in temporal probability of these events is indicated.

Landslide event	Hazard scenarios	Buildings likely to be affected (Rocksliding)	Buildings likely to be affected (debris sliding)	Buildings likely to be affected (Total)	Temporal probability	
					Minimum AP (1/RP)	Maximum AP (1/RP)
Minor	$H_{Mn}D_{min}$	4	1	5	0.2 (1/5)	0.33 (1/3)
	$H_{Mn}D_{max}$	13	4	17		
Moderate	$H_{Md}D_{min}$	6	2	9	0.1 (1/10)	0.25 (1/4)
	$H_{Md}D_{max}$	30	10	40		
Major	$H_{MJ}D_{min}$	37	5	42	0.02 (1/50)	0.05 (1/20)
	$H_{MJ}D_{max}$	62	16	78		
Extreme	H_{Ext}	2194	-	2194	0.002 (1/500)	0.003 (1/300)

AP = Annual probability; **RP** = Return period in years.

The building losses shown in Table 7.4 above can be graphically represented in the form of risk curves (Fig. 7.6), where the variation in losses (expressed as number of buildings likely to be affected) is shown as minimum and maximum curves. The minimum risk curve is made based on the minimum values for temporal and spatial probabilities, and the maximum risk curve considers the corresponding maximum temporal and spatial probability values. The difference between the two curves is an indication of the degree of uncertainty in the risk analysis. The effect of including the extreme event is evident from Fig. 7.6b where the risk curves result in very different values if such an event was excluded. Extreme events are only modeled with rocksliding events because; the large un-dated pre-1968 landslides are mostly deep-seated rockslides.

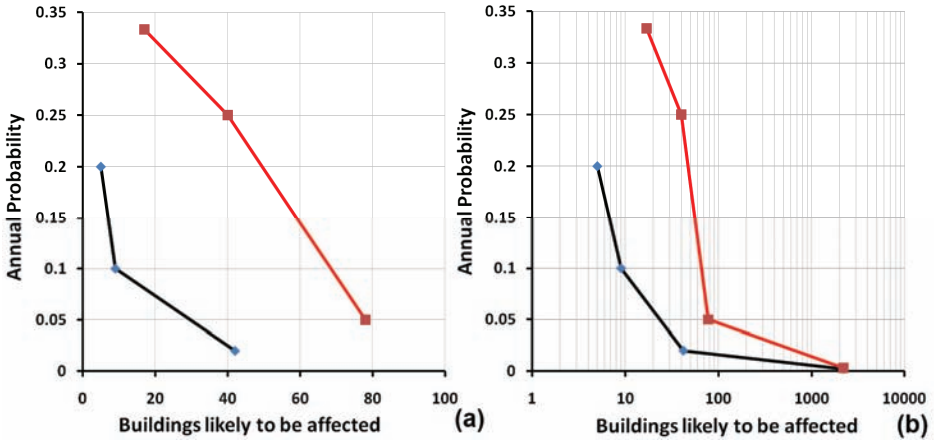

Fig. 7.6 Loss curves showing the ranges in "the number of buildings likely to be affected" in landsliding events of different magnitudes against minimum and maximum temporal probabilities (see Table 7.4). The lower level loss curves in "black" represent the minimum losses plotted against minimum temporal probabilities and the upper level curves in "red" represent the maximum losses plotted against the maximum temporal probabilities. The curves at (a) include only major, moderate and minor landsliding events. The curves at (b) include landsliding events of all magnitudes including the extreme event.

The expected buildings losses presented above can be directly used to calculate the number of people likely to be affected by modelling both day and night time population. The corresponding results of such expected population losses for different hazard scenarios are presented in Table 7.5.

Table 7.5 Values for day-time and night-time population living in buildings likely to be affected for different landslide hazard scenarios.

Landslide event	Hazard scenarios	Population likely to be affected (Rocksliding)		Population likely to be affected (Debris sliding)		Population likely to be affected (Total)		Temporal probability	
		Day	Night	Day	Night	Day	Night	Minimum AP (1/RP)	Maximum AP (1/RP)
Minor	$H_{Mn}D_{min}$	14	21	6	9	20	30	0.2 (1/5)	0.33 (1/3)
	$H_{Mn}D_{max}$	48	70	14	22	62	92		
Moderate	$H_{Md}D_{min}$	20	32	8	13	28	45	0.1 (1/10)	0.25 (1/4)
	$H_{Md}D_{max}$	105	157	43	65	148	222		
Major	$H_{MJ}D_{min}$	124	188	24	36	148	224	0.02 (1/50)	0.05 (1/20)
	$H_{MJ}D_{max}$	183	293	66	99	249	392		
Extreme	H_{Ext}	7910	11646	-	-	7910	11646	0.002 (1/500)	0.003 (1/300)

AP = Annual probability; **RP** = Return period in years.

For population living inside buildings, it is most unlikely that exposure of a person or group of person at risk are similar for both day and night time (Table 7.5). Accordingly, the expected number of people (N) likely to be affected for each landslide event magnitude (see columns 7 and 8 of Table 7.5) are plotted in a log-log scale (Fig. 7.7) against the respective annual frequency (*F*) of such people at risk, which are equal to the annual probability of landsliding events (columns 9 and 10 in Table 7.5).

Since the annual probability estimates of landslide events of all magnitudes are quite higher in this case, all the F-N curves in Fig. 7.7 fall in the higher level of F-N space, which signifies that due to lower range of return periods of landslide events in the study area, the people at risk are most likely to be affected due to future similar landslide events and as a societal risk, the system is most likely to be unacceptable, although, for landslide risk evaluation, no such limit of tolerance presently exists in India.

Spatially the variability of likely losses to buildings can also be illustrated through various risk scenario maps by computing the losses based, for example on a 50-year time period (Fig. 7.8). Fig. 7.8a represents that for minimum losses which have been calculated based on minimum spatial and temporal probabilities of landsliding events. Most of the settlement units in the study area have a low range of losses (buildings affected ≤1) with a few areas (e.g. Tindharia) having moderate losses (buildings affected 1-4). The Fig. 7.8b which has been prepared based on maximum range of spatial and temporal probabilities of landsliding events shows that the number of settlement units having moderate losses increase from that of Fig.7.8a and the areas around Tindharia has high losses (buildings affected 4-10). In Fig.

7.8c, the extreme landsliding event that might occur due to a large earthquake trigger in the vicinity has also been included. The likely-losses in Tindharia area become very high (buildings affected 10-15) including some parts of Kurseong municipality which also show high losses. It is important to mention that the actual number of affected buildings in such an extreme earthquake related scenario would be much larger due to the effects of ground shaking. In this study only the possible effects of landslides are taken into account. The estimation of such losses considering the 50-year time period and the annualized loss estimates for buildings and population are also shown in Table 7.6. Table 7.6 indicates that the maximum annualized and 50-year losses of buildings and population increase manifold if extreme landslide events are included along with predicted minor, moderate and major landslide events. Assuming an average value of INR 120,000 per building (about 2000 Euros), the cost towards maximum annualized losses of buildings in the study area could range between 44,000 Euros (INR 26,40,000) and 144,000 Euros (INR 86,40,000) depending on varying range of losses.

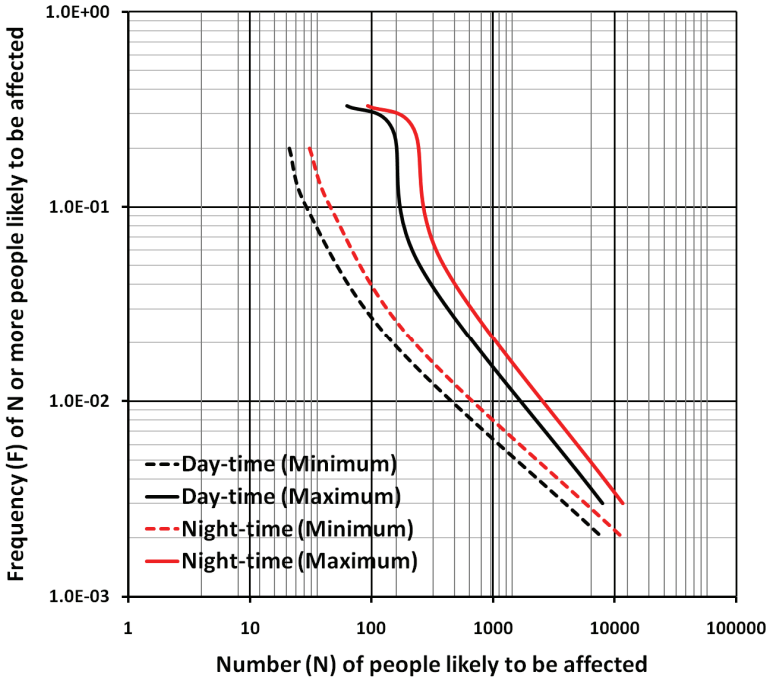

Fig. 7.7 F-N curves showing annual frequency (F) of N or more people likely to be affected plotted on a log-log scale against the corresponding number of people likely to be affected for both day-time and night-time scenarios. For each case, both "minimum" and "maximum" F-N curves are shown, which represents the minimum and maximum likely losses calculated on the basis of minimum and maximum spatial and temporal probability scenarios respectively (see Table 7.5).

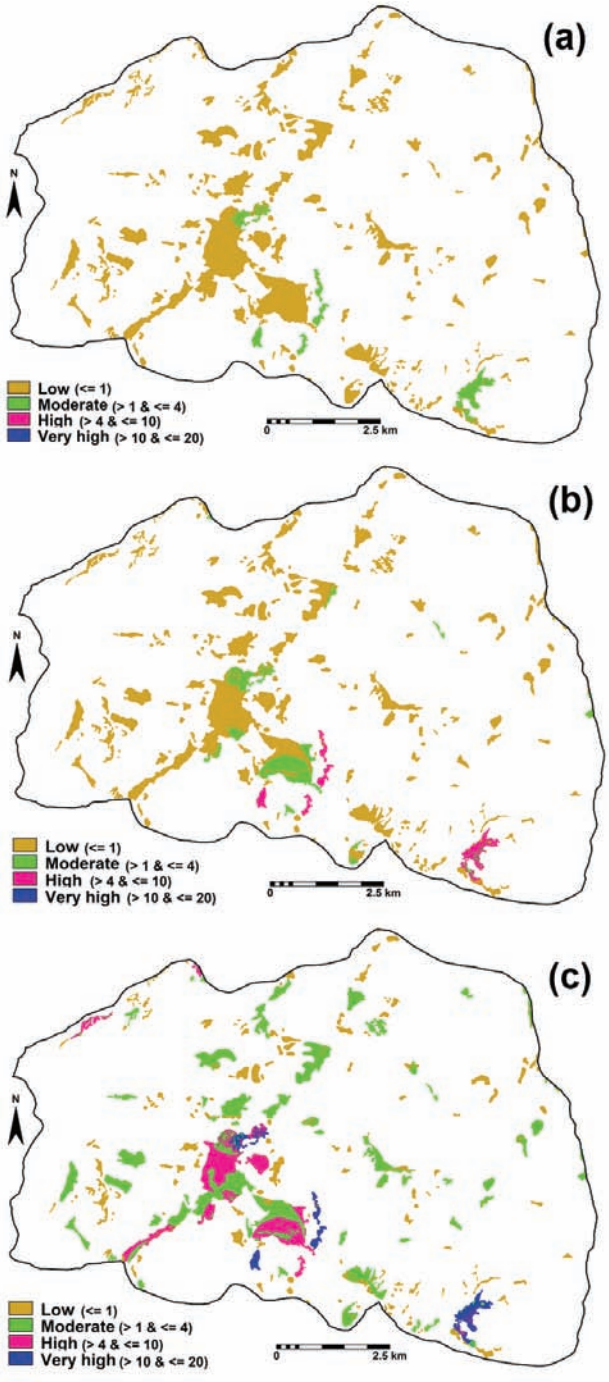

Fig. 7.8 Risk map showing spatial distribution of likely losses of affected buildings based on 50-year period due to different landslide hazard scenarios. (a) Risk map showing minimum losses based on minimum temporal and spatial probabilities; (b) risk map showing maximum losses based on maximum temporal and spatial probabilities and, (c) risk map showing extreme losses using maximum landslide density and including the probable extreme events.

Table 7.6 The annualized and 50-year loss estimates for buildings and population of the study area.

Landslide events		Buildings likely to be affected				Population likely to be affected (Day-time)				Population likely to be affected (Night-time)			
		Annualized		50-Year		Annualized		50-Year		Annualized		50-Year	
		Minimum	Maximum	Minimum	Maximum	Minimum	Maximum	Minimum	Maximum	Minimum	Maximum	Minimum	Maximum
Minor+ Moderate+ Major	Rocksliding	4	17	34	100	14	56	113	322	22	85	172	497
	Debris sliding	1	5	9	35	5	20	14	57	7	30	44	179
Total		5	22	43	135	19	76	127	379	29	115	216	676
Minor+ Moderate+ Major+ Extreme	Rocksliding	26	72	243	438	93	253	866	1538	138	376	1281	2288

7.4.2.2 Direct losses to major roads

Following the above exposure-based method of loss estimation, the likely losses to the 162 km long road network have also been estimated in the study area (Table 7.7). This table shows that about 893 m of road is likely to be affected if maximum densities of major landsliding events are taken into account. Like building and population losses, length of roads (m) likely to be affected increases about 13 times if the extreme landslide events are considered. Although, one important observation is noticed in case of expected losses to road network as compared to those for buildings and population that a substantially higher proportion of the road network is affected by debris slides as compared to rock slides (Table 7.7) because debris slides are mostly concentrated along the major roads.

Table 7.7 Expected direct losses to road network against the different landslide hazard scenarios.

Landslide event	Hazard scenarios	Road (m) likely to be affected (Rocksliding)	Road (m) likely to be affected (debris sliding)	Road (m) likely to be affected (Total)	Temporal probability	
					Minimum AP (1/RP)	Maximum AP (1/RP)
Minor	$H_{Mn}D_{min}$	23	43	66	0.2 (1/5)	0.33 (1/3)
	$H_{Mn}D_{max}$	72	121	193		
Moderate	$H_{Md}D_{min}$	50	77	127	0.1 (1/10)	0.25 (1/4)
	$H_{Md}D_{max}$	174	266	440		
Major	$H_{Mj}D_{min}$	255	75	329	0.02 (1/50)	0.05 (1/20)
	$H_{Mj}D_{max}$	577	316	893		
Extreme	H_{Ext}	11686	-	11686	0.002 (1/500)	0.003 (1/300)

AP = Annual probability; **RP** = Return period in years.

7.5 Discussion and conclusions

Due to non-availability of any proper damage records, it becomes quite difficult to properly validate the results obtained in this study, although, a general indication can be obtained from reports of damage data in some recent (e.g., 1998, 2003) major landsliding events in the area, which indicate that due to such major triggering event, a substantial portion of road network (about 1 km) was affected causing road-blockades for more than 15-days

along with partial to substantial damage to 30-40 houses in the study area. Nevertheless, any major or extreme landsliding events in the study area can cause more indirect and long-standing losses to various elements-at-risk than the direct ones, although, calculation of which are quite complicated due to want of suitable data and therefore, the same is also beyond the scope of the present study.

Landslide risk assessment at medium-scales (1:25,000) relies primarily on the predictive mapping and thus, landslide susceptibility estimation has always been the first step in the process. The second and more difficult step is to convert the landslide susceptibility into a landslide hazard map by adding information on spatial, temporal and size probability of future events. One way to achieve that is to consider a number of landslide triggering events, and analyse them for their return periods, and the landslide density in the various susceptibility classes. These specific landslide hazard scenarios are relevant because they allow calculating specific risks or losses to elements at risks. The landslide susceptibility models used for this study were prepared for two types of landslides. The risk estimation could be further improved by generating separate susceptibility maps for different landslide types for each triggering event (so separate susceptibility maps for triggering events with say 5, 10, 50, 100 and 500 year return periods) and use these in combination with their respective event-based inventories to estimate specific spatial and magnitude probabilities. This was not attempted in this study because of the lack of reliable event-based inventories and also because it would make the risk models perhaps too complex given the medium-scale of assessment.

It is important to mention that despite the reasonably-good quality susceptibility models used in this study, there are still some landslides within "low" and "moderate" susceptibility classes, which definitely introduced some amount of uncertainty in risk estimation since separate susceptibility models using only landslide occurrences of different magnitudes were not carried out and used due to paucity of complete landslide event-magnitude data.

In the method presented in this chapter the magnitude probability was not included in the hazard component, and the susceptibility maps were converted into hazard using only the spatial and temporal probability. The magnitude probability as indicated in Table 3.6, in which $P[A_L<1000\ m^2]$ and $P[A_L>10{,}000\ m^2]$ are specified could be incorporated in the analysis, although we don't have these values for rockslides and debris slides separately, nor for the different susceptibility classes. However, the magnitude probability could

be used to estimate the number of cells affected by landslides of a given magnitude by calculating

$$Cell_{aff_{SU}} = P_s * Pm * N_{Cell_{SU}}$$

In which *Pm* would be for instance $P[A_L<1000\ m^2]$ or $P[A_L>10{,}000\ m^2]$. This could then be used to estimate the number of buildings affected by large landslides, and by small landslides. And this could then be used as a proxy for landslide magnitude in assigning different vulnerability values for buildings. However, as the aim was to only represent the number of buildings that might be affected by landslides at a medium scale, this was considered not appropriate. Also given the large uncertainties involved, the inclusion of more uncertainties related to the probability of landslides that would have to potential to destroy buildings, and also the vulnerability of the building themselves, was not considered justifiable.

For landslide risk assessment, modelling of different consequences is required and that is possible if the landslide triggering events and their magnitudes are known. The determination of landslide triggering event magnitudes is more reliable if a complete historical record of landslide events is available (Rossi et al., 2010b; Salvati et al., 2010). But in most cases one has to deal with incomplete data and unavoidable gaps in landslide inventories such as in this study area. The only alternative was to establish an empirical relation between landslides and triggering events (Aleotti and Chowdhury, 1999; Crozier, 1999; Chowdhury and Flentje, 2002; Jaiswal and van Westen, 2009), assuming that all the landslides are rainfall-triggered (Starkel and Basu, 2000; Starkel, 2004; Soja and Starkel, 2007; Dahal and Hasegawa, 2008), and that earthquake-triggered landslide events occur infrequently, but could generate many more landslides than the rainfall events. Due to non-availability of any record of earthquake-triggered landslide events, consequence modelling in the study area was mainly based on the available record of the 40-years period (1968-2007) using only the rainfall-triggered landslides, although, this 40-year period could be quite a small period for estimating/visualizing the entire range of landslide event-magnitude scenarios. Moreover, definite data gaps even within the 40-year period of analysis made the above study more challenging that resulted in varying levels of uncertainty in loss estimation.

Due to the above data gaps, it was also difficult to characterize the landslide event magnitude, although, an arbitrary assumption of minor, moderate and major landsliding events worked well in practice in the assessment of losses. The above framework can be followed better if a more complete set of historical data of landslide event-magnitudes are available in an area, where,

identification of events of different magnitudes and assessment of their respective temporal probabilities are less uncertain.

The risk assessment framework presented in this study is mainly aimed for the use in regional or medium-scale risk assessment and therefore, separate run out assessment was not included. Moreover, due to the variable resolutions of source data, for many smaller landslides that are mapped for different landsliding events, separation of the initiation area from the deposition and run out had been quite difficult; therefore, separate run out assessment at medium scales could include more uncertainties in hazard estimation. Another simplified assumption followed in this study was not considering the vulnerability, and therefore only estimate the number of affected rather than the number of destroyed elements at risk. This was due to several reasons, such as the absence of detailed building data (both building footprint data as well as building characteristics), the lack of suitable landslide magnitude estimation (as mentioned earlier) and the lack of quantitative vulnerability curves and historic damage data. The risk assessment model presented in this study is a general one which is applicable at medium scale and mostly relies on good susceptibility maps and on event-based landslide inventories. Based on the distribution of known landslide occurrences, the ranges of uncertainty in losses for different elements-at-risk were quantitatively determined.

Given the substantial differences in landslide densities for inventories that were grouped in the same triggering magnitude class, hazard and subsequent risk or loss estimates were calculated for minimum and maximum values of spatial and temporal probabilities. The study has shown that the expected building losses per annum can range between 0.01% and 0.16% of total number of buildings (13736), expected population losses can range between 0.02% and 0.15% of the total population (76126) of the area and the expected direct losses to roads range between 0.04% and 0.55% of the 162 km road lengths of the study area for landslide events of different magnitudes (minor, moderate and major). This variation can be considered as a measure of uncertainty in loss estimation in situations when there is incomplete information on historic landslides, as evident for the study area.

Chapter 8: Synthesis and conclusions

8.1 Introduction

For quantitative landslide hazard assessment, data-driven methods are generally preferred over knowledge-driven ones because the latter involve a substantial subjectivity in the selection of factors and the assigning of their weights. Data-driven methods (e.g., statistical or mathematical) depend on two types of spatial associations: (a) spatial associations of individual spatial factors with historic landslides of a certain type; and (b) the relative importance of individual spatial factors with respect to one another in relation to landslide occurrences. Although, multivariate statistical methods can simultaneously model both the above two types of empirical spatial associations yet some of the spatial factors selected and used by them according to certain (statistical) criteria are sometimes not representative of specific genetic processes associated with the type of landslides being studied. Whereas, bivariate statistical methods, although intuitive, can only model the first type of spatial association, and thereby, exhibit moderate prediction rates. Therefore this research proposes a suitable empirical method to study the spatial association by suitably incorporating expert knowledge to (a) select the most appropriate spatial factors that approximate realistic genetic associations with landslides of a certain type, and (b) objectively determine the importance of every spatial factor with respect to the others in relation to the landslide type under study and combine them using multivariate methods. The proposed empirical technique can interactively and iteratively augment the empirical model processes that estimate landslide susceptibility, which is subsequently used to prepare the landslide hazard and risk maps.

Landslide hazard is estimated by integrating temporal and magnitude probabilities with the spatial probability derived from the susceptibility map in combination with a series of inventory maps that are linked to certain triggering events, with particular landslide densities and return periods. Difficulties arise when data on past landslides are inadequate, source data sets are of different spatial and temporal resolutions, and dates of landslides and triggers (e.g., rainfall) do not match, as observed in the study area. Given these constraints, this research also focuses on the development of suitable methods for the determination of temporal and magnitude probability by generating and using event-based landslide inventory maps prepared with the available source datasets.

This chapter describes the main results of the various components of this research (chapter 2 to chapter 7), their interrelationships and outlines the limitations and the scope for future research.

8.2 Evaluating the existing method of landslide susceptibility mapping in India

Heuristic landslide susceptibility mapping methods are based either on direct geomorphological mapping or on the assignment of expert-derived weights to a set of pre-defined factors. Application of such specified weights of factors can lead to poor prediction results when applied to different areas because the spatial relations between landslides and their causal factors for different types of landslides are variable in nature. The study described in chapter 2 evaluated the performance of the officially adopted method in India for medium-scale (1:50,000) landslide susceptibility assessment (the so-called BIS method), with a fixed set of causal factors and a fixed set of weights (e.g., Anbalagan, 1992; BIS, 1998). The results were compared with those of a well-known bivariate data-driven method (Weights-of-Evidence modelling).

The study demonstrated that the maps derived using the BIS method had a substantially lower predictive power than those derived from the data-driven method. The study indicated that developing knowledge on prevalent landslide types and processes and establishing empirically their spatial relations with different site-specific spatial factors are essential for medium scale landslide susceptibility mapping, of which, the first and foremost step was to understand the past landslide processes through the generation of event-based landslide inventory maps (chapter 3). From the results of this study it can be recommended that for each study area, experts should select those combinations of relevant factors that best predict the occurrence of specific landslide types. A guideline for medium-scale (1:25,000-1:50,000) landslide susceptibility mapping should therefore be based on the methods that iteratively and interactively analyze the importance of the individual factor using various intuitive tools of empirical spatial association analyses (chapters 4 to 6). Therefore, the findings of this PhD research will facilitate in formulating a suitable guideline for medium-scale predictive mapping of landslides in India.

8.3 Event-based landslide inventory mapping

The application of empirical methods for susceptibility assessment and the conversion of these maps into landslide hazard maps require good amount of information on past landslide triggering events and the landslide inventories caused by them (Guzzetti et al., 1999; Glade et al., 2005; Fell et al., 2008;

van Westen et al., 2008). Moreover, landslide inventory mapping facilitates to understand landslide types and processes, their specific association with causal factors, which are essential inputs for any predictive mapping of landslide susceptibility. In chapter 3 a method was presented to generate event-based landslide inventory maps for landslide-triggering events based on all available source data sets. The study was carried out over a 40-year period (1968 to 2007) in a highly landslide-prone area in Darjeeling Himalayas (India). In India, as in many other countries, such source data sets are in general incomplete, and of various scales and resolutions. This study demonstrated that event-based landslide inventories can be generated in such data-scarce conditions which can be used for estimating temporal and magnitude probability. The following main results were obtained (chapter 3):

- Temporal probability of triggering events in a data-scarce environment can be determined by identifying unknown events through statistical analysis using triggering rainfall variables as predictors and known landslide events as response variables.
- Inadequate information on past landslides or gaps in source data makes it difficult to correctly estimate spatial, temporal and magnitude probabilities. Therefore, for effective landslide hazard and risk assessment, availability of a good quality past landslide inventory is of utmost necessity, which should be implemented at all possible scales (large, medium and regional) through launching a nation-wide landslide inventory mapping programme. The same is highly recommended for geo-environment like India for using such essential data for future hazard and risk analysis.
- The method presented in this thesis focused on the development of so-called event-based landslide inventories, which are inventories of landslides that occurred simultaneously as the consequence of a triggering event which has a certain return period. The use of such event-based inventories is only possible in environments where there is a clear relation between triggering events and the landslides caused by them.

8.4 Fault/fracture and slope controls on rocksliding

In an active tectonic environment like the Himalayas, regional faults and fractures have an evident control on landsliding. Several works on predictive mapping of landslide susceptibility consider proximity to linear geological structures as a spatial factor without considering the types and orientations of such structures (e.g., Saha et al., 2002; Champati ray et al., 2007; Sharma and Kumar, 2008; Mathew et al., 2009). However, the control of these structural features on landsliding is strongly related to the distribution of stress that generally varies widely with respect to the prominent regional

tectonic plates (e.g., MCT/MBT) (Pandey et al., 1999; Singh and Thakur, 2001; Joshi and Hayashi, 2008).

Therefore, a study (chapter 4) was carried out with the hypothesis that the proximity to structures of certain types and trends is likely to yield better predictive maps of landslide susceptibility. This study demonstrated that analyses of the spatial pattern of landslides of certain types and their spatial association with certain types and trends of regional faults and fractures allows a better selection of the most relevant sets of structures that control landslide occurrence. Analytical tools like Fry analysis and distance distribution analysis were applied to determine sets of faults and fractures that are likely involved in slope controls on rockslide. In addition, data-driven evidential belief functions (Carranza, 2002; Carranza and Hale, 2003; Carranza and Castro, 2006) were applied for representation and integration of spatial evidence layers of mutual fault/fracture and slope controls on rockslides.

The above study further revealed that the geometric (and, thus, mutual) relationship between orientations of certain linear geological rock structures (e.g., bedding, foliation, rock joint etc.) and orientations of certain slopes (Goodman and Bray, 1976; Hoek and Bray, 1981; Romana, 1985; Wagner et al., 1988) show good results which can be used in spatial modelling of different rock slope failure modes (e.g., planar, wedge, topple) (chapter 5).

8.5 Rock slope stability analysis using structural orientations

The most challenging task of modelling rock slope failure modes is to prepare 2-D maps (digital structural models) of structural orientations (i.e., trends and dips) by interpolating 3-D discontinuity orientation data (De Kemp, 1998; Günther, 2003). Structural orientation data are in general sparse due to poor rock exposures, thick vegetation and/or overburden cover, and inaccessibility of the terrain and moreover, their regionalisation onto a 2-D GIS is also not straight-forward. In this study (chapter 5), several techniques were applied for regionalization of 3-D orientations of structural discontinuities in rocks in order to create digital structural models at two different spatial scales. These are realized together with DEM-derived terrain properties in order to assess the kinematical possibility of different modes of rock slope failures and interpret their respective causal failure mechanisms. The following results were obtained (chapter 5):

- The assessment of rock slope instability performs better in smaller test areas with a higher density of structural discontinuity data and good controls of regional faults and fractures.

- Individual sets of structural discontinuities (i.e., foliation planes and joint sets) in rocks are good controls of rock instability at all spatial scales. Nevertheless, wedge is the predominant slope failure mode, followed by topple and plane failures.

- Results further showed that rock discontinuities are more important controls on deep-seated rockslides than on shallow translational rockslides, and the discontinuity-controlled rock slope instability also increases with increasing levels of water saturation (see Annexure III in the enclosed CD).

- The slope instability maps obtained in this study are actually maps of multivariate factors which can be used as input maps in predictive modelling of landslide susceptibility (chapter 6).

8.6 Selecting and weighting spatial factors of landslide susceptibility

Empirical analysis for predictive mapping of landslide susceptibility can be achieved by employing bivariate or multivariate analyses of spatial associations between predictors and target variables. Whereas spatial associations of landslides with causal factors and among the factors themselves are complex and likely non-linear, multivariate methods, especially those with non-linear functions, are more often employed in predictive modelling of landslide susceptibility. Although, predictors selected by multivariate methods are not always related to certain genetic processes associated with the type of landslides being studied (Baeza and Corominas, 2001; van Westen et al., 2008). Such results are related, nevertheless, to statistical or mathematical assumptions behind the algorithms of every method of multivariate analysis (e.g., independence among predictors with respect to target variables, etc). Therefore, in chapter 6, a two-stage methodology is presented involving expert knowledge and bivariate analysis to select predictors and objectively assign weights to the predictors for predictive modelling of susceptibility, followed by a multivariate analysis. The following results were obtained (chapter 6):

- Predictive maps of landslide susceptibility based on selected and weighted spatial predictors outperform the models prepared using all the possible spatial factors and on selected but un-weighted predictors.
- Results of quantified bivariate spatial associations between landslides and spatial factors are useful indicators because they help to reduce subjectivity of expert knowledge that is applied in the analysis of inter-predictor weights via analytical hierarchy process (AHP).
- In the study area, predictors selected and weighted via the proposed methodology are more realistic than those obtained via multivariate methods (e.g., logistic regression).

8.7 Developing quantitative methods for landslide hazard and risk analysis

In an area where information on past landslides is sparse and the source data has long spatio-temporal gaps, correctly predicting the landslide hazard scenarios is a difficult task which impedes subsequent quantitative risk assessment. Nevertheless in such a data-scarce environment, as is the case in most of the areas in India, these attempts should still be carried out as best as possible. This study (chapter 7) presented a method for quantitative landslide hazard and risk analysis, by generating a series of hazard scenarios based on the magnitude of triggering events, and the corresponding variation in landslide density and temporal probability. The aim of this study was to convert the landslide susceptibility maps (chapter 6) into a landslide hazard map and use this for a quantitative medium-scale landslide risk assessment. The following results were obtained (chapter 7):

- In a data-scarce environment, the empirical relations between triggering events (e.g., rainfall) and landslides can be used to classify the events with varying levels of severity or magnitudes (major, moderate and minor). Accordingly, different ranges of temporal probability can be estimated from their respective return periods based on the data set that covers a sufficiently large period (e.g. 40 years or more). Nevertheless this 40-year period might still be insufficient to capture the real large landslide events such as earthquake-triggered or rainfall triggered ones of higher return periods.
- Using variations in the densities of known event-based landslide inventories for the three magnitude levels, twelve different landslide hazard scenarios are generated based on minimum and maximum temporal and spatial probabilities of triggering events, which yielded

different levels of annual losses to various elements-at-risk (buildings, people, road etc.).

- The number of annual affected elements-at-risk sharply increases as the densities of landslides in an event of certain magnitude increase. This study has shown that the expected annual buildings affected can range between 0.01% and 0.16% of total number of buildings (13736), expected population affected can range between 0.02% and 0.15% of the total population (76126) of the expected sections of roads affected ranges between 0.04% and 0.55% of the 162 km road lengths of the study area for landslide events of different magnitudes (minor, moderate and major).
- The variable amounts of such losses that are shown against variable temporal and spatial probabilities can be considered as a measure of uncertainty in risk estimation in situations when there is incomplete information on historic landslides, as evident in the study area. The above results are quite plausible according to the losses occurred during similar landslide events in the recent past.
- This study also demonstrated that losses to any elements-at-risk exponentially increase if an extreme landslide event occurs in the area due to a major triggering event such as an earthquake. The above estimate used distributions of all pre-1968 old/inactive landslides as hypothetical examples of such extreme event because the study area is located in a highly earthquake-prone zone. This is worth mentioning here that such assumption of considering landslide distributions from a single extreme triggering event is completely arbitrary and no such record of similar such destabilization due to such large-scale triggering event is available for the study area unlike the landslide event triggered by the recent Wenchuan earthquake, China.

8.8 Limitations and future scope of research

This research on the development of a knowledge-guided empirical method for landslide hazard assessment has some inherent limitations owing mainly to the limitations of specific source data sets. In order to have enough suitable data, the following investigations should be taken up as part of the national landslide hazard and risk assessment programme in India:

- The first and foremost step is that a national programme for landslide inventory mapping should be initiated, that should be web-based and should allow for collaborative mapping, and the reporting of landslides in a simple and spatial way by local authorities (e.g., PhD thesis of Pankaj Jaiswal, 2011). To correctly estimate the temporal and magnitude probabilities, the event-based inventory maps should be produced, be it

with the help of Remote Sensing and/or possibly with the semi-automated techniques of landslide inventory mapping (e.g., PhD thesis of Tapas Martha, 2011).

- Due to the scarcity of the past landslide inventory data, for modelling landslide events and their magnitudes, the present research used daily rainfall data of one rainfall station (Goomtee Tea Garden), because this is centrally located and has a continuous record of daily rainfall for the entire period of analysis (1968-2007). Nevertheless, there is variability in monsoon rainfall in four nearby rainfall stations in their absolute amount of daily rainfall due to the orographic setting of this part of Eastern Himalaya. Therefore, more study on the spatial variability of rainfall should be carried out for improved modelling of the landslide event-magnitudes.
- This research revealed that the fitted probability density functions of landslide areas mapped from high-resolution remote sensing data are somehow consistent with the 'Double Pareto' and 'Inverse Gamma' functions reported in the literature, whereas this is not the case for the inventory maps that are field-based. This can be investigated further by comparing the results of magnitude-frequency analyses of landslide areas from inventories produced by different mapping techniques.
- The proposed model of mutual fault/fracture and slope controls on rockslides presented in this research is constrained by the lack of dip data for regional discontinuities (e.g., fault). When more such data become available, the model of mutual fault/fracture and slope controls on rockslides proposed in this research can be improved considerably.
- Although, it is plausible that the area has undergone a series of major earthquake triggered landslides events in the past, the lack of such suitable source data precludes development of scenario-based maps based on a spatially distributed model of dynamic loading due to earthquake triggering. This is obviously an important parameter for slope instability assessment in a tectonically active geo-environment like the Himalayan Fold-thrust belt, and should be studied more in detail in future research.
- The proposed rock slope instability model involving digital structural models and topography parameters (inclination and aspect) creates a large number of individual structural variables, which have variable controls over rocksliding. Therefore, in future, the predictive slope instability assessment should be made using all such structural variables as factors in a suitable multivariate method.
- The results of the proposed bivariate analyses of spatial associations presented in this research are intuitive and instructive. In contrast, some of the spatial associations quantified via logistic regression analysis are

difficult to understand. Although, the validity of the above observation need to be tested in similar other geo-environments.

This research therefore outlines the obvious limitations of medium-scale landslide hazard and risk estimation and simultaneously outlines the necessary steps for similar studies in a geo-environment where historical records of past landslide events are either incomplete or scarce, such as in India. Therefore, the research recommends that the first and foremost steps for successful implementation of such studies is to maintain a continuous landslide event record in future with recording of date(s) of events, landslide type, location of affected area, damage, if any along with the intensity and duration of the triggering factor by developing preferably an online national network. This research also recommends that predictive mapping for landslide susceptibility which remains to be the foremost step of any landslide hazard and risk analysis should be based on quantifying the spatial associations between spatial factors and landslide type under study instead of relying only on the heuristically-identified causal factors. Therefore, methods proposed in this research can be used as a reasonably-reliable framework or guidelines for future studies in similar landslide-prone areas of India.

References

Acharya, S.K., Ray, S.K., 1977. Geology of Darjeeling-Sikkim Himalaya, Guide to 4th International Gondwana Symposium, Calcutta, 25 pp.

Acharya, S.K., 1989. The Daling Group, its nomenclature, tectonostratigraphy and structural grain: with notes on their possible equivalents. Geological Survey of India Special Publication No. 22, 5-13.

Aksoy, H., Ercanoglu, M., 2007. Fuzzified kinematic analysis of discontinuity-controlled rock slope instabilities. Engineering Geology 89, 206-219.

Aleotti, P., Chowdhury, R., 1999. Landslide hazard assessment: summary review and new perspectives. Bulletin of Engineering Geology and Environment 58, 21-44.

Aleotti, P., 2004. A warning system for rainfall-induced shallow failures. Engineering Geology 73, 247-265.

Altman, E., 1968. Financial ratios, discriminant analysis and the prediction of corporate bankruptcy. Journal of Finance, 189-209.

An, P., Moon, W.M., Bonham-Carter, G.F., 1994. Uncertainty management in integration of exploration data using the belief function. Nonrenewable Resources 3, 60-71.

Anbalagan, R., 1992. Landslide hazard evaluation and zonation mapping in mountainous terrain. Engineering Geology 32, 269-277.

Anbalagan, R., Singh, B., 1996. Landslide hazard and risk assessment mapping of mountainous terrains -- a case study from Kumaun Himalaya, India. Engineering Geology 43, 237-246.

Anbarasu, K., Sengupta, A., Gupta, S., Sharma, S., 2010. Mechanism of activation of the Lanta Khola landslide in Sikkim Himalayas. Landslides 7, 135-147.

Antinao, J.L., Gosse, J., 2009. Large rockslides in the Southern Central Andes of Chile (32-34.5°S): Tectonic control and significance for Quaternary landscape evolution. Geomorphology 104, 117-133.

Ayalew, L., Yamagishi, H., 2005. The application of GIS-based logistic regression for landslide susceptibility mapping in the Kakuda-Yahiko Mountains, Central Japan. Geomorphology 65, 15-31.

Baeza, C., Corominas, J., 2001. Assessment of shallow landslide susceptibility by means of multivariate statistical techniques. Earth surface processes and landforms 26, 1251-1263.

Banerji, P.K., Guha, P.K., Dhiman, I.C., 1980. Inverted metamorphism in the Sikkim-Darjeeling Himalaya. Journal of the Geological Society of India 21, 330-342.

Basu, S.R., De, S.K., 2003. Causes and consequences of landslides in Darjeeling-Sikkim Himalayas. Geographia Polonica 76, 37-52.

Bayes, T., 1764. An essay toward solving a problem in the doctrine of chances. Philosophical Transactions of the Royal Society of London 53, 370-418.

Begueria, S., 2006. Changes in land cover and shallow landslide activity: A case study in the Spanish Pyrenees. Geomorphology 74, 196-206.

Berman, M., 1977. Distance distributions associated with Poisson processes of geometric figures. Journal of Applied Probability 14, 195-199.

Berman, M., 1986. Testing for spatial associations between a point processes and another stochastic process. Applied Statistics 35, 62-64.

Beven, K., Kirby, M.J., 1979. A physically based, variable contributing area model of basin hydrology. Hydrological Science Bulletin 24, 43-69.

Bhattacharya, A., Mishra, P., Ghoshal, T.B., Bahuguna, H., Ghatak, T., 1998. A geotechnical appraisal of landslides on 7th July, 1998 along National Highway No. 55. Progress report (F.S. 1998-99): GSI.

Bieniawski, Z.T., 1989. Engineering Rock Mass Classifications. Wiley, New York.

Binnie, S.A., Phillips, W.M., Summerfield, M.A., Fifield, L.K., 2007. Tectonic uplift, threshold hillslopes and denudation rates in developing mountain range. Geology 35, 743-746.

BIS, 1998. Preparation of landslide hazard zonation maps in mountainous terrains - Guidelines, Bureau of Indian Standards (BIS) IS 14496 (Part - 2).

BIS, 2002. Criteria for earthquake resistant design of structures: General provisions and buildings, Bureau of Indian Standards (BIS) IS 1893:2002 (Part-1).

Blahut, J., van Westen, C.J., Sterlacchini, S., 2010. Analysis of landslide inventories for accurate prediction of debris-flow source areas. Geomorphology 119, 36-51.

Bonham-Carter, G.F., 1985. Statistical association of gold occurrences with Landsat derived lineaments, Timmins-Kirkland Lake area, Ontario. Canadian Journal of Remote Sensing 11, 195-211.

Bonham-Carter, G.F., 1994. Geographic Information Systems for Geoscientists: Modeling with GIS. Pergamon, Elsevier Science Ltd., 398 pp.

Bonham-Carter, G.F., Agterberg, F.P., Wright, D.F., 1989. Weights of evidence modelling: a new approach to mapping mineral potential. In: Agterberg, F.P., Bonham-Carter, G.F. (Eds.),

Statistical Applications in the Earth Sciences. Geological Survey of Canada Paper, pp. 171-183.

Boots, B.N., Getis, A., 1988. Point Pattern Analysis. Sage University Scientific Geography Series No. 8. Sage Publications, Baverly Hills, 99 pp.

Boroushaki, S., Malczewski, J., 2008. Implementing an extension of the analytical hierarchy process using ordered weighted averaging operators with fuzzy quantifiers in ArcGIS. Computers & Geosciences 34, 399-410.

Brabb, E., 1984. Innovative approaches to landslide hazard mapping, Proceeding of IV International Symposium on Landslides, Toronto, pp. 307-324.

Brand, E.W., Premchitt, J., Phillipson, H.B., 1984. Relationship between rainfall and landslides, Proceedings of the fourth International Symposium on Landslides, Vancouver, pp. 377-384.

Brardinoni, F., Church, M., 2004. Representing the landslide magnitude-frequency relation: Capilano River basin, British Columbia. Earth Surface Processes and Landforms 29, 115-124.

Burbank, D.W., Leland, J., Fielding, E., Anderson, R.S., Brozovic, N., Reid, M.R., Duncan, C., 1996. Bedrock incision, rock uplift and threshold hillslopes in the northwestern Himalayas. Nature 379, 505-510.

Cadoppi, P., Giardino, M., Perrone, G., Tallone, S., 2007. Litho-structural control, morphotectonics, and deep-seated gravitational deformations in the evolution of Alpine relief: A case study in the lower Susa Valley (Italian Western Alps). Quaternary International 171-172, 143-159.

Caine, N., 1980. The rainfall intensity duration control of shallow landslides and debris flows. Geografiska Annaler 62A, 23-27.

Cardinali, M., Reichenbach, P., Guzzetti, F., Ardizzone, F., Antonini, G., Galli, M., Cacciano, M., Castellani, M., 2002. A geomorphological approach to the estimation of landslide hazards and risks in Umbria, Central Italy. Natural Hazards and Earth System Sciences 2, 57-72.

Carranza, E.J.M., 2002. Geologically-Constrained Mineral Potential Mapping (Examples from the Philippines).PhD Thesis, Delft University of Technology, The Netherlands. ITC Publication No. 86, ITC, Enschede, 496 pp.

Carranza, E.J.M., Hale, M., 2003. Evidential belief functions for data-driven geologically constrained mapping of gold potential, Baguio district, Philippines. Ore Geology Reviews 22, 117-132.

Carranza, E.J.M., 2004. Weights of Evidence Modeling of Mineral Potential: A Case Study Using Small Number of Prospects, Abra, Philippines. Natural Resources Research 13, 173-187.

Carranza, E.J.M., Castro, O., 2006. Predicting Lahar-Inundation Zones: Case Study in West Mount Pinatubo, Philippines. Natural Hazards 37, 331-372.

Carranza, E.J.M., Wibowo, H., Barritt, S.D., Sumintadireja, P., 2008a. Spatial data analysis and integration for regional-scale geothermal potential mapping, West Java, Indonesia. Geothermics 37, 267-299.

Carranza, E.J.M., Hale, M., Faassen, C., 2008b. Selection of coherent deposit-type locations and their application in data-driven mineral prospectivity mapping. Ore Geology Reviews 33, 536-558.

Carranza, E.J.M., 2008. Geochemical anomaly and mineral prospectivity mapping in GIS. Handbook of exploration and environmental geochemistry, Vol. 11. Elsevier, Amsterdam, 366 pp.

Carranza, E.J.M., 2009. Controls on mineral deposit occurrence inferred from analysis of their spatial pattern and spatial association with geological features. Ore Geology Reviews 35, 383-400.

Carrara, A., 1983. Multivariate models for landslide hazard evaluation. Mathematical Geology 15, 403-426.

Carrara, A., Cardinali, M., Detti, R., Guzzetti, F., Pasqui, V., Reichenbach, P., 1991. GIS techniques and statistical models in evaluating landslide hazard. Earth surface processes and landforms 16, 427-445.

Carrara, A., 1999. Use of GIS Technology in the Prediction and Monitoring of Landslide Hazard. Natural Hazards 20, 117-135.

Carrara, A., 1989. Landslide hazard mapping by statistical methods: a "black box" model approach. In: CNR-USNSF (Eds.), Proceed. Int. Workshop Natural Disasters in Europe-Mediterr. Countries, Perugia, pp. 205-224.

Carrara, A., Cardinali, M., Guzzetti, F., Reichenbach, P. (Eds.), 1995. GIS technology in mapping landslide hazard. Geographical information systems in assessing natural hazards. Kluwer Academic Publishers, 135-175 pp.

Carrara, A., 1993. Potentials and pitfalls of GIS technology in assessing natural hazards. In: Guzzetti, F., Reichenbach, P., Carrara, A. (Eds.), Geographical Information Systems in Assessing Natural Hazards — Abstracts. CNR, Perugia, pp. 128-137.

Census of India, 2001. Directorate of Census Operations, West Bengal, Census of India.

Champati ray, P., Dimri, S., Lakhera, R., Sati, S., 2007. Fuzzy-based method for landslide hazard assessment in active seismic zone of Himalaya. Landslides 4, 101-111.

Chleborad, A.F., Baum, R.L., Godt, J.W., 2006. Rainfall Thresholds for Forecasting Landslides in the Seattle, Washington, Area—Exceedance and Probability. In: USGS (Eds.), Open-File Report 2006-1064. USGS, pp. 35.

Chowdhury, R., Flentje, P., 2002. Uncertainties in rainfall-induced landslide hazard. Quarterly Journal of Engineering Geology and Hydrogeology 35, 61-70.

Chung, C.-J.F., Fabbri, A.G., 1993. The representation of geoscience information for data integration. Nonrenewable Resources 2, 122-139.

Chung, C.-J.F., Fabbri, A.G., 1999. Probabilistic prediction models for landslide hazard mapping. Photogrammetric Engineering and Remote Sensing 65, 1389-1399.

Chung, C.-J.F., 2006. Using likelihood ratio functions for modeling the conditional probability of occurrence of future landslides for risk assessment. Computers & Geosciences 32, 1052-1068.

Chung, C.-J.F., Fabbri, A.G., van Westen, C.J., 1995. Multivariate regression analysis for landslide hazard zonation. In: Carrara, A., Guzzetti, F. (Eds.), Geographical Information Systems in Assessing Natural Hazards. Kluwer Academic Publishers, Netherlands, pp. 107-133.

Coe, J.A., Michael, J.A., Crovelli, R.A., Savage, W.Z., Laprade, W.T., Nashem, W.D., 2004. Probabilistic Assessment of Precipitation-Triggered Landslides Using Historical Records of Landslide Occurrence, Seattle, Washington. Environmental and Engineering Geoscience 10, 103-122.

Crovelli, R.A., 2000. Probability models for estimation of number and costs of landslides, US Geological Survey Open File Report 00-249, available at http://pubs.usgs.gov/of/2000/ofr-00-0249/ProbModels.html.

Crozier, M., 2005. Multiple-occurrence regional landslide events in New Zealand: Hazard management issues. Landslides 2, 247-256.

Crozier, M.J., 1999. Prediction of rainfall-triggered landslide: a test of antecedent water status model. Earth surface processes and landforms 24, 825-833.

Cruden, D., Varnes, D.J., 1996. Landslide types and processes. In: Turner, A.K., Schuster, R.L. (Eds.), Landslides Investigation and Mitigation. Special Report 247. Transportation Research Board, National Academy of Sciences, Washington, D.C., pp. 36-75.

Cruden, D.M., 1989. Limits to common toppling. Canadian Geotechnical Journal 26, 737-742.

Cruden, D.M., 1997. Estimating the risk from landslides using historical data. In: Cruden, D., Fell, R. (Eds.), Landslide risk assessment. A.A. Balkema, Rotterdam, pp. 177-184.

Dahal, R.K., Hasegawa, S., 2008. Representative rainfall thresholds for landslides in the Nepal Himalaya. Geomorphology 100, 429-443.

Dai, F.C., Lee, C.F., 2001. Frequency-volume relation and prediction of rainfall-induced landslides. Engineering Geology 59, 253-266.

Dai, F.C., Lee, C.F., 2002. Landslide characteristics and slope instability modeling using GIS, Lantau Island, Hong Kong. Geomorphology 42, 213-228.

Dapporto, S., Aleotti, P., Casagli, N., Polloni, G., 2005. Analysis of shallow failures triggered by the 14–16 November 2002 event in the Albaredo valley, Valtellina (Northern Italy). Advances in Geociences 2, 305-308.

Dasgupta, S., Mukhopadhyay, M., Nandy, D.R., 1987. Active transverse features in the central portion of the Himalaya. Tectonophysics 136, 255-264.

De Kemp, E.A., 1998. Three-dimensional projection of curvilinear geological features through direction cosine interpolation of structural field observations. Computers & Geosciences 25, 269-284.

De Kemp, E.A., 1999. Visualization of complex geological structures using 3-D Bézier construction tools. Computers & Geosciences 25, 581-597.

Dempster, A.P., 1967. Upper and lower probabilities induced by a multivalued mapping. Annals of Mathematical Statistics 38, 325-339.

Dempster, A.P., 1968. A generalization of Bayesian inference. Journal of the Royal Statistical Society B30, 205-247.

DeRose, R.C., Trustrum, N.A., Blaschke, P.M., 1991. Geomorphic change implied by regolith - Slope relationships on steepland hillslopes, Taranaki, New Zealand. Catena 18, 489-514.

Di Luzio, E., Saroli, M., Esposito, C., Bianchi-Fasani, G., Cavinato, G.P., Scarascia-Mugnozza, G., 2004. Influence of structural framework on mountain slope deformation in the Maiella anticline (Central Apennines, Italy). Geomorphology 60, 417-432.

Dietrich, W.E., Wilson, C.J., Reneau, S.L., 1986. Hollows, colluvium and landslides in soil-mantled landscapes. In: Abrahams, A.D. (Eds.), Hillslope Processes. Allen and Unwin, Boston, pp. 361-386.

Einstein, H.H., 1997. Landslide risk - Systematic approaches to assessment and management. In: Cruden, D., Fell, R. (Eds.), Landslide risk assessment. A.A. Balkema, Rotterdam, pp. 25-50.

Fabbri, A.G., 2003. Is prediction of future landslides possible with a GIS? Natural Hazards 30, 487-503.

Fawcett, T., 2006. An introduction to ROC analysis. Pattern Recognition Letters 27, 861-874.

Fell, R., Corominas, J., Bonnard, C., Cascini, L., Leroi, E., Savage, W.Z., 2008. Guidelines for landslide susceptibility, hazard and risk zoning for land use planning. Engineering Geology 102, 85-98.

Fisher, R.A., 1922. On the mathematical foundations of theoretical statistics. Philosophical Transactions of the Royal Society of London Series A, 309-368.

Fleiss, J.L., 1991. Statistical Methods for Rates and Proportions. John Wiley and Sons, Chichester.

Frattini, P., Crosta, G., Carrara, A., 2010. Techniques for evaluating the performance of landslide susceptibility models. Engineering Geology 111, 62-72.

Fry, N., 1979. Random point distributions and strain measurements in rocks. Tectonophysics 60, 89-105.

Gabet, E.J., Burbank, D.W., Putkonen, J.K., Pratt-Sitaula, B.A., Ojha, T., 2004. Rainfall thresholds for landsliding in the Himalayas of Nepal. Geomorphology 63, 131-143.

Gabet, E.J., Wolff-Boenisch, D., Langner, H., Burbank, D.W., Putkonen, J., 2010. Geomorphic and climatic controls on chemical weathering in the High Himalayas of Nepal. Geomorphology 122, 205-210.

Galli, M., Ardizzone, F., Cardinali, M., Guzzetti, F., Reichenbach, P., 2008. Comparing landslide inventory maps. Geomorphology 94, 268-289.

Ghosh, S., van Westen, C.J., Carranza, E.J.M., Ghoshal, T., Sarkar, N., Surendranath, M., 2009a. A quantitative approach for improving the BIS (Indian) method of medium-scale landslide susceptibility. Journal of the Geological Society of India 74, 625-638.

Ghosh, S., Günther, A., Carranza, E.J.M., van Westen, C.J., Jetten, V.G., 2010. Rock slope instability assessment using spatially distributed structural orientation data in Darjeeling Himalaya (India). Earth surface processes and landforms 35, 1773-1792.

Ghosh, S., Carranza, E.J.M., 2010. Spatial analysis of mutual fault/fracture and slope controls on rocksliding in Darjeeling Himalaya, India. Geomorphology 122, 1-24.

Ghosh, S., van Westen, C.J., Carranza, E.J.M., Jetten, V.G., Cardinali, M., Rossi, M., Guzzetti, F., 2011a. Generating event-based landslide maps in a data-scarce Himalayan environment for estimating temporal and magnitude probabilities. Engineering Geology In Press, Corrected Proof.

Ghosh, S., Carranza, E.J.M., van Westen, C.J., Jetten, V.G., Bhattacharya, D.N., 2011b. Selecting and weighting spatial predictors for empirical modeling of landslide susceptibility in the Darjeeling Himalayas (India). Geomorphology 131, 35-56.

Ghosh, S., van Westen, C.J., Carranza, E.J.M., Jetten, V.G., Submitted in Landslides. Integrating spatial, temporal and magnitude probability for medium scale landslide hazard and risk analysis in Darjeeling Himalayas (India)" Landslides.

Ghosh, S., van Westen, C.J., Carranza, E.J.M., Jetten, V.G., 2009b. Generation of event - based landslide inventory maps in a data - scarce environment : case study around Kurseong, Darjeeling district, West Bengal, India. In: Malet, J.P., Remaitre, A., Bogaard, T. (Eds.). Landslide processes : from geomorphologic mapping to dynamic modeling : proceedings of the landslide processes. European Centre on Geomorphological Hazards (CERG), 2009, Strasbourg, France, pp. 37-44.

Ghoshal, T.B., Sarkar, N.K., Ghosh, S., Surendranath, M., 2008. GIS based landslide susceptibility mapping - a study from Darjeeling-Kalimpong area, Eastern Himalaya, India. Journal of the Geological Society of India 72, 763-773.

Glade, T., Anderson, M., Crozier, M.J., 2005. Landslide Hazard and Risk. John Wiley & Sons, Ltd., Chichester, England, 802 pp.

Gokceoglu, C., Sonmez, H., Ercanoglu, M., 2000. Discontinuity controlled probabilistic slope failure risk maps of the Altindag (settlement) region in Turkey. Engineering Geology 55, 277-296.

Good, I.J., 1950. Probability and the Weighing of Evidence. Griffin, London, 119 pp.

Goodman, R.E., Bray, J.W., 1976. Toppling of rock slopes. Proc. Speciality Conference on Rock Engineering for Foundations and Slopes. American Sociey of Civil Engineers (ASCE), Boulder, Colorado.

Günther, A., 2003. SLOPEMAP: programs for automated mapping of geometrical and kinematical properties of hard rock hill slopes. Computers and Geoscience 865-875.

Günther, A., Carstensen, A., Pohl, W., 2004. Automated sliding susceptibility mapping of rock slopes. Natural Hazards and Earth System Sciences 4, 95-102.

Günther, A., Thiel, C., 2009. Combined rock slope stability and shallow landslide susceptibility assessment of the Jasmund cliff area (Rügen Island, Germany). Natural Hazards and Earth System Sciences 9, 687-698.

Gupta, R.P., Joshi, B.C., 1990. Landslide hazard zoning using the GIS approach--A case study from the Ramganga catchment, Himalayas. Engineering Geology 28, 119-131.

Gupta, R.P., Kanungo, D.P., Arora, M.K., Sarkar, S., 2008. Approaches for comparative evaluation of raster GIS-based landslide susceptibility zonation maps. International Journal of Applied Earth Observation and Geoinformation 10, 330-341.

Gupta, S.K., Saha, A.K., Arora, M.K., Kumar, A., 1999. Landslide hazard zonation in a part of the Bhagirathi valley, Garhwal Himalayas, using integrated remote sensing - GIS. Himalyan Geology 20, 71-85.

Gupta, V., 2005. The relationship between tectonic stresses, joint patterns and landslides in higher Indian Himalaya. Journal of Nepal Geological Society 31, 51-58.

Guthrie, R.H., Evans, S.G., 2004. Analysis of landslide frequencies and characteristics in a natural system, coastal British Columbia. Earth Surface Processes and Landforms 29, 1321-1339.

Guzzetti, F., Carrara, A., Cardinali, M., Reichenbach, P., 1999. Landslide hazard evaluation: a review of current techniques and their application in a multi-scale study, Central Italy. Geomorphology 31, 181-216.

Guzzetti, F., Cardinali, M., Reichenbach, P., Carrara, A., 2000. Comparing landslide maps: A case study in the upper Tiber River Basin, central Italy. Environmental Management 25, 247-263.

Guzzetti, F., 2000. Landslide fatalities and the evaluation of landslide risk in Italy. Engineering Geology 58, 89-107.

Guzzetti, F., Malamud, B.D., Turcotte, D.L., Reichenbach, P., 2002. Power-law correlations of landslide areas in central Italy. Earth and Planetary Science Letters 195, 169-183.

Guzzetti, F., Cardinali, M., Reichenbach, P., Cipolla, F., Sebastiani, C., Galli, M., Salvati, P., 2004. Landslides triggered by the 23 November 2000 rainfall event in the Imperia Province, Western Liguria, Italy. Engineering Geology 73, 229-245.

Guzzetti, F., Reichenbach, P., Cardinali, M., Galli, M., Ardizzone, F., 2005. Probabilistic landslide hazard assessment at the basin scale. Geomorphology 72, 272-299.

Guzzetti, F., Ardizzone, F., Cardinali, M., Galli, M., Reichenbach, P., Rossi, M., 2008. Distribution of landslides in the Upper Tiber River basin, central Italy. Geomorphology 96, 105-122.

Hack, Hack, R., Price, Price, D., Rengers, Rengers, N., 2003. A new approach to rock slope stability – a probability classification (SSPC). Bulletin of Engineering Geology and the Environment 62, 167-184.

Hansen, A., 1984. Landslide hazard analysis. In: Brunsden, D., Prior, E. (Eds.), Slope Instability. John Wiley & Sons., New York, pp. 523-602.

Harp, E.L., Jibson, R.L., 1996. Landslides triggered by the 1994 Northridge, California earthquake. Seismological Society of America Bulletin 86, S319–S332.

Hoek, E., Bray, J.W., 1981. Rock slope engineering, London.

Holm, K., Bovis, M., Jakob, M., 2004. The landslide response of alpine basins to post-Little Ice Age glacial thinning and retreat in southwestern British Columbia. Geomorphology 57, 201-216.

Hosmer, D.W., Lomeshow, S., 2000. Applied logistic regression. John Wiley & Sons, New York.

Hubbard, M., 1996. Ductile shear as a cause of inverted metamorphism: example from Nepal Himalaya. Journal of Geology 194, 493-499.

Hungr, O., Evans, S.G., Hazzard, J., 1999. Magnitude and frequency of rock falls and rock slides along the main transportation corridors of southwestern British Columbia. Can. Geotech. J. 36, 224-238.

Ives, J.D., Messerli, B., 1989. The Himalayan Dilemma - Reconciling development and conservation. The United Nations University, Routledge, London-New York, 295 pp.

Jaboyedoff, M., Baillifard, F., Philippossian, F., Rouiller, J.D., 2004. Assessing fracture occurrence using "weighted fracturing density": a step towards estimating rock instability hazard. Natural hazards Earth System Science 4, 83-93.

Jaboyedoff, M., Couture, R., Locat, P., 2009. Structural analysis of Turtle Mountain (Alberta) using digital elevation model: Toward a progressive failure. Geomorphology 103, 5-16.

Jaiswal, P., van Westen, C.J., 2009. Estimating temporal probability for landslide initiation along transportation routes based on rainfall thresholds. Geomorphology 112, 96-105.

Joshi, G.R., Hayashi, D., 2008. FE stress analysis and Quaternary deformation in the fold-and-thrust belt of the Garhwal Himalaya. Bulletin of the Faculty of Science of the University of Ryukyus 85, 1-37.

Kanungo, D., Arora, M., Gupta, R., Sarkar, S., 2008. Landslide risk assessment using concepts of danger pixels and fuzzy set theory in Darjeeling Himalayas. Landslides 5, 407-416.

Kanungo, D.P., Arora, M.K., Sarkar, S., Gupta, R.P., 2006. A comparative study of conventional, ANN black box, fuzzy and combined neural and fuzzy weighting procedures for landslide susceptibility zonation in Darjeeling Himalayas. Engineering Geology 85, 347-366.

Kienholz, H., Hafner, H., Schneider, G., Tamrakar, R., 1983. Mountain Hazards Mapping in Nepal's Middle Mountains Maps of Land Use and Geomorphic Damages (Kathmandu-Kakani Area). Mountain Research and Development 3, 195-220.

Kinakin, D., Stead, D., 2005. Analysis of the distributions of stress in natural ridge forms: implications for the deformation mechanisms of rock slopes and the formation of sackung. Geomorphology 65, 85-100.

Kirschbaum, D., Adler, R., Hong, Y., Hill, S., Lerner-Lam, A., 2010. A global landslide catalog for hazard applications: method, results, and limitations. Natural Hazards 52, 561-575.

Komac, M., 2006. A landslide susceptibility model using the Analytical Hierarchy Process method and multivariate statistics in perialpine Slovenia. Geomorphology 74, 17-28.

Korup, O., Densmore, A.L., Schlunegger, F., 2010. The role of landslides in mountain range evolution. Geomorphology 120, 77-90.

Lee, E.M., Jones, D.K.C., 2004. Landslide risk assessment. ThomasTelford, London, 454 pp.

Lee, S., Choi, J., 2004. Landslide susceptibility mapping using GIS and weight of evidence model. International Journal Geographical Information Science 18, 789-814.

Lee, S., Dan, N., 2005. Probabilistic landslide susceptibility mapping in the Lai Chau province of Vietnam: focus on the relationship between tectonic fractures and landslides. Environmental Geology 48, 778-787.

Lu, P., Rosenbaum, M.S., 2003. Artificial Neural Networks and Grey Systems for the Prediction of Slope Stability Natural hazards 30, 383-398.

Lumb, P., 1975. Slope failures in Hong Kong. Engineering Geology 8, 31-65.

Malamud, B.D., Turcotte, D.L., Guzzetti, F., Reichenbach, P., 2004. Landslide inventories and their statistical properties. Earth Surface Processes and Landforms 29, 687-711.

Mallet, F., 1875. On the geology and mineral resources of the Darjeeling district and the western Duars. Memoirs of Geological Survey of India, 11, 1-50 pp.

Mark, R.K., Ellen, S.D., 1995. Statistical and simulation models for mapping debris-flow hazard. In: Carrara, A., Guzzetti, F. (Eds.), Geographical information systems in assessing natural hazards. Kluwer Academic Publishers, Dordrecht, pp. 93-106.

Martha, T.R., Kerle, N., Jetten, V., van Westen, C.J., Vinod Kumar, K., 2010. Characterising spectral, spatial and morphometric properties of landslides for (semi-) automatic detection using object-oriented methods. Geomorphology 116, 24-36.

Matheson, G.D., 1983. Rock stability assessment in preliminary site investigations - graphical methods. Transport and Road Research Laboratory, Crownthorne, Berkshire, UK, Report 1039.

Mathew, J., Jha, V.K., Rawat, G.S., 2007. Weights of evidence modelling for landslide hazard zonation mapping in part of Bhagirathi valley, Uttarakhand. Current Science 92, 628-638.

Mathew, J., Jha, V.K., Rawat, G.S., 2009. Landslide susceptibility zonation mapping and its validation in part of Garhwal Lesser

Himalaya, India, using binary logistic regression analysis and receiver operating characteristic curve method. Landslides 6, 17-26.

Mathur, H.N., 1982. Influence of human activities on landslides, mudflows and slope movements in India and efforts at reducing their negative impact. In: Sheko, A.I. (Eds.), Landslides and mudflows-Reports of the Alma-Ata International seminar, GKNT, Moskow, pp. 20-44.

Meentemeyer, R.K., Moody, A., 2000. Automated mapping of conformity between topographic and geological surfaces. Computers and Geoscience 26, 815-829.

Nadim, F., Kjekstad, O., 2009. Assessment of Global High-Risk Landslide Disaster Hotspots. In: Sassa, K., Canuti, P. (Eds.), Landslides - Diaster Risk Reduction. Springer, pp. 213-221.

Nandy, D.R., Dasgupta, S., 1991. Seismotectonic domains of northeastern India and adjacent areas. Physics and Chemistry of The Earth 18, 371-384.

NDMA, 2009, Management of Landslides and Snow Avalanches, 2009. National Disaster Management Authority (NDMA), Government of India, New Delhi, 144 pp.

Neuhäuser, B., Terhorst, B., 2007. Landslide susceptibility assessment using "weights-of-evidence" applied to a study area at the Jurassic escarpment (SW-Germany). Geomorphology 86, 12-24.

Neuland, H., 1976. A prediction model of landslips. Catena 3, 215-230.

OFDA/CRED, 2010. EM-DAT International Disaster Database - www.em-dat.net. Université Catholique de Louvain, Brussels, Belgium.

Orr, C.M., 1996. Use of Rock Mass Rating (RMR) system in assessing the stability of rock slopes, Milestones in rock mechanics. Balkema, pp. 159-172.

Pachauri, A.K., Gupta, P.V., Chander, R., 1998. Landslide zoning in a part of the Garhwal Himalayas. Environmental Geology 36, 325-334.

Pan, G.C., Harris, D.P., 2000. Information Synthesis for Mineral Exploration. Oxford University Press, 461 pp.

Pandey, M.R., Tandukar, R.P., Avouac, J.P., Vergne, J., Héritier, T., 1999. Seismotectonics of the Nepal Himalaya from a local seismic network. Journal of Asian Earth Sciences 17, 703-712.

Pantelidis, L., 2009. Rock slope stability assessment through rock mass classification systems. International Journal of Rock Mechanics and Mining Sciences 46, 315-325.

Park, H.J., West, T.R., Woo, I., 2005. Probabilistic analysis of rock slope stability and random properties of discontinuity parameters,

Interstate Highway 40, Western North Carolina, USA. Engineering Geology 79, 230-250.

Paul, C., Sarkar, N.K., 2003. A note on the recent landslide damage assessment along different road stretches in Darjeeling Hills, West Bengal (as an aftermath of July 2003 deluge). Progress report (F.S. 2003-04): GSI.

Peters, T., Mool, P.K., 1983. Geological and Petrographic Base Studies for the Mountain Hazards Mapping Project in the Kathmandu-Kakani Area, Nepal. Mountain Research and Development 3, 221-226.

Petley, D., Hearn, G., Hart, A., Rosser, N., Dunning, S., Oven, K., Mitchell, W., 2007. Trends in landslide occurrence in Nepal. Natural Hazards 43, 23-44.

Petley, D.N., Dunning, S.A., Rosser, N.J., 2005. The analysis of global landslide risk through the creation of a database of worldwide landslide fatalities. In: Hungr, O., Fell, R., Couture, R., Eberhardt, E. (Eds.), Landslide risk management. Taylor & Francis Group, London, pp. 367-373.

Poli, S., Sterlacchini, S., 2007. Landslide Representation Strategies in Susceptibility Studies using Weights-of-Evidence Modeling Technique. Natural Resources Research 16, 121-134.

Pradhan, B., 2010. Remote sensing and GIS-based landslide hazard analysis and cross-validation using multivariate logistic regression model on three test areas in Malaysia. Advances in Space Research 45, 1244-1256.

Pratt, J.W., 1976. F. Y. Edgeworth and R. A. Fisher on the efficiency of Maximum Likelihood Estimation. The Annals of Statistics 4, 501-514.

R Development Core Team, 2010. R: A language and environment for statistical computing, R Foundation for Statistical Computing, Vienna, Austria, ISBN 3-900051-07-0. http://www.R-project.org.

Rasmussen, H.H., Pitt, E.A., Ibels, L.S., McNeil, D.R., 1985. Prediction of outcome in acute renal failure by discriminant analysis of clinical variables. Archives of Internal Medicine 145, 2015-2018.

Rautela, P., Lakhera, R.C., 2000. Landslide risk analysis between Giri and Tons Rivers in Himachal Himalaya (India). International Journal of Applied Earth Observation and Geoinformation 2, 153-160.

Regmi, N.R., Giardino, J.R., Vitek, J.D., 2010. Assessing susceptibility to landslides: Using models to understand observed changes in slopes. Geomorphology 122, 25-38.

Rib, H.T., Liang, T. (Eds.), 1978. Recognition and Identification: Landslides-Analysis and control Special Report, 176, National Academy of Sciences. Transport Research Board, Washington D.C., 34-80 pp.

Roering, J.J., Kirchner, J.W., Dietrich, W.E., 2005. Characterizing structural and lithologic controls on deep-seated landsliding: Implications for topographic relief and landscape evolution in the Oregon Coast Range, USA. Geological Society of America Bulletin 117, 654-668.

Rogers, N.W., Selby, M.J., 1980. Mechanisms of Shallow Translational Landsliding during Summer Rainstorms: North Island, New Zealand. Geografiska Annaler. 62, 11-21.

Romana, M. (Ed.), 1985. A geomechanics classification for slopes: Slope Mass Rating. Comprehensive rock engineering. Pergamon Press, 575-600 pp.

Rossi, M., Guzzetti, F., Reichenbach, P., Mondini, A.C., Peruccacci, S., 2010a. Optimal landslide susceptibility zonation based on multiple forecasts. Geomorphology 114, 129-142.

Rossi, M., Witt, A., Guzzetti, F., Malamud, B.D., Peruccacci, S., 2010b. Analysis of historical landslide time series in the Emilia-Romagna region, northern Italy. Earth Surface Processes and Landforms 35, 1123-1137.

Roy, S., Mandal, N., 2009. Modes of hill-slope failure under overburden loads: Insights from physical and numerical models. Tectonophysics 473, 324-340.

Saaty, T.L., 1977. A scaling method for priorities in hierarchical structures. Journal of the Mathematical Psychology 15, 234-281.

Saaty, T.L., 1996. The Analytic Hierarchy Process. McGraw Hill, 1980, New York.

Saha, A.K., Gupta, R.P., Arora, M.K., 2002. GIS-based Landslide Hazard Zonation in the Bhagirathi (Ganga) Valley, Himalayas. International Journal of Remote Sensing 23, 357 - 369.

Salvati, P., Bianchi, C., Rossi, M., Guzzetti, F., 2010. Societal landslide and flood risk in Italy. Nat. Hazards Earth Syst. Sci. 10, 465-483.

Schill, W., Jockel, K.H., Drescher, K., Timm, J., 1993. Logistic analysis in case-control studies under validation sampling. Biometrika 80, 339-352.

Searle, M.P., Szulc, A.G., 2005. Channel flow and ductile extrusion of the high Himalayan slab-the Kangchenjunga-Darjeeling profile, Sikkim Himalaya. Journal of Asian Earth Sciences 25, 173-185.

Selby, M.J., 1993. Hillslope materials and processes. Oxford University Press, Oxford.

Sengupta, C.K., 1995. Detailed study of geofactors in selected hazard prone stretches along the surface communication routes in parts of Darjeeling and Sikkim Himalaya, Phase-I, Part-I (Rongtong-Kurseong road section). Progress report (F.S. 1993-94):GSI.

Serafim, J.L., Pereira, J.P. (Eds.), 1983. Considerations on the geomechanical classification of Bieniawski Proc. Int. Symp. Eng. Geol. Underground Constr. Balkema, Rotterdam.

Shafer, G., 1976. A Mathematical Theory of Evidence. Princeton University Press, Princeton (N.J.).

Sharma, M., Kumar, R., 2008. GIS-based landslide hazard zonation: a case study from the Parwanoo area, Lesser and Outer Himalaya, H.P., India. Bulletin of Engineering Geology and the Environment 67, 129-137.

Shroder, J.F., 1998. Slope failure and denudation in the western Himalaya. Geomorphology 26, 81-105.

Shroder, J.F., Bishop, M.P., 1998. Mass movement in the Himalaya: new insights and research directions. Geomorphology 26, 13-35.

Singh, K., Thakur, V.C., 2001. Microstructures and strain variation across the footwall of the Main Central Thrust Zone, Garhwal Himalaya, India. Journal of Asian Earth Sciences 19, 17-29.

Sinha-Roy, S., 1982. Himalayan Main Central Thrust and its implication for Himalayan inverted metamorphism. Tectonophysics 84, 197-224.

Sitar, N., MacLaughlin, M.M., Doolin, D.M., 2005. Influence of Kinematics on Landslide Mobility and Failure Mode. Journal of Geotechnical and Geoenvironmental Engineering 131, 716-728.

Soja, R., Starkel, L., 2007. Extreme rainfalls in Eastern Himalaya and southern slope of Meghalaya Plateau and their geomorphologic impacts. Geomorphology 84, 170-180.

Sorriso-Valvo, M., Antronico, L., Gaudio, R., Gullà, G., Iovine, G., Merenda, L., Minervino, I., Nicoletti, P.G., Petrucci, O., Terranova, O., 2004. Map of mass movement, erosion and flooding coused in south Calabria by the 8-10 september 2000 storms, CNR Gruppo Nazionale per la Difesa dalle Catastrofi Idrogeologiche Publication n. 2859, Rubettino Industrie Grafiche ed Editoriali, map at 1:50,000 scale (in Italian and English).

Stark, C., P., Hovius, N., 2001. The characterisation of landslide size distributions. Geophysical Research Letters 28, 1091-1094.

Starkel, L., Basu, S., 2000. Rains, landslides and floods in the Darjeeling Himalaya. Indian National Science Academy, New Delhi, 168 pp.

Starkel, L., 2004. Extreme rainfall at 5-7 July 1998 in the Darjeeling Himalaya. In: Sing, S., Sharma, H.S., De, S.K. (Eds.), Geomorphology and environment. ABC Publications, Kolkata, pp. 26-31.

Strahler, A.N., 1957. Quantitative analysis of watershed geomorphology. Trans. Amer. Geophy. Union 38, 913-920.

Surendranath, M., Ghosh, S., Ghoshal, T.B., Rajendran, N., 2008. Landslide Hazard Zonation in Darjeeling Himalayas: a Case Study

on Integration of IRS and SRTM Data. In: Nayak, S., Zlatanova, S. (Eds.), Remote Sensing and GIS Technologies for Monitoring and Prediction of Disasters, pp. 121-135.

Süzen, M.L., Doyuran, V., 2004. Data driven bivariate landslide susceptibility assessment using geographical information systems: a method and application to Asarsuyu catchment, Turkey. Engineering Geology 71, 303-321.

Swan, A.R.H., Sandilands, M., 1995. Introduction to Geological Data Analysis. Blackwell, 446 pp.

Swanson, F.J., Dyrness, C.T., 1975. Impact of clear-cutting and road construction on soil erosion by landslides in the western Cascade Range, Oregon. Geology 3, 393-396.

Taylor, G., Eggleton, R.A., 2001. Regolith geology and geomorphology. John Wiley & Sons, Ltd., 367 pp.

Terlien, M.T.J., 1998. The determination of statistical and deterministic hydrological landslide-triggering thresholds. Environmental Geology 35, 124-130.

Thiery, Y., Malet, J.P., Sterlacchini, S., Puissant, A., Maquaire, O., 2007. Landslide susceptibility assessment by bivariate methods at large scales: Application to a complex mountainous environment. Geomorphology 92, 38-59.

UNESCO-WP/WLI, 1990. A suggested method for reporting a landslide. Bulletin of the International Association of Engineering Geology, 5-12.

UNESCO-WP/WLI, 1993. Multilingual Landslide Glossary. Bitech Publishers Ltd, Richmond, 34 pp.

Van Den Eeckhaut, M., Reichenbach, P., Guzzetti, F., Rossi, M., Poesen, J., 2009. Combined landslide inventory and susceptibility assessment based on different mapping units: an example from the Flemish Ardennes, Belgium. Nat. Hazards Earth Syst. Sci. 9, 507-521.

van Westen, C.J., 1993. Remote Sensing and Geographic Information Systems for Geological Hazard Mitigation. ITC-Journal 4, 393-399.

van Westen, C.J., 2000. The modelling of landslide hazards using GIS. Surveys in Geophysics 21, 241-255.

van Westen, C.J., Rengers, N., Soeters, R., 2003. Use of geomorphological information in indirect landslide susceptibility assessment. Natural Hazards 30, 399-419.

van Westen, C.J., van Asch, T.W.J., Soeters, R., 2006. Landslide hazard and risk zonation—why is it still so difficult? Bulletin of Engineering Geology and Environment 65, 167-184.

van Westen, C.J., Castellanos, E., Kuriakose, S.L., 2008. Spatial data for landslide susceptibility, hazard, and vulnerability assessment: An overview. Engineering Geology 102, 112-131.

Varnes, D.J., 1984. Landslide Hazard Zonation: a review of principles and practice. UNESCO Press, Darantiere, Paris, 61 pp.

Varnes, D.J., 1978. Slope movements types and processes. In: Schuster, R.L., Krizek, R.L. (Eds.), Landslides: Analysis and Control. Special Report 176. Transportation Research Board, National Academy of Sciences, Washington, D.C., pp. 11-33.

Vearncombe, J., Vearncombe, S., 1999. The spatial distribution of mineralization: applications of Fry analysis. Economic Geology 94, 475-486.

Vuichard, D., 1986. Geological and Petrographical Investigations for the Mountain Hazards Mapping Project, Khumbu Himal, Nepal. Mountain Research and Development 6, 41-51.

Wagner, A., Leite, E., Olivier, R., 1988. Rock and debris-slides risk mapping in Nepal -- a user-friendly PC system for risk mapping. In: Bonnard, C. (Eds.), Proc 5th International Symposium on Landslides. Publ Rotterdam: A A Balkema, Lausanne, pp. 1251-1258.

Wallbrecher, E., 1986. Tektonische und gefügeanalytische Arbeitsweisen. Enke-Verlag, Stuttgart (in German).

Walley, P., 1987. Belief function representations of statistical evidence. The Annals of Statistics 15, 1439-1465.

Weidinger, J.T., Schramm, J.-M., Surenian, R., 1996. On preparatory causal factors, initiating the prehistoric Tsergo Ri landslide (Langthang Himal, Nepal). Tectonophysics 260, 95-107.

Weidinger, J.T., 2006. Predesign, failure and displacement mechanisms of large rockslides in the Annapurna Himalayas, Nepal. Engineering Geology 83, 201-216.

Weidinger, J.T., Korup, O., 2009. Frictionite as evidence for a large Late Quaternary rockslide near Kanchenjunga, Sikkim Himalayas, India -- Implications for extreme events in mountain relief destruction. Geomorphology 103, 57-65.

Weidinger, J.T., 2007. Petrologic and structural control on geomorphology of rapid landscape changing large rockslides in the Himalayas. In: Kellerer-Pirklbauer, A., Embleton-Hamann, C., Keiler, M., Stötter, J. (Eds.). Geomorphology for the Future. Conference Series, Innsbruck university press (online available under: www.geomorph.at), pp. 185-192.

Wesnousky, S.G., Kumar, S., Mohindra, R., Thakur, V.C., 1999. Uplift and convergence along the Himalayan Frontal Thrust of India. Tectonics 18, 967-976.

Wieczorek, G.F., 1984. Preparing a detailed landslide-inventory map for hazard evaluation and reduction. Bulletin of the Association of Engineering Geologists XXI, 337-342.

Woodcock, N.H., 1977. Specification of fabric shapes using an eigenvalue method. Geological Society of America Bulletin 88, 1231-1236.

Wu, T.W., Swanston, D.N., 1980. Risk of Landslides in Shallow Soils and its Relation to Clearcutting in Southeastern Alaska. Forest Science 26, 495-510.

Yalcin, A., 2008. GIS-based landslide susceptibility mapping using analytical hierarchy process and bivariate statistics in Ardesen (Turkey): Comparisons of results and confirmations. CATENA 72, 1-12.

Yin, K.L., Yan, T.Z., 1988. Statistical prediction models for slope instability of metamorphosed rocks. In: Bonnard, C. (Eds.), Proc 5th International Symposium on Landslides. Publ Rotterdam: A Balkema, Lausanne, pp. 1269-1272.

Zaruba, Q., Mencl, V., 1969. Landslides and their control. In: Cepek, L. (Eds.). Elsevier Publication, Amsterdam, pp. 205.

Zêzere, J.L., Garcia, R.A.C., Oliveira, S.C., Reis, E., 2008. Probabilistic landslide risk analysis considering direct costs in the area north of Lisbon (Portugal). Geomorphology 94, 467-495.

Zimmermann, M., Bichsel, M., Kienholz, H., 1986. Mountain Hazards Mapping in the Khumbu Himal, Nepal. Mountain Research and Development 6, 29-40.

Summary

Every year during monsoon large parts of the Indian mountains experience a substantial loss of properties and lives due to various types of landsliding events. For mitigating this disaster, predictive maps of landslide hazard and risk, preferably at medium scales (1:25,000 to 1:50,000) provide vital geo-information to the administrators/planners. Landslide hazard maps that are currently available in India are, at best, qualitative landslide susceptibility maps based mainly on the heuristic guidelines for quickly assessing large areas where landslides can occur. Due to the absence of suitable methods pertaining to the Indian geo-environment (e.g. the Himalayas), translating those maps into the actual expected impacts of landslides is a difficult task, which precludes the subsequent hazard and risk analysis. Therefore, the prime aim of this research is to propose an effective method for medium scale landslide hazard and risk analysis suitable for the Indian geo-environment which can be readily used by the public research Institutes/Organisations engaged in landslide research in India. The proposed method considered the variability and complexities of the one of the predominant landslide-prone terrains (e.g., the Darjeeling Himalayas) and the landsliding processes prevalent there, so that the aspects of variable controls of landsliding factors can be better understood and the potential adverse impacts of landslides to life and property can suitably be minimised. This proved challenging because landslide source data sets in India like many other countries are usually scarce and/or filled with incomplete information.

Predictive mapping of landslide susceptibility still remains to be the first and foremost step for any hazard and risk analysis. This research demonstrated that due to variable terrain conditions and different landsliding processes, predictive mapping of landslide susceptibility based only on heuristic/subjective guidelines, where a specified number of factors and/or specified factor-weights are considered could be of limited use. In contrast, the empirical methods of landslide susceptibility can perform better and can easily be transformed into maps that are able to portray the actual impacts of landslide events.

The empirical methods (e.g., statistical or mathematical) of landslide susceptibility mapping depend on two types of spatial associations: (a) spatial associations of individual spatial factors with historic landslides of a certain type; and (b) the relative importance of individual spatial factors with respect to one another in relation to landslide occurrences. Although, multivariate statistical methods can simultaneously model both the above two types of empirical spatial associations, yet some of the spatial factors selected and

used by them according to certain (statistical) criteria are sometimes not representative of specific genetic processes associated with the type of landslides being studied. Whereas, bivariate statistical methods, although intuitive, can only model the first type of spatial association, and thereby, exhibit moderate prediction rates. Therefore this research demonstrates a suitable empirical method to study the spatial association to (a) select the most appropriate spatial factors that approximate realistic genetic associations with landslides of a certain type, and (b) objectively determine the importance of every spatial factor with respect to the others in relation to the landslide type under study and combine them using the multivariate methods. The proposed empirical technique can interactively and iteratively augment the empirical model processes that estimate susceptibility, which is subsequently used to prepare the landslide hazard and risk maps.

Scarcity of information on past landslides acts as a serious deterrent in correctly predicting the landslide hazard scenarios and thereby affects the quantitative risk assessment because quantitative landslide hazard and risk analysis requires the availability of sufficient historical landslide information in order to correctly estimate the spatial, temporal and magnitude probabilities. This could be another main reason why landslide scientists in India rely more on susceptibility maps to do a qualitative landslide impact assessment. Despite the above unavoidable constraints, this research proposes suitable methods for the determination of temporal and magnitude probabilities of landsliding events by generating and using event-based landslide inventory maps prepared with the available source datasets. Thus, this research presented a method for quantitative landslide hazard and risk analysis, by generating a series of landslide hazard scenario maps based on the magnitude of triggering events and landslide event-days from a continuous record of 40 years (1968-2007), and to study and analyse their corresponding variation in landslide density and temporal likelihoods. Based on the above plausible landslide hazard scenarios, this research presents suitable methods of medium-scale (1:25,000) landslide risk estimation with varying levels of uncertainty in expected loss assessment to buildings, population, and roads. The varying levels of uncertainty in such loss assessment were caused due to the obvious limitations in the past landslide and its damage data. With the above, the present research addresses the fact that in literature, not much research on landslide hazard and risk estimation in a data-scarce environment is available, where varying levels of uncertainties that are expected to propagate in quantitative landslide hazard and risk assessment are shown.
This research recommends that the predictive mapping for landslide susceptibility which remained to be the foremost step of any landslide hazard and risk analysis should be based on quantifying the spatial associations

between spatial factors and the landslide type under study instead of relying solely on the heuristically or subjectively identified causal factors and its pre-defined weights and further, to lessen the uncertainty in hazard and risk estimation, this research demonstrates that maintaining a continuous landslide event database for use in future are of prime necessity.

Samenvatting

Tijdens de jaarlijkse moessonperiode ondervinden grote delen van de berggebieden in India problemen met aardverschuivingen, die kunnen resulteren in aanzienlijke schade aan eigendommen en verlies van mensenlevens. Om tot vermindering van de negatieve effecten van deze rampen te komen, hebben lokale autoriteiten en planners behoefte aan gevaren- en risicokaarten, meestal op een middelgrote schaal (1:25.000 tot 1:50.000). De gevarenkaarten die momenteel beschikbaar zijn in India kunnen gekarakteriseerd worden als relatieve gevoeligheidskaarten, vervaardigd volgens richtlijnen waarin informatie van experts gebruikt wordt voor een snelle inventarisatie van mogelijk gevaarlijke gebieden voor aardverschuivingen. Vanwege het ontbreken van geschikte methodes gericht op de Indiase geologische omgeving (bijvoorbeeld het Himalaya gebergte) is het gebruik van dit type kaarten voor het schatten van de te verwachten negatieve effecten van massabewegingen een moeilijke taak, en is het vaak onmogelijk om deze te gebruiken in gevaren en risicoanalyse. Gezien het voorgaande probleem is het belangrijkste doel van dit onderzoek om een geschikte methode te ontwikkelen voor gevaren en risicoanalyse voor aardverschuivingen op middelgrote schaal, toegespitst op de Indiase situatie, en die toegepast kan worden door Indiase instituten en onderzoeksorganisaties. De voorgestelde methode is uitgetest in een van de meest complexe gebieden in de Indiase Himalaya (Darjeeling), dat gekenmerkt wordt door een grote variabiliteit aan processen. Het doel is om de verschillende oorzaken voor deze fenomenen het beste in de analyse te kunnen integreren, zodat op basis van de resultaten de mogelijke negatieve impact voor eigendommen en mensenlevens tot een minimum beperkt kan worden. Dit is een grote uitdaging, mede omdat de beschikbaarheid van historische informatie over het voorkomen van aardverschuivingen in India zeer beperkt en incompleet is.

Het voorspellen van de gevoeligheid van het terrein voor aardverschuivingen is de eerste belangrijke stap in een gevaren en risicoanalyse. Dit onderzoek heeft aangetoond dat, vanwege de grote variabiliteit van het terrein en de types van aardverschuivingen, het onvoldoende is om zulke gevoeligheidskartering te baseren op subjectieve, expert-gebaseerde richtlijnen, waarin gebruikt wordt gemaakt van vaste weegfactoren voor een beperkt aantal aspecten. Het is beter om gebruikt te maken van empirische methodes waarin de relatie tussen massabewegingen en hun oorzaken wordt onderzocht op basis van statistische analyse. Deze methoden geven een betere mogelijkheid voor het maken van kaarten welke gebruikt kunnen worden om de impact van deze gevaren te kwantificeren.

Deze empirische methodes (bijv. statistisch of mathematisch) voor het bepalen van de gevoeligheid voor aardverschuivingen zijn afhankelijk van twee soorten van ruimtelijke associaties: (a) ruimtelijke associaties van individuele ruimtelijke factoren met historische locaties van aardverschuivingen van een bepaald type; and (b) het relatieve belang van individuele ruimtelijke factoren in relatie tot andere factoren voor het voorkomen van massabewegingen.

Hoewel *multivariate statistische* methoden beide bovengenoemde ruimtelijke associaties tegelijk kunnen modelleren, bestaat er toch de mogelijkheid dat sommige van de ruimtelijke factoren die door het model gebruikt worden volgens bepaalde (statistische) criteria niet representatief zijn voor de specifieke genetische processen die gerelateerd zijn aan bepaalde types van massabewegingen. *Bivariate statistische* methoden aan de andere kant zijn meer intuïtief in het gebruik, maar kunnen enkel het eerste type van bovengenoemde ruimtelijke associaties modelleren, en resulteren over het algemeen in voorspellingen van mindere kwaliteit. Dit onderzoek presenteert een bruikbare empirische methode voor de studie van ruimtelijke associaties om (a) de meest geschikte ruimtelijke factoren te selecteren die de realistische associaties met het ontstaan van aardverschuivingen kunnen benaderen met behulp van *bivariate statistische* methodes, en (b) objectief te bepalen wat het belang is van elke ruimtelijke factor in samenhang met andere factoren en met specifieke types van massabewegingen gebruik makend van *multivariate statistische* methodes. De gepresenteerde methode is in staat om interactief en iteratief een optimaal model voor de gevoeligheid voor massabewegingen te genereren, welke vervolgens gebruikt kan worden voor het maken van gevaren en risicokaarten.

Het gebrek aan informatie met betrekking tot historische massabewegingen is een belangrijk obstakel voor het correct voorspellen van scenario's voor massabewegingen, en het bepalen van de te verwachte schade, omdat deze informatie essentieel is voor het bepalen van de ruimtelijke, temporele en magnitude waarschijnlijkheden. Dit is een belangrijke reden waarom onderzoekers in India meer belang hechten aan relatieve gevoeligheidskaarten voor het maken van kwalitatieve schade analyses. Dit onderzoek toont een bruikbare methode voor het bepalen van temporele en magnitude waarschijnlijkheid door middel van het reconstrueren van kaarten van massabewegingen die ontstaan zijn door hetzelfde voorval (zoals extreme regenval of aardbevingen) vanuit bestaande datasets en satellietbeelden. Het onderzoek presenteert een methode voor kwantitatieve gevaren en

risicoanalyse voor massabewegingen, door middel van het genereren van een aantal aardverschuivingskaarten veroorzaakt door extreme regenval periodes in de afgelopen 40 jaar (1968 to 2007), waarbij elke periode wordt gekenmerkt door de hoeveelheid regenval, de tijdsduur, de dichtheid van massabewegingen, en de terugkeerperiode. De gevarenscenario's worden vervolgens gebruikt in combinatie met informatie over gebouwen, bevolking en wegen, voor het bepalen voor de te verwachte schade op een middelgrote schaal (1:25.000) met een variabele mate van onzekerheid. Deze onzekerheid wordt voornamelijk veroorzaakt door de beperkte hoeveelheid historische informatie.

Dit onderzoek levert een belangrijke bijdrage, aangezien in de literatuur relatief weinig gepubliceerd is over het maken van aardverschuivinggevaar en risicoschatting in een omgeving met beperkt beschikbare gegevens, en de daarmee samenhangende niveaus van onzekerheid. De belangrijkste aanbeveling uit dit onderzoek is om gedetailleerde reconstructies te maken van historische aardverschuivingskaarten voor de belangrijkste regenval periodes en aardbevingen, en deze te gebruiken voor een analyse van de ruimtelijke associaties tussen de verschillende types van massabewegingen en de ruimtelijke factoren zoals topografie, gesteentes, oppervlaktematerialen, structurele geologie en landgebruik. Deze methode zal leiden tot meer betrouwbare risicokaarten dan die welke gebaseerd zijn of kwalitatieve methodes met behulp van vaste weegfactoren. Het zal leiden to een vermindering van de onzekerheid in gevaar en risicoanalyse, en is aanbevolen als standaardmethode voor Indiase berggebieden. Het in stand houden van een continue inventarisatie en digitale database van massabewegingen is daarom van groot belang.

Curriculum vitae

SAIBAL GHOSH was born on 15th December 1967 in Kolkata, India. He completed his higher-secondary level (10+2) education from the Hare School, Kolkata, India in 1986. He did his graduation (Bachelor of Science) with a major in Geology from the Presidency College, Kolkata, India in 1989. He completed his Master of Science (M.Sc.) degree in Applied Geology in 1991 from the Indian Institute of Technology (IIT), Kharagpur, India and subsequently completed his Master of Technology (M.Tech.) degree in Applied Geology in 1993 from the same institute after successfully qualifying the Graduate Aptitude Test in Engineering (GATE) in 1991. He joined as a Geologist in the Geological Survey of India (GSI) on 14th June 1994 through UPSC's Indian Geologists' Examination and is still working there presently as a Senior Geologist. During his Masters level, he did his dissertation on the evolution of recent sedimentary structures in a deltaic environment (M.Sc.) and on the sedimentary evolution of the Gilbert-type deltaic formations of the Lower Gondwana rocks in the Talchir Gondwana Basin, Orissa, India (M.Tech.) respectively. In GSI, he has been associated with a number of hydroelectric projects in the north-east and eastern Himalayas of India (Arunachal Pradesh, Sikkim, Darjeeling) as a consultant engineering geologist. Apart from taking up geological investigations in various such engineering geology projects, he has also been engaged simultaneously in various regional and site-specific landslide investigations in Darjeeling-Sikkim Himalayas since 2001. In 2007, he has been selected by GSI as one of the research-fellows to pursue the present Ph.D. research on landslide hazard and risk at ITC, The Netherlands, under an Indo-Dutch Joint Research Agreement between ITC, GSI and NRSC. He is married and has one son.

List of Publications

Ghosh, S., Carranza, E.J.M., van Westen, C.J., Jetten, V.G., Bhattacharya, D.N., 2011. Selecting and weighting spatial predictors for empirical modeling of landslide susceptibility in the Darjeeling Himalayas (India). Geomorphology 131, 35-56..

Ghosh, S., van Westen, C.J., Carranza, E.J.M., Jetten, V.G., Cardinali, M., Rossi, M., Guzzetti, F., 2011. Generating event-based landslide maps in a data-scarce Himalayan environment for estimating temporal and magnitude probability. Engineering Geology (accepted, in press).

Ghosh, S., Carranza, E.J.M., 2010. Spatial analysis of mutual fault/fracture and slope controls on rocksliding in Darjeeling Himalaya, India. Geomorphology 122, 1-24.

Ghosh, S., Günther, A., Carranza, E.J.M., van Westen, C.J., Jetten, V.G., 2010. Rock slope instability assessment using spatially distributed structural orientation data in Darjeeling Himalaya (India). Earth surface processes and landforms 35, 1773-1792.

Ghosh, S., van Westen, C.J., Carranza, E.J.M., Ghoshal, T., Sarkar, N., Surendranath, M., 2009a. A quantitative approach for improving the BIS (Indian) method of medium-scale landslide susceptibility. Journal of the Geological Society of India 74, 625-638.

Ghosh, S., van Westen, C.J., Carranza, E.J.M., Jetten, V.G., 2009b. Generation of event - based landslide inventory maps in a data - scarce environment : case study around Kurseong, Darjeeling district, West Bengal, India. In: Malet, J.P., Remaitre, A., Bogaard, T. (Eds.). Landslide processes : from geomorphologic mapping to dynamic modeling : proceedings of the landslide processes. European Centre on Geomorphological Hazards (CERG), 2009, Strasbourg, France, pp. 37-44.

Ghosh, S., van Westen, C.J., Carranza, E.J.M., Jetten, V.G., 2011. Integrating spatial, temporal and magnitude probability for medium scale landslide hazard and risk analysis in Darjeeling Himalayas (India)". Landslides (under review).

Ghoshal, T.B., Sarkar, N.K., **Ghosh, S.**, Surendranath, M., 2008. GIS based landslide susceptibility mapping - a study from Darjeeling-Kalimpong area, Eastern Himalaya, India. Journal of the Geological Society of India 72, 763-773.

Surendranath, M., **Ghosh, S.**, Ghoshal, T.B., Rajendran, N., 2008. Landslide Hazard Zonation in Darjeeling Himalayas: a Case Study on Integration of IRS and SRTM Data. In: Nayak, S., Zlatanova, S. (Eds.), Remote Sensing and GIS Technologies for Monitoring and Prediction of Disasters, pp. 121-135.

ITC Dissertation List

http://www.itc.nl/Pub/research/Graduate-programme/Graduate-programme-PhD_Graduates.html